THE UNIVERSITY *of* EDINBURGH

PaleoENSO Reconstructions of the Holocene and Last Glacial Period

Robin Eleanor Driscoll

Thesis submitted for the degree of
Doctor of Philosophy
University of Edinburgh

July 2014

Declaration:

This thesis and the work presented therein is my own original composition. Where it draws on the work of others, this is acknowledged at the appropriate points in the text.

Robin Driscoll

Acknowledgements

First and foremost I would to thank my supervisors, Mary Elliot and Sandy Tudhope for all of their help. I would like to acknowledge the help of Colin Chilcott for assistance with stable isotopic analysis, Wolfgang Müller and Viola Warter for trace element analysis, Nic Odling for X-ray diffraction analysis, and Mike Hall for thin section preparation.

Special thanks go to Kevin Welsh and Tom Russon for the masses of help given. Thanks too to the Oceans and Past Climate group for many fascinating (but sporadic) meetings.

Thanks to all my friends and family. In Edinburgh, Emma Turner for housing me on visits to Edinburgh and providing pizza and fun, Gillian McCay for Grant Institute gossip, and Rachel Kilgallon, Robyn Tuerena, Carley Iles, Sian Henley, Luke Ridley and Amber Annett. In London and Wales, Jen, Louisa, Naomi and Sarah have all provided much moral support over the past four years. Thanks also to USSP attendees, to Paddy, Anna Joy, Tom, Rosanna, Michael and Will for conference adventures in Italy, Sitges and London. Particular thanks to Joe Rayner, and to Maggie Driscoll for proof-reading this thesis and correcting my split infinitives.

Abstract

In this study, specimens of *Tridacna* sp., which are reef dwelling bivalve molluscs and have been shown to live up to 60 years, collected from the Huon Peninsula, Papua New Guinea, were sampled for geochemical profiles. The Huon Peninsula is in the heart of the Western Pacific Warm Pool (WPWP), which plays a key role in ENSO dynamics. The uplifted reef terraces of the Huon Peninsula have been extensively studied, and are well dated, which gives the opportunity to reconstruct the local climate of this region at key intervals during the past.

Previous work on *Tridacna* sp. has shown that they precipitate their aragonite shell in equilibrium with the surrounding seawater, and the $\delta^{18}O$ profile of a modern *T. gigas* from the Huon Peninsula has been shown to correlate with precipitation and temperature anomalies, and the Niño 3.4 temperature anomaly record. Fossil samples from this region are therefore assumed to have the ability to capture changes in $\delta^{18}O$ attributable to ENSO.

Seasonally resolved $\delta^{18}O$ measurements from *Tridacna* sp. from early Holocene and Marine Isotope Stage 3 (MIS3) reefs were used to reconstruct changes in mean climate, seasonality and inter-annual variability (e.g. ENSO). Reconstructions of the mean state tend to agree with previously published studies of Holocene and MIS3 climate, showing similar temperatures to today during the early Holocene, and an average cooling of 2-3°C during MIS3. The early Holocene *Tridacna* sp. samples show a reduction in seasonality, consistent with the reduction in seasonal insolation at this time, while those from MIS3 show variable seasonality between 30-60ka. ENSO appears to have been supressed during the early Holocene by up to 50% compared with the late 20th century, which is consistent with coral data and modelling studies. During MIS3, ENSO appears to have been more variable with some records showing anomalous warm and cool events as strong as those seen in the modern *T. gigas*, used here as a benchmark.

Trace element profiles derived from the *Tridacna* sp. used in this study show a tentative link with temperature and local productivity, but these relationships are subject to species specific and intra-shell effects.

Contents

1. Introduction 1
1.1 Modern ENSO 1
1.1.1 ENSO in the instrumental record 5
1.2 PaleoENSO reconstructions 7
1.2.1 The tropical Pacific over the past 65 ka 8
1.2.2 Orbital forcing and ENSO 9
1.3 Aims of this study 10
2. Study area and *Tridacna* sp. as a climate archive 13
2.1 The study site 14
2.1.1 Geological setting and uplift rates 14
2.1.2 Holocene reef terrace 17
2.1.3 MIS3 terraces 17
2.1.4. Sample collection 19
2.2 Modern oceanographic and climatological setting 19
2.3 The ecology of *Tridacna sp.* 24
2.3.1 Growth in bivalves 27
2.3.2 Geochemical tracers measured on *Tridacna* sp.: the climate archive 29
2.4 *Tridacna* sp. used in this study 30
2.4.1 Dating and chronology 31
2.4.2 Preservation 34
2.5 Concluding remarks 35
3. Methods and Results 37
3.1 Introduction 38
3.2 Methods 39
3.2.1 Sample preparation 39
3.2.2 Screening for diagenesis 40
3.2.3 Stable isotopes ($\delta^{18}O$ and $\delta^{13}C$) 40
3.2.4 Geochemical analysis and data processing 43
3.2.5 Chronology construction 44
3.3 Results from Holocene reef *Tridacna gigas* (10 – 6.5 ka BP) 52
3.4 Results from MIS3 *Tridacna* sp. (~60 – 34 ka BP) 55
3.5 Effects of processing $\delta^{18}O$, $\delta^{13}C$ and trace element data 59
4. Background Climate Conditions at the Huon Peninsula during the Holocene and MIS3 65
4.1 Introduction 66
4.2 Correcting for ice volume effect 70
4.2.1 Mean $\delta^{18}O$ in the Holocene 70
4.2.2 Mean $\delta^{18}O$ in MIS3 72

4.3 Discussion: Reconstructing the mean state of the tropical Pacific 74
4.3.1 Mean state derived from *T. gigas* $\delta^{18}O$ profiles during the Early Holocene 74
4.3.2 Mean state derived from *Tridacna* sp. $\delta^{18}O$ during MIS3 77
4.4 The carbon isotope record ($\delta^{13}C$) 80
4.4.1 Mean $\delta^{13}C$ results from modern and fossil *Tridacna* sp 81
4.4.2 Effects of ontogeny 82
4.4.3 Relationship between $\delta^{18}O$ and $\delta^{13}C$ 83
4.5 Conclusions 85
5. Potential Use of Trace Element Ratios Measured in Fossil *Tridacna* sp. 87
5.1 Introduction 88
5.2 Summary of previous findings in *Tridacna* sp. 91
5.3 Methods 95
5.4 Results: Trace element ratios in fossil *Tridacna* sp. 96
5.5 Discussion 101
5.5.1 The limitations of Sr/Ca and Mg/Ca as a tool for SST reconstructions in *Tridacna* sp. 101
5.5.2 Can Sr/Ca be used as a temperature proxy? 102
5.5.3 Mg/Ca – is growth masking the temperature signal? 104
5.6 The use of Ba/Ca as a productivity proxy 106
5.6.1 Ba/Ca in Holocene *Tridacna gigas* 109
5.6.2 Ba/Ca in MIS3 *Tridacna* sp. 109
5.6.3 Ba/Ca over the past 60 ka 111
5.7 Conclusions 113
6. Reconstructing ENSO variability from *Tridacna* sp. $\delta^{18}O$ time series 115
6.1 Introduction 116
6.2 Methods 118
6.3 Methods for reconstructing ENSO variance in proxy climate records 119
6.3.1 Quantitative methods of calculating inter-annual variability 119
6.3.2 Comparison of methods in modern records 123
6.3.3 Calculating events using a threshold 124
6.4 Results: Reconstructing ENSO in modern and fossil *Tridacna* sp. 125
6.4.1 Results from the modern *Tridacna gigas* 125
6.4.2 Reconstructing ENSO variability in Holocene *Tridacna gigas* 127
6.4.3 Reconstructing ENSO variability in MIS3 *Tridacna* sp. 129
6.5 Discussion 133
6.5.1 Comparison of ENSO metrics 133
6.5.2 Comparison of methods in Holocene *T. gigas* samples 134
6.5.3 Comparison of methods in MIS3 fossil *Tridacna* sp. 135
6.5.4 Frequency of El Niño and La Niña recorded by fossils 136
6.5.5 Comparison of variance derived from fossil corals, SST and *Tridacna* 137

6.5.6 PaleoENSO recorded at the Huon Peninsula....139
6.6 Conclusions....141
7. Changes in Seasonality and ENSO over the past 60 ka....143
7.1 Introduction....144
7.2 Methods....146
7.3 Results....148
7.3.1 Seasonally resolved profiles of *T. gigas* $\delta^{18}O$ during the Early Holocene....148
7.3.2 Seasonally resolved $\delta^{18}O$ profiles of MIS3 *Tridacna* sp. 150
7.4 Discussion....157
7.4.1 Seasonality recorded in early Holocene *T. gigas*....157
7.4.2 Seasonality recorded in MIS3 *Tridacna* sp. $\delta^{18}O$....161
7.4.3 Reduced ENSO variability recorded in Holocene *T. gigas* $\delta^{18}O$ profiles 163
7.4.4 Potential mechanisms on Early Holocene ENSO 168
7.4.5 Variable ENSO during MIS3....170
7.4.6 Potential mechanisms acting on MIS3 ENSO 172
7.4.7 Relationship between ENSO and seasonality....175
7.5 Conclusions....176
8. Conclusions and Future Work....177
8.1 General conclusions....177
8.2 Further work....178
References....181

Chapter 1

1. Introduction

The El Niño Southern Oscillation (ENSO) arises from large-scale interactions between the ocean and the atmosphere in the core region of the tropical Pacific and Indian Ocean basins. It is the largest source of annual variability in the modern climate system (Jin et al., 2003, Collins, 2005), and has worldwide ecological and economic impacts (Cane, 2005). ENSO is associated with basin-wide fluctuations in sea surface temperature and precipitation, caused by an interaction between oceanic and atmospheric processes, which operates on a semi-periodic timescale (typically 2-7 years). Data from the tropical Pacific have shown that ENSO has been active in the climate system for the past 130,000 years (Tudhope et al., 2001), with El Niño-like events observed as far back as the Eocene (56 – 33.4 Ma) (Huber and Caballero, 2003, Ivany et al., 2011) and the Miocene (23.03 – 5.33 Ma) (Galeotti et al., 2010). These seasonally resolved climate archives suggest that ENSO variability (the intensity, frequency and timing of events) has not remained constant over time (e.g. Tudhope et al., 2001, McGregor and Gagan, 2004, Cobb et al., 2013) and may be forced by changes in background climate such as mean global temperature (Tudhope et al., 2001), Milankovitch forcing (Clement et al., 1999), and volcanic forcing (Mann et al., 2005). Developing an understanding of the dynamics of ENSO and its response to different global background states is crucial to understanding how ENSO will develop in the future. There is, as yet, no consensus as to the development and behaviour of ENSO under increasing atmospheric CO_2 (Collins, 2000, Zelle et al., 2005, Merryfield, 2006, Collins et al., 2010, Kim and Yu, 2012, Cai et al., 2014). The aim of this work is to reconstruct past ENSO variability under different background states, which can help to improve the understanding of how the ENSO system responds to changes in climatic boundary conditions. There is a lack of high-resolution proxy climate data from the last glacial period, and the data presented here

1.1 Modern ENSO

El Niño and the Southern Oscillation (SO) are the oceanic and atmospheric components of a single phenomenon, referred to as ENSO (Cane, 1986). ENSO occurs semi-periodically on typically 2-7 year periods, with two distinct events (states); i.e. El Niño and La Niña. El Niño (Figure 1.1) is associated with or characterised by changes in the

surface winds over the tropical Pacific Ocean, and occurs when trade winds are weak, pressure is anomalously low over the eastern Pacific and anomalously high over the western tropical Pacific, and there are higher than normal sea surface temperatures (SSTs) in the central and eastern Pacific (Philander, 1990).

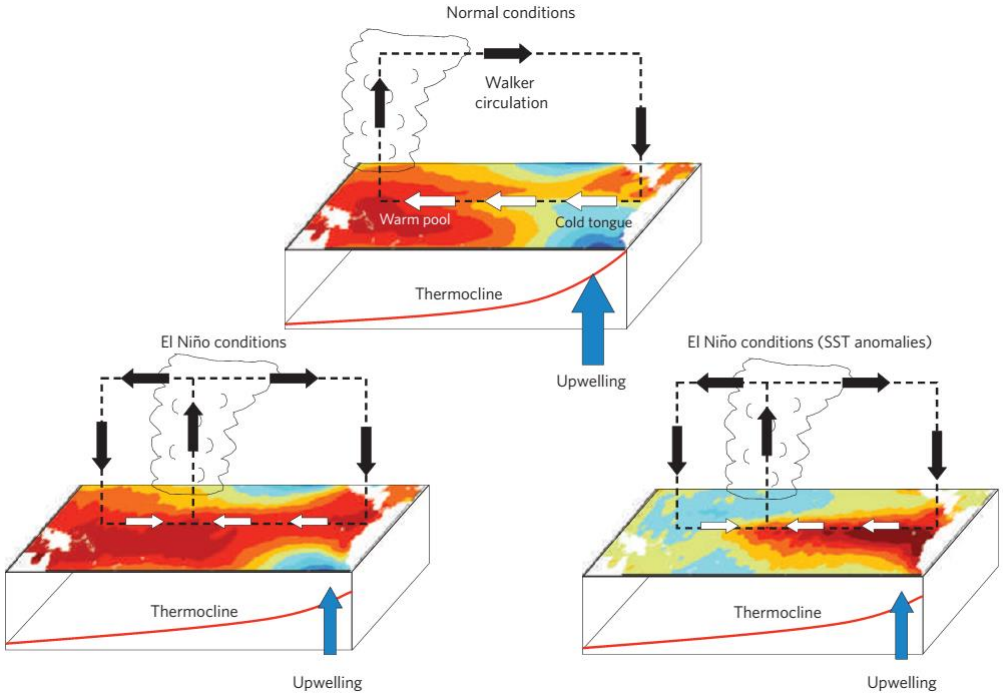

Figure 1.1 Idealised schematic view of atmospheric and oceanic conditions of the tropical Pacific region during normal and El Niño conditions. Top – mean climate conditions indicating SSTs, surface wind stress and Walker circulation, the mean position of convection and the mean upwelling and position of the thermocline.
Below – typical conditions during an El Niño event. SSTs are anomalously warm in the east, convection moves into the central Pacific, the trade winds weaken in the east and the Walker circulation is disrupted, the thermocline flattens and upwelling is reduced (Collins et al., 2010)

Theoretical explanations of ENSO dynamics tend to fall in to one of two categories. The first is that ENSO is a stable mode of the coupled ocean-atmosphere system, triggered by stochastic forcing or noise (Wyrtki, 1975), such as westerly wind bursts or larger than usual sea surface elevation gradients (Tsonis et al., 2003). The second is that El Niño is one phase of a self-sustained, unstable oscillating mode. Both categories involve the positive feedback mechanism first described by Bjerknes (1969).

While every El Niño event is different, a "composite" El Niño can be described based on many past events (Cane, 1986). Preceding an El Niño event, there are stronger than average easterlies in the western equatorial Pacific. Water is moved westward,

resulting in higher sea level than normal in the west, and lower than normal in the east. Equatorial SST is slightly warmer in the west, and colder east of 160°E. The northward extension across the equator of the south Pacific warm anomaly is associated with the northeast shift of the South Pacific Convergence Zone (SPCZ). Easterlies west of the date line start to diminish, and the sea level gradient is reduced, accompanied by positive precipitation anomalies west of the date line. The actual El Niño event begins in the first months of the year, with an anomalous warming off the coast of South America. This is accompanied by a rise in sea level and a deepening of the thermocline along the coast. The SST anomaly persists between February and June, westerly wind anomalies occur along the equator from 110°W to 170°E, and the Intertropical Convergence Zone shifts towards the equator in the east, resulting in enhanced convergence and precipitation. From June onwards, the warm anomaly spreads northwestward and westward along the equator, and the eastern anomaly merges with the central Pacific anomaly. During the mature phase of El Niño, SST drops sharply after reaching a peak (i.e. the maximum anomaly), and is slightly colder than normal by March-April, with sea level following a similar pattern (Cane, 1986). During El Niño, the barometric pressure over vast areas of the south east Pacific falls, while the pressure rises over Indonesia and northern Australia (Gates, 1993). There are also changes in salinity during El Niño events, with sea surface salinity (SSS) decreases in the equatorial band around 150°E - 140°W as a result of zonal advection of low salinity water by anomalous eastward surface currents and rainfall excess (Picaut et al., 1996, Delcroix et al., 1998), with the reverse occurring during La Niña. Although there are some general characteristics which remain similar (described above), no two El Niño events are identical (Figure 1.2), and there is variability in the generation of different episodes (Molnar and Cane, 2007).

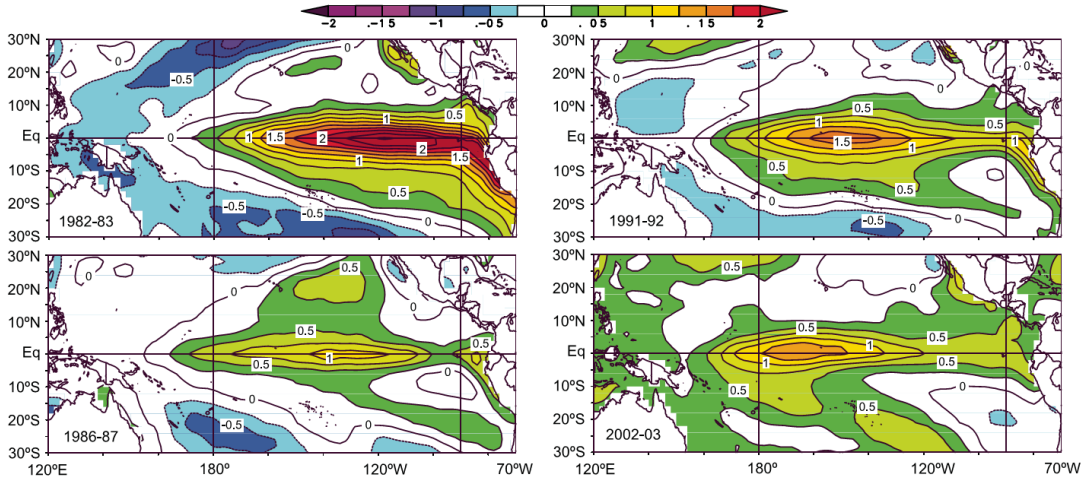

Figure 1.2 Map of equatorial Pacific sea surface temperature anomalies for four recent major El Niño events (1982-83, 1986-87, 1991-92, 2002-03) (Molnar and Cane, 2007)

La Niña involves unusually low SSTs in the central and eastern tropical Pacific, with very intense trade winds (Philander, 1990), which lead to a basin-wide cooling (Trenberth, 1997). A La Niña may form when, towards the end of an El Niño, the trade winds strengthen rather than returning to normal, leading to the cold-water tongue normally found in the eastern Pacific stretching farther westward than normal due to increased upwelling, confining water to the western tropical Pacific (Tsonis et al., 2003). During a La Niña, the pressure increases over the eastern Pacific and becomes lower over the western Pacific and the Indian Ocean (Gates, 1993). The climatic effects of El Niño and La Niña events are not limited to the Pacific Ocean, but have a significant influence on the global climate through atmospheric teleconnections (e.g. Figure 1.3) (Diaz and Kiladis, 1992). ENSO appears to modulate temperature and precipitation in the Rio Grande basin, south western USA, with higher precipitation, streamflow and lower temperatures during El Niño, and the opposite occurring during La Niña (Lee et al., 2004). In north-eastern Africa, increased precipitation occurs during El Niño, which can cause an amplification of the regular Nile River flooding (Tsonis et al., 2003). These are only two examples of ENSO teleconnections. As well as climatic effects, El Niño and La Niña also have global effects on ecological processes such as plant development and flowering (e.g. Holmgren et al., 2001, Kitzberger et al., 2001).

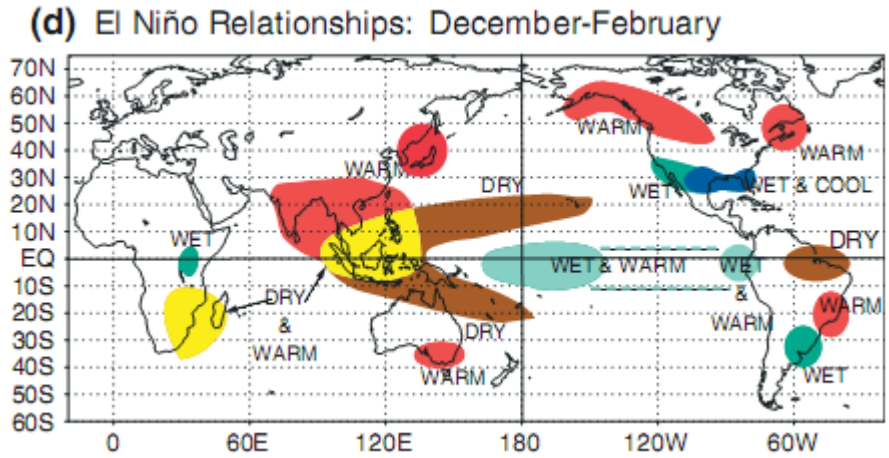

Figure 1.3 Schematic of teleconnections during El Niño conditions in Northern Hemisphere winter (December-February) (Vecchi and Wittenberg, 2010)

1.1.1 ENSO in the instrumental record

ENSO variability is controlled by a balance of feedbacks, and the physical processes responsible for determining the characteristics of ENSO are likely to be modified by climate change (Collins et al., 2010). Extreme El Niños (such as the 1982-83 and 1997-98 events) are likely to increase as a result of warmer SSTs in the equatorial Pacific, as a weaker SST anomaly is required to establish warmer water over the equatorial eastern Pacific (Cai et al., 2014). Changes in the background climate state go some way in explaining why the properties of ENSO differ over time (Fedorov and Philander, 2000), with some time periods having more frequent/intense or longer El Niño episodes and vice versa with La Niña, even within the instrumental temperature record (Figure 1.4) (e.g. Allan, 2000, Fedorov and Philander, 2000, Tudhope et al., 2001, Juillet-Leclerc et al., 2006, Gergis and Fowler, 2009).

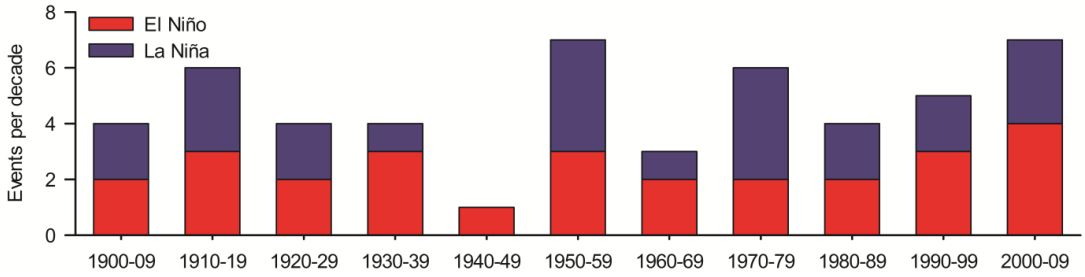

Figure 1.4 El Niño and La Niña events per decade from 1900 to 2009

Current climate models provide a range of responses of ENSO to increasing atmospheric CO_2 (Merryfield, 2006, Collins et al., 2010, Kim and Yu, 2012), from little change from the present (Zelle et al., 2005) to increased (Cai et al., 2014) or decreased amplitude and frequency (Collins, 2000). As there is no consensus as to the development of ENSO in a warming climate, seasonally resolved proxy records of ENSO may therefore provide information about ENSO under different background climates.

As El Niño and La Niña are identified by anomalous SSTs in the tropical Pacific, they can be seen in temperature records from these regions. There are a number of indices used to describe the phase and strength of ENSO events, including four Pacific SST indices, the Japan Meteorological Agency, and the Southern Oscillation Index (SOI). The equatorial Pacific indices are Niño 1+2 (0°-10°S, 90°-80°W), Niño 3 (5°N-5°S, 150°-90°W), Niño 4 (5°N-5°S, 160°E-150°W), and Niño 3.4 (5°N-5°S, 170°-120°W) (Figure 1.5), and are calculated using a reconstructed 100 year SST anomaly dataset (Hanley et al., 2003), while the SOI is measured by the mean sea level pressure (SLP) difference between Darwin (12.4°S, 130.9°E) and Tahiti (17.5°S, 149.6°W).

The temperature-based Pacific indices are defined with a mean SST from specified regions of the equatorial Pacific (shown in Figure 1.5) (Hanley et al., 2003). The region covered by the Niño 1+2 indices records upwelling off the Peruvian coast, while that covered by the Niño 4 index tends to be warmer throughout the year than the other three SST indices (Figure 1.5) as it encompasses the Western Pacific Warm Pool (WPWP). Strong El Niño events, such as the 1982-83 and 1997-98 events, have lower SST anomalies recorded in the Niño 4 index than the other indices (Figure 1.6). The Niño 3.4 index is commonly used as it encompasses the western half of the equatorial cold tongue region, and therefore captures changes in SST and SST gradients that result from fluctuations in tropical convection.

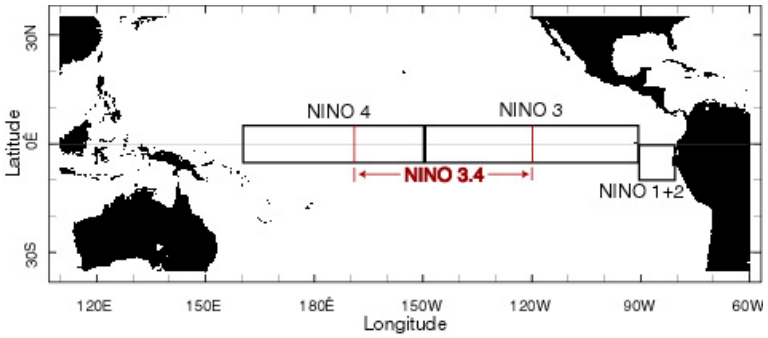

Figure 1.5 Areas taken into account when calculating the Niño indices regions in the equatorial Pacific (IRI, 2007)

These indices are based on a single environmental parameter, e.g. SST or SLP, in a key region affected by La Niña and El Niño episodes. Although all the indices record El Niño and La Niña events as positive and negative SST anomalies (Figure 1.6), the strength of the anomalies differs between the indices.

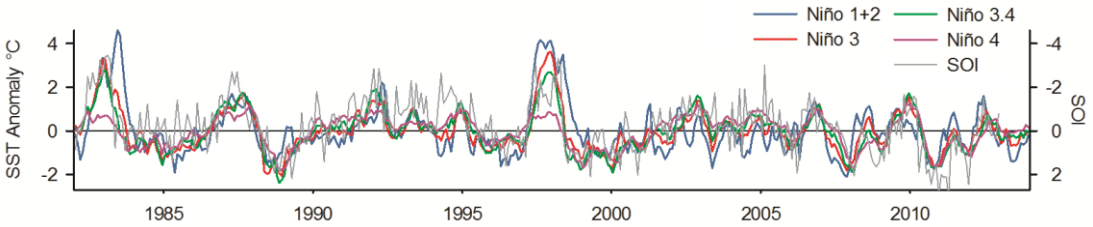

Figure 1.6 SST anomalies for Niño 1+2, 3, 3.4 and 4 (left axis) and the Southern Oscillation Index (right axis) for 1982-2013

1.2 PaleoENSO reconstructions

Our knowledge of ENSO prior to instrumental records is based on natural archives, including tree rings, corals, and lake sediments. These archives record variations in temperature and precipitation that have been associated with modern ENSO at specific sites (Otto-Bliesner et al., 2006).

Data typically used in order to reconstruct past ENSO tend to fit into one of two categories – either low resolution (e.g. several measurements per decade/century) data from lake or deep seas sediments, which can span hundreds to thousands of years, or high resolution (seasonal or monthly) data from corals or bivalves, which are shorter (typically decades to centuries). Low resolution data provides information about the mean climate state, and can record transitions in climate, while higher resolution data

can provide information about changes on a seasonal or inter-annual timescale, such as ENSO. Coral records from the tropical Pacific provide, in some respects, the best ENSO proxy data, as corals are found in the "core" ENSO region. However, corals are susceptible to diagenetic alteration, particularly when sub-aerially exposed. Proxies from regions affected by ENSO through teleconnections (e.g. Figure 1.3), outside the core ENSO region (such as lake varves or Northern Hemisphere tree rings), require the assumption that these teleconnections existed during the time period in question, which may not have been the case throughout the past (Huber and Caballero, 2003). Modern ENSO teleconnections are a reflection of the coupling between the tropical ocean and global atmosphere (Horel and Wallace, 1981), and temperature anomalies in the equatorial Pacific ocean can affect the climate across the globe. High resolution records obtained from the tropical Pacific capture the seasonal and inter-annual variability of SSTs and sea surface salinity (SSS), which are in turn controlled by ENSO variability (Sandweiss et al., 1996, Hughen et al., 1999, Cane et al., 2000, Corrège et al., 2000, Tudhope et al., 2001, Rimbu et al., 2003, Ayliffe et al., 2004, Gagan et al., 2004, Quinn et al., 2006, Donders et al., 2008, Duprey et al., 2012, Sadekov et al., 2013, Cobb et al., 2013, McGregor et al., 2013).

1.2.1 The tropical Pacific over the past 65 ka

Paleoclimate records from the tropical Pacific are abundant during the Holocene (~12 ka BP to present), and include both low-resolution records from foraminifera, and annually or seasonally resolved records from corals (Figure 1.7). Prior to the Holocene, during Marine Isotope Stage 3 (MIS3, 60-27 ka BP) and the Last Glacial Maximum (LGM, ~21 ka BP), higher resolution records are less abundant due to reduced accessibility and quality of samples (Tudhope et al., 2001).

A number of paleoclimate records from the tropical Pacific (Shulmeister and Lees, 1995, Sandweiss et al., 2001, Tudhope et al., 2001, McGregor and Gagan, 2004, Koutavas et al., 2006, Brijker et al., 2007, Cobb et al., 2013) indicate a dampened or absent ENSO during the early to mid-Holocene, while others (Carré et al., 2005, Rein et al., 2005) suggest strengthened El Niño events during the early Holocene, with coral records from the central Pacific showing highly variable ENSO activity over the past 7,000 years (Cobb et al., 2013). With regards to the mean climate state, geochemical

profiles obtained from foraminifera from the western tropical Pacific suggest warmer and saltier conditions than at present (Stott et al., 2004), while bivalves and corals from the western and southern Pacific suggest 1-2°C cooling during the early to mid-Holocene (Abram et al., 2009, Duprey et al., 2012).

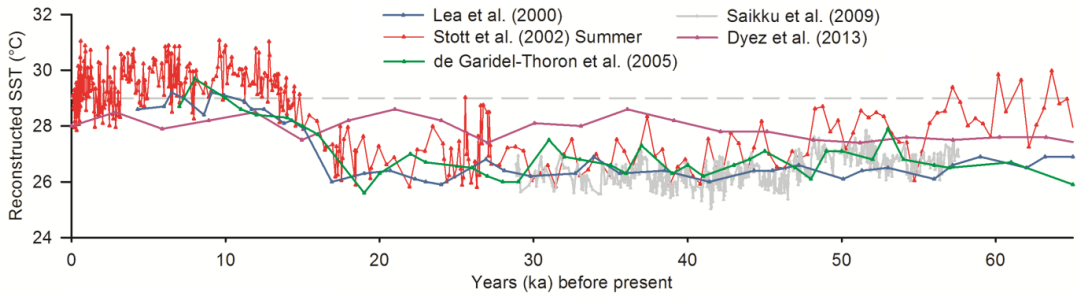

Figure 1.7 Reconstructed SST from tropical Pacific foraminifera (location map shown in Chapter 7) over the past 65 ka. Dashed line represents the modern mean annual SST at the Huon Peninsula. Reconstructed SST from foraminifera suggest similar or slightly higher SSTs during the Holocene, and a reduction of up to 4.5°C during MIS3

High resolution data are scarce prior to the Holocene, however $\delta^{18}O$ from *Porites* suggest a cooling of 2-3°C between 70 and 30 ka BP (Tudhope et al., 2001), while temperature reconstructions from Western Pacific foraminifera at the LGM suggest a cooling of 2°C (Shiau et al., 2012) and 2.8±0.7°C (Lea et al., 2000). Due to the lack of high resolution data during MIS3, there is no consensus as to the behaviour of ENSO during glacial climates. Modelling studies on glacial climates focus on the LGM, and general circulation models (GCMs) disagree as to whether the frequency, strength or amplitude of ENSO events was enhanced (Otto-Bliesner et al., 2003, An et al., 2004, Peltier and Solheim, 2004, Leduc et al., 2009, Merkel et al., 2010), or reduced (Otto-Bliesner et al., 2006).

1.2.2 Orbital forcing and ENSO

Orbital forcing modulates the phase and amplitude of the annual cycle of short wave radiation due to changes in the tilt of the earth's axis relative to the plan of orbit (obliquity), the precession of the equinoxes, and the eccentricity of the earth's orbit around the sun (Figure 1.8) (Timmermann et al., 2007). The long-term variation in these parameters cause the astronomical (Milankovitch) forcing of the climate system (Milankovitch, 1941). Eccentricity has cycles with a periodicity of ~100,000 years,

obliquity ~41,000 years, and precession ~21,000 years (e.g. Milankovitch, 1941, Berger, 1988). In the tropics, orbital forcing is dominated by precession (Berger and Loutre, 1991), which modulates the annual insolation cycle and affects the seasonal strength of winds, upwelling intensity (Clement et al., 1999, Koutavas et al., 2002), sea-breeze circulations and precipitation (Merlis et al., 2013). Numerical experiments have shown that changes in the precessional cycle can supress ENSO behaviour (Bush, 2007). Clement et al. (1999) studied ENSO-like variability over the past 150 kyr using a simplified coupled ocean atmosphere model in the tropical Pacific (Figure 1.8). In this model, the character of ENSO can be significantly altered by seasonally varying solar forcing (Clement et al., 1999).

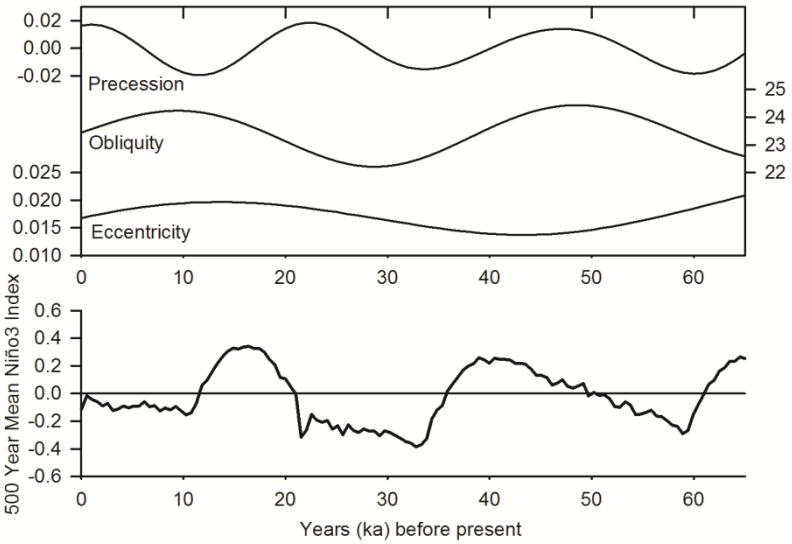

Figure 1.8 Top panel: Orbital parameters over the past 65 ka (Laskar et al., 2004) for 6.5°S. Bottom panel: 500 year mean Niño3 from Zebiak-Cane model forced with Milankovitch solar forcing over the past 65,000 years (after Clement et al. (1999))

1.3 Aims of this study

This study follows on from the work of Kevin Welsh, who collected samples of *Tridacna* sp. from the raised coral terraces of the Huon Peninsula. The collection, dating and bulk oxygen ($\delta^{18}O$) and carbon ($\delta^{13}C$) isotope measurements, as well as seasonal profiles of several *Tridacna* sp. shells is presented in Welsh (2009) . The aim of this study was to take the work further, and to sample more *Tridacna* sp. shells at a seasonal resolution, as well as measuring trace elements.

Chapter 1

Climatic and environmental conditions in the tropical Pacific will be reconstructed in this work, based on geochemical profiles (stable oxygen ($\delta^{18}O$) and carbon ($\delta^{13}C$) isotopes and trace elements) from the marine bivalve *Tridacna* sp., from the Huon Peninsula, Papua New Guinea. These fossil *Tridacna* sp. were collected from raised coral reefs dated to two key periods with different mean climate states – the early Holocene (~10-6 ka BP) and Marine Isotope Stage 3 (~60-30 ka BP). The $\delta^{18}O$ profiles derived from *Tridacna* sp. potentially reveal information about the strength and frequency of ENSO events during the period of growth, while trace element time series are potentially recorders of local environmental variables such as SST, salinity and productivity. Geochemical profiles from fossils will be compared to those published from a modern *Tridacna gigas* collected from the same region. The methods of reconstructing ENSO variability most commonly used will be compared to a modern *T. gigas*, the local SST record and a *Porites* coral from the same location, as well as within the fossil data set.

The remainder of this study is set out as follows:
Chapter 2 - the location of the study site and the area from which fossil *Tridacna* sp. samples were collected is described, including modern climatological and oceanographic features.
Chapter 3 - the geochemical methods used to obtain profiles of $\delta^{18}O$ and $\delta^{13}C$ and trace elements is described, and the mean results of these analyses are presented.
Chapter 4 - corrections made to $\delta^{18}O$ to remove the ice volume effect, and the interpretation of mean $\delta^{18}O$ as well as the issues surrounding the use of $\delta^{13}C$.
Chapter 5 - the potential uses of trace elements for reconstruction of environmental conditions, and the limitations of these in *Tridacna* sp.
Chapter 6 - the methods commonly used for reconstructing ENSO variability in proxy climate records, and the most appropriate method is used to compare variability reconstructed using fossil *Tridacna* to published records from the Holocene and MIS3.
Chapter 7 - the $\delta^{18}O$ profiles obtained from fossil *Tridacna* sp. samples are used to reconstruct seasonality and ENSO during the Holocene and MIS3.

Detailed descriptions and geochemical profiles of the fossils used in this study are shown in the Appendix.

2. Study area and *Tridacna* sp. as a climate archive

Chapter Abstract

The Huon Peninsula is in the heart of the Western Pacific Warm Pool (WPWP), one of the warmest bodies of water in the world, and is strongly affected by changes in evaporation/precipitation and temperature associated with the El Niño Southern Oscillation (ENSO). The ages of samples collected from the raised coral reefs at the Huon Peninsula are well constrained due to extensive sampling and dating of these reefs over the last 40 years. A modern *Tridacna gigas* from the region has been shown to capture accurately changes in SST and precipitation due to ENSO at this site, and it is suggested that fossil *Tridacna* sp. may reveal past environmental conditions.

A combination of changes in sea level and tectonic activity has led to fossil coral reefs at the Huon Peninsula, Papua New Guinea, being elevated above sea level to form raised coral reef terraces. These terraces contain fossil bivalves and corals which reveal information about past climate and environmental conditions through geochemical sampling of their carbonate structure.

Chapter 2

2.1 The study site

The Huon Peninsula (147.5°E, 6.5°S) is found on the north east coast of Papua New Guinea. It is at the heart of the Western Pacific Warm Pool (WPWP), the warmest body of ocean water in the world, with average sea surface temperatures over 28°C, and small seasonal fluctuations in temperature (Figure 2.1).

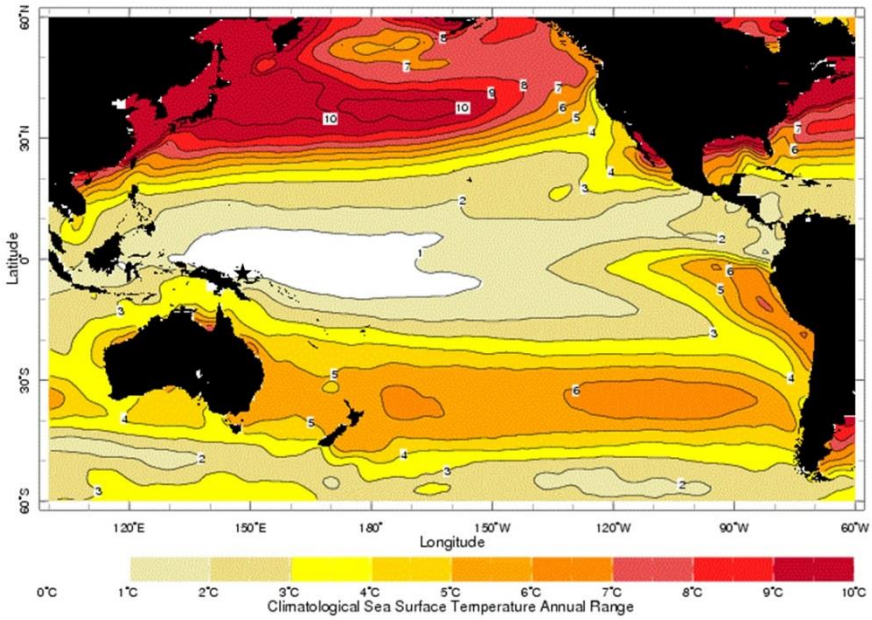

Figure 2.1 Map of the Pacific Ocean with average annual range of SST from IGOSS nmc (Integrated Global Ocean Services System Products Bulletin, National Meteorological Center) for 1981-2014 (Reynolds et al., 2002). Location of the Huon Peninsula is marked by a star, which is within the region which experiences an annual SST range of 0-1°C

2.1.1 Geological setting and uplift rates

The Huon Peninsula is located at a tectonic boundary between the West Pacific and Australian plates (Figure 2.2 insert), which causes uplift along the coast. Uplifted reef terraces reach 1000 m above sea level, and run parallel to the coast for 80 km (Fairbridge, 1960). The youngest reefs are of Holocene age and closest to the present sea level (Bloom et al., 1974, Chappell and Polach, 1976, Aharon et al., 1980, Ota et al., 1993, Chappell et al., 1996b). The oldest dated reefs are over 600 m high and have been Uranium/Thorium (U/Th) dated to at least 250 ka BP (Chappell, 1974). The terraces run continuously along the coast, and individual terraces are traced from

section to section and are named according to a numerical system presented in Chappell (1974).

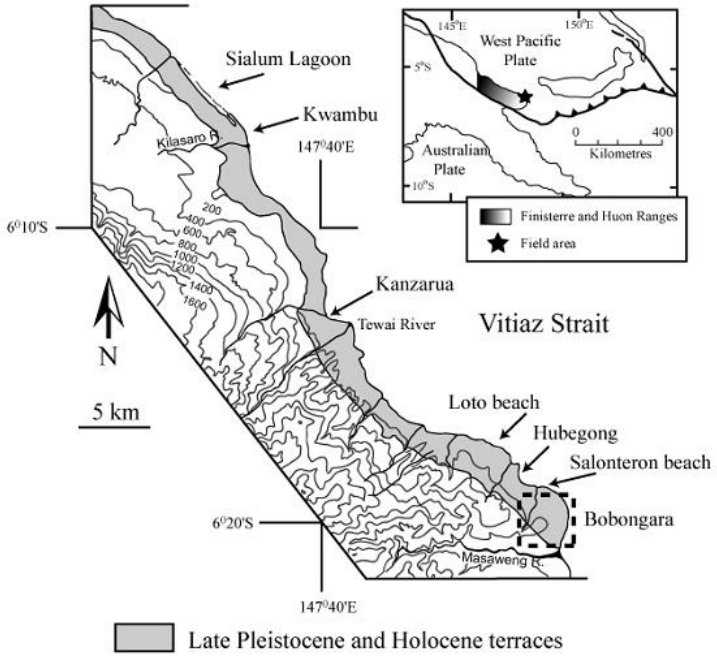

Figure 2.2 Map showing the coast line of the Huon Peninsula with areas of sample collection highlighted (modified after Ota et al. (1993)). Dashed box indicates the location of MIS3 shell collection. Insert shows the geological setting of the West Pacific and Australian tectonic plates. Modern sample (MT7) was collected near to Kanzarua (Welsh, 2009)

Despite significant differences in sea surface temperature, CO_2 and global sea level, the taxonomic composition and species diversity is similar between fossil reefs at Huon Peninsula (Pandolfi, 1996). The fossil reefs have been extensively dated (Chappell et al., 1996a, Yokoyama et al., 2000, Yokoyama et al., 2001, Thompson and Goldstein, 2006), using the radiometric dating of corals and bivalve molluscs. This provides good stratigraphic control on the age of materials collected from these terraces. Sea level changes which occurred during the Pleistocene (~2.5 Ma – 12 ka BP) and the Holocene (~12 ka BP – present) have been reconstructed using both stratigraphic analysis and topographic surveys (Bloom et al., 1974, Chappell, 1974, Edwards et al., 1993, Chappell et al., 1996b, Yokoyama et al., 2000, Yokoyama et al., 2001, Chappell, 2002).

The fossil *Tridacna* sp. used in this study were collected from two main time periods: the mid to early Holocene reefs which have been dated between 10 and 6.5 ka BP (Bloom et al., 1974, Chappell and Polach, 1976, Aharon et al., 1980, Ota et al., 1993,

Chappell et al., 1996b, Edinger et al., 2007), and reefs at Bobongara (Figure 2.2) dated between approximately 62 and 30 ka BP (Bloom et al., 1974, Chappell and Polach, 1976, Aharon et al., 1980, Chappell et al., 1996a, Yokoyama et al., 2000, Yokoyama et al., 2001). The terraces of Marine Isotope Stage 3 age (MIS3, ~60-27 ka BP) are thought to have been formed in response to episodic rapid sea level rises that occurred between 65 and 30 ka BP (Chappell and Shackleton, 1986, Pandolfi and Chappell, 1994, Yokoyama et al., 2001, Yokoyama et al., 2003). The growth of these terraces has been directly linked to sea level rises occurring after ice-calving episodes during Heinrich events (described in greater detail in Chapter 4) (Yokoyama et al., 2001). Coral reefs can respond in three ways to changes in sea level, by "keeping-up", "catching-up" or "giving-up". Keep-up reefs maintain their crests at or near sea level, building vertically if they accrete at a rate equal to sea level rise. Catch-up reefs catch up with rising sea level, usually after the rate of sea level rise slows. Give-up reefs are those which stop growing, perhaps as a response to too-rapid sea level rise (Neumann and Macintyre, 1985). Sea level rise therefore allows corals to construct large coral platforms due to increases in accommodation space, which have subsequently been uplifted at this location (Yokoyama et al., 2001). The MIS3 reefs from which *Tridacna* sp. shells were collected are assumed to include both keep-up and catch-up reefs (Yokoyama et al., 2001, Chappell, 2002, Welsh, 2009). Material from the Last Glacial Maximum (LGM, ~21 ka BP) and early pre-Holocene deglaciation is submerged or covered by the Holocene reefs due to the rise in sea level following the LGM.

The coral reefs which grew along the shoreline at the Huon Peninsula have been uplifted to create the sub-aerially exposed terraces seen today. This tectonic uplift occured more rapidly in the south-east, at approximately 3.3 m/ka, compared to rates of approximately 1.9 m/ka in the west (Ota and Chappell, 1999), and also occurs in 2-4 m incremental coseismic events (Ota et al., 1993, Chappell et al., 1996b, Ota and Chappell, 1999). Uplift at this location is thought to have occurred at a relatively constant rate over the last glacial cycle. This has been tested by comparing the mean Holocene rate to that of the last interglacial reef VII (MIS 5e), which give very similar results (Ota et al., 1993). Sea level reconstructions extrapolated from different sections of the coast with different average uplift rates match closely, which would be unlikely if these varied significantly over time (Chappell, 2002).

2.1.2 Holocene reef terrace

The Holocene terrace is composed of transgressive coral reefs which grew during post glacial sea level rise, and forms prominent cliffs along the coast of the Huon Peninsula. The Holocene terraces emerged at approximately 7-6 ka BP, when the post glacial sea level rise began to slow, no longer keeping up with tectonic uplift (Ota and Chappell, 1999). The height above sea level of the Holocene terraces varies between 8-12 m at Sialum to 20-23 m near Bobongara, with widths of between 100 and 500 m.

2.1.3 MIS3 terraces

Samples from MIS3 (reefs dated to 62-30 ka BP) were collected from Bobongara (147.48°E, 6.19°S) on the southeasterly end of the Huon Peninsula (Figure 2.3).

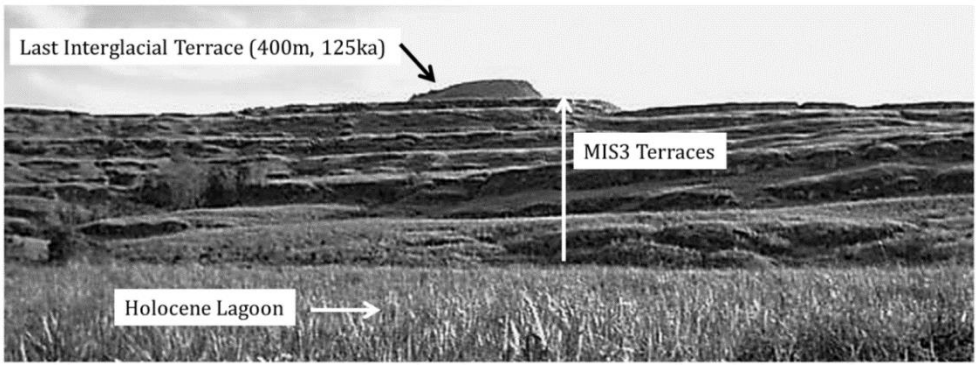

Figure 2.3 Southward view of terraces at Bobongara, viewed from the Holocene reef (Esat and Yokoyama, 2006)

The rate of uplift of these terraces has been estimated to be 3.2 m/ka (Chappell et al., 1996a), and they are some of the highest terraces on the Huon Peninsula. The Bobongara terraces have been extensively surveyed (Chappell, 1974, Pandolfi and Chappell, 1994, Chappell et al., 1996a). Field evidence has shown that these reefs grew as transgressive "catch up" or "keep up" reefs in response to changes in sea level over the past 60 ka (Figure 2.4 and Figure 2.5) (Pandolfi and Chappell, 1994).

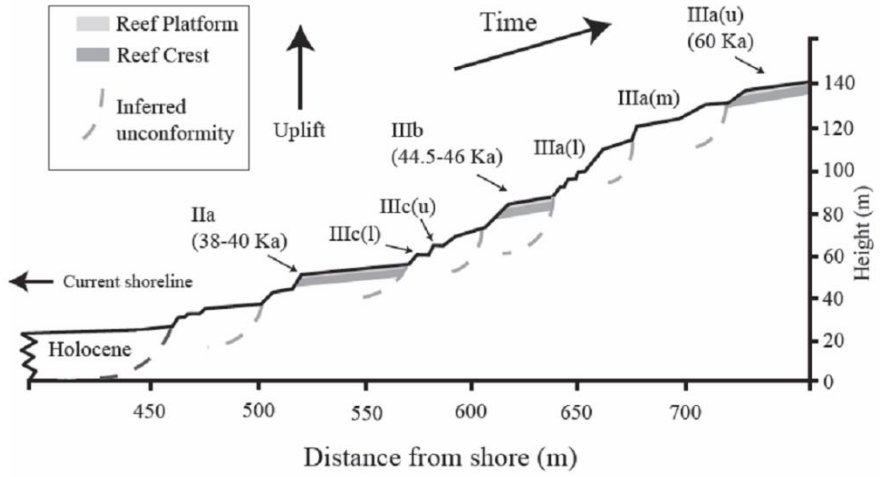

Figure 2.4 Cross section of Bobongara reef terrace sequence (Pandolfi and Chappell, 1994, Welsh, 2009)

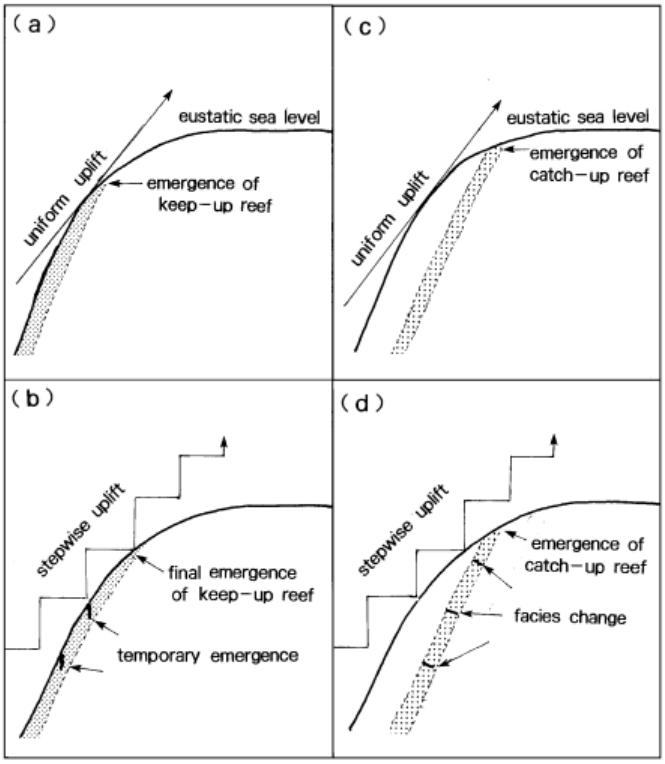

Figure 2.5 Schematic diagram showing the emergence of Holocene transgressive corals as composite results of eustatic sea level rise and different types of tectonic uplift.

(a) Eustatic sea level rise and uniform uplift for "keep-up" reefs;
(b) Eustatic sea level rise and stepwise uplift for emergence of "keep-up" reefs;
(c) Eustatic sea level rise and uniform uplift for emergence of "catch-up" reefs, and
(d) Eustatic sea level rise and stepwise uplift for "catch-up" reefs. From Ota and Chappell (1999)

2.1.4. Sample collection

A total of 75 samples of modern and fossil *Tridacna* sp. were collected from several localities along the Huon Peninsula in 2004 (described in Welsh (2009)). MIS3 samples were collected from the Bobongara terraces shown in Figure 2.3, by walking across the surface and face of each terrace. Sample position was noted using GPS and the distance of samples from the top of each reef terrace was recorded for *in situ* samples (Welsh, 2009).

The samples of Holocene age used in this study were collected between Bobongara and Kwambu (Figure 2.2, exact location of individual samples is described in the Appendix). The samples were either collected *in situ*, i.e. still attached to the reef in life position with both valves together, or *ex situ*, fallen from the face of the reefs or eroded on the surface of the terrace. *Tridacna* sp. samples from the Holocene, IIa and IIIc reefs were radiocarbon dated to ascertain their age (Welsh, 2009). The ^{14}C ages also confirmed that *ex situ* fossils were not modern samples which had been washed up on the beaches.

Samples were collected *in situ* from uplifted mid to early Holocene reefs, dated between 10 and 6.5 cal ka BP (Bloom et al., 1974, Chappell and Polach, 1976, Aharon et al., 1980, Ota et al., 1993) and MIS3 reefs dated 62 to 30 ka BP (Bloom et al., 1974, Chappell and Polach, 1976, Aharon et al., 1980, Chappell et al., 1996a, Yokoyama et al., 2000, Yokoyama et al., 2001). The modern *Tridacna gigas* shell (MT7) used in this study to compare with fossil *Tridacna* sp. was extracted live by villagers in 2002, and has been described in Welsh et al. (2011).

2.2 Modern oceanographic and climatological setting

Oceanographic setting

The coastline of the Huon Peninsula is adjacent to the Vitiaz Strait (Figure 2.2, Figure 2.6), which is a deep (up to 1200 m) and narrow (30 km wide) body of water with a low residence time (around 6 days (Lacan and Jeandel, 2001)) of sea water (Aharon and

Chappell, 1986, Cresswell, 2000). The New Guinea Coastal Current flows westwards during the southeast monsoon in boreal (Northern Hemisphere) summer, while during the northwest monsoon (boreal winter) the current flows eastwards (Fine et al., 1994, Kuroda, 2000). Annual surface salinity is low in this region, ranging from an average of 33.9‰ at 147.5°E, 5.5°S to 34.1‰ at 148.5°E, 6.5°S (Antonov et al., 2010).

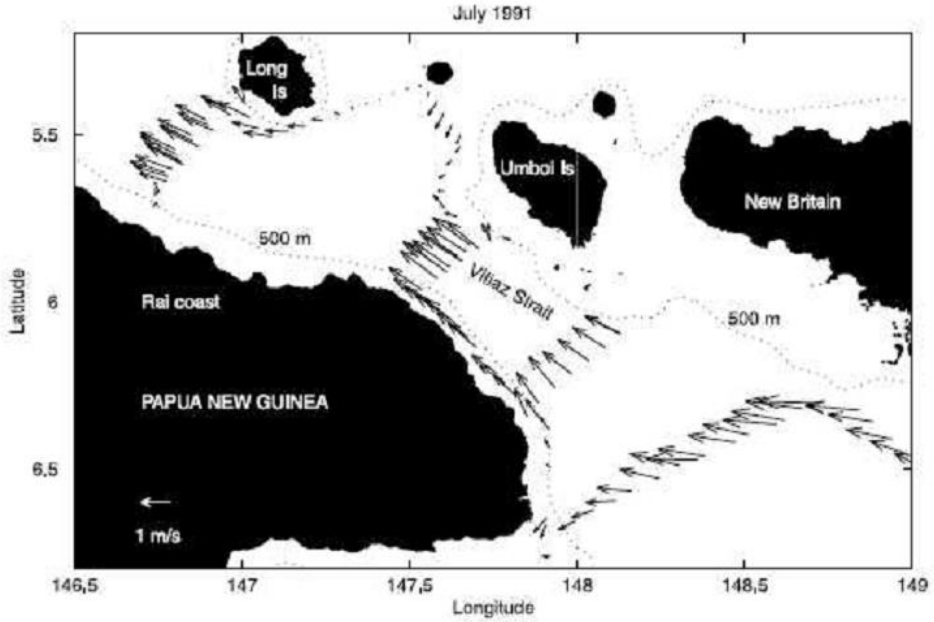

Figure 2.6 The position of the Huon Peninsula on the north east coast of Papua New Guinea, adjacent to the Vitiaz Strait. Arrows show near surface current vectors measured on the Ship-mounted Acoustic Doppler Current Profiler (SADCP) on the *Franklin* on a voyage in July 1991 (Cresswell, 2000)

Climatological setting

In the modern climate, water circulation in the study area is affected by the seasonal movement of the Intertropical Convergence Zone (ITCZ), which passes over the equator twice a year as a response to changes in the North West Monsoon and South East trade winds, driven by seasonal changes in insolation. There are two main seasons, a wet and a dry season, which coincide with Austral (Southern Hemisphere) summer and winter (Figure 2.7).

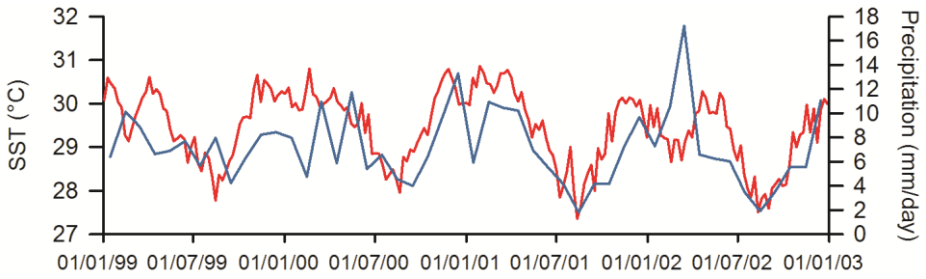

Figure 2.7 Weekly SST from IGOSS (red) (Reynolds et al., 2002) for 147.5°E, 6.5°S and monthly precipitation (blue) (Adler et al., 2003, Huffman et al., 2009) for 147.25°E, 6.25°S

There is a lack of *in situ* climatological data from the Huon Peninsula as there are no permanent stations to monitor sea surface temperature (SST) or sea surface salinity (SSS), but satellite and ship data are available for this region (e.g. Figure 2.1, Figure 2.7). This study uses data from two available data sets - the Integrated Global Ocean Services System Products Bulletin, National Meteorological Center (IGOSS nmc) (Reynolds et al., 2002) for 6.5°S, 147.5°E and the Hadley Centre Global Sea Ice and Sea Surface Temperature (HadISST) (Rayner et al., 2003) for the same location. Welsh et al. (2011) showed that the HadISST dataset and IGOSS nmc data reproduce extremely well temperatures recorded at Huon by a temperature logger (Figure 2.8). The precipitation data used in this study come from blended satellite and gauge data for 6.25°S, 147.25°E (Adler et al., 2003, Huffman et al., 2009).

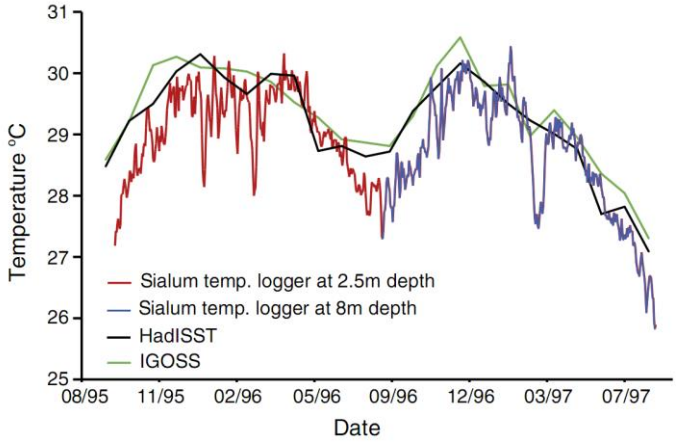

Figure 2.8 Temperature loggers placed behind the Lagoon Barrier at 2.5 m below Mean Low Water Springs (MLWS) (red line: 13/09/95–12/08/97) and at the base of the fringing reef opposite the lagoon entrance, 8 m below MLWS (blue line, 25/08/96–12/08/97) in Sialum Lagoon. SST record derived from HadISST and IGOSS data sets for the degree square centred on 147.5°E, 6.5°S. Correlation coefficient between Loggers over period 25/08/96–12/08/97 is 0.97. (NB temperature logger at 2.5 m spans both years, but 1997 results are identical to 8 m temperature logger) (Welsh et al., 2011)

The effects of ENSO at the Huon Peninsula

The Western Pacific Warm Pool (WPWP, Figure 2.9) plays a key role in El Niño Southern Oscillation dynamics, and therefore proxy climate archives from this region are often used in ENSO studies (e.g. McCulloch et al., 1996, Tudhope et al., 2001, McGregor and Gagan, 2004).

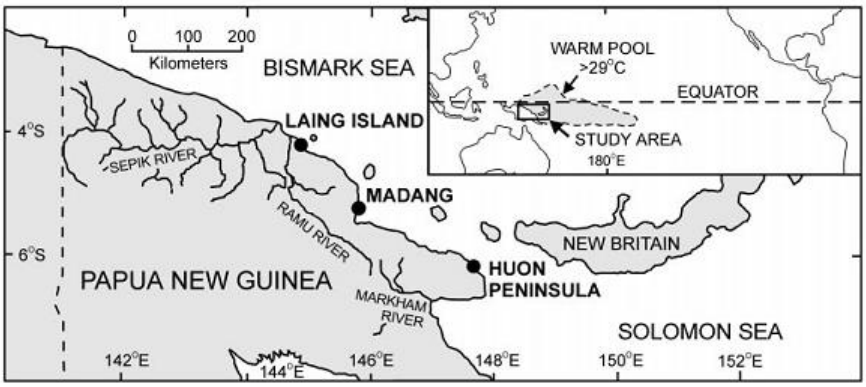

Figure 2.9 Location of the Huon Peninsula and two sites from which modern coral $\delta^{18}O$ profiles have been published (Tudhope et al., 2001)

During El Niño events, weaker trade winds and westerly wind bursts cause a shift of precipitation from the western Pacific to the central Pacific, resulting in reduced precipitation (Figure 2.10). This is accompanied by cooler temperatures in the western Pacific, while the eastern Equatorial Pacific (EEP) experiences warmer and wetter conditions. During a La Niña event, stronger trade winds result in warm surface water being piled up in the west Pacific, causing an increase in SSTs at the Huon Peninsula (Figure 2.10).

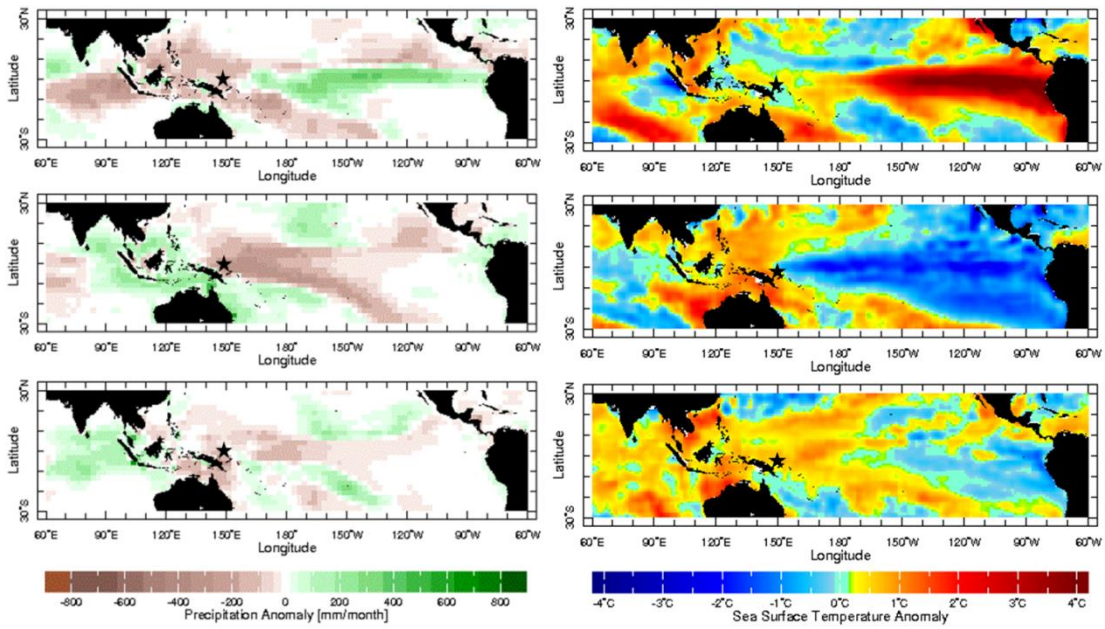

Figure 2.10 Left: December precipitation anomalies in the Pacific Ocean during the 1997 El Niño (top), 2010 La Niña (middle) and normal conditions (2012)(Reynolds et al., 2002). Right: December SST anomalies in the Pacific Ocean during the 1997 El Niño (top), 2010 La Niña (middle) and normal conditions (2012) (Reynolds et al., 2002). Location of the Huon Peninsula is starred

Precipitation data from Madang (located approximately 100 km north-west of the Huon Peninsula, Figure 2.9) are correlated to SST, Niño indices and sea level pressure (SLP) (Tudhope et al., 2001). Negative rainfall anomalies (i.e. drought) coincide with negative SST anomalies (i.e. cooler conditions), and positive Niño 3.4 and SLP anomalies, and vice versa (Figure 2.11). Changes in local SST and rainfall may therefore be associated with ENSO variability at this site. ENSO variability has been shown to fluctuate over longer periods (Figure 2.11), with times of weak and irregular ENSO (e.g. 1920-1960), as well as those of stronger and more regular ENSO (e.g. 1960-present).

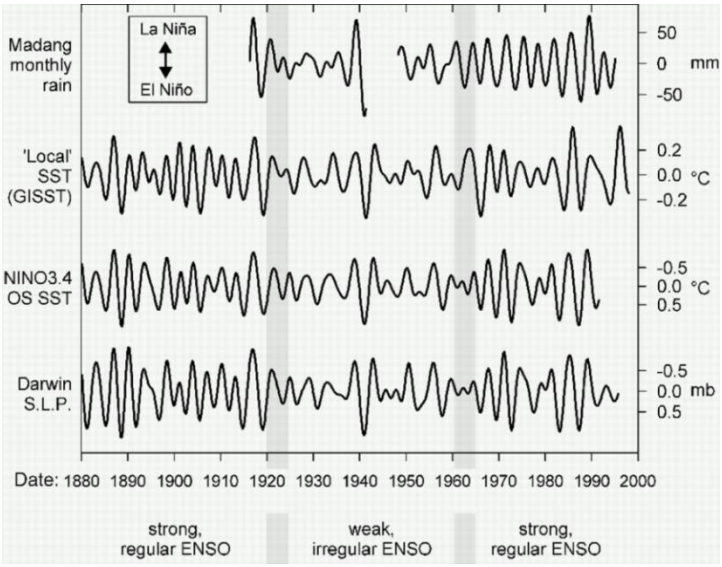

Figure 2.11 Instrumental records of ENSO variability since 1880: from top to bottom – rainfall, local SST, Niño 3.4 and Darwin sea level pressure. Instrumental climate records have been filtered with a Gaussian bandpass filter to reveal the 2.5-7 year ENSO components of variability (described in greater detail in Chapter 4). Local SST record is the reconstruction for 146.5°E, 5.5°S from the GISST2.3b data set of the UK Meteorological Office. Niño 3.4 OS SST is the optimally smoothed SST reconstruction for Niño 3.4 region. Modified after Tudhope et al. (2001)

2.3 The ecology of *Tridacna sp.*

Bivalves from the family Tridacnidae are found in the Indo-Pacific region (Figure 2.12), with six extant species found at the Huon Peninsula (Rosewater, 1965).

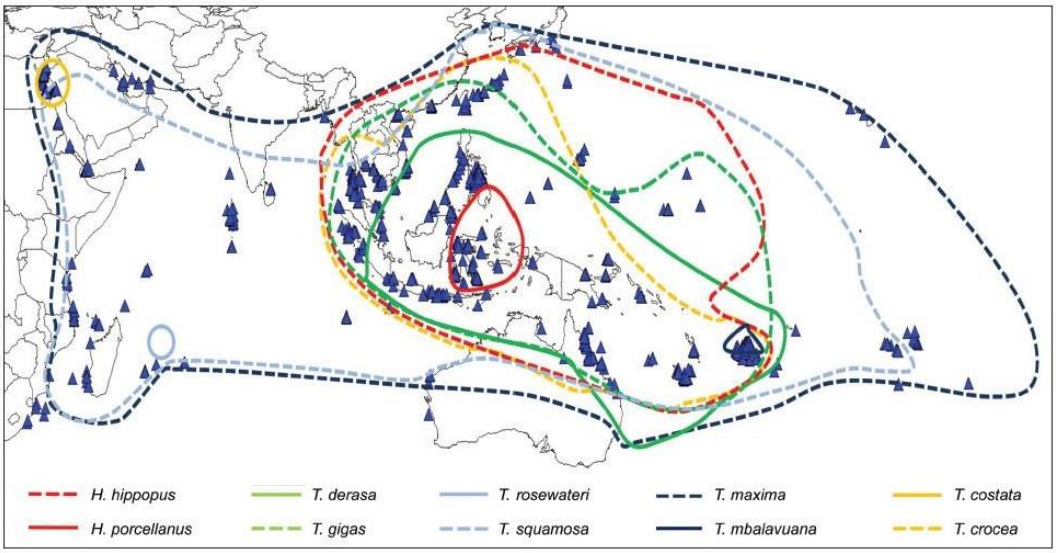

Figure 2.12 Modern distribution of giant clams (bin Othman et al., 2010)

Tridacna sp. are highly specialised and are able to "farm" food in their tissues due to a symbiotic relationship with large numbers of unicellular, symbiotic algae called zooxanthellae (Norrish and Smith, 1936, Rosewater, 1965). They live in the photic zone, which is limited by the penetration of light strong enough to permit the growth of zooxanthellae. *Tridacna* sp. attach to reefs in different ways depending on the species – *Tridacna crocea* burrow into coral, while *Tridacna gigas* rest unattached on the sea floor (Rosewater, 1965). Five species have been used in this study – *Tridacna gigas*, *T. maxima*, *T. deresa*, *T. squamosa* and *T. crocea* (Figure 2.13). *T. gigas* is the largest of the family, and can attain a very large size (~1.5 m) (Rosewater, 1965). *T. deresa* is the next largest, growing up to ~50 cm (Rosewater, 1965). *T. crocea* is the smallest of the family (between 10 and 15 cm), and is often found deeply imbedded in coral.

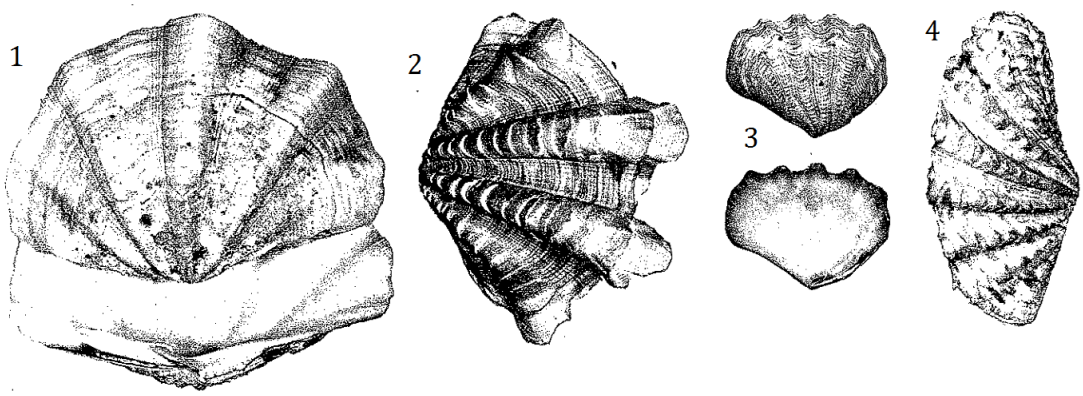

Figure 2.13 Examples of *Tridacna* species. 1 – *T. gigas*; 2 – *T. squamosa*; 3 – *T. crocea*; 4 – *T. maxima* (Rosewater, 1965). Pictures are not to scale

At the Huon Peninsula, *T. gigas* are the most common of the species found (Aharon and Chappell, 1986), which may be in part due to their large size and excellent preservation (e.g. Figure 2.14).

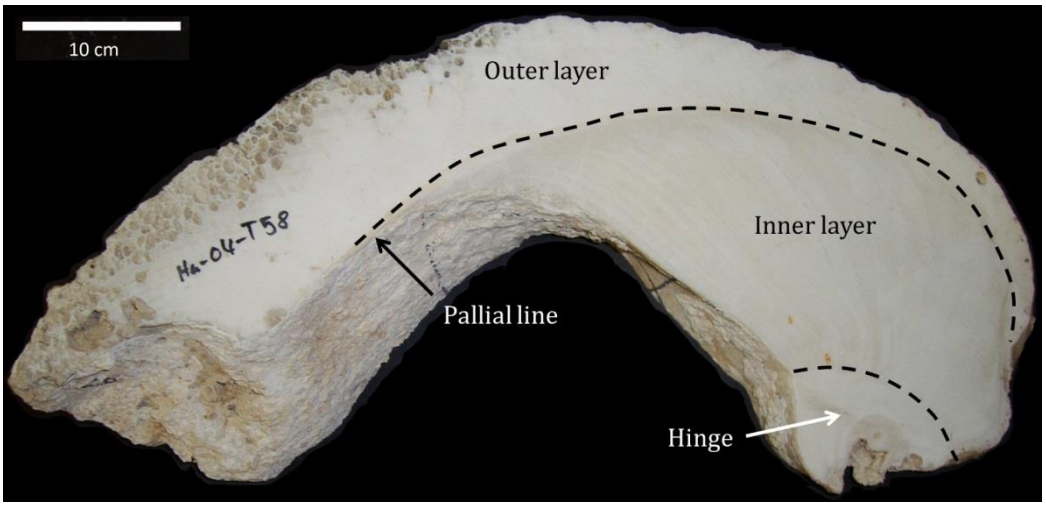

Figure 2.14 Example of a slab of a Holocene *Tridacna gigas* (T58) shell from which thin sections were made. Shell layers are labelled. Pallial line separates the outer part of the shell from the inner layers. Borings can be seen in the outer layer of the shell, which was not used in this study

Geochemical profiles in freshwater and marine bivalves have been used as a proxy for seasonally resolved records of environmental variables. These environmental variables include SST (Kennedy et al., 2001, Richardson et al., 2004, Ford et al., 2010), salinity (Roopnarine et al., 1998, Takesue et al., 2008), and productivity (Vander Putten et al., 2000, Lazareth et al., 2003). *Tridacna* sp. have been studied from a number of locations, including the south Pacific (Jones et al., 1986, Romanek et al., 1987, Romanek and Grossman, 1989), the western Pacific (Pätzold et al., 1991, Elliot et al., 2009, Welsh et al., 2011, Duprey et al., 2012), the Great Barrier Reef (Aharon, 1991, Elliot et al., 2009), Japan (Watanabe et al., 2004, Sano et al., 2012), Vietnam and Indonesia (Batenburg et al., 2011), the Philippines (Faylona et al., 2011), the South China Sea (Yan et al., 2013) and the Kenyan coast (Accordi et al., 2010). These include studies on modern, Holocene (Watanabe et al., 2004, Duprey et al., 2012) and Miocene (Batenburg et al., 2011) shells, as well as live laboratory or field studies.

Although *Tridacna* sp. are large, long-lived, reef dwelling bivalves (Figure 2.14), and have been shown to live to up to 60 years (Watanabe et al., 2004), most recently published records are between 10 and 20 years (Elliot et al., 2009, Batenburg et al., 2011, Welsh et al., 2011, Duprey et al., 2012, Duprey et al., 2014). All studies on modern *Tridacna* sp. have shown that they secrete their shell in isotopic equilibrium with seawater, meaning that the $\delta^{18}O$ measured does not need to be calibrated, as in corals (Aharon and Chappell, 1986, Romanek and Grossman, 1989, Aharon, 1991, Elliot

et al., 2009, Welsh et al., 2011). *Tridacna* sp. shell structure consists of densely packed aragonite crystals, which preserves these fossils from diagenesis (Welsh et al., 2011). This is particularly important in this study, as some fossil samples had been sub-aerially exposed for in excess of 50 ka at the Huon Peninsula. Scanning Electron Microscopy (SEM) images of modern and fossil (Figure 2.15) shells have been used to verify the state of preservation. The aragonitic crystals and growth band structure are clearly visible in both modern and fossil samples.

2.3.1 Growth in bivalves

Growth in bivalves (including growth rate, duration of growing season and timing of growth line formation (Hallmann et al., 2009)) can be affected by a number of environmental and biological factors, such as water temperature (Chauvaud et al., 1998, Hart et al., 1998, Carré et al., 2005, Hippler et al., 2009), exposure (Hart et al., 1998) salinity (Hart et al., 1998, Goodwin et al., 2003), location (Goodwin et al., 2003) and age (Chauvaud et al., 1998, Hallmann et al., 2009). In species from outside the tropics, growth cessations are common due to changes in environmental conditions which are not beneficial for growth (Goodwin et al., 2003). In many species, growth rate slows with ontogeny, with rapid growth during the juvenile phase, and slow growth during the adult phase (Carré et al., 2005, Hallmann et al., 2009).

The growth rate of marine bivalves varies considerably from species to species, with low values of 30 µm/year in *Arctica islandica* (Schöne et al., 2011) and at the higher end up to 20 mm/year in *Tridacna gigas*.

Previous work on *Tridacna* sp. (e.g. Table 2.1) shows that there is a reduction in growth throughout individuals' lifespans from ~8-16 mm/year during the juvenile phase to ~1-2 mm/year once the individual has reached maturity (e.g. Romanek et al., 1987, Aharon, 1991, Elliot et al., 2009, Welsh et al., 2011). Growth in *Tridacna* sp. also varies seasonally and is thought to be related to variations in temperature – more transparent bands (with larger aragonite crystals) correlate with more negative $\delta^{18}O$ shell carbonate (Pätzold et al., 1991, Elliot et al., 2009).

Table 2.1 Published findings of growth in giant clams (*Tridacna* sp. and *Hippopus hippopus*)

Species (Reference)	Findings
T. crocea (Hart et al., 1998)	• Temperature and exposure most important variables influencing growth • Salinity negatively correlated with survival
T. deresa; T. maxima (Hart et al., 1998)	• Exposure and geographic location most important variables influencing growth • Salinity positively correlated with survival of *T. maxima*
T. crocea; T. maxima (Hean and Cacho, 2003)	• Growth is sensitive to photosynthesis; respiration and surplus energy intake, and temperature dependent respiratory response parameters
T. gigas; T. crocea; T. squamosa; H. hippopus (Klumpp and Griffith, 1994)	• Growth is initially slow, then rapid and nearly linear over several years, after which there is a significant slowing • *T. gigas* is largest and fastest, *T. crocea* is smallest and slowest growing
T. gigas (Lin et al., 2006)	• Outer layer formed from dense structured layers of aragonitic needles approximately 1-5µm in length • Growth bands thought to contain thin organic matrix, partially separating layers of cross-lamellar aragonitic needles
T. gigas (Moir, 1989)	• Considerable variability in growth rates in *T. gigas* • Rate of growth fastest during early years of life, slowing as clams grow larger
T. maxima (Romanek et al., 1987)	• Rapid juvenile shell growth followed by slower growth
T. maxima (Romanek and Grossman, 1989)	• Growth suppressed by high temperatures in summer once maturity is reached
T. deresa (Sano et al., 2012)	• Growth lines are formed daily • Growth rate is variable among individuals living under the same environmental conditions
H. hippopus (Schwartzmann et al., 2011)	• Daily growth is highly variable in New Caledonia (21°C – 28°C) • Non-linear relationship between growth and temperature

Annual growth bands in *T. gigas* were first identified in the 1960s (Bonham, 1965), and more recent studies have identified daily growth bands (Figure 2.16), which decrease in width as the organism matures and growth slows (Watanabe et al., 2004). The width of these bands will be used in this study to assess the length of the time period covered in individual *Tridacna* sp. sample profiles (Chapter 3).

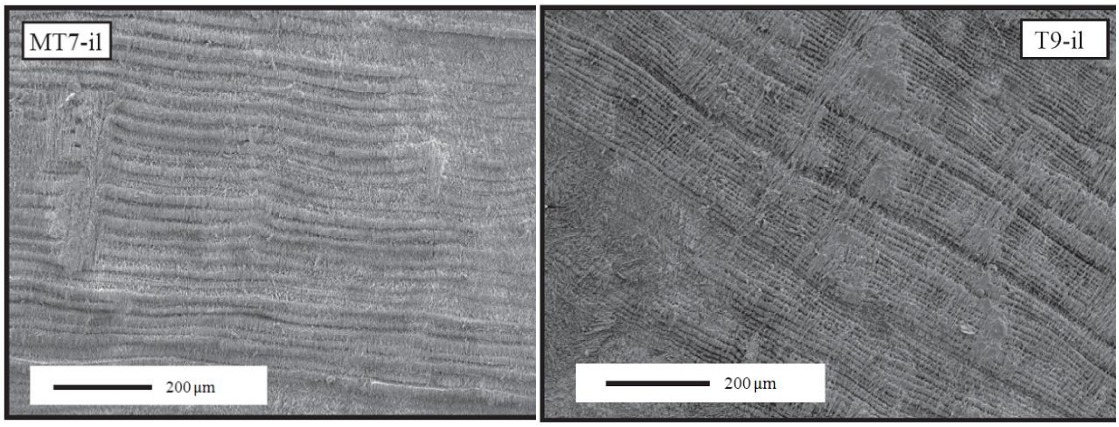

Figure 2.15 SEM image of modern *T. gigas* MT7 inner layer (left) and fossil *T. gigas* T9 (right) (Welsh, 2009)

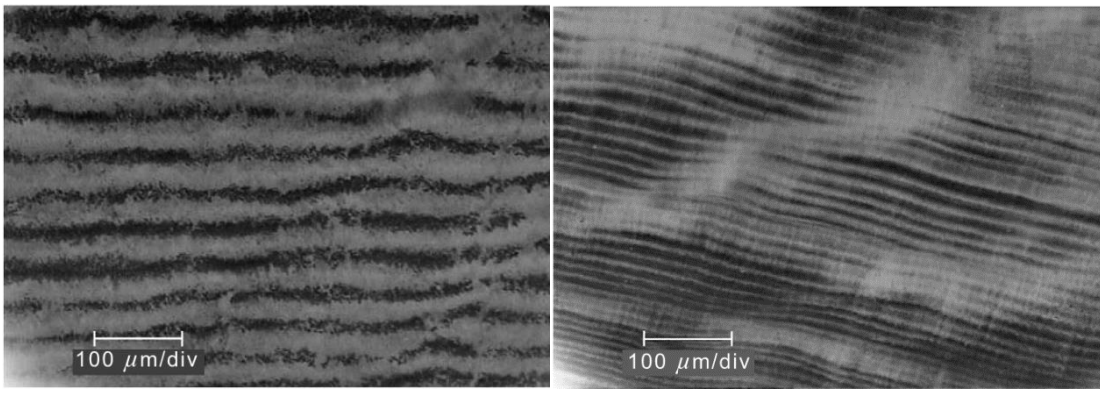

Figure 2.16 Growth banding in the inner layer of a fossil *T. gigas* from Japan. Juvenile phase of growth is shown on the left and adult on the right (Watanabe et al., 2004)

2.3.2 Geochemical tracers measured on *Tridacna* sp.: the climate archive

Oxygen isotopic ($\delta^{18}O$) measurements of marine carbonates have been used since the 1950s to reconstruct past ocean temperatures, as the $\delta^{18}O$ composition of marine carbonate reflects both the temperature and the isotopic composition of the water ($\delta^{18}O_w$) in which it was formed (Epstein et al., 1951, Shackleton, 1967). The relationship between *Tridacna* sp. $\delta^{18}O$ and $\delta^{13}C$ and environmental conditions was first examined in the 1980s and early 1990s (e.g. Romanek et al., 1987, Romanek and Grossman, 1989, Aharon, 1991, Pätzold et al., 1991). More recently, geochemical and trace element profiles from *Tridacna* sp. have shown the potential of the use of Sr/Ca as a proxy for parameters of the daily light cylce (Sano et al., 2012), as well as demonstrating substantial inter-annual SST variability during the Miocene (Batenburg et al., 2011), and decadal variability during the Holocene (Watanabe et al., 2004,

Duprey et al., 2012). The $\delta^{18}O$ profile of a modern *T. gigas* collected from the Huon Peninsula has been shown to capture local changes in SST and rainfall, and records shifts in $\delta^{18}O$ attributable to ENSO (Welsh et al., 2011). Due to the combination of changes in temperature and precipitation during ENSO events (as shown in Figure 2.10), the isotopic signature of a modern *T. gigas* at the Huon Peninsula increases by 1 to 1.2‰ to more positive values (Figure 2.17) during an El Niño, reflecting a temperature anomaly of ~0.5-1°C and a rainfall anomaly of 2-4mm/day (Welsh et al., 2011). $\delta^{18}O$ measurements from fossil samples will be presented in Chapter 3.

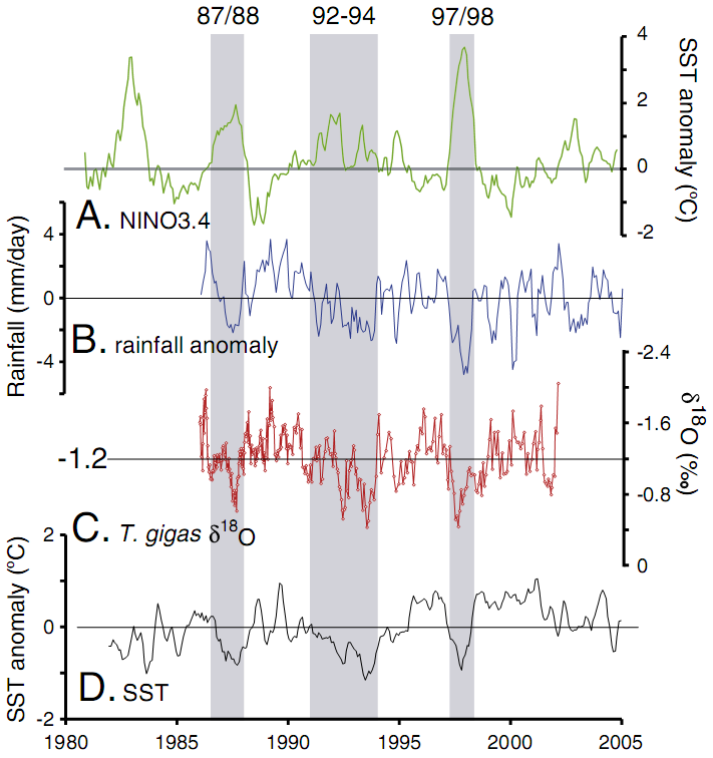

Figure 2.17 Comparison of T. gigas $\delta^{18}O$ profile with ENSO and local temperature and rainfall data.
A: NIÑO3.4 index,
B: monthly rainfall anomaly (mm/day), 3pt smoothed data from NASA/GPCPV2 for 146.25°E, 6.25°S,
C: *T. gigas* $\delta^{18}O$ record, and
D: SST monthly anomaly, 3pt smoothed data is taken from IGOSS data set for the same grid box as the rainfall data (Welsh et al., 2011)

2.4 *Tridacna* sp. used in this study

Four *Tridacna gigas* from the Holocene reefs, and seventeen *T. maxima*, *T. gigas*, *T. squamosa* and *T. crocea* from the MIS3 reefs at Bobongara (Figure 2.2) were sampled in

this study. The dating of these samples is described in the following sections. The Holocene and MIS3 *Tridacna* sp. were selected for use based on their bulk isotopic measurements and amount of calcite (shells with less than 1% calcite were selected) (Welsh, 2009). As many samples of different ages and from different reefs as possible were chosen in order to reconstruct climatic and environmental conditions at discrete intervals throughout the variable climate of MIS3.

2.4.1 Dating and chronology

Fossil samples were dated using ^{14}C direct dating (Table 2.2) and reef location extrapolation for those which could not be directly dated (Table 2.3). Samples from the inner layer (Figure 2.14) of *Tridacna* sp. were used for radiocarbon dating. These were analysed in two different laboratories, the NERC Radiocarbon Laboratory in East Kilbride and the Department of Nuclear Engineering and Management at Tokyo University (Welsh, 2009). Once ^{14}C dates were obtained, they were calibrated in order to give a calendar date before present (cal ka BP). An average marine reservoir correction of 407±52 years was applied to Holocene samples (Edwards et al., 1993), and a correction of 400 years was applied to those from MIS3 with the caveat that shell ages might have an error of several hundred years, as changes in marine circulation during MIS3 are not well constrained (Yokoyama et al., 2000). Dates were calibrated using the Calib 7.0 program (Stuiver and Reimer, 1993) with Marine 13.14 calibration.

Corals which exceed the age limit for radiocarbon dating (~42 kyr) are often dated by U/Th techniques. However, the amount of uranium in molluscs can be at least two orders of magnitude smaller than in corals (Broeker, 1965), which makes dating using this technique complicated (Chappell, 1974). More recently, U/Th techniques have been used with *Tridacna* sp. from Kenya (Accordi et al., 2010), although there are large uncertainty intervals associated with the ages produced. Dating of *Tridacna* sp. shells by U/Th was not attempted in this study, because of the large uncertainties involved, and due to the fact that the ages of reefs at the Huon Peninsula are well constrained. The reefs from which the samples were collected have been extensively dated by U/Th dating of corals and molluscs (Bloom et al., 1974, Chappell and Polach, 1976, Aharon et al., 1980, Ota et al., 1993, Chappell et al., 1996a, Yokoyama et al., 2000, Yokoyama et al., 2001, Thompson and Goldstein, 2006) and the age of *in situ* samples was extrapolated

from their position within the reef. Ages were based on the location of the shell on the reef terrace, and on the chronology of the terraces presented in Chappell (2002). Uncalibrated radiocarbon ages and extrapolated ages are those presented in Welsh (2009).

Table 2.2 Ages of radiocarbon dated *Tridacna* sp.

Sample	Species	Reef	Radiocarbon age (uncalibrated)	Age (cal ka BP)	Uncertainty (2σ)
T66	*T. gigas*	Holocene	6480	6.49	0.37
T73	*T. gigas*	Holocene	7129	7.26	0.20
T58	*T. gigas*	Holocene	7527	7.59	0.23
T75	*T. gigas*	Holocene	8592	8.73	0.39
T28	*T. maxima*	IIa	30450	34.1	0.63
T27	*T. maxima*	IIa	31820	35.4	1.6
T9	*T. gigas*	IIa	32794	36.5	2.6
T11	*T. squamosa*	IIa	33413	37.2	2.5
T32	*T. maxima*	IIIc (lower)	34520	38.6	0.83
T39	*T. maxima*	IIIc (upper)	36550	40.8	1.12
T40	*T. maxima*	IIIc (upper)	37758	41.5	3

Table 2.3 Extrapolated ages of *Tridacna* sp.

Sample	Species	Reef	Elevation (m)	Extrapolated Age (cal ka BP)	Reef Age (Chappell, 2002)
T24	*T. crocea*	IIIb	84	44.9	44.5-46
T37	*T. maxima*	IIIb	79	46	44.5-46
T41	*T. crocea*	IIIa (lower)	99	50.7	49-51
T18	*T. gigas*	IIIa (middle)	114	52.8	52-54
T6	*T. squamosa*	IIIa (upper)	135	60.7	60-62
T15	*T. gigas*	IIIa (upper)	138	60	60-62
T22	*T. gigas*	IIIa (upper)	138	60	60-62
T38	*T. crocea*	IIIa (upper)	134	60.9	60-62
T44	*T. maxima*	IIIa (upper)	138	60	60-62
T45	*T. gigas*	IIIa (upper)	138	60	60-62

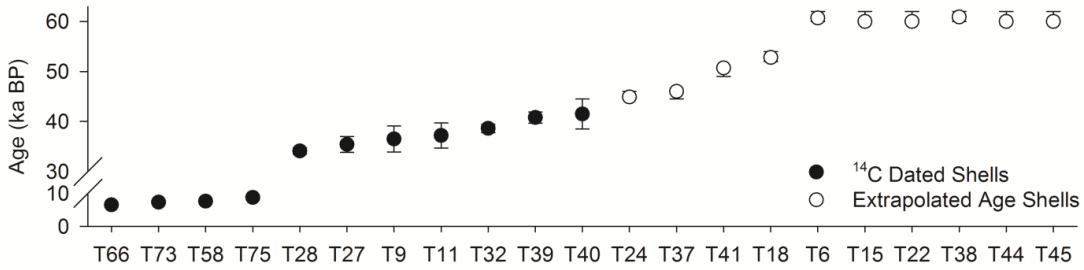

Figure 2.18 Calibrated ages (ka BP) and extrapolated ages of *Tridacna* sp. used in this study. Error bars represent age uncertainty. For samples older than ~42 ka BP, the error given is the age range of the reef from Chappell (2002)

Constraints on chronology

The ages of *Tridacna* sp. dated and described by Welsh (2009) and used in this study can be compared with published ^{14}C and U/Th dates of corals collected from the same terraces and presented by Yokoyama et al. (2000) to verify the accuracy of the *Tridacna* sp. dating (Figure 2.19). The mean uncalibrated radiocarbon ages for Reef IIa and IIIc are consistent with radiocarbon ages from corals from the same reefs. The standard deviation of ^{14}C ages is less than those from Yokoyama et al. (2000) (Welsh, 2009). The consistency of the ^{14}C ages obtained on independent fossil material collected from the same reefs illustrates the accuracy of the chronology of the fossil *Tridacna* sp.

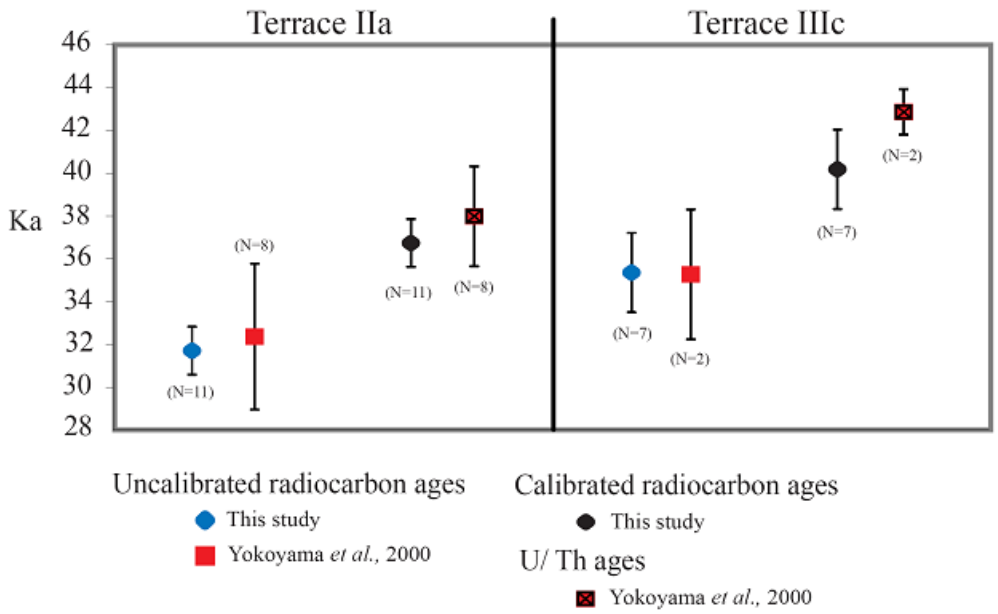

Figure 2.19 Comparison of mean age results from Welsh (2009) with Yokoyama et al. (2000) from two reef terraces. Bars represent the standard deviation of results. Calibrated ^{14}C dates are similar to U/Th dates reported in Yokoyama *et al.* (2000). From Welsh (2009)

The calibrated radiocarbon ages of fossil *Tridacna* sp. from the IIa and IIIc reefs (Figure 2.19) are younger than coral U/Th ages presented in Chappell et al. (1996a), Yokoyama et al. (2000) and Tudhope et al. (2001). The difference in age is in the order of 500 - 1,000 years and remains within the error bars of the method. There are several possibilities for this discrepancy. The *Tridacna* sp. could be contaminated by younger carbon. However, low % calcite values and the small range of ages proposed for shells from each reef (indicated by the standard deviation of values in Figure 2.19) suggests this effect would be small (Welsh, 2009). Alternatively, Yokoyama et al. (2000) put

forward that younger radiocarbon ages could be caused by fluctuations in the thermohaline circulation (THC), where the slow-down or cessation of the THC during climatic events such as Heinrich Events causes an excess of atmospheric ^{14}C, which would otherwise be delivered to the deep ocean by the THC (Welsh, 2009). Such a process could explain the difference between the U/Th dates and calibrated ^{14}C age of reef terrace IIa (correlated to Heinrich Event 4 (Yokoyama et al., 2000)). However, reef terrace IIIc has not been definitively linked with any Heinrich Events, so it is unclear as to the reason for this discrepancy.

2.4.2 Preservation

Calcareous fossils such as bivalves and corals are susceptible to changes in their composition as a result of being sub-aerially exposed over time. Diagenesis in fossil corals or bivalves can involve the precipitation of secondary aragonite or calcite or the replacement of skeletal aragonite with calcite (Bathurst, 1975). This transformation involves the exchange and removal of trace elements and isotopes, and therefore changes the geochemistry of the bivalve or coralline matrix (McGregor and Gagan, 2003). It is therefore essential to screen for any sign of diagenesis.

This can be identified in a number of ways:

- the amount of aragonite and calcite in carbonate powder removed from shells can be screened by X-ray diffraction (XRD);
- sections can be scanned using a Scanning Electron Microscope (SEM); or
- thin sections can be examined if there is calcite visible on the shell surface.

Thin sections reveal differences in fossil coral structure (Figure 2.20) between well-preserved corals (b) and when the aragonite skeleton has been replaced by calcite (c) (McGregor and Gagan, 2003). Similarly, diagenetic alteration can be seen in a MIS3 fossil *T. maxima* from the Huon Peninsula (Figure 2.21).

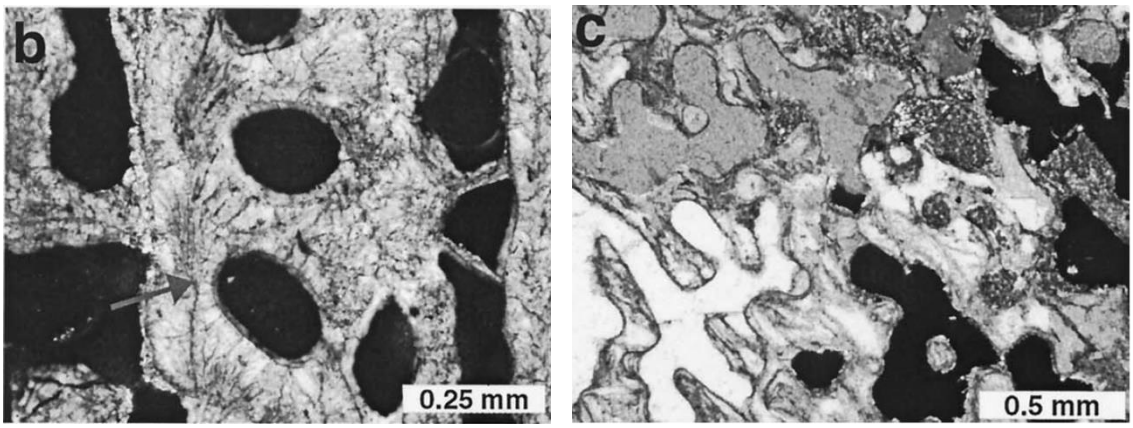

Figure 2.20 Comparison of fossil corals under crossed polarised light. (b) Well preserved fossil coral. Arrow points to centre of calcification. (c) Fossil coral with 75-100% calcite. From McGregor and Gagan (2003)

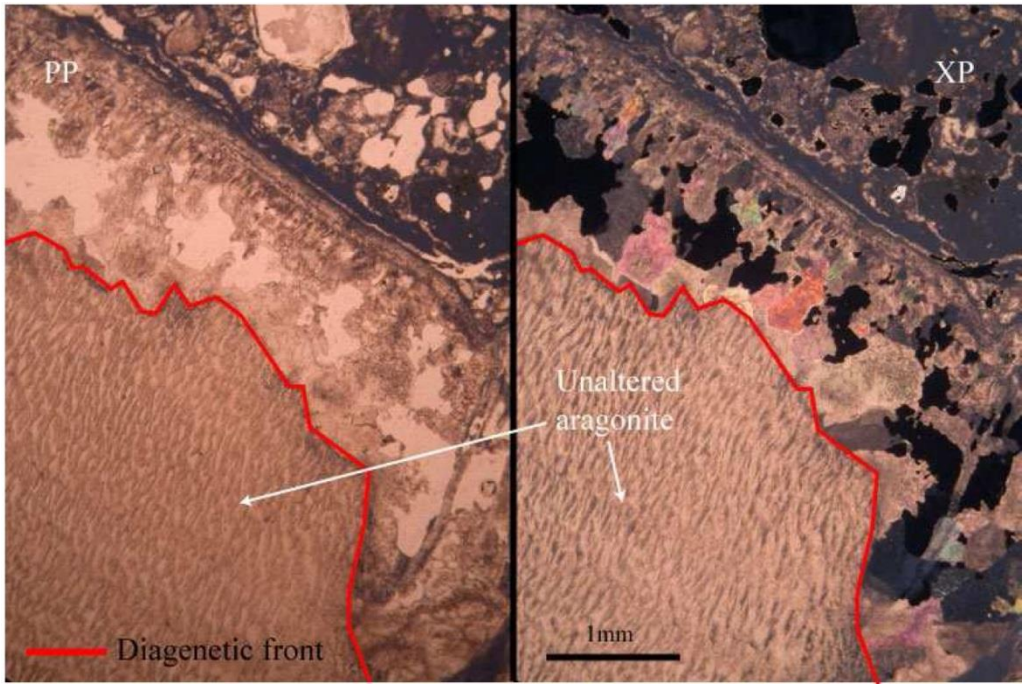

Figure 2.21 Optical thin section of fossil *Tridacna maxima* (T48), which shows diagenetic alteration in the form of calcite crystals filling voids left by the dissolution of the original aragonite. Calcite crystals can be seen above and to the right of the diagenetic front with high birefringence colours. From Welsh (2009)

2.5 Concluding remarks

The fossil *Tridacna* sp. collected from the Huon Peninsula and used in this study are from extensively dated uplifted reef terraces, and record environmental conditions at discrete time intervals over the past 60 ka.

The modern *T. gigas* from the Huon Peninsula has been shown to record local changes in SST and precipitation associated with ENSO events in this region. It is therefore possible to assume that fossil *Tridacna* sp. from this location can be used to examine the variability of ENSO during the past.

3. Methods and Results

Chapter Abstract

Several geochemical methods are used in this chapter in order to reveal environmental information recorded in fossil shell carbonate. Stable oxygen ($\delta^{18}O$) and carbon ($\delta^{13}C$) isotope profiles were measured using mass spectrometry on thin sections of *Tridacna* shell. Trace metal element ratios, including magnesium (Mg/Ca), strontium (Sr/Ca) and barium (Ba/Ca) were measured using Laser Ablation ICP-MS. In order to relate these to environmental conditions, the profiles obtained must be assigned a chronology to transform them to a temporal resolution. The width of micro-growth bands, thought to be deposited daily, was used in combination with the $\delta^{18}O$ and Mg/Ca profiles in order to build a growth chronology of Holocene and MIS3 *Tridacna* sp. shells.

Chapter 3

3.1 Introduction

The geochemistry of carbonate shells of bivalves has the potential to reveal information about past climates. The oxygen isotope ratio ($^{18}O/^{16}O$) recorded in bivalve shell is controlled by temperature and the oxygen isotope ratio of the water ($\delta^{18}O_w$) from which the shell is precipitated. Trace element concentrations such as magnesium (Mg) and strontium (Sr) have been shown to be influenced by temperature in bivalves (Klein et al., 1996, Yan et al., 2013) and corals (Smith et al., 1979, Sinclair et al., 1998), and have been used in a multi-proxy approach with $\delta^{18}O$. In order to extract this information from a bivalve, the shell must be sampled and the resultant carbonate powder analysed.

Slabs of *Tridacna* sp. shell were initially sectioned and sub-sampled to obtain profiles of stable oxygen ($\delta^{18}O$) and carbon ($\delta^{13}C$) isotopes with weekly to monthly resolution. Trace element profiles were obtained by analysing along a continuous growth track. Both sets of data provide information about environmental conditions. The temporal resolution was between 6 and 20 samples per year for isotope measurements, and over 52 per year for trace element measurements, meaning changes could be examined at an annual, seasonal, monthly or higher resolution. Mean results representing the entirety of the shell growth period may provide information on mean environmental conditions recorded by the shell.

The method of sampling for $\delta^{18}O$ and $\delta^{13}C$ is based on that used in published studies using *Tridacna* sp. (e.g. Elliot et al., 2009, Welsh et al., 2011), while the method of sampling for trace elements was based on Sinclair et al. (1998) and Elliot et al. (2009).

Tridacna sp. were selected based on their age, bulk $\delta^{18}O$ value, preservation and estimated length of record. All samples were collected during a field season in 2003 and much of the background work was initially conducted by Kevin Welsh (2009). One modern *T. gigas* (MT7) and five fossil shells (T58, T39, T40, T41 and T45) were previously sampled for $\delta^{18}O$ and $\delta^{13}C$ at a seasonal resolution, and the data is reproduced here with additional samples measured. In additional to the previously sampled shells, 16 fossil shells were sampled at a seasonal resolution for this thesis. The $\delta^{18}O$ profile of the modern *Tridacna gigas* (MT7) has been published in Welsh et al.

(2011). Mg/Ca, Sr/Ca and Ba/Ca profiles of three modern *T. gigas* shells from the tropical Pacific, including MT7 from the Huon Peninsula have been published in Elliot et al. (2009).

In the following sections, results from fossil *Tridacna* sp. from which seasonal profiles were derived from are summarised. Additional shells were collected from the Holocene and Marine Isotope Stage 3 (MIS3) reef terraces at Huon and bulk measurements from these are presented in Welsh (2009).

3.2 Methods

3.2.1 Sample preparation

One valve for each shell was selected and sliced along the maximum growth axis. An area on the hinge or inner layer of the shell was chosen (Figure 3.1), then the areas were cut into a sequence of overlapping 25 X 75 mm slabs. These thin sections were mounted onto glass slides using epoxy resin, then trimmed and polished with diamond paste. Duplicates of the thin sections were made – one was approximately 1 mm thick and used for geochemical ($\delta^{18}O$, $\delta^{13}C$ and trace element) sampling, while the other was 0.3 mm thick and used to examine growth patterns. The thin sections were scanned using a digital scanner and mounted on a Perspex sample plate, attached using carbon conductive adhesive tabs.

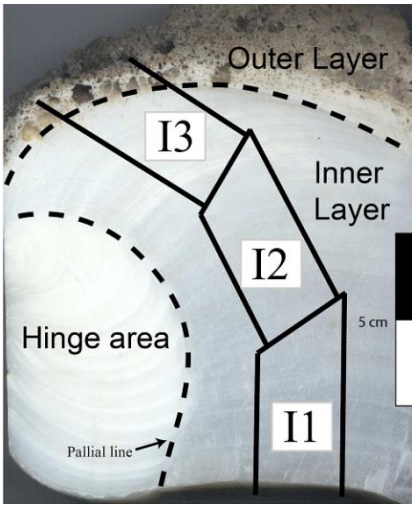

Figure 3.1 Cross section of modern Tridacna gigas (MT7) with shell areas marked and location of thin sections made from the inner layer (labelled Inner 1, 2 and 3). The transition between the hinge and inner layer corresponds to the pallial line (Welsh, 2009)

3.2.2 Screening for diagenesis

Fossil *Tridacna* sp. samples were screened for their mineralogical composition and microstructure preservation before geochemical analysis, using X-ray diffraction (XRD) (described in greater detail in Welsh (2009)). Carbonate powder was collected using a handheld drill across the inner section of samples, and a Bruker-AXS D8 Advance XRD using Cu K-alpha radiation (40kV) as the source. A Sol-X energy dispersive detector was used to determine % calcite in carbonate powders. The modern sample (MT7) had a 100% aragonite composition and all fossils used here had less than 1% calcite. Additionally, SEM imaging of fossil *Tridacna sp.* (shown in Chapter 2) shows excellent preservation of aragonite fibre and daily growth bands in all regions analysed (Welsh, 2009). In shells where diagenetic alteration had taken place, areas of calcite were clearly visible on the surface (Figure 3.2). Fossil shells with high % values of calcite and signs of diagenesis on shell surfaces or thin sections and SEM were not used in this study.

Figure 3.2 Large section of IIa reef *Tridacna gigas*, T14. Areas of calcite are circled

3.2.3 Stable isotopes ($\delta^{18}O$ and $\delta^{13}C$)

Bulk measurements (i.e. one measurement per shell) of $\delta^{18}O$ and $\delta^{13}C$ (Welsh, 2009) were obtained by sampling across the entire hinge or inner layer using a handheld drill. Bulk measurements provide information about mean environmental conditions over the entire growth period of the shell, while subsampling provides information at seasonal resolution. The results included in this chapter are from fossil *Tridacna* sp. from which seasonal profiles were derived (see Chapter 2, Table 2.2 and Table 2.3), which is a sub-sample of all the samples presented in Welsh (2009) (Table 3.1).

Table 3.1 Samples collected and dated by Kevin Welsh and presented in Welsh (2009)

Sample name	Species	Reef (terrace)	Bulk $\delta^{18}O$	Radiocarbon age (uncorrected years)	% Calcite
T72	*T. maxima*	Holocene	-1.8	4150	0.6
T66	*T. gigas*	Holocene	-1.9	6480	0.6
T59	*T. squamosa*	Holocene	-0.8	6890	0.6
T60	*T. gigas*	Holocene	-0.7	7025	0.8
T65	*T. maxima*	Holocene	-0.6	7330	0.8
T73	*T. gigas*	Holocene	-0.6	7129	0.1
T58	*T. gigas*	Holocene	-0.8	7257	0.1
T49	*T. gigas*	Holocene	-0.5	8230	0.5
T51	*T. gigas*	Holocene	-0.7	8548	0.2
T75	*T. gigas*	Holocene	-0.7	8592	0.2
T14	*T. gigas*	IIa	-0.1	31694	0.5
T29	*T. gigas*	IIa	0.2	31780	0.4
T28	*T. maxima*	IIa	0.1	30450	0.4
T10	*T. gigas*	IIa	0.1	30810	0.7
T13	*T. maxima*	IIa	-0.5	31750	0.3
T27	*T. gigas*	IIa	-0.3	31820	0.0
T70	*T. gigas*	IIa	-0.3	31590	0.6
T11	*T. maxima*	IIa	-0.1	33413	0.4
T9	*T. gigas*	IIa	-0.1	32794	0.5
T12	*T. squamosa*	IIa	0.3	33210	0.3
T32	*T. maxima*	IIIc (l)	0.1	34520	0.2
T31	*T. gigas*	IIIc (l)	0.2	32808	0.3
T34	*T. maxima*	IIIc (l)	0.1	33162	1.0
T33	*T. crocea*	IIIc (l)	0.1	36613	0.0
T39	*T. maxima*	IIIc (u)	0.2	36550	0.8
T30	*T. crocea*	IIIc (u)	0.3	36710	0.5
T40	*T. maxima*	IIIc (u)	-0.2	37758	0.6
T24	*T. crocea*	IIIb	-0.4		0.3
T48	*T. maxima*	IIIb	-0.2		1.0
T37	*T. maxima*	IIIb	-0.0		0.9
T23	*T. crocea*	IIIa (l)	-0.2		0.7
T41	*T. crocea*	IIIa (l)	0.1		0.6
T42	*T. crocea*	IIIa (m)	-0.0		0.4
T15	*T. gigas*	IIIa (u)	-0.3		0.8
T22	*T. gigas*	IIIa (u)	-0.1		0.5
T44	*T. maxima*	IIIa (u)	-0.1		0.5
T6	*T. gigas*	IIIa (u)	0.1		0.7
T38	*T. crocea*	IIIa (u)	0.0		0.5

Profiles of $\delta^{18}O$ and $\delta^{13}C$ were obtained by sampling thin sections of the hinge or inner layer (e.g. Figure 3.1). A high precision MicroMill (New Wave) equipped with a 300 µm tungsten carbide drill bit was used to sample the shell. Lines of carbonate powder were drilled along growth lines shown under reflected or transmitted light (Figure 3.3).

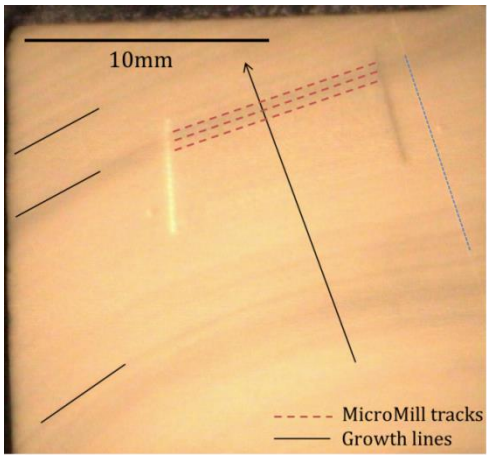

Figure 3.3 Thin section of Holocene *T. gigas* shell T58 under reflected light. Dashed lines show tracks of the MicroMill, while solid black lines show examples of growth bands. Arrow points to direction of growth. Laser ablation track is shown as the dotted line at the right of the picture

The mean distance between parallel lines was between 0.2 and 0.25 mm, and lines were approximately 10 mm in length, depending on the area of the shell sampled. Samples were milled with a depth of approximately 200 - 250 µm, with three or four passes of 50 – 70 µm depth to prevent the thin sections from fracturing. Powder was collected by tapping the sample plate onto weighing paper and transferring the powder into 0.5 mL polypropylene microcentrifuge tubes. Photographs were taken of every line milled using the Leica GZ6 camera attached to the MicroMill (Figure 3.3).

$\delta^{18}O$ and $\delta^{13}C$ analyses were performed on 0.02 - 0.1 mg sub-samples of the powder collected. The carbonate samples were reacted with 100% orthophosphoric acid at 75 °C in a Kiel Carbonate III preparation device and the resulting CO_2 was then analysed on a Thermo Electron Delta + Advantage stable isotope ratio mass spectrometer.

The standard deviation (n=360) of a powdered coral laboratory standard (COR1D, $\delta^{13}C$ = -0.647, $\delta^{18}O$ = -4.923) run as a sample on the same days as the study samples (between 27/09/10 and 22/04/13) was ± 0.06‰ for $\delta^{13}C$ and ± 0.06‰ for $\delta^{18}O$. All carbonate isotopic values are quoted relative to VPDB.

Due to costs constraints, it was decided to measure alternate samples for larger shells, while for smaller shells every sample was measured. For those with more than one thin section, growth bands visible on the shell were used to calculate the overlap between thin sections. This resulted in a temporal resolution of 6 to 20 samples per year.

3.2.4 Geochemical analysis and data processing

Laser Ablation Inductively Coupled Plasma Mass Spectrometry (LA-ICP-MS)

Trace element (Me/Ca) ratios were obtained from the same thin sections used for isotopic profiles. Me/Ca ratios were measured by Laser Ablation Inductively Coupled Plasma Mass Spectrometry (LA-ICP-MS) at Royal Holloway, University of London in 2011 and 2013. The equipment used was an ArF excimer (193 nm) laser-ablation system coupled to a two-volume laser-ablation cell. The LA unit was coupled to an Agilent 7500ce/cs quadrupole ICPMS for elemental analysis (Müller et al., 2009). A laser track was selected close to the micromilled area of the shell (Figure 3.3). Thin sections were cleaned with methanol, then the laser ablation track was pre-ablated using a spot size of 74 μm, 50 Hz and a speed of 6 mm/min. Thin sections were then ablated using a spot size of 57 μm, 15 Hz and a speed of 30 μm/sec. 17 elemental ratios were measured - Li, B, Mg24, Mg25, Al, P, Mn, Zn, Pb, Sr88, Sr89, Y, Ba, La, Ce, Pb, and U. Internal glass standards with known elemental values (NIST610/612) were used as well as external standards (MACS and Gor-128) in order to correct for any eventual instrumental drift. Data was produced in counts per second (CPS) and was converted to parts per million (ppm) using IGOR Pro software (Wavemetrics), using the trace element reduction scheme. Each Me/Ca time series was then converted to mmol/mol or μmol/mol. The average experimental error for the three main elements examined (Mg/Ca, Sr/Ca and Ba/Ca) ranged from 2% (1σ) in Ba/Ca to 3.4% (1σ) in Sr/Ca, by repeated measurements of a glass standard. Minimum, maximum and mean values were calculated for each shell and are shown in Section 3.3.

Correlating $\delta^{18}O$ and trace element profiles

In order to compare stable isotope and trace element profiles, both sets of data must be on the same scale, which requires cross-correlation between the two sets of data. Measurements of $\delta^{18}O$ were taken at discrete distances between lines (approximately 200 – 250 μm apart), while trace elements were measured continuously along a timed laser track with a constant step of 14 μm. As $\delta^{18}O$ and trace elements were measured on the same thin sections (Figures 3.3 and 3.4), the records produced could be matched

up with ease. This was done by measuring the distance into the laser track the MicroMill drilling started, and thenscaling the $\delta^{18}O$ record to the laser track.

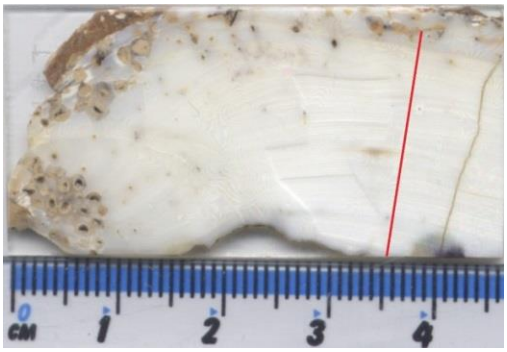

Figure 3.4 Thin section of IIIb reef shell T24. Red line represents the laser track from which trace element profiles were derived. The gap between the start of the laser track and MicroMill samples is due to borings which can be seen at the top of the shell

3.2.5 Chronology construction

In many bivalve species, annual growth can be seen as alternating dark and light bands (Figure 3.4). This banding results from quantitative changes in calcareous and organic deposition, related to physiological changes in molluscs (Kobayashi, 1969). In *Tridacna* sp. from tropical regions, this annual banding is less clear, making it more difficult to assign years of growth to the $\delta^{18}O$ or Me/Ca profile, and so daily banding was used to assign growth (described in the following section). Staining agents such as Mutvei's Solution (Schöne et al., 2005) can been used in many species of bivalve (Schöne, 2008, Hallmann et al., 2009, Schöne et al., 2010, Schöne et al., 2011, Schwartzmann et al., 2011) in order to view banding in greater detail. However, when used with *Tridacna* sp. from Papua New Guinea, annual banding could not be seen any more clearly than using transmitted light, which implies low concentrations of organic material (Welsh et al., 2011).

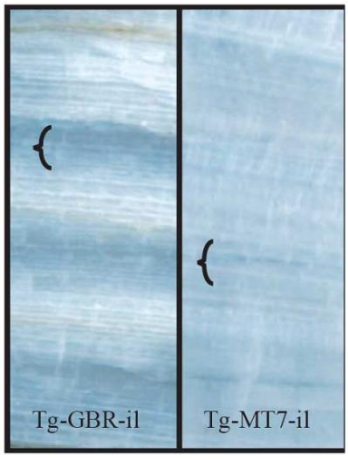

Figure 3.5 Thin sections from the inner layer of *Tridacna gigas* shells from Great Barrier Reef (GBR) (left) and the Huon Peninsula (right). The *T. gigas* from GBR comes from an environment with greater seasonal variability in temperature, and annual banding can be seen more clearly than in the *T. gigas* from the Huon Peninsula (Welsh, 2009)

{ shows the transparent part of annual bands, apparent in GBR shell and less apparent in MT7

One method of assigning a chronology to geochemical profiles is to identify annual variations in $\delta^{18}O$. In areas outside the tropics, with stronger seasonality (e.g. Watanabe et al., 2004), such as the Great Barrier Reef (Elliot et al., 2009), annual banding is clear (Figure 3.5) and there are regular seasonal cycles in $\delta^{18}O$ (Figure 3.6). In the tropical region, seasonal variations in sea surface temperature are small, for example 1-2°C at the Huon Peninsula. The variations in $\delta^{18}O$ profiles obtained in these areas reflect the inter-annual variations in local seawater ($\delta^{18}O_w$) rather than annual seasonality. Annual cycles in $\delta^{18}O$ are thus often difficult to identify, and information from the growth record is needed to build a chronology.

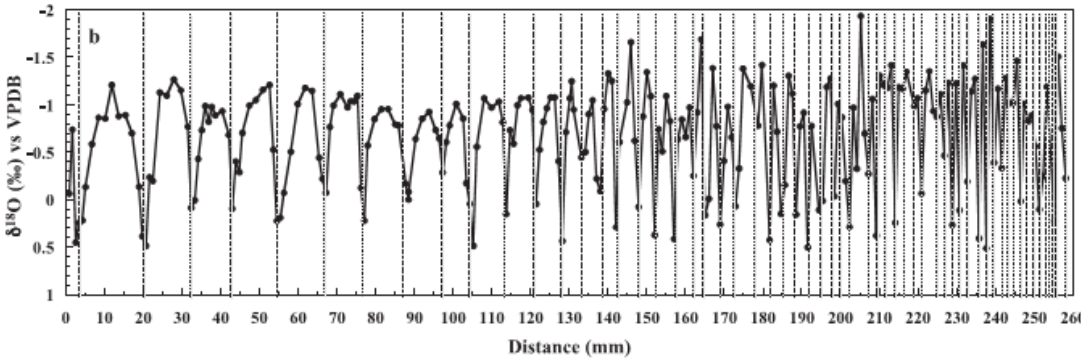

Figure 3.6 Oxygen isotopic profile of a Holocene *Tridacna gigas* from Japan. Seasonal cycles are marked by large changes of 1 – 1.5‰ in $\delta^{18}O$. Vertical lines represent the timing of the winter season and the location of dark layers in the shell (Watanabe et al., 2004)

Day/night banding in Tridacna sp.

The thickness of pairs of day/night micro-growth bands seen in *Tridacna* sp. was used to derive information on growth rates of the samples used in this study. This

information was in turn used together with geochemical profiles to develop the chronology of individual shells.

Tridacna sp. have fine day/night growth increments observed in the inner shell under a microscope (Aharon and Chappell, 1986, Pätzold et al., 1991, Watanabe et al., 2004). These appear as pairs of dark and light bands with variable widths (Figure 3.7). They have been shown to be daily growth lines (Bonham, 1965, Watanabe et al., 2004, Sano et al., 2012), caused by the daily photosynthetic activity of the symbiotic zooxanthellae within *Tridacna* sp. which influence calcification (Pannella and Macclintock, 1968, Ohno, 1985, Pätzold et al., 1991).

In order to assign a chronology to the profiles of *Tridacna* sp. $\delta^{18}O$ and trace element data, the thickness of these pairs of day and night bands was estimated. The results were extrapolated and converted into growth rate changes through the lifespan of each shell. These daily growth bands were viewed on thin sections of approximately 30µm, (see Section 3.1.1). Photographs were taken using a microscope fitted with a Leica DFC420C camera every 1 mm of growth across a transect. A scale of 100µm was superimposed onto each photographic image in order to calculate the width of bands (Figure 3.7).

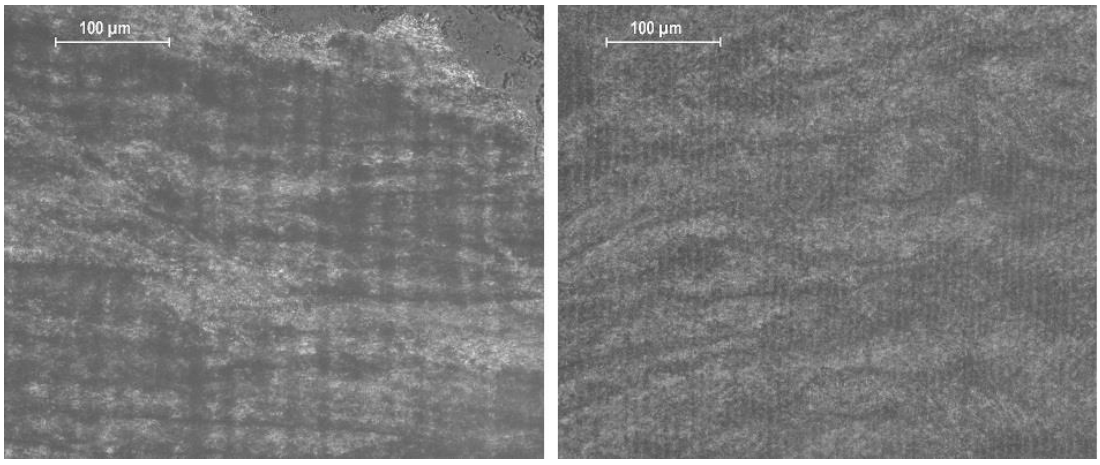

Figure 3.7 Pairs of day/night bands visible in the juvenile (left) and adult (right) stage of life in the hinge area of Holocene shell T58. The mean thickness of these pairs of bands was 20-25 µm (corresponding to a growth rate of 7-9 mm/year) in the juvenile portion of the shell and 5 µm (corresponding to a growth rate of 2 mm/year) in the adult portion of the shell

In four fossil MIS3 *T. maxima* and *T. gigas* shells (T28, T39, T40 and T41) these bands were not visible, and therefore the chronology of these was based on the $\delta^{18}O$ and Mg/Ca profiles.

Initially the number of pairs of bands was counted per 100 μm by eye. This was replicated once, and then to try and refine this method, Visilog Image Processing Software (Noesis) was used. For each image, a histogram was created which measured the greyscale intensity of the image (shown for Holocene *T. gigas* shell T58 in Figure 3.8). This meant that pairs of bands within a given distance (up to 600 μm per image) could be counted and a more reliable estimate of bands per 100 μm was obtained.

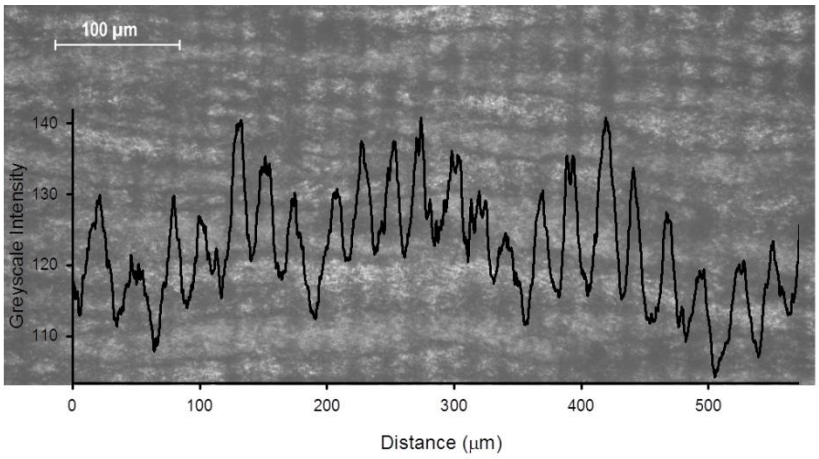

Figure 3.8 Photograph of pairs of day/night bands under the microscope (T58), and the resulting graphical representation (overlying) of the greyscale intensity of these bands produced by Visilog

Once pairs of day/night bands were counted, a growth curve was constructed for each shell by calculating the distance at which a year of growth (365 pairs of bands) had been reached. With this information, years of growth could be assigned to the oxygen stable isotope and trace element records. As the thin sections used for isotope analysis and daily banding counting came from the same slab of *Tridacna* shell, distances could be matched up. Typical error attributed to this method is ±1mm due to human error, which would encompass 2 - 4 isotope measurements depending on the portion of the shell sampled (i.e. hinge or inner layer).

Comparing methods for deriving an age model

In order to test this method, the growth curve produced by measuring the day/night band thickness was compared to that of the published $\delta^{18}O$ profile of the modern *T. gigas*, MT7 (Figure 3.9). The growth curve of MT7 was initially obtained by using a combination of information from the visible annual growth bands and the $\delta^{18}O$ record (Welsh et al., 2011). The comparison demonstrates that growth rates obtained by both methods are similar, with overall growth rates of 7.4 mm/year using the Welsh et al. (2011) calculation and 7.1 mm/year using the day/night banding. There are small discrepancies between the two methods, with the day/night band method suggesting slightly slower overall growth than the published age model, with juvenile growth rates of between 11 and 17 mm/year using the Welsh et al. (2011) calculation and 10 and 15 mm/year using the day/night banding, and adult growth rates of around 2.6 and 2.5 mm/year respectively . This discrepancy may be because the width of the day/night bands was counted at discrete intervals across each thin section, which therefore assumes that growth is constant at the rate suggested by the width of the bands counted. In bivalves, growth rates are not constant, and daily growth width increments can vary throughout the year (Goodwin et al., 2003, Hallmann et al., 2009, Schwartzmann et al., 2011). This assumption will create differences within an annual cycle between the growth rate suggested by the day/night bands and growth rates derived from the $\delta^{18}O$ signal.

Although there are discrepancies of up to 2 mm/year between the two methods, the overall growth rate is not significantly different (Figure 3.9). The width of day/night bands and the calculated growth rate was therefore used to construct chronologies of fossil shell $\delta^{18}O$, $\delta^{13}C$ and trace element profiles.

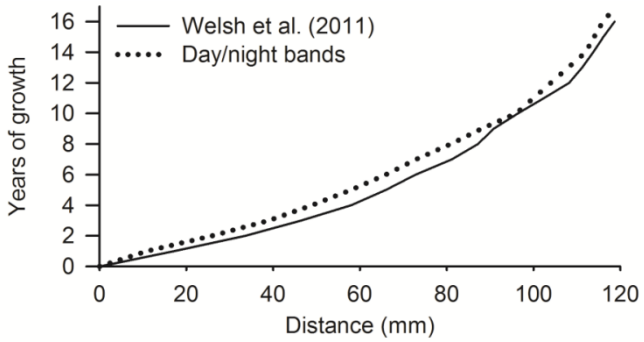

Figure 3.9 Comparison of growth rates of a modern *T. gigas* (MT7) by using pairs of day/night bands to calculate growth rate, and the published $\delta^{18}O$ record from Welsh (2011)

With the estimated growth curves, approximate years of growth were assigned to the $\delta^{18}O$ and Mg/Ca profiles (Mg/Ca was chosen as these profiles show some seasonality) (Figures 3.9 and 3.10). Chronologies for the shells were built using Analyseries (Paillard et al., 1996) using the anchor method described by de Brauwere et al. (2009). This method uses the proxy record and a fixed profile for the time series (in this case based on the modern average seasonal cycle in SST at the Huon Peninsula) and linearly interpolates between two anchor points. It therefore assumes that the growth rate between two points is constant, and any wrongly assigned date will generate an error in the reconstructed time series. However, if records do not show clear seasonality then this method is the only way of creating a time series without making assumptions about its shape (de Brauwere et al., 2009). For the *Tridacna* sp. used in this study, $\delta^{18}O$ maxima were assigned a mid-August date, based on the modern SST pattern at the Huon Peninsula, which records SST minima during August. This assumes that SST minima have constantly occurred during August over the past 60 ka, and the potential error associated with this assumption is discussed later in this chapter.

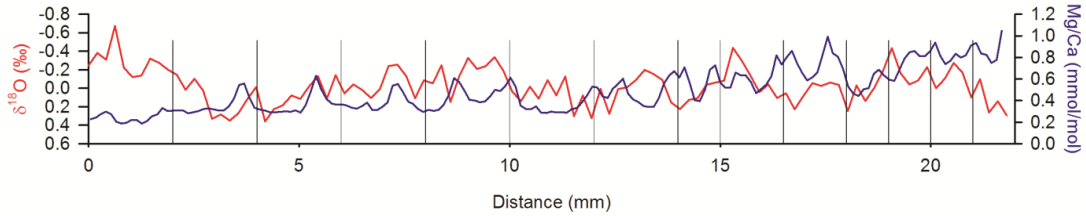

Figure 3.10 $\delta^{18}O$ (red) and Mg/Ca (blue) profiles. Grey vertical lines highlight ~13 years of growth as suggested by the thickness of day/night bands for T32 (38.6 ka BP)

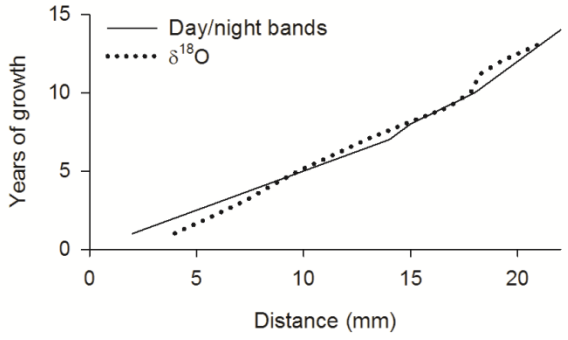

Figure 3.11 Comparison of the growth model estimated by the day/night band method, and the growth model estimated from the $\delta^{18}O$ profile in Analyseries for IIIc (l) shell T32

August SST minima were then matched with $\delta^{18}O$ maxima (Figure 3.12) and the samples between these were interpolated linearly to give a regular number of samples per year (Figure 3.13). There was no additional matching of $\delta^{18}O$ minima to SST maxima, due to the double peak in summer SST which occurs in the modern SST cycle

(Chapter 2, Figure 2.7) and complicates matching this with $\delta^{18}O$ minima. Although linear interpolation assumes a constant growth rate between the two points, this was preferred to forcing a match between the proxy record and the SST cycle.

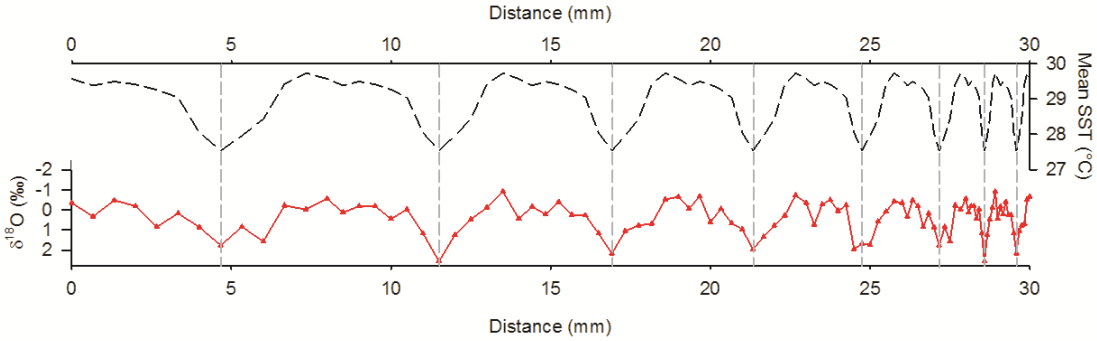

Figure 3.12 Mean SST curve (top panel) and pseudo-$\delta^{18}O$ profile (bottom panel) demonstrating how SST minima were matched to $\delta^{18}O$ maxima in order to convert profiles from a distance scale to a time series

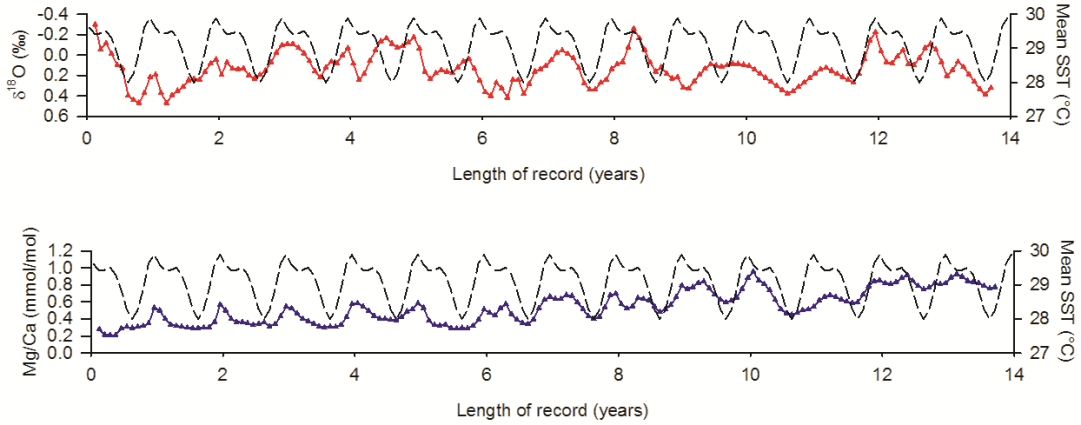

Figure 3.13 Resultant $\delta^{18}O$ (above) and Mg/Ca (below) time series after being interpolated to 12 samples a year for IIIc (l) shell T32. On the right axis is the mean SST curve used as a guide for data interpolation

Potential errors in chronology

To avoid forcing the data the most positive $\delta^{18}O$ values were assigned a mid-August date, and maximum temperatures were not matched to $\delta^{18}O$ minima. However, minimum temperatures might have occurred during a different month due to changes in the seasonal cycle of incoming solar radiation (Figure 3.14). Minimum SST values currently occur one month (during August) after minimum solar radiation (currently during July, Figure 3.14). In the past, minimum SST values might have taken place during a different month due to changes of the seasonal cycle, so knowledge of past

annual insolation cycles assists in estimating any potential chronological error associated with attributing August SST minima to $\delta^{18}O$ maxima.

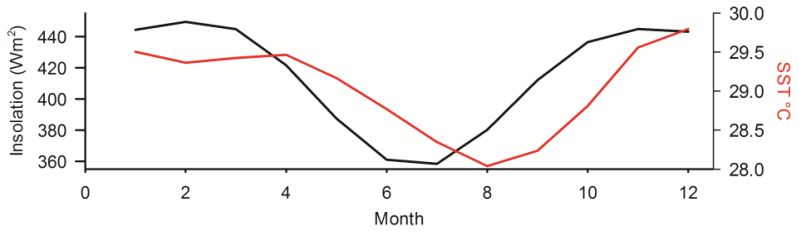

Figure 3.14 Mean monthly insolation for 6.5°S (black line) (Laskar et al., 2004) compared to mean IGOSS SST (red line) for 1986-2002 at the Huon Peninsula

The amplitude of seasonal insolation shows that the minimum insolation occurred either during June or July at 6.5°S over the past ~60 kyr (Figure 3.15). The Holocene shells, one from the IIa reef (T28), and all of those from the IIIa reef grew during periods where the least amount of insolation occurred during June, while all other samples grew when the least amount of insolation took place during July. This would have resulted in minimum temperatures occurring in July rather than August, as in the modern SST cycle at the Huon Peninsula. This means that there could be an error on the chronology of the Holocene samples, T28 and the IIIa samples of one month, as maximum $\delta^{18}O$ was consistently assigned a mid-August date.

However, for the sake of consistency and because no conclusions can be drawn on the timing of the seasonal cycle (rather the amplitude of the annual cycle in $\delta^{18}O$ will be discussed in Chapter 7), the chronology of all samples assume that minimum temperatures occurred during August throughout the Holocene and MIS3. Unless there were major changes to the timing of the seasonal cycle during MIS3, the error on the *Tridacna* sp. $\delta^{18}O$ chronology is unlikely to be greater than one month.

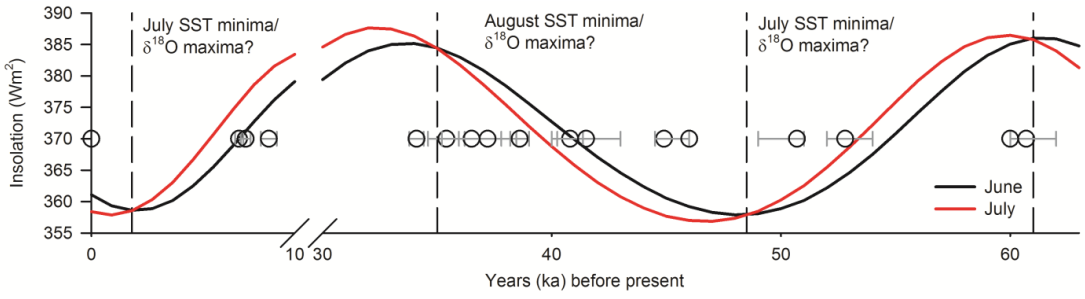

Figure 3.15 Mean monthly insolation for June and July at 6.5°S (Laskar et al., 2004). Fossil *Tridacna* sp. with error bars representing age uncertainties (described in Chapter 2) are shown by circles

3.3 Results from Holocene reef *Tridacna gigas* (10 – 6.5 ka BP)

Stable oxygen and carbon isotopes

The mean $\delta^{18}O$ recorded in *Tridacna* sp. reflects global ice volume as well as local SST and $\delta^{18}O_w$. Removing the ice volume component in order to reveal changes in local SST and salinity is discussed in Chapter 4. The mean, minimum and maximum $\delta^{18}O$ and $\delta^{13}C$ derived from raw profiles measured as described in Section 3.2.3 are presented for four Holocene shells in Table 3.2 and Figures 3.16 – 3.17. The mean $\delta^{18}O$ and $\delta^{13}C$ values were calculated from all the samples measured for each shell, so may show a bias toward the juvenile portion of the shell, where growth is more rapid. Results show that mean values of $\delta^{18}O$ are 0.2-0.3‰ more positive than the modern shell in three of the Holocene *T. gigas*, while one shell (T66) has a mean value 0.6‰ more negative than MT7. For all four Holocene samples, the mean $\delta^{13}C$ value is 0.7-0.9‰ more positive than the modern shell.

Table 3.2 Range of raw $\delta^{18}O$ and $\delta^{13}C$ values for four Holocene *T. gigas*

Shell	Age (ka BP)	$\delta^{18}O$ (‰)				$\delta^{13}C$ (‰)			
		Min	Max	Mean	Range	Min	Max	Mean	Range
MT7	0	-2.1	-0.42	-1.2	1.6	1.1	2.2	1.9	1.1
T66	6.49	-2.5	-1.2	-1.8	1.3	2.3	2.9	2.7	0.57
T73	7.26	-1.3	-0.50	-0.96	0.87	2.3	3.1	2.8	0.80
T58	7.59	-1.7	-0.29	-0.96	1.4	2.2	3.2	2.7	1
T75	8.73	-1.4	-0.40	-0.92	0.99	2.2	3.2	2.6	1

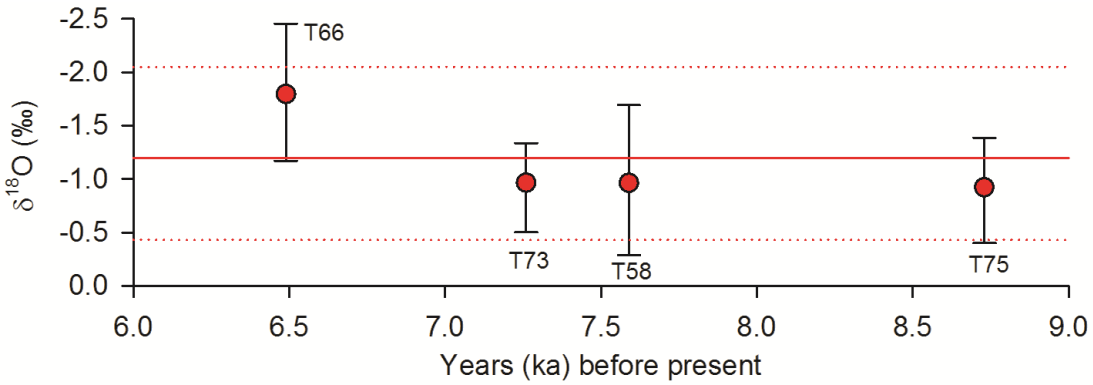

Figure 3.16 Holocene mean $\delta^{18}O$ values (filled circles). Vertical bars represent maximum and minimum $\delta^{18}O$. Solid line represents the modern $\delta^{18}O$ mean value (-1.2‰), while dotted lines represent the modern maximum and minimum $\delta^{18}O$ values

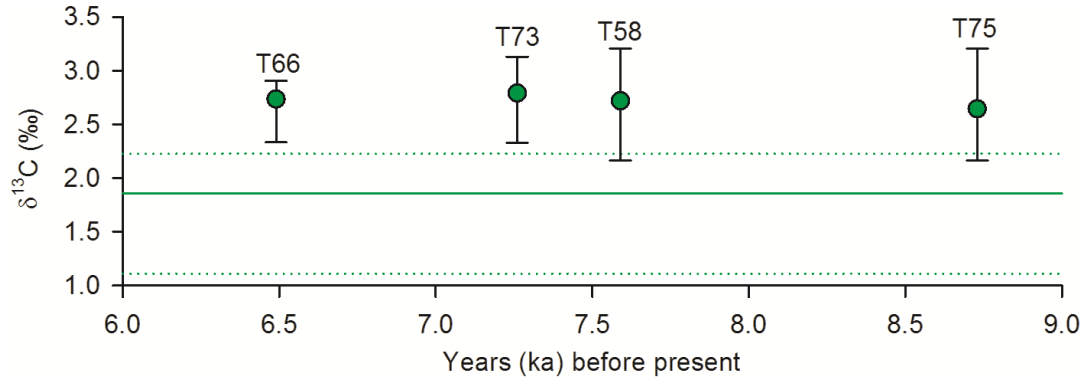

Figure 3.17 Holocene mean $\delta^{13}C$ values (filled circles). Vertical bars represent maximum and minimum $\delta^{13}C$. Solid line represents the modern $\delta^{13}C$ mean value 1.86‰), while dotted lines represent the modern maximum and minimum $\delta^{13}C$ values

Trace elements

In the following section, the mean trace element data is compared to the modern shell (MT7) data sampled at the same locality. Hinge and inner layer values are separated, as differences in trace elements have been observed between these areas of the shell (Elliot et al., 2009). The minimum, maximum and mean values of Mg/Ca, Sr/Ca and Ba/Ca, derived from the raw profiles measured as described in Section 3.2.3 are shown in Tables 3.3 – 3.5 and Figure 3.18.

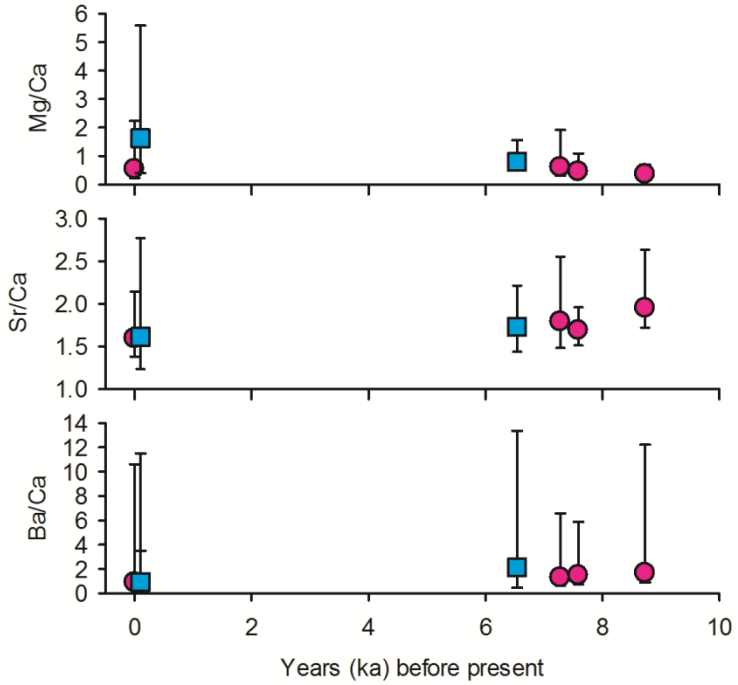

Figure 3.18 Mg/Ca (top panel), Sr/Ca (middle panel) and Ba/Ca (bottom panel) in MT7 and Holocene *T. gigas*. Vertical bars represent maximum and minimum values (mmol/mol). Squares represent where the inner layer was sampled, circles represent where the hinge was sampled

Mean Mg/Ca values are higher in the modern inner layer than the hinge by approximately 1.1 mmol/mol (Table 3.3). In the fossil data, Mg/Ca measured in the inner layer of T66 is 0.2-0.4 mmol/mol higher than values measured in the hinge of the remaining three shells.

Table 3.3 Mg/Ca in modern and Holocene *T. gigas*

Shell	Age	Mg/Ca			
		Min	Max	Mean	Range
MT7-H	0	0.22	2.2	0.53	2.0
MT7-IL	0	0.39	5.6	1.6	5.2
T66	6.49	0.48	1.5	0.79	1.1
T73	7.26	0.3	1.9	0.60	1.6
T58	7.59	0.26	1.1	0.44	0.82
T75	8.73	0.24	0.69	0.35	0.45

Mean Sr/Ca values in the hinge and inner layer of the modern *T. gigas* are almost identical (Table 3.4). In the fossil samples, mean Sr/Ca values are 0.1-0.2 mmol/mol higher than mean values measured in MT7.

Table 3.4 Sr/Ca in modern and Holocene *T. gigas*

Shell	Age	Sr/Ca			
		Min	Max	Mean	Range
MT7-H	0	1.4	2.1	1.6	0.76
MT7-IL	0	1.2	2.8	1.6	1.5
T66	6.49	1.4	2.2	1.7	0.8
T73	7.26	1.5	2.6	1.8	1.1
T58	7.59	1.5	2	1.7	0.45
T75	8.73	1.7	2.6	1.9	0.9

Mean values of Ba/Ca are nearly identical in the hinge and inner layer of the modern shell (Table 3.5). Mean values in the fossils are consistently higher than MT7 by 0.6-1.2 µmol/mol.

Table 3.5 Ba/Ca in modern and Holocene *T. gigas* (µmol/mol)

Shell	Age	Ba/Ca			
		Min	Max	Mean	Range
MT7-H	0	0.38	11	0.9	10
MT7-IL	0	3.5	12	0.95	8
T66	6.49	0.47	13.4	2.1	12.9
T73	7.26	0.66	6.6	1.3	5.9
T58	7.59	0.77	5.9	1.5	5.1
T75	8.73	0.9	12.2	1.7	11.3

3.4 Results from MIS3 *Tridacna* sp. (~60 – 34 ka BP)

Stable oxygen and carbon isotopes

The mean, minimum and maximum $\delta^{18}O$ and $\delta^{13}C$ derived from raw profiles measured as described in Section 3.2.3 are presented for 15 MIS3 shells in Table 3.6 and Figures 3.19 – 3.20. As with the Holocene *T. gigas*, the mean $\delta^{18}O$ and $\delta^{13}C$ values were calculated from all the samples measured for each shell, so may show a bias toward the juvenile portion of the shell, where growth is more rapid. All mean $\delta^{18}O$ values of fossil *Tridacna* sp. shells are more positive than MT7 by 0.7-1.5‰, but there is no trend through time. Mean $\delta^{13}C$ values of fossils are consistently more positive than MT7 by 0.1-1.1‰.

Table 3.6 Range of raw $\delta^{18}O$ and $\delta^{13}C$ values for 15 MIS3 *Tridacna* sp.

Shell	Age (ka BP)	$\delta^{18}O$ (‰)				$\delta^{13}C$ (‰)			
		Min	Max	Mean	Range	Min	Max	Mean	Range
MT7	0	-2.1	-0.42	-1.2	1.6	1.1	2.2	1.9	1.1
T28	34.1	-0.86	-0.11	-0.24	0.75	2	2.8	2.4	0.83
T27	35.4	-0.96	0.27	-0.23	1.2	1.9	2.9	2.5	0.92
T9	36.5	-0.63	0.42	0.045	1.0	2.2	2.9	2.7	0.79
T11	37.2	-0.023	0.72	0.38	0.74	2.5	3.1	2.8	0.68
T32	38.6	-0.67	0.36	-0.03	1.0	1.8	2.8	2.4	1.1
T39	40.8	-0.51	1.0	0.32	1.5	2	3.4	2.6	1.5
T40	41.5	-0.99	-0.15	-0.48	0.83	1.8	2.2	1.9	0.41
T24	44.9	-0.45	0.48	0.085	0.93	2.6	3.0	2.8	0.50
T37	46	-0.13	0.68	0.37	0.81	2.7	3.4	3	0.70
T41	50.7	-0.68	0.83	0.064	1.50	1.7	3.3	2.5	1.6
T18	52.8	-0.72	0.25	-0.24	0.97	1.9	2.7	2.4	0.76
T15	60	-0.81	0.094	-0.35	0.9	2.1	3.2	2.5	1.1
T22	60	-0.57	0.86	0.13	1.4	2.0	3.3	3.0	1.3
T45	60	-0.44	0.72	0.19	1.2	2.4	3.5	2.9	1.1
T6	60.7	-0.31	0.87	0.33	1.2	2.6	3.3	3.0	0.68

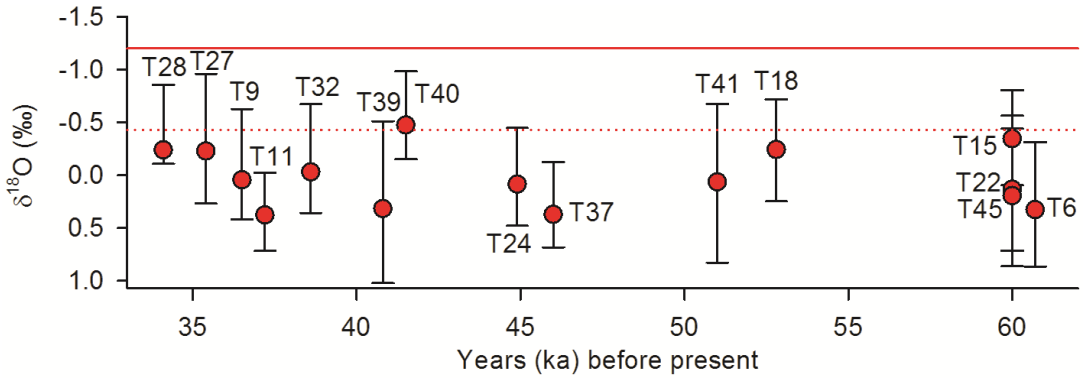

Figure 3.19 MIS3 mean $\delta^{18}O$ values (filled circles). Vertical bars represent maximum and minimum $\delta^{18}O$. Solid line represents the modern $\delta^{18}O$ mean value (-1.2‰), while dotted line represents the modern maximum $\delta^{18}O$ value

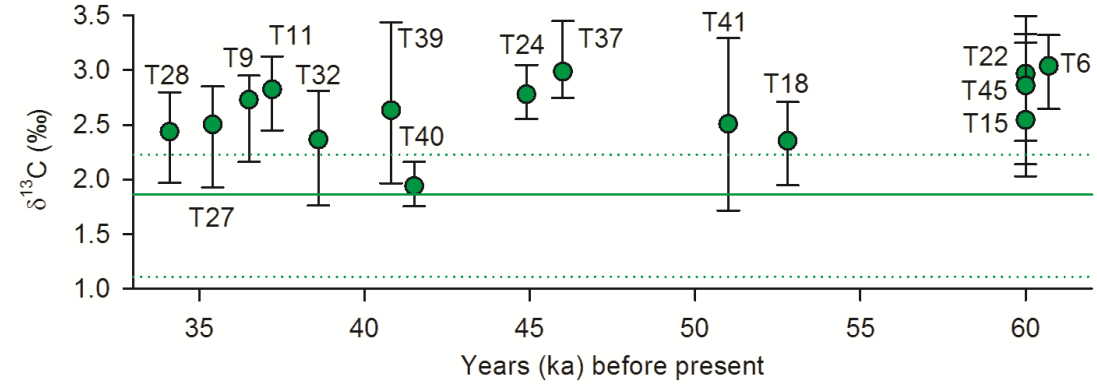

Figure 3.20 MIS3 mean $\delta^{13}C$ values (filled circles). Vertical bars represent maximum and minimum $\delta^{13}C$. Solid line represents the modern $\delta^{13}C$ mean value (1.86‰), while dashed lines represent the modern maximum and minimum $\delta^{13}C$ values

Trace elements

Trace element ratios measured in the hinge and inner layer of MIS3 *Tridacna* sp. samples are shown in Figure 3.21 and Tables 3.7 – 3.9. Mg/Ca and Sr/Ca are shown in mmol/mol, while Ba/Ca is shown in µmol/mol.

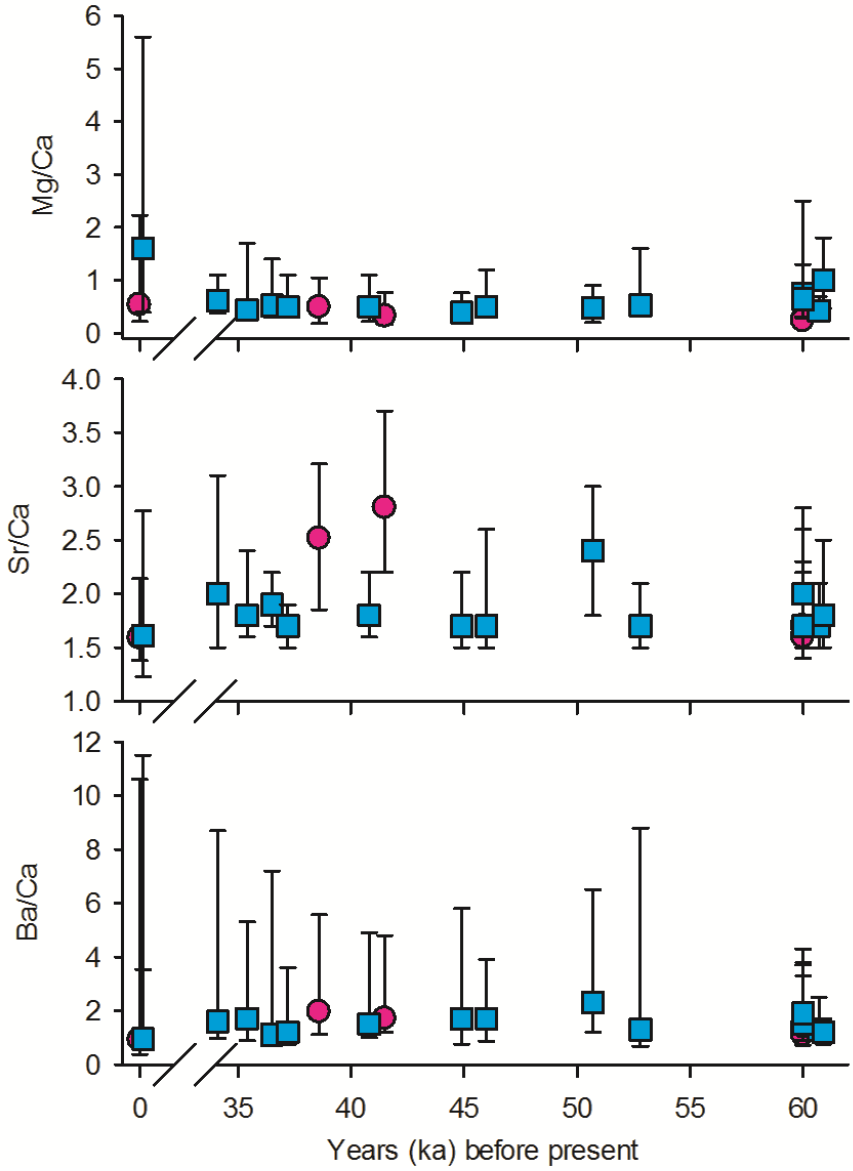

Figure 3.21 Mg/Ca (top panel), Sr/Ca (middle panel) and Ba/Ca (bottom panel) in MT7 and MIS3 *Tridacna* sp. Vertical bars represent maximum and minimum values (mmol/mol). Squares represent where the inner layer was sampled, circles represent where the hinge was sampled

Hinge values of Mg/Ca are lower in fossil *Tridacna* sp. than the mean hinge value of MT7 and inner layer mean values are lower in the fossils than the modern shell.

Table 3.7 Range of Mg/Ca values (mmol/mol) in MT7 and 17 MIS3 *Tridacna* sp.

Shell	Age	Mg/Ca			
		Min	Max	Mean	Range
MT7-H	0	0.22	2.2	0.53	2.0
MT7-IL	0	0.39	5.6	1.6	5.2
T9	36.5	0.3	1.4	0.52	1.1
T11	37.2	0.35	1.1	0.49	0.72
T27	35.4	0.24	1.7	0.44	1.5
T28	34.1	0.38	1.1	0.61	0.67
T32	38.6	0.19	1	0.49	0.86
T39	40.8	0.22	1.1	0.5	0.84
T40	41.5	0.16	0.77	0.32	0.62
T24	44.9	0.24	0.76	0.39	0.52
T37	46	0.31	1.2	0.5	0.9
T41	50.7	0.2	0.9	0.48	0.7
T18	52.8	0.35	1.6	0.52	1.3
T6	60.7	0.3	0.69	0.42	0.39
T15	60	0.1	0.51	0.24	0.41
T22	60	0.31	2.5	0.75	2.2
T45	60	0.13	0.47	0.23	0.34
T38	60.9	0.47	1.8	1	1.4
T44	60	0.29	1.3	0.64	1

As with the Holocene *Tridacna* sp, mean Sr/Ca values of MIS3 fossils are higher by 0.1-1.2 mmol/mol than those recorded in MT7.

Table 3.8 Range of Sr/Ca values (mmol/mol) in MT7 and 17 MIS3 *Tridacna* sp.

Shell	Age	Sr/Ca			
		Min	Max	Mean	Range
MT7-H	0	1.4	2.1	1.6	0.8
MT7-IL	0	1.2	2.8	1.6	1.5
T9	36.5	1.7	2.2	1.9	0.5
T11	37.2	1.5	1.9	1.7	0.5
T27	35.4	1.6	2.4	1.8	0.8
T28	34.1	1.5	3.1	2	1.7
T32	38.6	1.9	3.2	2.5	1.4
T39	40.8	1.6	2.2	1.8	0.6
T40	41.5	2.2	3.7	2.8	1.5
T24	44.9	1.5	2.2	1.7	7.2
T37	46	1.5	2.6	1.7	1.1
T41	50.7	1.8	3	2.4	1.2
T18	52.8	1.5	2.1	1.7	0.6
T6	60.7	1.5	2.1	1.7	0.6
T15	60	1.4	2.3	1.6	0.9
T22	60	1.5	2.2	1.7	0.7
T45	60	1.4	2.6	1.7	1.2
T38	60.9	1.5	2.5	1.8	1
T44	60	1.7	2.8	2	1.1

Mean Ba/Ca values of fossil shells are higher by 0.2-1.4 µmmol/mol than the values recorded in MT7 (Table 3.9), while peak values are lower (Figure 3.21) and this will be discussed in Chapter 5.

Table 3.9 Range of Ba/Ca values (µmol/mol) in MT7 and 17 MIS3 *Tridacna* sp.

Shell	Age	Ba/Ca			
		Min	Max	Mean	Range
MT7-H	0	0.38	11	0.9	10
MT7-IL	0	3.5	12	0.95	8
T9	36.5	0.76	7.2	1.1	6.4
T11	37.2	0.73	3.6	1.2	2.9
T27	35.4	0.88	5.3	1.7	4.4
T28	34.1	0.97	8.7	1.6	7.7
T32	38.6	1.1	5.6	1.9	5.6
T39	40.8	1.0	4.9	1.5	3.9
T40	41.5	1.2	4.8	1.7	3.6
T24	44.9	0.76	5.8	1.7	5
T37	46	0.87	3.9	1.7	3.1
T41	50.7	1.2	6.5	2.3	5.2
T18	52.8	0.68	8.8	1.3	8.1
T6	60.7	0.89	2.5	1.3	1.6
T15	60	0.72	4.3	1.1	3.6
T22	60	0.89	3.3	1.5	2.4
T45	60	0.9	3.7	1.4	2.8
T38	60.9	0.76	1.7	1.2	1
T44	60	1.3	3.8	1.9	2.5

3.5 Effects of processing $\delta^{18}O$, $\delta^{13}C$ and trace element data

In this chapter so far, mean, minimum and maximum values of $\delta^{18}O$, $\delta^{13}C$ and trace element concentrations have been produced from the "raw" data set. This is measured by distance and contains all the samples measured from each shell, and therefore may have an ontological bias as there will be more samples from the juvenile portion of the shell, where growth occurs more rapidly. In the majority of fossil shells, the sampling resolution was 12-20 samples per year in the juvenile portion, and 6-12 in the adult portion, depending on the size of the shell from which thin sections were created. In this section, the different approaches to resampling the data and the calculated mean, maximum and minimum values will be discussed for an example shell. Resampling the data does not affect the mean significantly but does decrease the maximum value recorded, which is particularly important when looking at peaks in Ba/Ca.

Resampling $\delta^{18}O$ and $\delta^{13}C$ time series

All interpolation of data series was performed using Analyseries (Paillard et al., 1996) (Figure 3.22). For $\delta^{18}O$ and $\delta^{13}C$, the difference between mean values calculated using the profiles at three different resolutions in the Holocene *T. gigas* T75 is insignificant, around 0.02‰ ($\delta^{18}O$) and 0.01‰ ($\delta^{13}C$) (Figures 3.23 – 3.24 and Tables 3.10 – 3.11).

In most samples, there is not a difference between the mean from the juvenile portion of the shell and the mean from the adult section. While the sampling resolution decreases as the shell ages, the range of $\delta^{18}O$ and $\delta^{13}C$ tends not to decrease. The maximum and minimum values calculated from the three data sets at different resolutions differ by up to 0.17‰ ($\delta^{18}O$) and 0.09‰ ($\delta^{13}C$). Due to decreased resolution, the smoothed $\delta^{18}O$ and $\delta^{13}C$ (maximum – minimum) records likely underestimate the true seasonal isotope change.

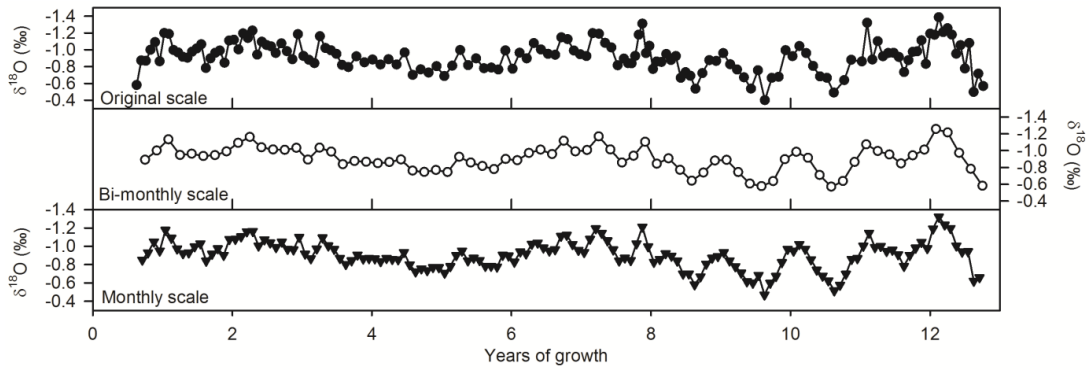

Figure 3.22 Comparison of $\delta^{18}O$ profiles in Holocene *T. gigas* T75 (8.73 ka BP).
Top panel: original resolution (all samples measured);
Middle panel: bi-monthly resolution (6 samples/year);
Bottom panel: monthly resolution (12 samples/year)

Table 3.10 Comparison of mean, maximum, minimum values of $\delta^{18}O$ at different resolutions in T75

Scale	original	bi-monthly	monthly
Mean	-0.92	-0.90	-0.91
Maximum	-0.4	-0.57	-0.47
Minimum	-1.4	-1.3	-1.32
Range	0.99	0.69	0.85

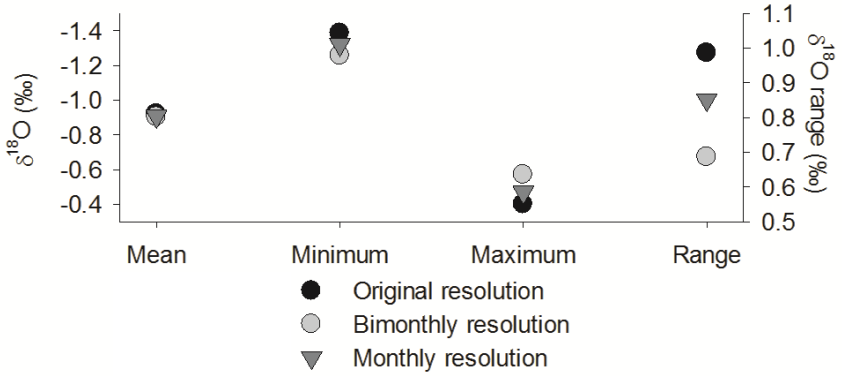

Figure 3.23 Comparisons of mean, maximum, minimum values of $\delta^{18}O$ at different resolutions (original, bi-monthly and monthly resolution) in T75. Left axis shows the measured minimum, maximum and mean $\delta^{18}O$, right axis shows the range of $\delta^{18}O$

Table 3.11 Comparison of mean, maximum, minimum values of $\delta^{13}C$ at different resolutions in T75

Scale	original	bi-monthly	monthly
Mean	2.79	2.78	2.78
Maximum	3.14	3.05	3.09
Minimum	2.33	2.40	2.36
Range	0.812	0.651	0.731

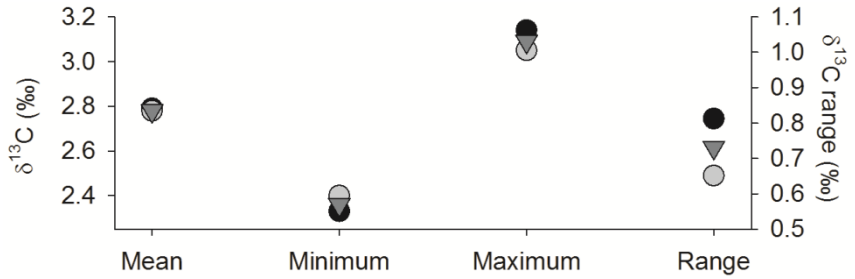

Figure 3.24 Comparisons of mean, maximum, minimum values of $\delta^{13}C$ at different resolutions (original, bi-monthly and monthly resolution) in T75. Figure legend same as Figure 3.23

Trace elements

LA-ICP-MS can result in up to 9,000 analyses per shell, and resampling the data is therefore a necessity. As with the $\delta^{18}O$ and $\delta^{13}C$, data at different resolutions alter the value of Me/Ca (Figure 3.25). Examples of this are shown in Figures 3.26 – 3.28 and Tables 3.12 – 3.14. As with $\delta^{18}O$ and $\delta^{13}C$, mean values do not vary significantly depending on resolution (Ba/Ca - 0. 22 µmol/mol; Mg/Ca – 0.007 mmol/mol; Sr/Ca – 0.01 mmol/mol), but the maximum values can change by up to 10%, depending on whether the raw data or interpolated data is used. The minimum and maximum values of Mg/Ca and Sr/Ca vary by ~0.1 mmol/mol, or around 10%, depending on the resolution, while for Ba/Ca maximum values vary by approximately 1 µmol/mol. Lowering the resolution smooths the profiles, (Figure 3.25), resulting in the removal of peaks in the data. In order to look at features of the Ba/Ca profile, such as the timing of peaks in the record, monthly resolution is not sufficient as these peaks do not appear in the lower resolution record (e.g. between 0 and 6 months in the profile in Figure 3.25).

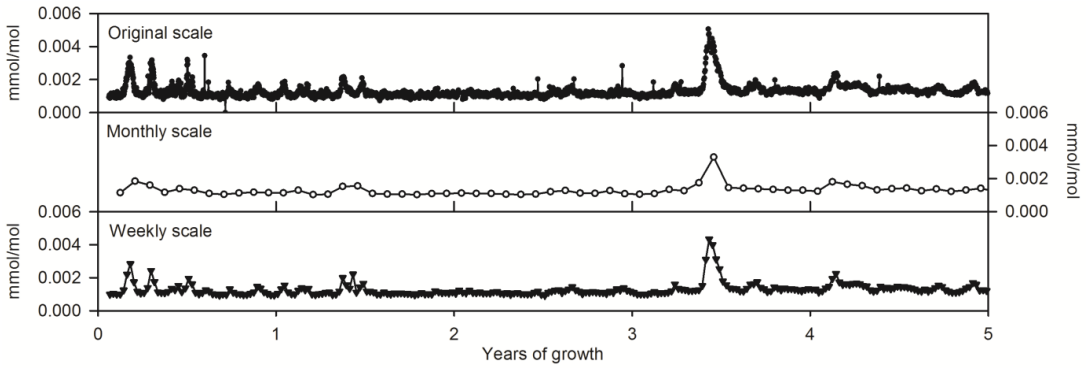

Figure 3.25 Comparison of Ba/Ca profiles in T75.
Top panel: original resolution;
Middle panel: monthly resolution (12 samples/year);
Bottom panel: weekly resolution (52 samples/year)

Table 3.12 Comparison of mean, maximum, minimum values at different resolutions in the Mg/Ca (mmol/mol) profile of T75

Scale	mm	Monthly	Weekly
Mean	0.35	0.36	0.36
Minimum	0.24	0.26	0.24
Maximum	0.69	0.66	0.67
Range	0.45	0.41	0.43

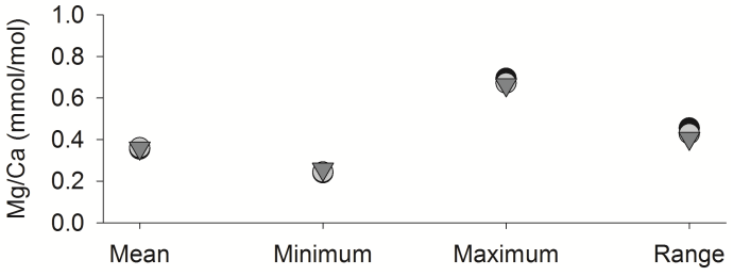

Figure 3.26 Comparison of mean, maximum, minimum values at different resolutions in the Mg/Ca (mmol/mol) profile of T75. Legend same as Figure 3.23

Table 3.13 Comparison of mean, maximum, minimum values at different resolutions in the Sr/Ca (mmol/mol) profile of T75

Scale	mm	Monthly	Weekly
Mean	1.9	2	2
Minimum	1.7	1.8	1.7
Maximum	2.6	2.5	2.6
Range	0.91	0.76	0.88

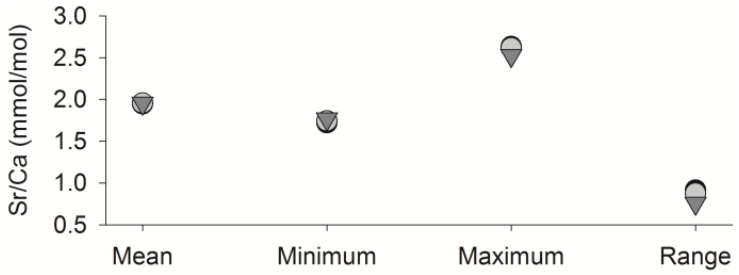

Figure 3.27 Comparison of mean, maximum, minimum values at different resolutions in the Sr/Ca (mmol/mol) profile of T75. Legend same as Figure 3.23

Table 3.14 Comparison of mean, maximum, minimum values at different resolutions in the Ba/Ca (µmol/mol) profile of T75

Scale	mm	Monthly	Weekly
Mean	1.7	1.9	1.9
Minimum	0.9	1	0.9
Maximum	12.2	11.4	12.2
Range	11.3	10.5	11.2

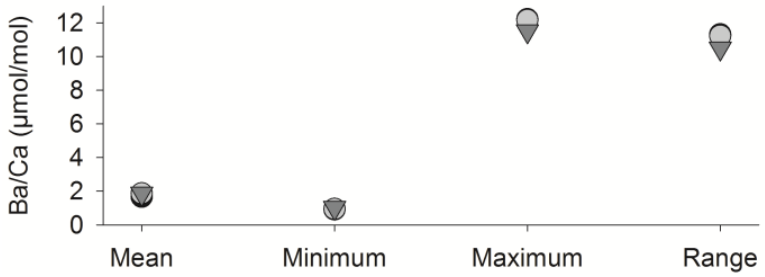

Figure 3.28 Comparison of mean, maximum, minimum values at different resolutions in the Ba/Ca (µmol/mol) profile of T75. Legend same as Figure 3.23

The fact that there is not a significant difference between the mean $\delta^{18}O$ values at lower resolutions suggests that for this shell at least, there is no strong growth bias as the original $\delta^{18}O$ profile includes more juvenile than adult growth due to the nature of the growth rate in this species. Lower resolution records consistently reduce the extreme values recorded in shell carbonate and may therefore underestimate variability in $\delta^{18}O$ and trace element records.

The following chapters will use $\delta^{18}O$ and $\delta^{13}C$ data at bi-monthly or monthly resolution, and trace element data at weekly resolution (specified in each chapter).

4. Background Climate Conditions at the Huon Peninsula during the Holocene and MIS3

Chapter Abstract

The stable oxygen isotope ratio ($\delta^{18}O$) of *Tridacna* sp. shell aragonite is affected by both SST and the local $\delta^{18}O$ of seawater, which in turn is affected by global ice volume, and a regional signal: $\delta^{18}O_{water}$. Regional changes in $\delta^{18}O_w$ reflect local changes in evaporation, precipitation and water advection. In order to reconstruct past regional changes in temperature and evaporation/precipitation, the global ice volume component was first removed.

In this chapter, results derived from Holocene *T. gigas* seasonally resolved $\delta^{18}O$ profiles are discussed and compared with the conditions recorded by a modern *T. gigas* $\delta^{18}O$ from the Huon Peninsula. The residual $\delta^{18}O$ from Holocene and Marine Isotope Stage 3 fossil *Tridacna* sp. suggest that conditions were cooler and/or drier both during the early Holocene and throughout MIS3. Low resolution SST reconstructions suggest that SSTs were similar to present during the early Holocene, so the *Tridacna* sp. $\delta^{18}O$ data could be reflecting drier conditions at the Huon Peninsula. MIS3 experienced an overall decrease in SSTs of approximately 2°C, as well as drier conditions, but this was far more variable.

Interpretation of the mean $\delta^{13}C$ records are more complex. Stable carbon isotope ($\delta^{13}C$) records have been used to reconstruct environmental factors such as the dissolved inorganic carbon (DIC) of sea water. Mean $\delta^{13}C$ values of fossil shells analysed in this study are consistently more positive than the modern *Tridacna gigas* from the Huon Peninsula, which could be reflecting the Suess effect. A relationship between $\delta^{13}C$ and ontogeny, previously observed in bivalves, is not apparent in this data set. Finally, all fossils show some degree of positive correlation with mean $\delta^{18}O$ values.

Chapter 4

4.1 Introduction

$\delta^{18}O$ measured in *Tridacna* sp. shell carbonate reflects global ice volume, SST and the $\delta^{18}O$ of the local seawater ($\delta^{18}O_w$). The local $\delta^{18}O_w$ mainly reflects changes in the evaporation/precipitation balance and shows a linear relationship with salinity (Schmidt, 1999). In order to discuss local changes in SST and salinity inferred from $\delta^{18}O_w$ during the period of growth of these bivalves, the first step is to remove the ice volume component.

There were global changes in temperature and ice volume over the Holocene and Marine Isotope Stage 3 (MIS3), as ice sheets expanded and contracted (Chappell et al., 1996a, Yokoyama et al., 2000, Siddall et al., 2003, Arz et al., 2007). Lighter isotopes (^{16}O) tend to be transported to the poles, meaning that when continental ice volume is increased, there is relative increase of the heavier isotope ^{18}O in the ocean (Shackleton, 1967). This affects the global $\delta^{18}O$ of seawater, from which the *Tridacna* sp. used in this study precipitated their shells. More negative values of $\delta^{18}O$ recorded in fossil carbonates tend to characterise periods where ice volume is small, and global temperatures are warm, while more positive $\delta^{18}O$ characterise large ice sheets and low global temperatures (Shackleton, 1967, Mix and Ruddiman, 1984).

Changes in sea level affect the growth of coral reefs due to changes in accommodation space (Chappell, 1974, Aharon, 1983, Chappell and Shackleton, 1986, Chappell et al., 1996a). Changes in sea level are estimated by a number of different methods, one of which is to use models of reef growth (Chappell and Polach, 1976, Chappell and Polach, 1991, Chappell et al., 1996a, Chappell, 2002). Sea level curves for this region and the period of study, based on their absolute ages, imply changes in sea level of 5-10 metres during the Holocene (Ota and Chappell, 1999), and 45-85 metres during MIS3 (Chappell, 2002, Siddall et al., 2003). In order to compare the fossil and modern $\delta^{18}O$ data and assess changes in SST and evaporation/precipitation balance, the effect of changes to global ocean $\delta^{18}O_w$ must first be corrected. Changes in $\delta^{18}O_w$ can be calculated using estimates of sea level during the period of *Tridacna* sp. shell growth, and the difference in $\delta^{18}O$ of sea water per metre change in sea level ($\delta^{18}O_w$ m^{-1}). In order to calculate this, a reference period of known sea level change and known global $\delta^{18}O_w$ composition must be used.

Tropical Pacific climate (e.g. SST and precipitation) during the Holocene has been well documented (see Chiang (2009) for a review), and it is therefore possible to compare the *Tridacna* sp. data to published data from the region (e.g. Table 4.1). The mid-Holocene is often simulated in general circulation models (GCMs), and is a major period of focus in the Paleoclimate Modeling Intercomparison Project (PMIP). Tropical Holocene data (Figure 4.1) are derived from seasonally resolved coral records from the tropical Pacific (Corrège et al., 2000, Tudhope et al., 2001, Cobb et al., 2003, McGregor and Gagan, 2004, Duprey et al., 2012, Cobb et al., 2013), bivalve records from the eastern Pacific (Carré et al., 2005) as well as lower resolution centennially resolved data from sediment cores (Koutavas et al., 2002, Rein et al., 2005, Koutavas et al., 2006, Brijker et al., 2007, Makou et al., 2010, Koutavas and Joanides, 2012, Sadekov et al., 2013) and lake sediments (Rodbell et al., 1999, Conroy et al., 2008). Prior to the Holocene, the available data are generally lower resolution from sediment cores (Figure 4.1 and Table 4.1).

Table 4.1 Published proxy data studies from the Western Pacific and their findings for Holocene and MIS3 climate (modified after Braconnot et al. (2012))

	Region	Proxy	Holocene change	MIS3 change	Record (ka BP)	Reference
1	Western Pacific	Foraminifera Mg/Ca	Warmer SSTs	2-3°C cooling	0-470	Lea et al. (2000)
2	Western Pacific	Foraminifera Mg/Ca	Similar SSTs	Summer: 0-3.5°C; Winter 0-3°C	0-70	Stott et al. (2002)
3	Western Pacific	Foraminifera Mg/Ca	Warmer SSTs		0-15	Stott et al. (2004)
4	Western Pacific	Foraminifera Mg/Ca	Similar SSTs	0.5-3°C cooling	0-1.75 Ma	de Garidel-Thoron et al. (2005)
5	Papua New Guinea	$\delta^{18}O$ foraminifera	Reduced variability		0-10	Brijker et al. (2007)
6	Western Pacific	Foraminifera Mg/Ca	Cooler SSTs	1.5-4.5°C cooling	0-130	Mohtadi et al. (2010)
7	Australia	Pollen	Wetter		0-30	Shulmeister and Lees (1995)
8	Australia	Pollen	Wetter		0-45	Turney et al. (2004)
9	Papua New Guinea	Charcoal deposits	Reduced seasonality		0-20	Haberle et al. (2001)
10	Papua New Guinea	Coral Sr/Ca	Colder SSTs		8-9	McCulloch et al. (1996)
11	Papua New Guinea	Coral $\delta^{18}O$ and Sr/Ca	Reduced variability	Reduced variability	0-130	Tudhope et al. (2001)
12	Western Pacific	Coral Sr/Ca	Colder SSTs		0-7.5	Abram et al. (2009)
13	South Pacific	Coral $\delta^{18}O$ and Sr/Ca	Colder SSTs		6-7	Duprey et al. (2012)
14	Western Pacific	Foraminifera Mg/Ca		0-3°C cooling	25-70	Dannenmann et al. (2003)
15	Western Pacific	Foraminifera Mg/Ca		1-3°C cooling	30-60	Saikku et al. (2009)
16	Western Pacific	Foraminifera Mg/Ca		0.5-1.5°C cooling	50-500	Dyez and Ravelo (2013)

Background conditions during MIS3 were characterised by cooler sea surface temperatures, both in the tropics (Stott et al., 2002) and at high latitudes (Bond and Lotti, 1995). Ice core records tend to show lower atmospheric CO_2 (Luthi et al., 2008) and greater ice sheet cover (Clark et al., 2007), associated with lower sea levels (Siddall et al., 2003). Although temperatures were on the whole cooler, this period was typified by a highly variable climate punctuated by a series of millennial-scale climatic events at high latitudes (Clark et al., 2007).

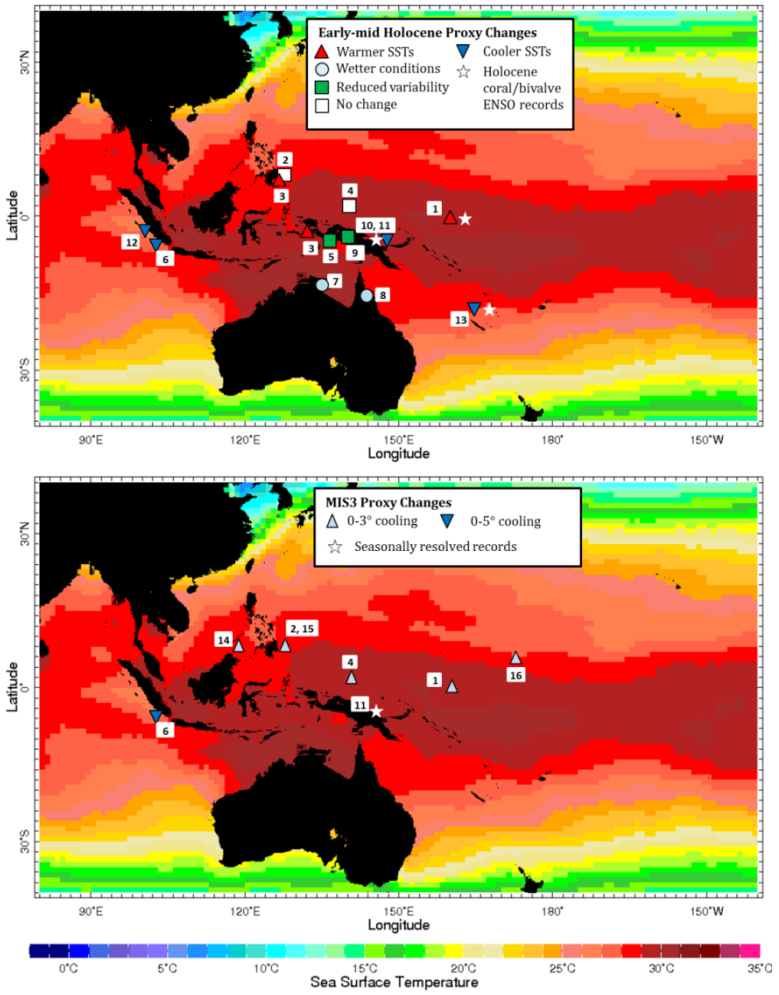

Figure 4.1 Map showing locations of published proxy data described in Table 4.1. Background shows modern December SSTs during the 1997 La Niña from Reynolds global data set (Reynolds et al., 2002)

These rapid millennial-scale climate oscillations, referred to as Dansgaard-Oeschger events (D/O events) and Heinrich events (HE) seem to have been triggered by major ice sheet instabilities from continental ice sheets, primarily the Laurentide ice sheet. They

were associated with massive discharges of ice into the North Atlantic (Bond and Lotti, 1995, Elliot et al., 1998, Elliot et al., 2002), and it is proposed that they affected climate variability in the tropical region (Stott et al., 2002, Turney et al., 2004). The abrupt events were linked with large amplitude changes in sea surface hydrology. They involved rapid warming at high latitudes, followed by a plateau phase, with slow cooling (Heinrich, 1988, Bond et al., 1993, Bond and Lotti, 1995), followed by a return to cold stadial conditions (Rahmstorf, 2002). The timing of D/O and Heinrich events can be seen in high latitude ice core records, such as the Greenland Ice Sheet Project Two (GISP2) $\delta^{18}O$ record (Grootes et al., 1993) (Figure 4.2). The *Tridacna* sp. from MIS3 in this study may have grown during D/O and Heinrich events at high latitudes in the Northern Hemisphere (Figure 4.2), which could have had an impact on the tropical regional climate. This hypothesis is supported by the fact that the fossilised reefs in Papua New Guinea were formed during periods of sea level rise that occurred during MIS3. Given the estimated rise in sea level, it is possible that the *Tridacna* sp. collected from these reefs lived during periods of rapid climate change. It is suggested that there was stronger precipitation in south-eastern Papua New Guinea during Northern Hemisphere cold periods (Shiau et al., 2011). If this also occurred at the Huon Peninsula, it may be reflected in the isotopic composition of samples which grew during these periods.

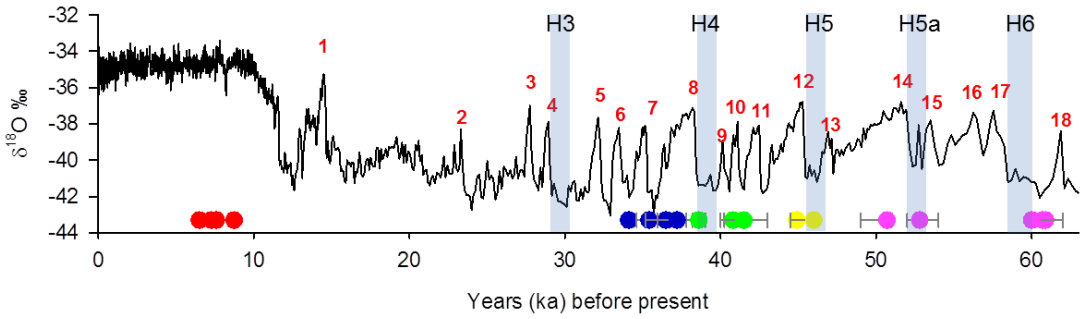

Figure 4.2 GISP2 $\delta^{18}O$ record (Grootes et al., 1993) with Dansgaard-Oeschger events numbered in red. Heinrich events are shaded and numbered in black. Circles represent *Tridacna* sp. used in this study, error bars show 2σ age uncertainty for ^{14}C dated shells and reef ages (based on Chappell (2002). Red circles are Holocene age samples, and MIS3 shells are separated into reefs IIa (blue), IIIc (lower and upper) (green), IIIb (yellow), IIIa (lower, middle and upper) (pink)

This chapter describes the methods used for correcting for ice volume (see Welsh (2009) for additional details), and the interpretation of mean $\delta^{18}O$ and $\delta^{13}C$ values.

4.2 Correcting for ice volume effect

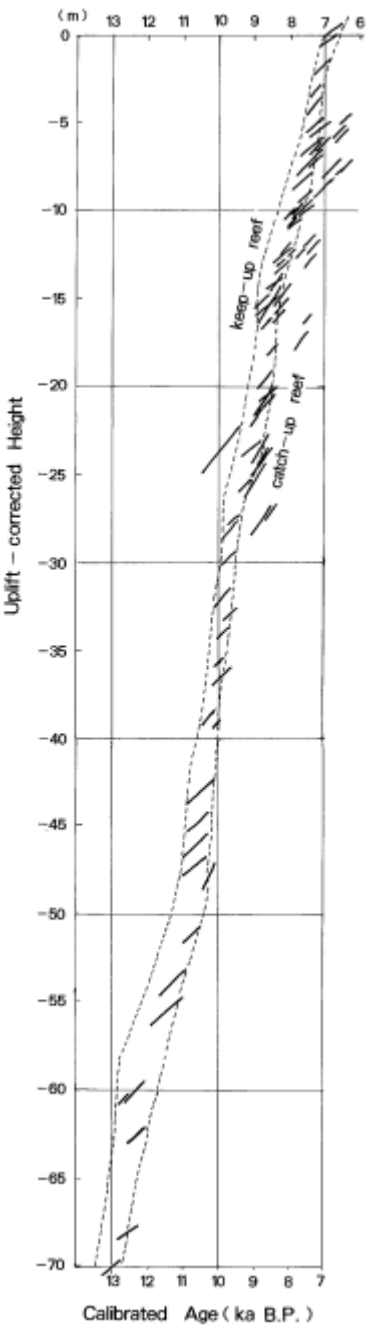

4.2.1 Mean $\delta^{18}O$ in the Holocene

Changes in sea level during the early Holocene have been extensively studied at the Huon Peninsula using radiometrically dated corals and molluscs (Chappell and Polach, 1976, Chappell and Polach, 1991, Edwards et al., 1993, Ota and Chappell, 1999). This has resulted in the establishment of several sea level curves (e.g. Figure 4.3). It is possible to use one of these published sea level curves to predict the $\delta^{18}O$ of sea water ($\delta^{18}O_w$) at the time when the *Tridacna* sp. grew and remove this from the measured $\delta^{18}O$. The Holocene sea level values used in this work are the same as for Welsh (2009), reported in Ota and Chappell (1999) (Figure 4.3). In order to predict $\delta^{18}O_w$ and calculate the residual $\delta^{18}O$ of the *Tridacna* sp., which should reflect SST and changes in the evaporation/precipitation balance, the relationship between sea level and $\delta^{18}O_w$ from Yokoyama et al. (2000) was used, which is based on a change of 0.0085‰ ±0.015m^{-1} per 1 m sea level change.

Figure 4.3 Relationship between uplift-corrected height and calibrated age of all the dated Holocene transgressive corals from the Huon Peninsula (from Ota and Chappell, 1999). This shows the rapid rise in sea level between 13 and 7 ka BP (pre-Holocene to early-mid Holocene).

Corrected mean $\delta^{18}O$ values (Table 4.2 and Figure 4.4) are more positive than the modern *T. gigas*, which has a mean of -1.2‰, in three Holocene *T. gigas* (T73, T58 and T75). This indicates that there was a cooler and/or drier climate, while one shell (T66) has a mean of -1.79, which is 0.8‰ more negative than the modern shell, suggesting

warmer and/or wetter conditions. T66 was collected from the edge of a Holocene lagoon at Bobongara, and has a very rapid growth structure and anomalously negative $\delta^{18}O$. In this work it is not considered a representative of mean Holocene conditions, and results will be discussed in more detail in the Appendix. The three remaining *T. gigas* have a mean residual $\delta^{18}O$ of -1.01‰, which is within error of measurements taken by Aharon (1983), who found Holocene *Tridacna* sp. shells from the Huon Peninsula had a mean $\delta^{18}O$ value of -1‰.

Table 4.2 Result of removing the ice volume component from Holocene *Tridacna* sp. $\delta^{18}O$ ($\delta^{18}O$ is at bi-monthly resolution)

Sample	Reef Terace	Elevation (m)	Mean $\delta^{18}O$ ‰	Age (ka BP)	Uncertainty 2σ (ka)	Predicted sea level (m)	Predicted $\delta^{18}O_w$ ‰	Residual $\delta^{18}O$ ‰
T66	Holocene	20	-1.79	6.49	0.37	0	0	-1.79
T73	Holocene	*Ex situ*	-0.95	7.26	0.20	-5	0.043	-1.0
T58	Holocene	6	-0.91	7.59	0.23	-10	0.085	-1.0
T75	Holocene	*Ex situ*	-0.90	8.73	0.39	-15	0.128	-1.03

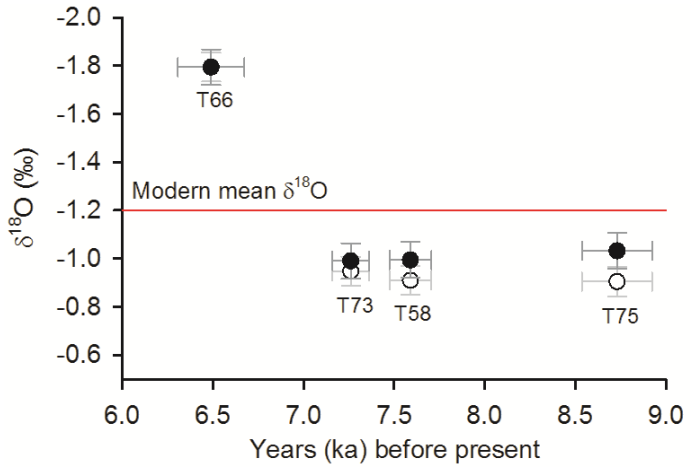

Figure 4.4 Mean $\delta^{18}O$ of Holocene *T. gigas* (open circles) and residual $\delta^{18}O$ once ice volume component has been removed (black filled circles). Horizontal error bars represent potential error in dating, vertical error bars represent sampling error and error created during calculating ice volume correction

Because of the uncertainty associated with the dating of the fossil samples (Chapter 2), there is a range of sea level corrections for each shell. The error bars in Figure 4.4 include the analytical error of ±0.06‰ for the raw data, while for the ice volume corrected data, the error includes both the analytical error and that associated with dating and therefore the suggested sea level at the time of growth. As in Welsh (2009), a sea level error of 5 metres was applied to the Holocene samples, resulting in a combined analytical and sea level error of ±0.074‰.

4.2.2 Mean $\delta^{18}O$ in MIS3

The same approach was used to correct for ice volume effect in the MIS3 *Tridacna* sp. as in the Holocene samples, although here the error is higher due to greater uncertainties in predicted sea level and age estimation (Table 4.3). The MIS3 samples used throughout this study were collected from the same reefs at the Huon Peninsula that had been previously used to calculate changes in sea level during MIS3 (Figure 4.5) (Chappell et al., 1996a, Chappell, 2002). While there is generally a good fit between the sea level curve and the sea level estimated from the *Tridacna* sp. samples, the two earliest shells show a discrepency of ~10m (Figure 4.5). This difference cannot easily be explained, but a similar result was found by Chappell (2002), as a coral sample from Reef IIa, dated to 34.8 ka BP was also bypassed by the sea level curve.

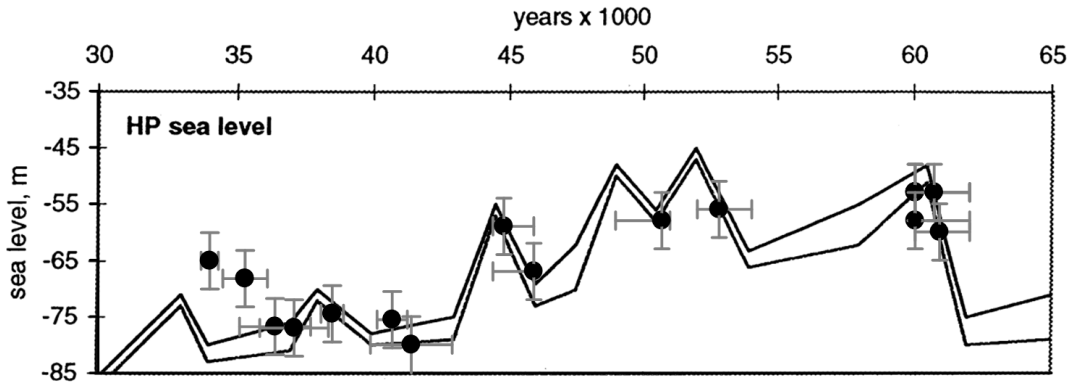

Figure 4.5 Huon Peninsula sea level curve for MIS3 from Chappell (2002). This sea level reconstruction is similar to that produced by Siddall (2003) in terms of highstands, but differs in terms of lowstands as reef material is buried. MIS3 *Tridacna* sp. samples are shown by circles. Error bars are 10m sea level error and age uncertainty.

Table 4.3 Result of removing the ice volume component from MIS3 *Tridacna* sp. $\delta^{18}O$. ($\delta^{18}O$ is at bi-monthly resolution). Figures in italics are bulk measurements where higher resolution samples have not been measured

Sample	Reef Terrace	Elevation (m)	Mean $\delta^{18}O$ ‰	Age (ka BP)	Uncertainty 2σ (ka)	Predicted sea level (m)	Predicted $\delta^{18}O_w$ ‰	Residual $\delta^{18}O$ ‰
T28	IIa	49	-0.26	34.1	0.63	-65	0.55	-0.81
T27	IIa	50	-0.23	35.4	1.6	-68	0.58	-0.81
T9	IIa	45	0.03	36.5	2.6	-77	0.65	-0.63
T11	IIa	47	0.38	37.2	2.5	-77	0.65	-0.27
T32	IIIc (l)	54	0.13	38.6	0.83	-75	0.63	-0.50
T39	IIIc (u)	60	0.33	40.8	1.12	-76	0.64	-0.32
T40	IIIc (u)	56	-0.47	41.5	3	-80	0.68	-1.15
					Reef age			
T24	IIIb	84	0.07	44.9	44.5-46	-59	0.50	-0.43
T37	IIIb	79	0.37	46	44.5-46	-67	0.57	-0.20
T41	IIIa (l)	99	0.03	50.7	49-51	-58	0.49	-0.46
T18	IIIa (m)	114	-0.2	52.8	52-54	-56	0.48	-0.69
T15	IIIa (u)	138	-0.34	60	60-62	-53	0.45	-0.79
T22	IIIa (u)	138	0.15	60	60-62	-53	0.45	-0.30
T44	IIIa (u)	138	*-0.14*	60	60-62	-53	0.45	*-0.59*
T45	IIIa (u)	138	0.19	60	60-62	-53	0.49	-0.26
T6	IIIa (u)	135	0.34	60.7	60-62	-58	0.49	-0.15
T38	IIIa (u)	134	*0.01*	60.9	60-62	-60	0.51	*-0.50*

As with the Holocene samples, the $\delta^{18}O$ data from the MIS3 fossils includes both analytical error and a sea level error estimated at 10 metres for each shell, resulting in an error calculation of ±0.1‰ (Figure 4.6).

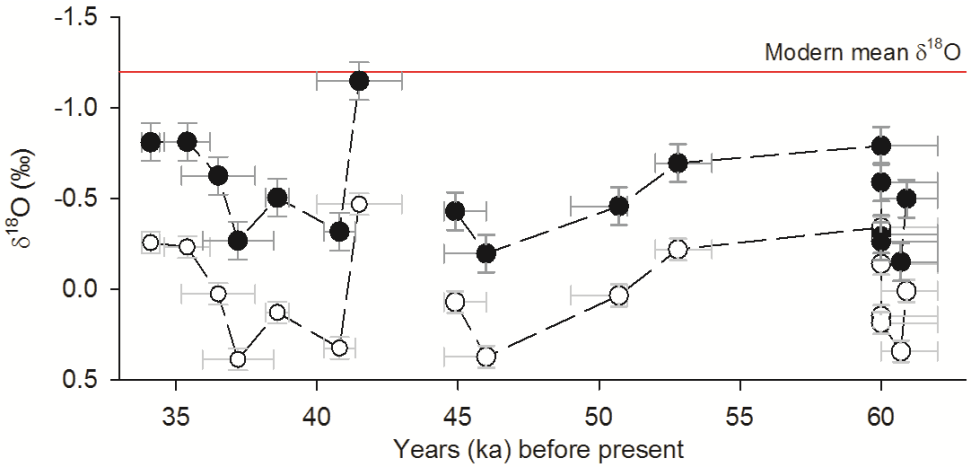

Figure 4.6 Mean $\delta^{18}O$ of MIS3 *Tridacna* sp. (open circles) and residual $\delta^{18}O$ once ice volume component has been removed (black filled circles). Horizontal error bars represent error in dating, vertical error bars represent analytical error and error related to the ice volume correction. Gap is between ^{14}C dated shells and those where the age is based on well-dated reef ages

From this point forward, and in subsequent chapters, the residual $\delta^{18}O$ will be referred to, representing $\delta^{18}O$ which has been corrected for an ice volume effect.

4.3 Discussion: Reconstructing the mean state of the tropical Pacific

The exact contributions of SST and evaporation/precipitation (i.e. salinity) to *Tridacna* sp. shell $\delta^{18}O$ ($\delta^{18}O_{Tridacna}$) are unknown. In the modern *T. gigas* from the Huon Peninsula, SST and salinity are thought to contribute equally to $\delta^{18}O_{Tridacna}$ (Welsh et al., 2011). For the fossil samples, reconstructions of SST and salinity from the *Tridacna* sp. $\delta^{18}O$ will be given in two ways: assuming an equal contribution of SST and salinity (i.e. 50% each to $\delta^{18}O_{Tridacna}$), and assuming a total contribution of either salinity or SST to $\delta^{18}O_{Tridacna}$ (i.e. 100%).

Following the removal of the ice volume component of fossil $\delta^{18}O$, the difference between the $\delta^{18}O$ of MT7 and the residual $\delta^{18}O$ of fossil *Tridacna* sp. can be converted into a quantitative temperature or salinity effect. The following equations were used, based on those utilised by Tudhope et al. (2001):

$$\underline{\Delta}(°C) = 4.69 * \underline{\Delta}\delta^{18}O_c \text{ (Epstein et al., 1953, Leder et al., 1996)}$$

$$\underline{\Delta}\ \delta^{18}O\ (‰) = 0.273‰\ \underline{\Delta}\ \text{Salinity (p.s.u)(Fairbanks et al., 1997) or } \underline{\Delta}S = 3.66\ \underline{\Delta}\ \delta^{18}O$$

Where a 1°C increase corresponds to a -0.21‰ shift in $\delta^{18}O$ and a 1 p.s.u. (=1‰) increase corresponds to a 3.66‰ shift in $\delta^{18}O$. Analytical error and that associated with the ice volume correction was transformed to SST/salinity error following the above equations, giving ±0.3°C/±0.3‰ for the Holocene and ±0.5°C/0.4‰ for MIS3.

4.3.1 Mean state derived from *T. gigas* $\delta^{18}O$ profiles during the Early Holocene

Mean $\delta^{18}O$ values of the three sampled Holocene *T. gigas* are more positive than modern $\delta^{18}O$ by 0.19‰, which translates to a theoretical cooling of approximately 0.9±0.3°C during the early Holocene (8.7-7.2 ka BP), or an increase in salinity of 0.7±0.3‰ p.s.u. Assuming an equal contribution of SST and $\delta^{18}O_w$ to fossil $\delta^{18}O_{Tridacna}$, this would subsequently result in a theoretical cooling of ~0.5±0.3°C and an increase in salinity of ~0.4±0.3‰.

Comparison with Holocene SST reconstructions

The transition from the LGM (~21 ka BP) to the Holocene saw the melting of ice caps and an increase in sea level, with a change from a dry and cool climate to a warm and humid climate (Greer and Swart, 2006). A number of studies have suggested that there was a permanent La Niña-like state during the early Holocene, with a more pronounced cold tongue and stronger easterly winds (Donders et al., 2008, Hernandez et al., 2010, Marchitto et al., 2010). Tropical alkenone records from the west Pacific (e.g. Rimbu et al., 2004, Lorenz et al., 2006, Shiau et al., 2012) show a warming trend over the Holocene, with cooler than present temperatures between 9 and 6 ka BP.

Proxy climate data from corals, bivalves and foraminifera using Mg/Ca, Sr/Ca and $\delta^{18}O$ have been used to reconstruct SSTs both continuously at low resolution, and also at discrete intervals using higher resolution data during the Holocene (Figure 4.7). Data from the western Pacific suggest slightly warmer SSTs (>29°C) using Mg/Ca measurements of foraminifera from a sediment core approximately 1,500 km north east of the Huon Peninsula (Lea et al., 2000) (Figure 4.7). $\delta^{18}O$ data from foraminifera from a sediment core approximately 1,600 km west of the Huon Peninsula suggest a cooling of 0.18°C or increase in salinity of 0.15‰ p.s.u. at 7.25 ka BP, a warming of 0.13°C or decrease in salinity of 0.1‰ p.s.u. at 7.5 ka BP and a warming of 0.3°C or decrease in salinity of 0.23‰ p.s.u. at 8.85 ka BP (Brijker et al., 2007). Stott et al. (2004) found that the Mg/Ca-derived SST from foraminifera was approximately 29.5°C in the western tropical Pacific during the early Holocene (~10-6.5 ka BP), and that surface water was over 35.2 p.s.u. during this time period.

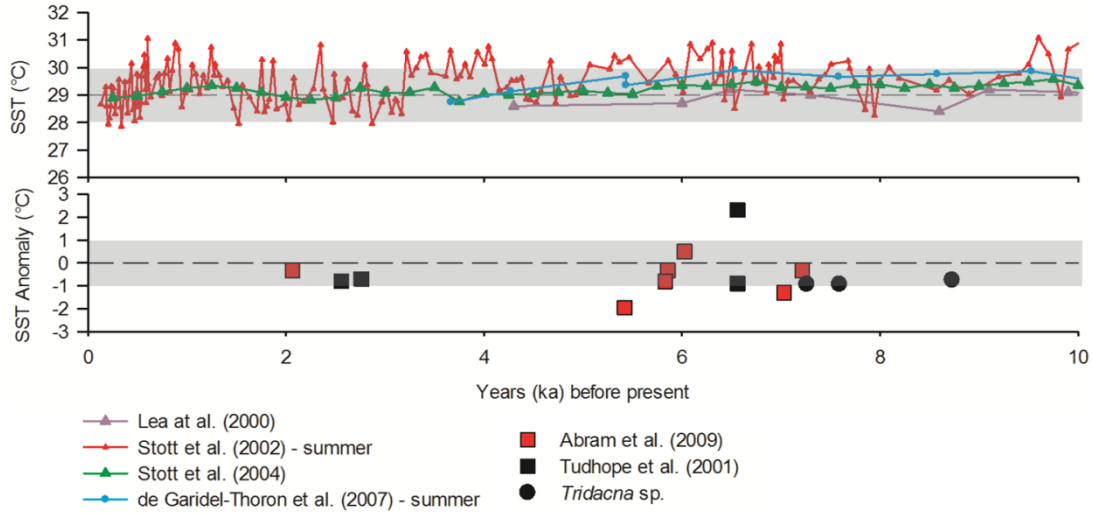

Figure 4.7 Reconstructed SST from tropical foraminifera in the West Pacific (top panel) and suggested SST anomaly from West Pacific coral and *Tridacna* sp. $\delta^{18}O$ (bottom panel) during the Holocene. Dashed line represents modern mean SST of 29°C, grey shaded box indicates ±1°C

Some higher resolution records such as coral $\delta^{18}O$ or Sr/Ca, which cover discrete periods of time, tend to indicate slightly cooler SSTs in the western Pacific during the early to mid-Holocene. The $\delta^{18}O$ of a *Porites* coral from the Huon Peninsula implies similar or slightly cooler SSTs (0.9-1.3°C) at 6.5 ka BP, whereas SST derived from Sr/Ca from the same coral suggests warmer SSTs (2.3°C) (Tudhope et al., 2001). Sr/Ca measurements from early Holocene *Porites* (9-7 ka BP) from Papua New Guinea suggest temperatures which were 2-3°C cooler than modern *Porites* from the same location (McCulloch et al., 1996). Sr/Ca measurements from *Porites* dated to 7.2and 7.6 ka BP from ~100km offshore northeast Papua New Guinea record a decrease in temperature of 0.32 and 3.27°C respectively, compared to modern corals from the same location (Abram et al., 2009).

From published data from the West Pacific, it therefore appears that low resolution records obtained from foraminifera show similar or warmer SSTs during the early Holocene, whereas higher resolution records mainly derived from coral Sr/Ca records suggest similar or cooler SSTs. Despite this, if SST and changes in the evaporation/precipitation balance contributed equally to the $\delta^{18}O_{Tridacna}$ signal, the shift in mean $\delta^{18}O$ might be explained by a cooling of ~0.5±0.3°C, which is within estimates of reconstructed SST for the tropical Pacific during the early Holocene (Figure 4.7). Based on the sediment core records (references in Figure 4.9) which provide a more

expansive record of SSTs in the western Pacific, it seems likely that the shift in $\delta^{18}O_{Tridacna}$ records mainly an increase in salinity and therefore drier conditions.

4.3.2 Mean state derived from *Tridacna* sp. $\delta^{18}O$ during MIS3

The mean values of $\delta^{18}O$ derived from MIS3 *Tridacna* sp. (shown in Table 4.3) are all between 0.1‰ and 1.1‰ more positive than MT7 after being corrected for ice volume, suggesting cooler and/or drier conditions between 60 and 34 ka BP (Figure 4.8). There are fewer available data than the Holocene, and much of the published data come from foraminifera Mg/Ca or alkenone SST reconstructions. The mean $\delta^{18}O$ value of all 15 *Tridacna* sp. from the MIS3 reefs equates to a reduction in mean temperature of 3.2±0.5°C, or an increase in salinity of 2.5±0.4‰ p.s.u. (assuming modern $\delta^{18}O$ temperature/salinity relationships have remained the same over time) or a combination of the two, compared to the mean $\delta^{18}O$ of MT7. This varies in the reefs in question between 2.5±0.5°C and 4.2±0.4°C (Table 4.4). Reconstructions of MIS3 SST suggest a cooling of 2-3°C for the region around the Huon Peninsula (Figure 4.9). If a 50/50 contribution of SST and $\delta^{18}O_w$ to $\delta^{18}O_{Tridacna}$ is assumed, these periods would have been characterised by a cooling of ~0-2.1±0.5°C in these reefs (Table 4.4).

Table 4.4 Measured mean residual $\delta^{18}O$ values and predicted temperature and salinity differences from MT7 (assuming the entire signal is either due to SST or salinity)

	MIS3 (17 shells)	IIa (4 shells)	IIIc (3 shells)	IIIb (2 shells)	IIIa (8 shells)
Shell ages (ka BP)	34.1-60.7	34.1-37.2	38.6-41.5	44.9-46	50.7-60.7
$\delta^{18}O_c$ (measured) (‰)	-0.52	-0.63	-0.66	-0.31	-0.47
$\delta^{18}O_c$ (MT7) - $\delta^{18}O_c$ (‰)	-0.68	-0.57	-0.54	-0.89	-0.73
Potential SST difference	-3.2°C	2.7°C	2.5°C	4.2°C	3.4 °C
Potential SSS difference	2.5	2.1	2	3.3	2.7

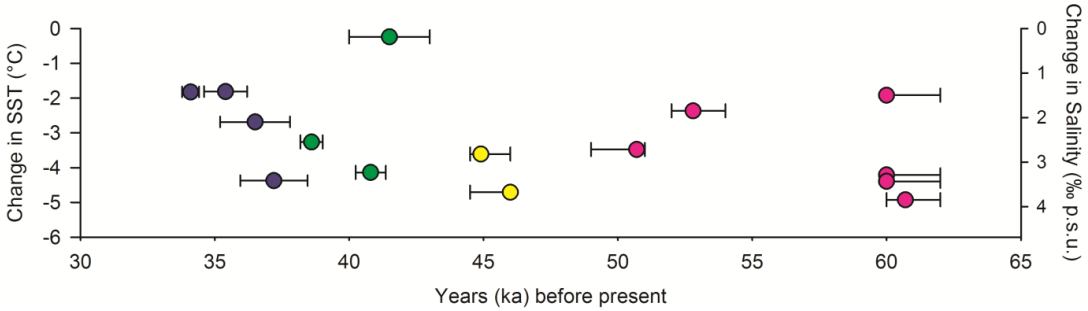

Figure 4.8 MIS3 *Tridacna* sp. and the SST and salinity equivalent of the change in mean $\delta^{18}O$ compared to the modern shell, MT7. Error bars represent the age uncertainty

Comparison with MIS3 SST Reconstructions

In the western Pacific, SST reconstructions from Mg/Ca measurements from foraminifera indicate a cooling of 0-4.5°C during MIS3 (60-30 ka BP) (e.g. Lea et al., 2000, Stott et al., 2002, Dannenmann et al., 2003, de Garidel-Thoron et al., 2005, Saikku et al., 2009, Mohtadi et al., 2010, Dyez and Ravelo, 2013), with summer suggested to have cooled less than winter (Stott et al., 2002). The increase in mean $\delta^{18}O$ between fossil and modern *Tridacna* sp. can be compared to the closest published SST reconstructions (Figure 4.9). This assumes that the change in $\delta^{18}O$ is solely attributable to SST. If SST were only contributing factor to the $\delta^{18}O$ recorded in *Tridacna* sp., this would translate into a reduction in temperature of 3.2±0.5°C across MIS3, which is slightly above many estimates for the region (Figure 4.9). However, the increase in $\delta^{18}O$ of individual MIS3 shells generally fits within reconstructed SSTs from the western Pacific (Figure 4.9). The range of variability (1‰ or ~4°C) is larger than the reconstructed SST records which show variability of 1-3°C across MIS3. This could be explained either by 1) *Tridacna* sp. providing more detailed records of local variability during this period (i.e. large changes in the evaporation/precipitation balance), or 2) a bias of sediment core SST records which tend to be lower resolution summer estimates. It seems likely to be a combination of these two explanations. The *Tridacna* sp. samples used in this study provide monthly-seasonal reconstructions of SST and have record lengths of up to 38 years. SSTs reconstructed from foraminifera (e.g. Figure 4.9) are at far lower resolution, with the highest resolution records averaging one sample every 50 years. Inter-annual changes in local SST and evaporation/precipitation changes will have been recorded in the $\delta^{18}O$ measured in *Tridacna* sp. samples, which are missed in SST records from foraminifera.

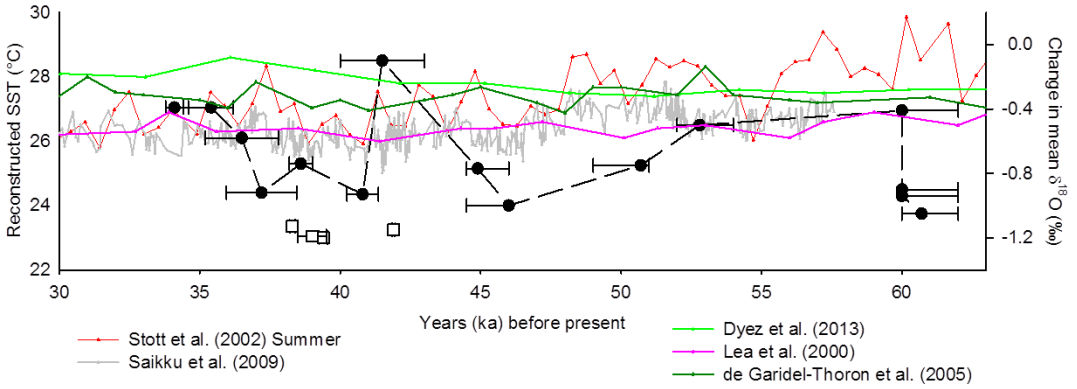

Figure 4.9 Reconstructed SST from foraminifera Mg/Ca from the West Pacific from sites MD-97 (de Garidel-Thoron et al., 2005), MD-98 (Stott et al., 2002, Saikku et al., 2009), ODP Site 806B (Lea et al., 2000) and ODP Site 871 (Dyez and Ravelo, 2013). The MIS3 *Tridacna* sp. data shown here (circles) are the changes in mean $\delta^{18}O$ compared to the modern shell, which has a mean of -1.2‰. Coral data from Tudhope et al. (2001) are shown by open squares. Error bars represent age uncertainty

The influence of Heinrich events at the Huon Peninsula

Several of the raised coral reef terraces at the Huon Peninsula are thought to have been formed in response to rises in sea level associated with Northern Hemisphere Heinrich events (Yokoyama et al., 2001). These periods of rapid sea level rise, associated with Heinrich event ice sheet collapses, created the accommodation space required for reefs to grow and expand. Reef IIa is suggested to be associated with Heinrich 4, Reef IIIb with Heinrich 5, and Reef IIIa (u) with Heinrich 6 (Yokoyama et al., 2001, Chappell, 2002). These reef terraces have been associated with discrete periods of prolific coral growth and sea-level high stands (Yokoyama et al., 2001). While there is not yet an established direct link between North Atlantic ice evens and sea level rise, it is likely that D/O cycles and Heinrich events lead to sea-level oscillations. The mechanism suggested by Yokoyama et al. (2001) is that a Heinrich events provides a perturbation in which sea level rises at the start of each event. After about 1,000 years, the ensuing warm interstadial leads to increased precipitation at northern latitudes, which results in a re-growth of the ice sheets and a fall in sea level (Yokoyama et al., 2001).

These correlations are hampered by age uncertainty of ^{14}C dated shells, with mean shell ^{14}C errors around ±0.9 ka, which is longer than the duration of Heinrich 4. The mean residual $\delta^{18}O$ from the Reef IIa shells increases over time (Figure 4.9), suggesting increasing SST or a decrease in salinity during the expansion of this reef. With the IIIb

and IIIa (u) samples, which are thought to be coeval with Heinrich events 5 and 6, individual shell ages are based on their position in well dated reefs so are constrained by the reef ages proposed by Chappell (2002). While the IIIc reef has not yet been definitely linked with any Heinrich events, these shells can, at present, be considered to have grown during a non-stadial background. There is not a statistically significant difference between the mean $\delta^{18}O$ recorded in the IIIc samples (Table 4.3) and the other reefs (one-way ANOVA, p=0.438).

Increased salinity during Heinrich events has been suggested from sediment cores from the Indo-Pacific Warm Pool (IPWP) (Levi et al., 2007) and the Western Pacific Warm Pool (Chen et al., 2005). There is not a significant difference between the $\delta^{18}O$ measured in the *Tridacna* sp. from Heinrich and non-Heinrich associated reefs (when factoring the uncertainty of the age models). There is not an independent measure of temperature and, hence, it is not possible to interpret the data in terms of reflecting global temperature or salinity changes due to Heinrich events. Further investigation and additional samples are required in order to examine changes in the WPWP caused by high latitude events.

4.4 The carbon isotope record ($\delta^{13}C$)

Changes in carbon isotopes have been related to a variety of factors, ranging from the $\delta^{13}C_{DIC}$ of water, to biological fractionation, or temperature (McConnaughey and Gillikin, 2008). Initially, it was hoped that carbon isotopes of biogenic carbonates might record the isotopic signature of dissolved organic carbon (DIC) in seawater (Mook and Vogel, 1968), which would in turn provide information on salinity, productivity or anthropogenic carbon (Gillikin et al., 2005a). However, due to the incorporation of metabolic CO_2, there are difficulties in interpreting $\delta^{13}C$ purely as a proxy for DIC. There are further complications with the use of $\delta^{13}C$, as there are interactions between physical parameters and chemical and physiological processes, including the composition of $\delta^{13}C_{DIC}$, growth rate of the bivalve, depth habitats and water salinity (e.g. Elliot et al., 2003).

Some species of bivalve record ontogenetic trends in $\delta^{13}C$. *Chesapecten madisonius* (Goewert and Surge, 2008), *Pinna nobilis* (Kennedy et al., 2001) and *Mercenaria mercenaria* (Elliot et al., 2003) show a decreasing trend in $\delta^{13}C$ over time, while *Saxidomus giganteus* (Gillikin et al. 2005a) shows either an increase, or no relationship with ontogeny. Within *Tridacna* sp., there are variations in $\delta^{13}C$ between species, and within different areas of the shell.

In the following sections, several effects are tested: 1) whether there is a relationship between $\delta^{13}C$ and ontogeny; 2) how $\delta^{13}C$ relates to $\delta^{18}O$, which might suggest an environmental control.

4.4.1 Mean $\delta^{13}C$ results from modern and fossil *Tridacna* sp.

Mean $\delta^{13}C$ values of fossil shells are consistently more positive than the mean value recorded by MT7 (Figure 4.10). All mean $\delta^{13}C$ values range from to 1.9 to 3‰, with no significant difference between mean values obtained from different species of *Tridacna*. There is also no significant difference between the mean values recorded in Holocene *T. gigas* and MIS3 *T. gigas.*

Values can be compared to published *Tridacna* sp. $\delta^{13}C$ from modern and Holocene samples. The mean of the four Holocene *T. gigas* (n = 4) samples is within error (<±0.06‰) of a Holocene *T. gigas* collected from Japan (Watanabe et al., 2004). Mean $\delta^{13}C$ from fossil shells has been found to be higher than modern values in *T. gigas* shells (Aharon, 1985, Aharon, 1991). With the exception of T40, which has a mean of 1.9‰, all *T. maxima* sampled have higher $\delta^{13}C$ values than modern and fossil *T. maxima* from Vanuatu (Duprey, 2012, Duprey et al., 2014), and a modern *T. maxima* from Rose Atoll (Romanek et al., 1987). The mean of the two *T. squamosa* from MIS3 is higher by 1.9‰ than a modern *T. squamosa* (Batenburg et al., 2011).

Higher $\delta^{13}C$ values in fossil *Tridacna* sp. are in part a result of modern *Tridacna* sp. using a DIC source depleted in ^{13}C compared to fossil *Tridacna* sp. (Duprey et al., 2014). This shift is seen in $\delta^{13}C$ records from corals, sclerosponges and other species of bivalve (e.g. Druffel and Benavides, 1986, Butler et al., 2010, Swart et al., 2010), and reflects the release of ^{13}C into the atmosphere due to fossil fuel burning since the Industrial

Revolution, referred to as the Suess effect (Revelle and Suess, 1957). The mean $\delta^{13}C$ of the modern *T. gigas* (MT7) is 0.84‰ lower than the mean of the Holocene and MIS3 *T. gigas* samples. This is consistent with the 0.9‰ reduction in $\delta^{13}C$ observed in Caribbean sclerosponges from pre-industrial times to 1990 (Druffel and Benavides, 1986, Bohm et al., 1996), which in turn are similar to mean changes in Pacific corals (Swart et al., 2010). This suggests that changes in mean $\delta^{13}C$ between MIS3 to the present are due to atmospheric changes in ^{13}C, rather than environmental changes.

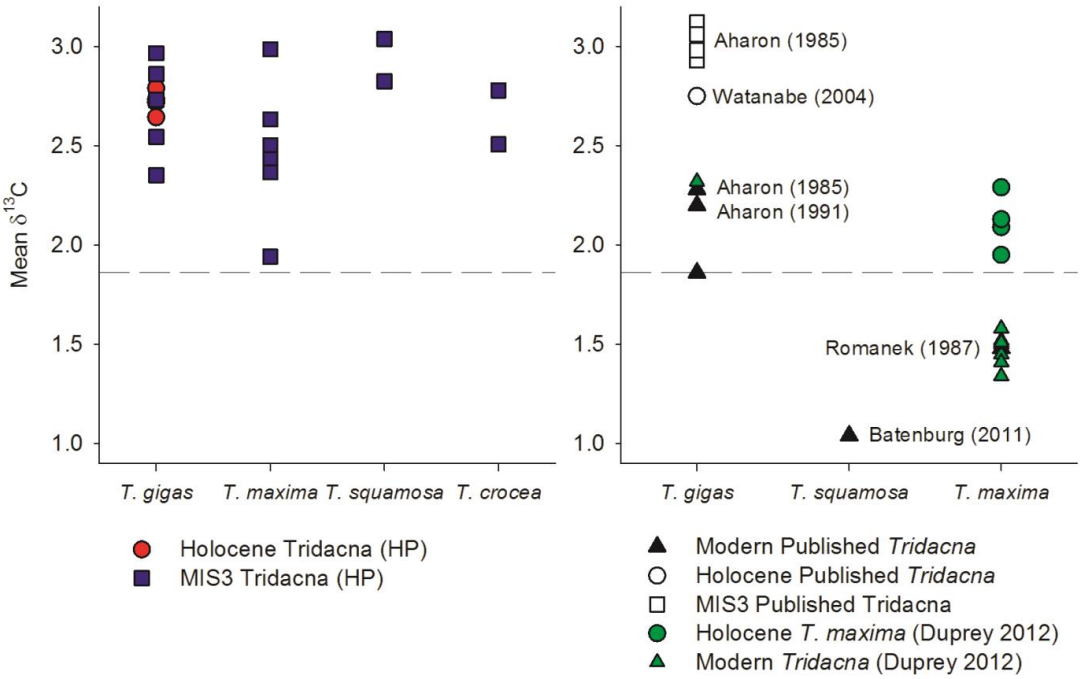

Figure 4.10 Comparison of mean $\delta^{13}C$ values of different *Tridacna* species from this study (left panel), published studies (Aharon, 1985, Aharon, 1991, Romanek et al., 1987, Watanabe et al., 2004, Batenburg et al., 2011) and Duprey (2012) (right panel). The mean $\delta^{13}C$ of MT7 is marked by the dashed line in both panels

4.4.2 Effects of ontogeny

T. gigas inner layer $\delta^{13}C$ profiles from the Huon Peninsula and the Great Barrier Reef show no relationship between $\delta^{13}C$ and ontogeny (Elliot et al., 2009), whereas *T. maxima* from Rose Atoll show more positive $\delta^{13}C$ values with age (Romanek et al., 1987). To illustrate the dispersion in results, the correlation coefficient between increasing shell age and $\delta^{13}C$ in modern and fossil *Tridacna* sp. used in this study was calculated, and compared with the different *Tridacna* species (Figure 4.11).

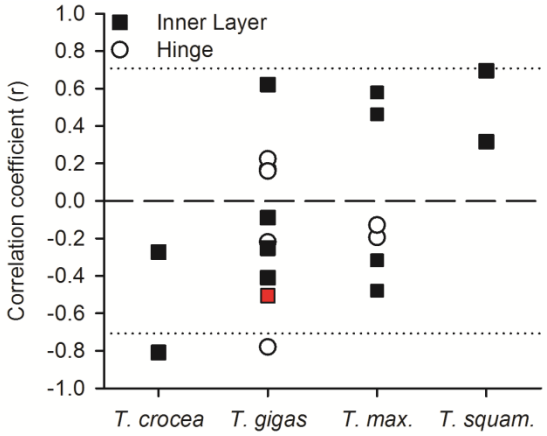

Figure 4.11 Correlation coefficient (r) between $\delta^{13}C$ and increasing shell age. Dotted lines represent the equivalent r^2 of 50%. Red square represents r value for modern *T. gigas* MT7.

In the *T. gigas* used in this study, one shell (T75) shows a significant (r^2 >0.6) decreasing trend in $\delta^{13}C$ with increasing shell age, while other *T. gigas* show no significant relationship, a slight increase, or a slight decrease in $\delta^{13}C$ with age. In *T. crocea*, one shell (T41) shows a significant (r^2 >0.65) decreasing trend in $\delta^{13}C$. In *T. maxima*, shells where the inner layer was sampled show both an increase and decreasing trend, while those where the hinge was sampled show no trend in $\delta^{13}C$. The two *T. squamosa* show an increasing trend in $\delta^{13}C$ with increasing age.

Within the fossil data set, there is therefore no overall pattern within species or shell area as to an effect of ontogeny on $\delta^{13}C$. The fossil *T. maxima* data are not consistent with a *T. maxima* from Rose Atoll, which showed increasing $\delta^{13}C$ with age (Romanek et al., 1987), as four *T. maxima* show a negative correlation between $\delta^{13}C$ and age (Figure 4.11). However, most *T. gigas* data are consistent with modern *T. gigas* which show no relationship between increasing shell age and $\delta^{13}C$ (Elliot et al., 2009). This result might suggest a species specific incorporation of $\delta^{13}C$ into *Tridacna* sp. shell carbonate.

4.4.3 Relationship between $\delta^{18}O$ and $\delta^{13}C$

In some species of bivalve (e.g. *Mercenaria mercenaria* (Elliot et al., 2003)), a relationship is seen between $\delta^{18}O$ and $\delta^{13}C$ recorded in the shell layers. A close relationship between $\delta^{18}O$ and $\delta^{13}C$ could suggest that both elements are governed by a common controlling mechanism. The mean values of $\delta^{18}O$ and $\delta^{13}C$ from the *Tridacna* sp. used in this study can therefore be compared to see if a relationship exists between the two possible proxies (Figure 4.12).

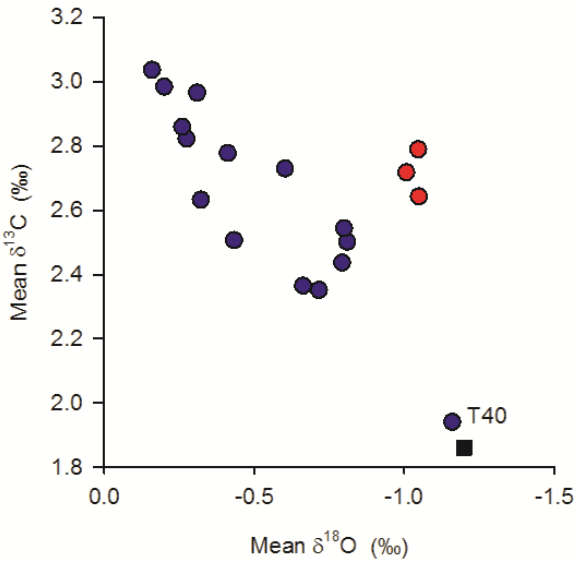

Figure 4.12 Relationship between mean $\delta^{18}O$ (corrected for ice volume effect) and mean $\delta^{13}C$ in Holocene (red) and MIS3 (blue) *Tridacna* sp. Modern *T. gigas* is marked by a black square. T40, a *T. maxima* with anomalously negative $\delta^{18}O$ is labelled

The mean $\delta^{18}O$ and $\delta^{13}C$ values of three Holocene *T. gigas* are similar (and offset due to more positive $\delta^{18}O$), while MIS3 samples show a trend towards more positive mean $\delta^{18}O$ values as $\delta^{13}C$ increases. Within shells, seasonally resolved time series of $\delta^{18}O$ and $\delta^{13}C$ are also correlated (Figure 4.13). All samples show a positive correlation between $\delta^{18}O$ and $\delta^{13}C$, but the strength of this varies from very weak in several *T. gigas* and *T.maxima* to strongly correlated in one *T. maxima* and *T. squamosa*.

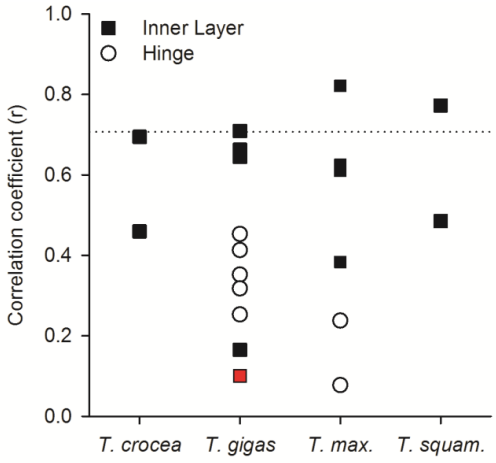

Figure 4.13 Correlation coefficient (r) between $\delta^{13}C$ and $\delta^{18}O$. Dotted lines represent the equivalent r^2 of 50%. Red square represents r value for modern *T. gigas* MT7

4.5 Conclusions

Once *Tridacna* sp. data have been corrected for an ice volume effect, the residual $\delta^{18}O$ reflects changes in SST and evaporation/precipitation. The three *T. gigas* from the early Holocene record slightly more negative mean $\delta^{18}O$ values than the modern *T. gigas*, which suggests a slight cooling or increase in salinity (reflecting drier conditions). A cooling of ~0.5±0.3°C is within estimates of early Holocene SSTs from foraminifera from the west Pacific. The Holocene data might also suggest similar temperatures to modern, but less precipitation and hence increased salinity, if the evaporation/precipitation signal is dominating the $\delta^{18}O$ signal.

Mean $\delta^{18}O$ from individual MIS3 *Tridacna* sp. give a theoretical reduction in SST of 1-2.5±0.5°C and an increase in salinity, assuming an equal contribution of SST and evaporation/precipitation to the $\delta^{18}O$. As this reduction in SST is slightly below the 2-3°C which is generally suggested from foraminifera data from the west Pacific, it might mean that SST is dominating the $\delta^{18}O$ signal, and the theoretical reduction in SST might be higher.

Mean $\delta^{13}C$ from fossil *Tridacna* sp. is consistently higher than the modern *T. gigas*, which is due to the Suess effect. Holocene $\delta^{13}C$ from four *T. gigas* is within error of a Holocene *T. gigas* from Japan, while MIS3 *T. maxima* $\delta^{13}C$ is higher than that recorded in South Pacific *T. maxima*. $\delta^{13}C$ values recorded in the inner layer of fossil *Tridacna* sp. tend to show a positive correlation with $\delta^{18}O$ values. More positive mean values of $\delta^{13}C$ also correlate to more positive mean values of $\delta^{18}O$ in MIS3 *Tridacna* sp. At this point it is not possible to interpret the $\delta^{13}C$ data in terms of environmental parameters, but in glacial samples in particular, there appears to be increasing $\delta^{13}C$ with a decrease in mean SST.

5. Potential Use of Trace Element Ratios Measured in Fossil *Tridacna* sp.

Chapter Abstract

The concentration of certain trace elements in biogenic calcium of fossil bio-carbonates has been used to reconstruct palaeo-environmental conditions. In corals, elements such as magnesium (Mg/Ca), strontium (Sr), and barium (Ba/Ca) have been used to reconstruct temperature, salinity and productivity. In bivalves, biological factors seem to play an important role in the incorporation of trace elements into the shell matrix, and there is not yet a general consensus on the relationship between trace element ratios and environmental conditions.

Mg/Ca in several fossil *Tridacna maxima* appears to show seasonal oscillations, suggesting that the Mg/Ca ratio is responding to seasonal changes in either temperature and/or salinity. However, in other species of *Tridacna*, the influence of growth appears to dominate environmental influences. In the modern *T. gigas* from the Huon Peninsula, there is a weak relationship between local SST and Mg/Ca, and the size of seasonal oscillations increases over time. Values of Sr/Ca differ from the modern shell by up to 1 mmol/mol, and individual profiles do not generally show any seasonal patterns in Sr/Ca, suggesting that factors other than temperature influence the uptake of Sr into *Tridacna* sp.

In modern *T. gigas* samples from both the Huon Peninsula and Great Barrier Reef, Ba/Ca has been shown to be related to local chlorophyll a concentrations and thus to productivity. This increase in productivity reflects the input of nutrients due either to increased rainfall and riverine runoff, or to an increase in upwelling. The Ba/Ca profile from the Huon Peninsula is marked by irregular peaks, which correlate with anomalous drought conditions and peaks in chlorophyll a.

Chapter 5

5.1 Introduction

This chapter follows from the work of Elliot et al. (2009), who measured trace elements in three modern *Tridacna gigas* samples from the Huon Peninsula, the Great Barrier Reef and Cocos Island in the Indian Ocean. The fossil data from the Huon Peninsula are compared to these previously published measurements of magnesium (Mg/Ca), strontium (Sr/Ca) and barium (Ba/Ca).

Metal elements exist in seawater in a variety of physical and chemical structures, including particulate and dissolved forms. They can exhibit a range of concentrations, which are controlled by a number of processes, including external sources of trace metals delivered by rivers, by wind-blown dust, and by hydrothermal circulation, while the removal of trace elements from seawater include active biological uptake or passive scavenging onto living or non-living particulate material (Bruland and Lohan, 2003).

Past studies have demonstrated how the trace element ratio of biogenic carbonate ($CaCO_3$) can be used. Trace element ratios are a useful tool for reconstructing water temperature in biogenic carbonates such as corals (e.g. Corrège, 2006) and foraminifera (e.g. Elderfield and Ganssen, 2000) as they are often independent of other environmental variables. In corals and foraminifera, trace element ratios have been used as proxies for sea surface temperature (SST) (Mg/Ca (Lea et al., 1999, Elderfield and Ganssen, 2000); Sr/Ca (Beck et al., 1992, McCulloch et al., 1994, McCulloch et al., 1996, Alibert and McCulloch, 1997, Ayliffe et al., 2004)), productivity (Ba/Ca, (McCulloch et al., 2003, Sinclair and McCulloch, 2004)), and salinity (Ba/Ca, B/Ca (Roopnarine et al., 1998)). This chapter specifically focuses on weekly resolved profiles of Mg/Ca, Sr/Ca and Ba/Ca in fossil *Tridacna* sp.

In bivalves there is as yet no general consensus, and many uncertainties surround the relationship between the incorporation of individual trace elements and environmental variables. One of the strengths of using bivalves is that they deposit daily growth bands (Richardson, 1987, Chauvaud et al., 1998, Watanabe et al., 2004, Chauvaud et al., 2005, Schwartzmann et al., 2011), and therefore the trace element profiles obtained from bivalve shells are able to provide high resolution, well constrained temporal records of past environmental conditions (Wanamaker et al., 2008). There are variations in trace

element ratios on a day night timescale (e.g. Sr/Ca (Sano et al., 2012) as well as seasonal variations (e.g. Mg/Ca (Elliot et al., 2009)); and changes due to ontogeny and growth (e.g. Mg/Ca (Elliot et al., 2009)).

A number of studies suggest a relationship between variations in Mg/Ca and growth within bivalve shells, but these appear to be highly species specific. In *Mytilus californianus* (Ford et al., 2010) there is a positive correlation between Mg/Ca and growth rate, while in *Arctica islandica* (Schöne et al., 2011) there is a negative correlation. In *Pinna nobilis* (Freitas et al., 2005); *Mytilus edulis* and *Pecten maximus* (Freitas et al., 2008) there is a very weak correlation between Mg/Ca and growth, while in *Andamussium colbecki* (Lartaud et al., 2010) and *Tridacna squamosa* (Batenburg et al., 2011) there is no relationship.

While the primary factor controlling elemental ratios in bivalves is the metal concentration in seawater in which the organisms live, there are a number of other factors which are summarised in Wanamaker et al. (2008). These include:
1) strong biological effects during the uptake of trace elements (e.g. Gillikin et al., 2005b, Freitas et al., 2006);
2) kinetic effects during biomineralisation (e.g. Takesue and Van Geen, 2004, Lorrain et al., 2005, Carré et al., 2006);
3) ontogeny (e.g. Freitas et al., 2005, Gillikin et al., 2005b);
4) hydrographic features including salinity, timing of phytoplankton blooms, or food levels which may impact the uptake of trace elements (e.g. Vander Putten et al., 2000).
In addition to these, there are species specific effects and environmental factors which affect the incorporation of trace elements into bivalve shells.

Separating these effects is not always easy even with the most precise observation and measurement strategies. Because of all of these potential effects, live culture experiments are particularly useful as they allow the separate evaluation of the influence of each environmental variable, including temperature, pH and salinity. Trace element ratios might be used in a multi-proxy approach to look at past water temperature and the isotopic signature of the seawater in which the bivalve grew ($\delta^{18}O_w$). However, individual species record different relationships between the trace element and $\delta^{18}O$, with some reporting no relationship (Batenburg et al., 2011), and

others an inverse relationship (Toland et al., 2000, Elliot et al., 2009, Batenburg et al., 2011).

In abiogenic calcium carbonate, Sr/Ca ratios are controlled by precipitation rate, which is a function of seed crystal rate (Lorens, 1981). An inverse relationship between seawater temperature and Sr content of inorganic and coral aragonite has often been found (Lea, 2003), and the possibility of using Sr/Ca as a proxy for SST in corals was first suggested in the 1970s (Smith et al., 1979). Since then, Sr/Ca ratios have commonly been used in corals to reconstruct SST (Beck et al., 1992, McCulloch et al., 1994, McCulloch et al., 1996, Alibert and McCulloch, 1997, Ayliffe et al., 2004). As with Mg/Ca, the relationship between Sr/Ca and SST in bivalves is more complex and may be affected by biological and environmental controls, such as ontogeny (Gillikin et al., 2005b, Schöne et al., 2011). In corals, diagenesis can significantly affect Sr/Ca estimates by ±1°C (Allison et al., 2007). However the structure of *Tridacna* sp. shell is more dense than corals, and the fossil *Tridacna* sp. used in this study all have a bulk XRD calcite value of below 1%.

Mg/Ca has been used as a proxy for reconstructing past ocean temperatures in foraminifera (Lea et al., 2000, Elderfield and Ganssen, 2000, Elderfield et al., 2002), corals (Sinclair et al., 1998) and some species of bivalves (Dodd, 1965, Klein et al., 1996), particularly in a multi-proxy approach with $\delta^{18}O$. However, biological factors may skew or mask the relationship between Mg/Ca and temperature, and so a strong and direct relationship is rarely observed (e.g. Vander Putten et al., 2000, Freitas et al., 2005, Freitas et al., 2006, Freitas et al., 2008, Wanamaker et al., 2008). There are a number of biological and environmental controls on Mg/Ca which can affect the relationship between SST and Mg/Ca concentration in biogenic carbonates. These include metabolic activity (Lorens and Bender, 1977, Vander Putten et al., 2000), ontogeny (Freitas et al., 2005, Ford et al., 2010), the organic matrix (Vander Putten et al., 2000, Takesue and Van Geen, 2004, Takesue et al., 2008, Schöne et al., 2010), and salinity (Dodd, 1965, Wanamaker et al., 2008). Inorganic precipitation data suggest an increase of 3%/°C, while foraminifera data range from 2% to 20%/°C at lower temperatures, and there is no consistent Mg/Ca concentration/temperature gradient (Lea, 2003).

The barium content of corals has been reported as a proxy for discharge and/or sediment load in riverine systems (McCulloch et al., 2003, Sinclair and McCulloch, 2004). In corals, barium substitutes into the skeleton lattice, and should be proportional to the Ba content of seawater (Lea et al., 1989). To convert coral Ba values to seawater Ba concentration requires the estimation of a distribution coefficient, calculated as follows: D = (Ba/Ca)coral/(Ba/Ca)seawater. This partition coefficient is generally $D_{Ba} \approx 1$ (Lea et al., 1989). Coralline Ba/Ca at the Great Barrier Reef has been shown to have a close but indirect relationship with local salinity (Figure 5.1), as the barium taken up into the coral skeleton originated from river runoff .

In many bivalve species, the Ba/Ca profile of shell carbonate is characterised by a stable background ratio, punctuated by intense maxima or peaks (e.g. *Mytilus edulis* (Vander Putten et al., 2000, Gillikin et al., 2006), *Mercenaria mercenaria* (Stecher et al., 1996), *Saxidomus giganteus* (Gillikin et al., 2008), *Pecten maximus* (Lorrain et al., 2000, Barats et al., 2009). Barium has been established as a paleo productivity tracer in marine waters, suspended particles and sediments (Dymond and Collier, 1996, Paytan and Kastner, 1996). Ba/Ca peaks have also been suggested to be related to phytoplankton blooms (Stecher et al., 1996, Vander Putten et al., 2000, Lazareth et al., 2003).

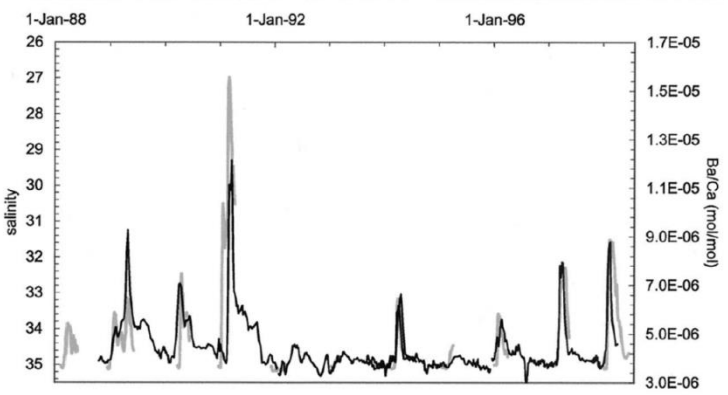

Figure 5.1 Coral Ba/Ca (black line) and daily model salinity (grey line) from the Great Barrier Reef

5.2 Summary of previous findings in *Tridacna* sp.

There have been few studies concentrating on trace element profiles in *Tridacna* sp. However, these studies have a number of similarities. *T. squamosa* and *T. gigas* show a

relationship between Mg/Ca and $\delta^{18}O$, although this relationship changes from the juvenile to adult phase of life. Peaks in Ba/Ca measured in *T. gigas* (Figure 5.2) show a promising link to productivity (Elliot et al., 2009).

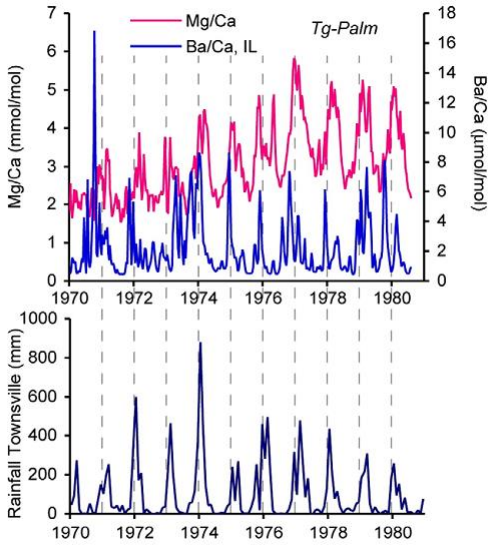

Figure 5.2 Comparison of *Tg-Palm* Ba/Ca and Mg/Ca profiles with local rainfall data. Peaks in Ba/Ca occur during increasing and high Mg/Ca (top panel) values, corresponding to late spring/summer growth. Bottom panel shows that the peaks in Ba/Ca are coeval with increases in rainfall within error of the age model (Elliot et al., 2009)

One important result when using trace elements in *Tridacna* sp. shells comes from the area of the shell analysed. Mg/Ca and Sr/Ca profiles differ depending on the area of the shell sampled in *T. gigas*, despite all regions being composed of aragonite (Elliot et al., 2009). Conversely, Ba/Ca profiles are highly reproducible in the hinge, inner and outer layers of the shell.

Previous work also highlights a species specific effect. Three species of *Tridacna* (*T. gigas*, *T. squamosa* and *T. deresa*) have published trace element profiles, but these were collected from different locations and the difference in results could be due to local environmental conditions. Minimum values of Mg/Ca are within error in *T. deresa* and *T. squamosa*, while *T. gigas* records a larger range of values (Table 5.1). Values of Sr/Ca in all three species are within the range of 1.1-2.8 mmol/mol (Table 5.2). A *T. squamosa* from Vietnam (Batenburg et al., 2011) records higher values of Ba/Ca than *T. gigas* and *T.deresa* (Table 5.3). These differences could be explained by a species specific effect, or they could be due to the Ba content of the local water.

The method used to measure trace elements also seems to provide different results (Yan et al., 2013), as these can integrate over different timescales. Yan et al. (2013)

found that using an Inductively Coupled Plasma Optical Emission Spectrometer (ICP-OES) resulted in Sr/Ca ratios which showed seasonal oscillations and a strong inverse relationship between Sr/Ca and SST in a *T. gigas* (Figure 5. 3), while Laser Ablation Inductively Coupled Plasma Mass Spectrometer (LA-ICP-MS) resulted in Sr/Ca profiles with no seasonal oscillations or relationship with SST. The relationship between Sr/Ca and SST using ICP-OES was found to be -0.0487 mmol/mol/°C, comparable to other bivalve species and corals in the region (Yan et al., 2013). Absolute values of Sr/Ca were lower in the *T. gigas* sampled using LA-ICP-MS than those using ICP-OES. The reason for the differences between the results obtained from the two methods remains inconclusive (Yan et al., 2013). Depending on the spot size, LA-ICP-MS as used in this study, can resolve daily-weekly signals, while ICP-OES, where measurements are made at discrete intervals, can resolve seasonal (weekly-monthly) signals.

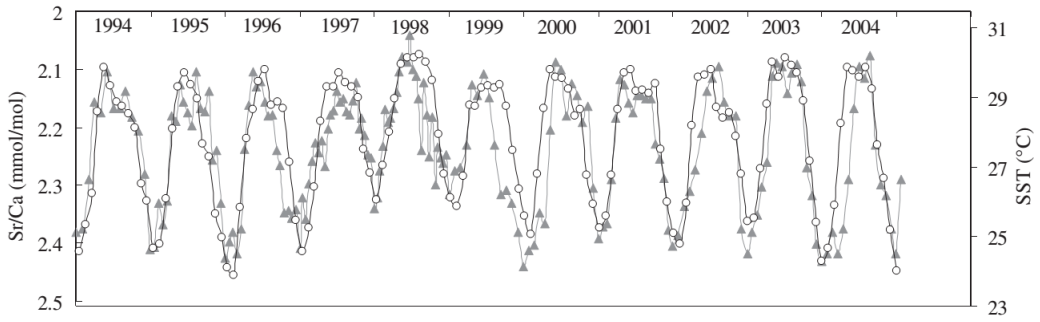

Figure 5. 3 Relationship between ICP-OES derived Sr/Ca of a modern *T. gigas* from South China Sea (solid triangles) and SST (open dots) from Yan et al. (2013)

Table 5.1 Values of Mg/Ca in published studies using *Tridacna* sp., and their relationships with environmental parameters and $\delta^{18}O$. Measurements were taken using Laser Ablation Inductively Coupled Plasma Mass Spectrometer (LA-ICP-MS); Inductively Coupled Plasma Optical Emission Spectrometer (ICP-OES) and the NanoSIMS microprobe

Species (reference)	Method	Values Recorded (mmol/mol)	Findings
T. gigas (Elliot et al., 2009)	LA-ICP-MS	Hinge: 0.2-1.9 Inner: 0.5-4.2	High Mg/Ca associated with negative $\delta^{18}O$, i.e. summer/higher SST (Figure 5.4)
T. squamosa (Batenburg et al., 2011)	LA-ICP-MS	0.46-1.65	Peaks in Mg/Ca coincide with low values of $\delta^{18}O$ (same as *T. gigas*)
T. deresa (Sano et al., 2012)	NanoSIMS LA-ICP-MS	0.3-1.5 0.2-1.4	Irregular diurnal cycle; positive correlation (0.465) between Mg/Ca and SST

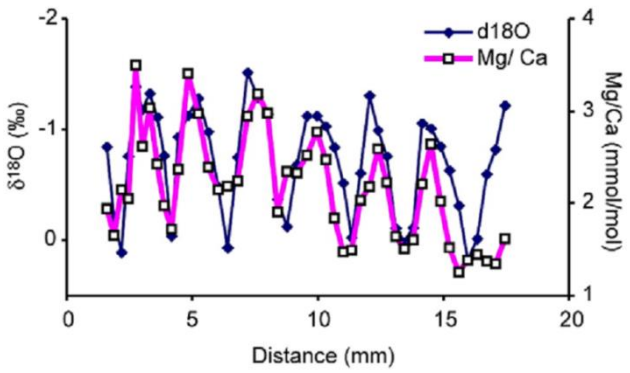

Figure 5.4 Relationship between ICP-AES derived Mg/Ca and $\delta^{18}O$ from a modern *T. gigas* from Palm Island (GBR) (Elliot et al., 2009)

Table 5.2 Values of Sr/Ca in published studies using *Tridacna* sp., and their relationships with environmental parameters and $\delta^{18}O$

Species (reference)	Method	Range of Values Recorded (mmol/mol)	Findings
T. gigas (Elliot et al., 2009)	LA-ICP-MS	Hinge: 1.4-1.9 Inner: 1.3-2.3	No relationship between Sr and environmental parameters
T. squamosa (Batenburg et al., 2011)	LA-ICP-MS	1.44-2.84	No relationship with growth
T. deresa (Sano et al., 2012)	NanoSIMS LA-ICP-MS	1.1-2.2	Sr shows diurnal variations, and may be a proxy for parameters of the daily light cycle
T. gigas (Yan et al., 2013)	ICP-OES LA-ICP-MS	Inner layer of two shells: 2.04-2.44; 1.68-2.0 1.23-2.04; 1.58-2.22	Negative correlation between Sr and SST derived from ICP-OES

Table 5.3 Values of Ba/Ca in published studies using *Tridacna* sp., and their relationships with environmental parameters and $\delta^{18}O$

Species (reference)	Method	Values Recorded (µmol/mol)	Findings
T. gigas (Elliot et al., 2009)	LA-ICP-MS	Hinge: 0.4-5 Inner: 0.4-4.7	Ba peaks correlate with the timing of chlorophyll maxima in shells from GBR.
T. squamosa (Batenburg et al., 2011)	LA-ICP-MS	1.1-8.4	Ba negatively correlated with Mg/Ca with a phase lag of several months
T. deresa (Sano et al., 2012)	NanoSIMS LA-ICP-MS	0.2-2.2 0.6-1.6	Large amplitude variability but no diurnal cycle

From previously published work on trace element ratios in *Tridacna* sp., there are several possible relationships between the trace element ratio and environmental factors which can be tested using the fossil data set. These are: the influence of SST and growth on Mg/Ca and Sr/Ca; and the influence of local upwelling or productivity on Ba/Ca ratios.

5.3 Methods

Geochemical analysis methods and mean results are detailed in Chapter 3. Trace element profiles of individual shells are shown in the Appendix. In this study, seventeen elements were measured by LA-ICP-MS. The relationship between many minor elements and environmental features is not well understood. Therefore this study concentrates on Mg/Ca, Sr/Ca and Ba/Ca, and values are compared to the modern *T. gigas* (MT7 (Elliot et al., 2009)) and published values wherever available (Figure 5.6). LA-ICP-MS data was interpolated to give 52 measurements per year, or one/week, as lower resolution (i.e. monthly) data can smooth out any peaks in the data (Chapter 3).

To calculate whether differences in mean values were statistically significant, a Mann Whitney U Test was performed on mean values of Mg/Ca, Sr/Ca and Ba/Ca in fossils. This is discussed in Section 5.4 with the caveat that the small sampling size reduces the robustness of any results given.

Quantifying peaks in Ba/Ca

The size and duration of peaks in Ba/Ca is more variable than changes in only the mean value, and these have the potential to reveal information about local productivity (Elliot et al., 2009). In order to examine the peaks in Ba/Ca profiles, these were quantified using the following method. Once each record was interpolated to 52 samples/year, a baseline was calculated as follows:

1. Calculate the mean Ba/Ca value at weekly resolution
2. Discard values over the mean
3. Recalculate the mean – this gives the "baseline".

Peaks in Ba/Ca were classified as anything above double the baseline of each individual shell (Figure 5.5). Using this threshold means that only large peaks in Ba/Ca (generally over 2-3 μmol/mol in fossil shells) are discussed later. To quantify changes in peaks over time, the number of peaks/year was subsequently counted.

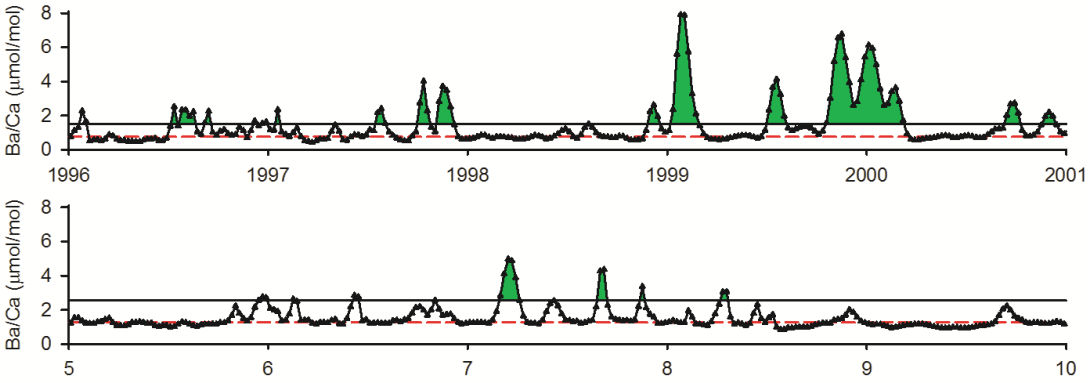

Figure 5.5 Ba/Ca profile for MT7 (top panel) and Holocene *T. gigas* T58 (bottom panel). The baseline for each Ba/Ca profile is marked by a red dashed line, double the baseline is marked by a solid black line. Anything above this (shaded in green) is counted as a Ba/Ca peak

5.4 Results: Trace element ratios in fossil *Tridacna* sp.

Mean values of trace elements

Initially the mean fossil results of Mg/Ca, Sr/Ca and Ba/Ca are presented over time (Figure 5.6), which enables values to be compared to the modern *T. gigas* (MT7) as well as to published values. The figure indicates where different species and areas of the shell (the hinge and inner layer) were sampled. Results are then presented separated into individual trace elements, and further subdivided by species and shell region (Figures 5.7 – 5.9), in order to highlight any potential species specific effects.

Although mean values of all trace elements fluctuate, there is no clear trend over time towards lower values. There is no difference between the mean values of Holocene and MIS3 samples.

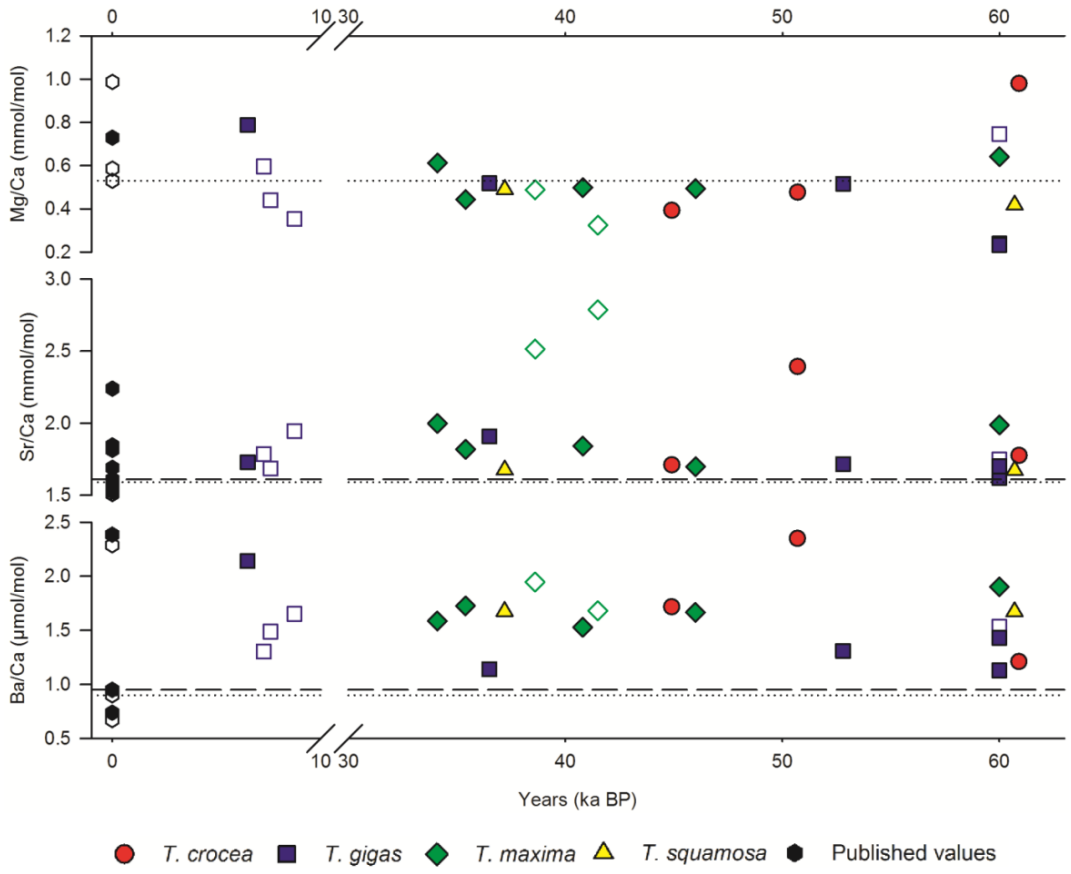

Figure 5.6 Mean Mg/Ca, Sr/Ca and Ba/Ca values of the four species of *Tridacna* used in this study. Samples are further separated by area of shell sampled. Mean values of the modern *T. gigas* hinge (dotted) and inner (dashed) layers are marked by lines. Filled shapes indicate that the inner layer of the shell was sampled while open shapes represent the hinge region of the shell. For Mg/Ca, the mean value of the inner layer of MT7 was higher than all fossil values (1.6 mmol/mol) and is outside the range of the y-axis in the figure (top panel)

Mg/Ca

In all four species sampled, and in both areas of the shell, mean values of Mg/Ca are lower than the mean value recorded in the inner layer of MT7 (1.6 mmol/mol) (Figure 5.6 and Figure 5.7). Fossil values range from 0.23 to 0.97 mmol/mol, with 11 fossils recording a mean value similar (difference of ±0.1 mmol/mol or less) to the MT7 mean hinge value. Mg/Ca mean values (0.4 and 0.5 mmol/mol) from fossil *T. squamosa* are lower than a modern *T. squamosa* from Vietnam (0.7 mmol/mol) (Batenburg et al., 2011).

In the *T. gigas* shells where the inner layer was sampled, mean values of Mg/Ca are significantly (Mann-Whitney U Test, p = 0.03) higher (by 0.3-0.6 mmol/mol) than the *T.*

gigas where the hinge was sampled. In the specimen of *T. maxima* where the inner layer was sampled, mean values are not significant different (p = 0.147) to the *T. maxima* where the hinge was sampled. The difference between the mean values obtained from the hinge and inner layers of MT7 is higher (>1 mmol/mol) than the difference between mean values obtained from all the fossil species of *Tridacna*. This could suggest that biological controls on the different areas of the shell affect the concentration of Mg/Ca more than any species specific effect, or that species specific effects are skewed or masked when looking at mean values of Mg/Ca. To illustrate this point, there was no statistically significant difference between the mean values obtained from the hinge of *T. gigas* and the hinge of *T. maxima* shells, and between mean values from the inner layer of *T. gigas* and the inner layer of *T. maxima* shells (Figure 5.7).

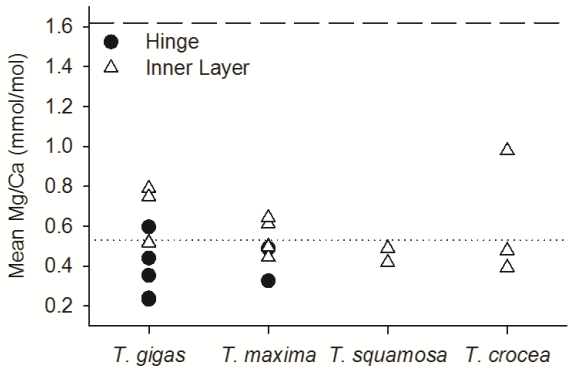

Figure 5.7 Mean values of Mg/Ca in fossil *Tridacna* sp., separated by species and area of shell sampled. The mean values recorded by MT7 are marked by a dashed line (inner layer) and a dotted line (hinge)

Sr/Ca

Mean values of Sr/Ca are similar in both areas sampled of the modern *T. gigas* shell (1.59 and 1.61 mmol/mol in the hinge and inner layers respectively), with all fossils recording similar or larger mean values (Figure 5.6 and Figure 5.8).

In *T. gigas* shells, there is no statistically significant difference between mean values obtained from the hinge and the inner layers (Figure 5.8). In *T. maxima* shells, there is a significant difference (p = 0.002) between the hinge and inner layer, with values recorded in the hinge approximately 0.7-1.2 mmol/mol higher than those recorded in the inner layer. The difference between the mean values recorded in the hinge of *T.*

gigas and the hinge of *T. maxima* is significantly different (p = 0.002), but those recorded in the inner layers of *T. gigas* and *T. maxima* are not significantly different.

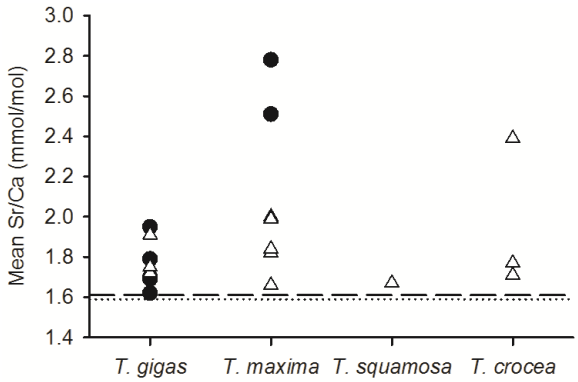

Figure 5.8 Mean values of Sr/Ca in fossil *Tridacna* sp., separated by species and area of shell sampled. The mean values recorded by MT7 are marked by a dashed line (inner layer) and a dotted line (hinge). Circles represent where the hinge was sampled, triangles the inner layer

Ba/Ca

In the modern *T. gigas*, mean Ba/Ca values are the same in all areas of the shell sampled (Elliot et al., 2009) (Figure 5.6). All fossil mean Ba/Ca values are higher than modern (MT7) (Figure 5.9), but the occurrence and size of Ba/Ca peaks is potentially more important as an environmental proxy than mean values, and will be discussed in section 5.6

There is no significant difference between values recorded in the hinge and inner layers in *T. gigas* and *T. maxima* shells (Figure 5.9). There is also none between the mean Ba/Ca values obtained in all four species. This may indicate that any species specific effect seemingly affecting Mg/Ca does not influence the incorporation of Ba/Ca.

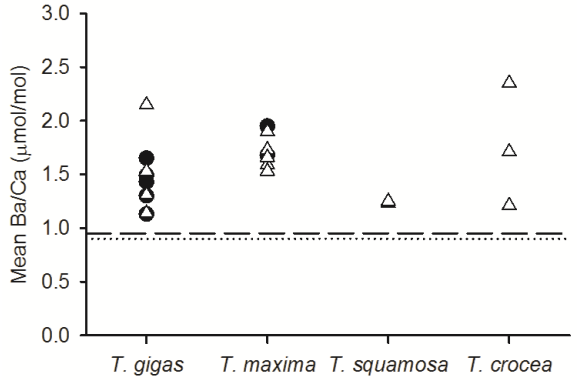

Figure 5.9 Mean values of Ba/Ca in fossil *Tridacna* sp., separated by species and area of shell sampled. The mean values recorded by MT7 are marked by a dashed line (inner layer) and a dotted line (hinge). Circles represent where the hinge was sampled, triangles the inner layer

Seasonally resolved trace element ratio profiles

Mean values of trace element ratios provide information about the mean climate state, while higher resolution records may provide information on seasonal or biological trends during the lifetime of an individual fossil (Figures 5.10 and 5.11). The seasonal patterns in Mg/Ca show differences between specimens of different species. In the Mg/Ca profile of hinge *T. gigas* shell T58 (Figure 5.10), seasonal oscillations have an average amplitude of ~0.2 mmol/mol during the juvenile portion of the shell, but increase to ~0.3-0.4 mmol/mol towards the adult portion. There is an increasing trend towards higher Mg/Ca values over time, from ~0.3 to 0.6 mmol/mol. In the Mg/Ca profile of the inner layer of a *T. maxima* shell T39 (Figure 5.11), the amplitude of these oscillations is higher, on average 0.5-0.7 mmol/mol throughout the growth of the shell. There are also differences in the structure of the Sr/Ca profile, with the Sr/Ca profile of T39 showing large oscillations, which are not seen in T58, despite mean values (T58 = 1.95, T39 = 1.84 mmol/mol) being similar. Finally, T58 shows more frequent and higher Ba/Ca peaks than T39.

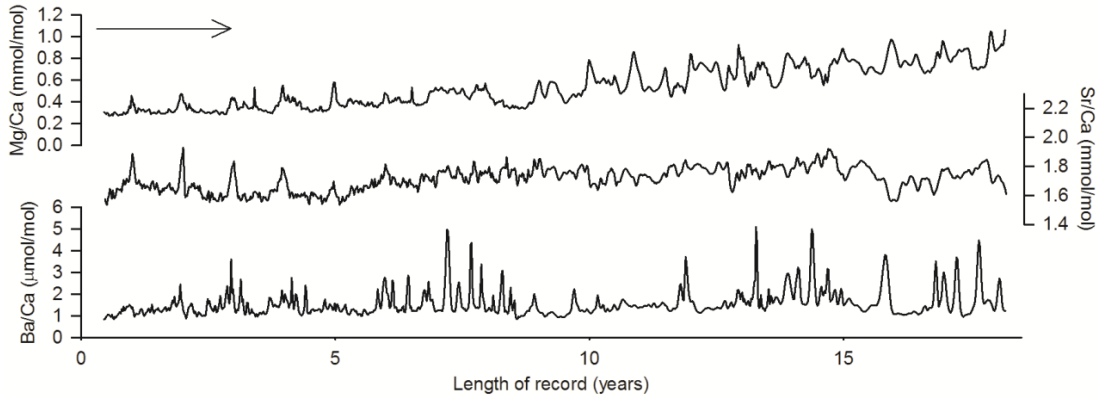

Figure 5.10 Results from *T. gigas* shell T58 (7.59 ka BP). Shown are Mg/Ca (top); Sr/Ca (middle) and Ba/Ca (bottom). Resolution is at 52 samples/year. Values of Mg/Ca and Sr/Ca are given in mmol/mol and Ba/Ca in µmol/mol. Arrow shows direction of growth from juvenile (left) to adult (right)

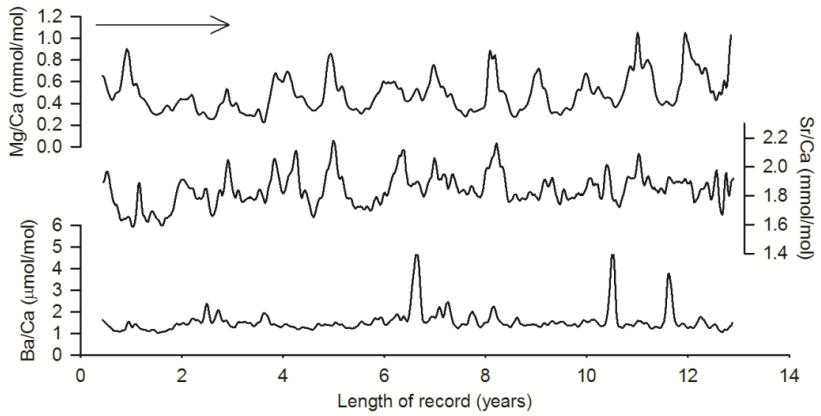

Figure 5.11 Results from *T. maxima* shell T39 (39.5 ka BP). Details in Figure 5.10 caption

5.5 Discussion

5.5.1 The limitations of Sr/Ca and Mg/Ca as a tool for SST reconstructions in *Tridacna* sp.

Results obtained from LA-ICP-MS of fossil *Tridacna* sp. offer a unique possibility to compare Sr/Ca and Mg/Ca profiles over the past 60 ka. The Sr/Ca and Mg/Ca profiles of the modern *T. gigas* (MT7) can be compared to SST for the same region (Figure 5.12). MT7 inner layer Sr/Ca (interpolated to 12 samples a year for linear regression) shows no relationship to SST ($r^2 = 0.0001$), while there is a weak positive correlation between monthly SST from IGOSS for the Huon Peninsula (Reynolds et al., 2002) and inner layer Mg/Ca ($r^2 = 0.3$). However, MT7 shows a strong ontogenetic trend in inner layer Mg/Ca ($r^2 = 0.7$). This suggests that the influence of SST may be dampened or masked by the influence of growth. If a linear trend is removed from the Mg/Ca profile, the correlation between SST and Mg/Ca increases ($r^2 = 0.4$), and oscillations of 1-2 mmol/mol in the residual Mg/Ca coincide with temperature fluctuations of 2-2.5°C in the SST record (Figure 5.13).

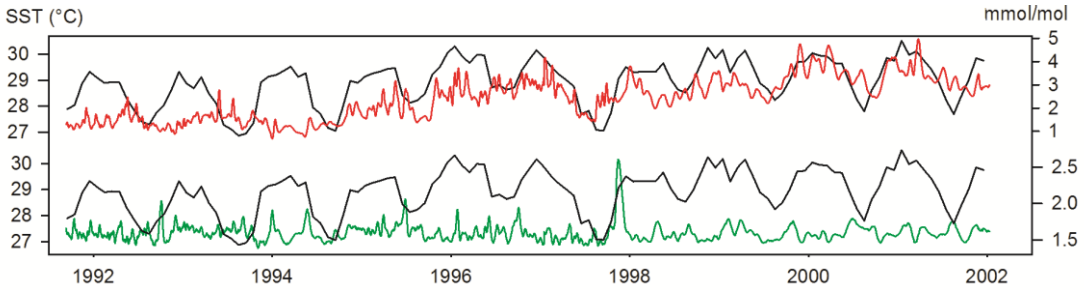

Figure 5.12 Comparison of MT7 inner layer Mg/Ca (top panel, red) and Sr/Ca (bottom panel, green) with monthly SST from IGOSS for 6.5°S 145.5°E (Reynolds et al., 2002). Resolution of MT7 profiles is at 52 samples/year

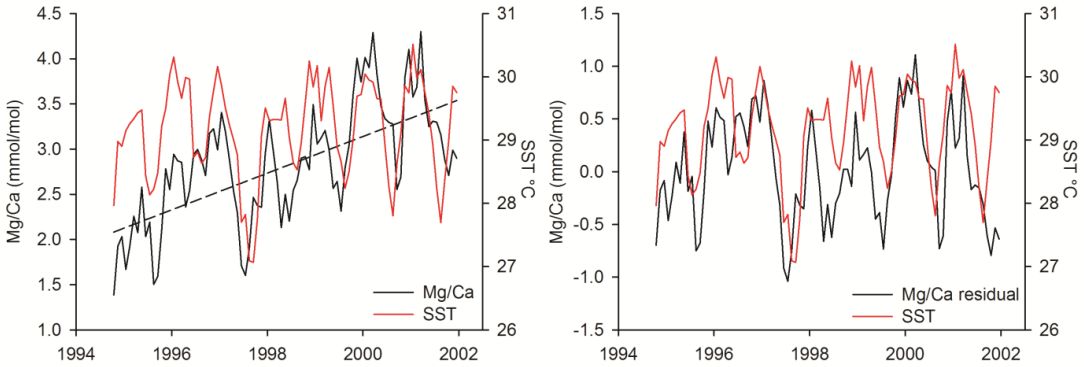

Figure 5.13 Relationship between monthly resolved Mg/Ca and SST (Reynolds et al., 2002). Left panel shows the MT7 Mg/Ca profile from 1994-2002, with the increasing Mg/Ca trend with age (dashed line). Right panel shows the Mg/Ca profile with this trend removed

5.5.2 Can Sr/Ca be used as a temperature proxy?

If there is an inverse relationship between SST and Sr/Ca in *Tridacna* sp., the modern samples from Cocos and GBR should have a higher mean Sr/Ca than the *T. gigas* from Huon, as the mean SST for an overlapping period is 1.4°C (Cocos) and 2.5°C cooler (GBR). However, mean Sr/Ca values are 0.08 (Cocos) and 0.04 (GBR) mmol/mol lower in the inner layer, and 0.08 (both samples) mmol/mol lower in the hinge than the mean values from Huon. Several *T. gigas* from the South China Sea (Yan et al., 2013) have a mean Sr/Ca value 0.1, 0.13 and 0.22 mmol/mol higher than MT7, with mean SSTs 1.2°C lower.

As Sr/Ca measurements from corals suggest that values were generally higher during glacial episodes (Stoll and Schrag, 1998, Stoll et al., 1999, Martin et al., 1999), the fact that modern *T. gigas* from different sites do not consistently show an increase in Sr/Ca

suggests that there may be site specific effects related to the ratio of Sr/Ca in local ocean water.

The monthly resolved Sr/Ca profile of MT7 does not correlate with SST at the Huon Peninsula (Figure 5.12), and mean values of modern Sr/Ca appear to be site specific, but mean Sr/Ca values may suggest shifts in temperature at this location. Fossil mean values of Sr/Ca are higher by up to 1.2 mmol/mol than MT7. When the difference in modern and fossil Sr/Ca is compared to the difference in modern and fossil $\delta^{18}O$ (which includes the influence of both SST and salinity), there are no significant differences in Sr/Ca between Holocene and MIS3 *Tridacna* sp. (Figure 5.14). In addition, the mean $\delta^{18}O$ of T66 (filled square, circled in Figure 5.14) suggests an increase in temperature/reduction in salinity of ~2.7°C/2.2‰, while the higher Sr/Ca value suggests a cooling of ~2.4°C compared to MT7. Yan et al. (2013) found a Sr/Ca SST relationship of ~0.05 mmol/mol/°C in modern *T. gigas* from the Huon Peninsula. In the Holocene *T. gigas*, this relationship would correspond to a cooling of ~4°C compared to modern (n = 3), while the MIS3 *T. gigas* would experience a cooling of ~2.8°C (n = 5).

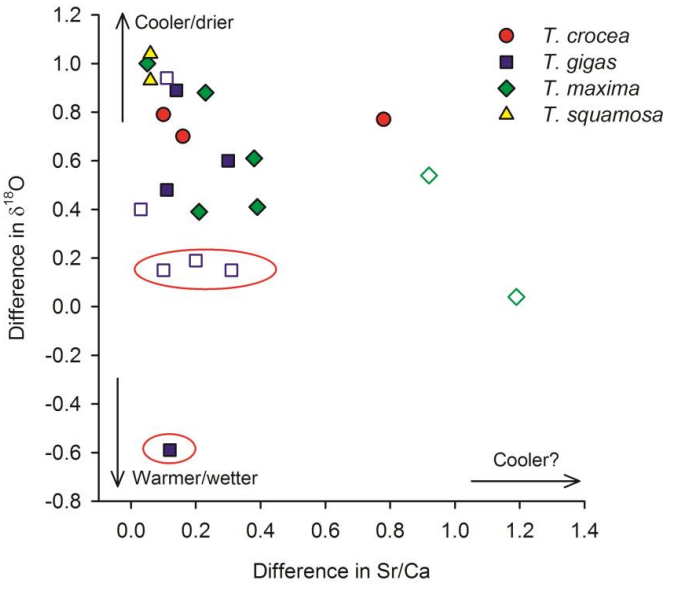

Figure 5.14 Difference between mean Sr/Ca of the modern *T. gigas* from the Huon Peninsula (MT7) and fossil *Tridacna* sp. compared to the difference between mean $\delta^{18}O$ of MT7. Filled shapes indicate that the inner layer of the shell was sampled while open shapes show that the hinge was used. Circled squares are the four Holocene *T. gigas*

Combined with comparisons of Sr/Ca from modern *T. gigas*, it appears that there is a site specific effect to consider when using Sr/Ca to infer changes in SST. Although it is

likely that SST affects Sr/Ca ratios in fossil shells, at this point biological or kinetic influences cannot be distinguished and separated from the SST signal.

5.5.3 Mg/Ca – is growth masking the temperature signal?

Day/night growth bands can be seen in thin sections of *Tridacna* sp. and the number of these bands was counted and used to calculate the growth rate of individual *Tridacna* shells (Chapter 3).

Growth rates have been shown to decrease in *T. gigas* and *T. maxima* during ontogeny, from 8-16 mm/year during the juvenile, to 1-2 mm/year during the adult phase of growth (e.g. Romanek et al., 1987, Aharon, 1991, Elliot et al., 2009, Welsh et al., 2011). *T. gigas* is the fastest growing, with a mean daily growth rate of 0.021 mm/day (~7 mm/year) until the onset of sexual maturity, while *T. crocea* is the slowest with a mean daily growth rate of 0.004 mm/day (~1.5 mm/year) (Klumpp and Griffith, 1994). These values are comparable the fossils used in this study, including *T. gigas*, which have a mean juvenile growth rate of 6-7 mm/year, and slightly lower than *T. crocea*, which have a mean juvenile growth rate of 1.6-1.8 mm/year. In order to examine the relationship between Mg/Ca and growth, the Mg/Ca profile of *Tridacna* sp. was compared with the growth model used to estimate the chronology of individual shells (Chapter 3).

The width of day and night bands decreases through the lifetime of the *Tridacna* sp. shells, which reflects the slowing of the growth rate of the shell. At the same time, the concentration of Mg/Ca increases. This results in an inverse relationship between growth rate and Mg/Ca in modern and fossil *Tridacna* sp (Figure 5.15). However, this relationship is not consistent between species (*T. maxima* does not show the same relationship as *T. gigas*, as illustrated in Figure 5.16).

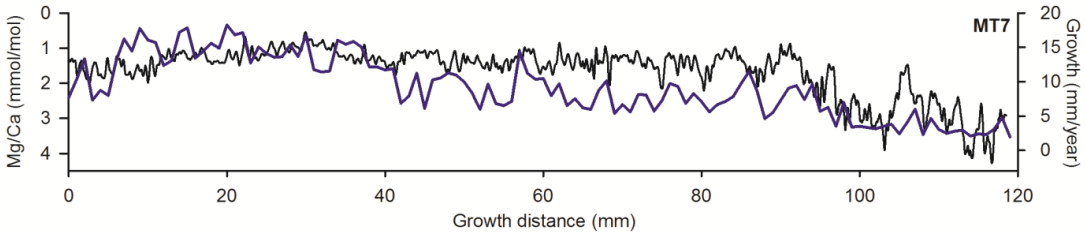

Figure 5.15 Comparison between Mg/Ca (mmol/mol) (black line) and growth rate (blue line) in MT7. Growth rate calculated using the number of day/night bands per 100µm (Chapter 3). Note that the Mg/Ca axis is reversed in order to see better the relationship between Mg/Ca and the growth rate

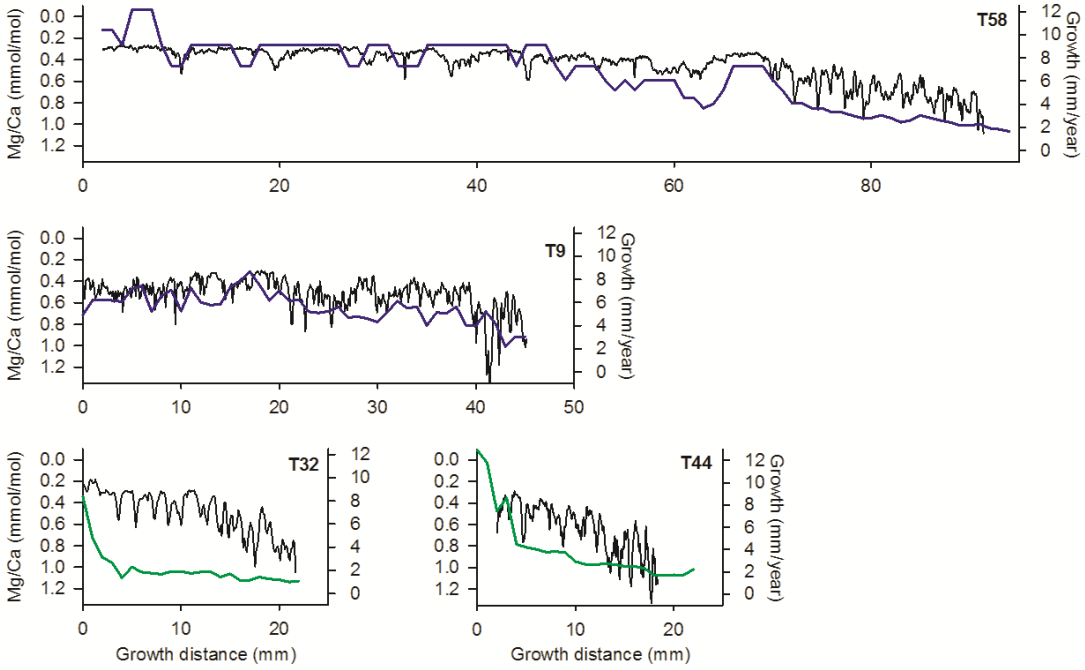

Figure 5.16 Comparison between Mg/Ca (mmol/mol) (black line) and growth rate (coloured line) in *Tridacna* sp. Shown are T58 (7.59 ka BP, *T. gigas*); T9 (35.6 ka BP; *T. gigas*); (T32 (38.6 ka BP, *T. maxima*) and T44 (60 ka BP, *T. maxima*). Growth rate calculated using the number of day/night bands per 100µm (Chapter 3). Note that the Mg/Ca axis is reversed in order to see better the relationship between Mg/Ca and the growth rate

Although there is apparent control of growth rate on Mg/Ca, there is also a temperature control on that recorded in *Tridacna* sp. In several individual shells, there are clear sinusoidal annual cycles of Mg/Ca (Figure 5.17), particularly in *T. maxima* and *T. crocea*.

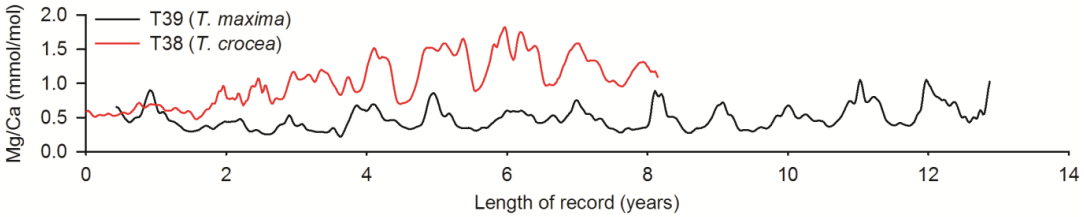

Figure 5.17 Seasonally resolved Mg/Ca profiles in MIS3 *T. maxima* and *T. crocea*. Resolution is at 52 samples/year

These results support the notion of a relationship between growth rate and Mg/Ca in modern and fossil *Tridacna* sp. The increasing trend in Mg/Ca with ontogeny must be removed if any environmental information is to be summarised from these profiles. Despite this relationship with growth, there appear to be seasonal oscillations in Mg/Ca which are likely to be responding to an environmental variable, most probably SST. Due to intra-shell differences in Mg/Ca profiles, as well as species specific effects, more investigation is needed into the use of Mg/Ca as a potential provider of environmental information.

5.6 The use of Ba/Ca as a productivity proxy

Peaks in a modern *T. gigas* shell from Palm Island on the Great Barrier Reef (*Tg-Palm*) and Cocos Island have been shown to be associated with peak chlorophyll values (Elliot et al., 2009). Peaks in Ba/Ca in a *T. gigas* from GBR occur at regular intervals, predominantly during the spring/summer period (Elliot et al., 2009).

In areas with a strong seasonal cycle and well defined wet and dry seasons, Ba/Ca peaks may be associated with rainfall, as in the Palm Island *T. gigas*. In modern corals from a site close to Papua New Guinea, enrichments in Ba during ENSO events have been linked to the shoaling of the coastal undercurrent, and coastal upwelling caused by westerly wind bursts (WWB) (Alibert and Kinsley, 2008). Ba/Ca peaks in the modern *T. gigas* from the Huon Peninsula do not appear to be related directly to ENSO, as the timing of the Ba/Ca peaks do not correlate with either El Niño or La Niña events (Figure 5.18), but appear to be associated with reduced rainfall and increased chlorophyll a.

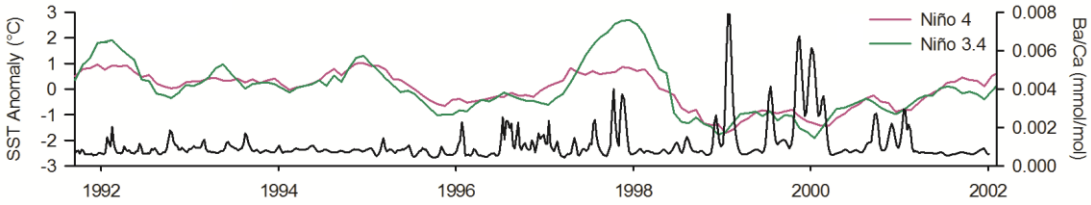

Figure 5.18 Ba/Ca profile of MT7 and Niño 3.4 and Niño 4 indices

Chlorophyll a concentrations are not constant throughout the year (Figure 5.19), and satellite measures of these have been used as a proxy for ocean productivity (e.g. Mantyla et al., 1995, Wilson and Adamec, 2001, Behrenfeld et al., 2006). Chlorophyll a concentrations are lower around the Huon Peninsula during austral winter (June, July, August), and highest during austral summer (December, January, February).

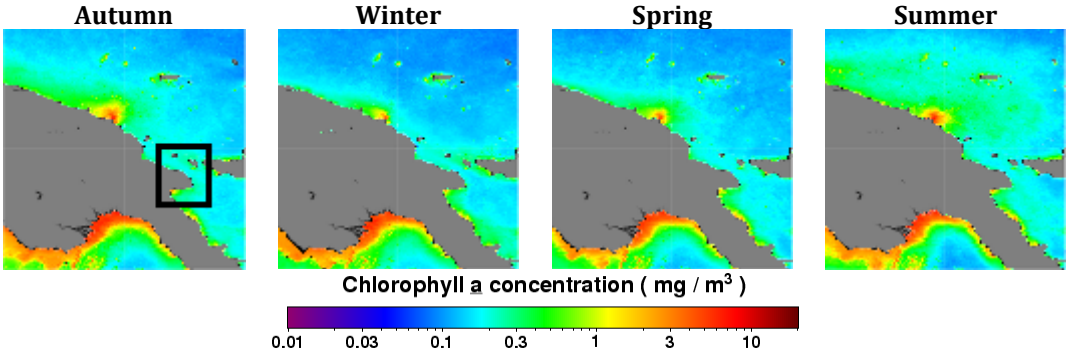

Figure 5.19 Chloropyll a concentration (from SeaWiFS) around the Huon Peninsula. Composite of 1997-2010. From left to right: Austral autumn (MAM), winter (JJA), spring (SON) and summer (DJF). Box marks the location of the Huon Peninsula

Although there is no immediate link between Ba/Ca in MT7 and rainfall as in *Tg-Palm*, it appears that peaks (Section 5.3) in the MT7 Ba/Ca profile occur during periods when the negative rainfall anomaly is large, e.g. periods where there may be drought conditions (Figure 5.20). Although not all large rainfall anomalies coincide with high peaks in Ba/Ca, these peaks in Ba/Ca coincide with a rainfall anomaly of at least 2-3 mm/day less than mean values from 1986-2002.

Chlorophyll a data is not as abundant as measures of other climate variables, but the MT7 Ba/Ca record from 1997-2002 can be compared to measures of chlorophyll a from 147°E, 5-6°S (Figure 5.20). Two large peaks in Ba/Ca in MT7of over 6µmol/mol (during 2000 and 2001) coincide with increases in chlorophyll a from background values of ~0.15 mg/m^3 (Elliot et al., 2009) to over 0.3 mg/m^3. Three smaller peaks in

Ba/Ca of over 3µmol/mol coincide with chlorophyll peaks of ~0.2 and 0.24 mg/m^3. However, there are additional chlorophyll a peaks within the record which do not correspond to peaks in Ba/Ca. One possible explanation is that the chlorophyll a record is not from the exact location of the *T. gigas*. Despite this, there appears to be the potential to use Ba/Ca records as an indicator of peaks in past productivity.

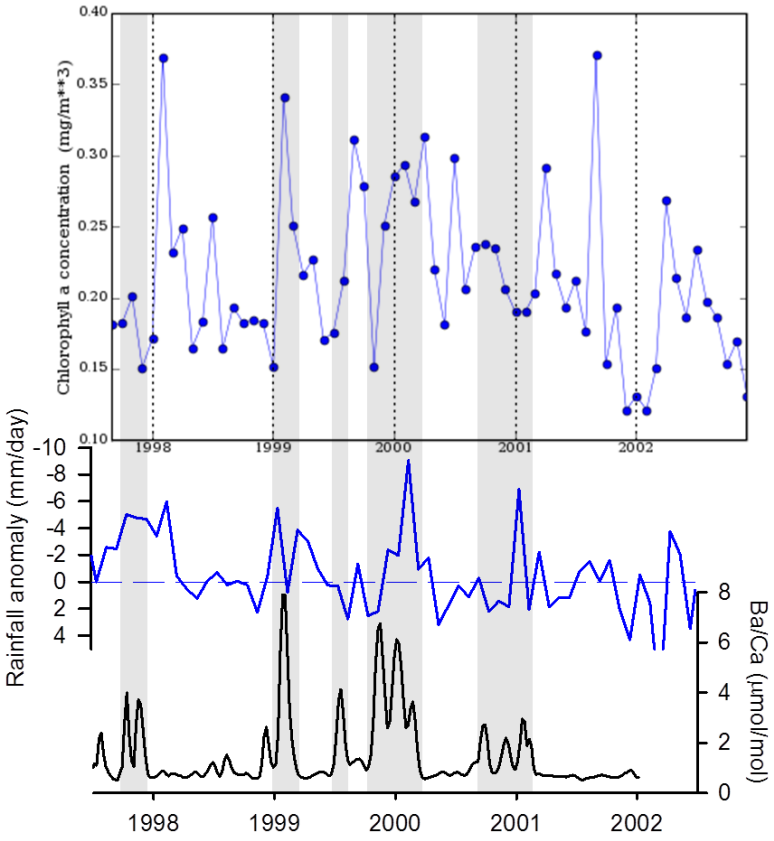

Figure 5.20 Top panel: Chlorophyll a time series for 147°E, 5-6°S (produced with the Giovanni online data system, developed and maintained by the NASA GES DISC).
Middle panel: rainfall anomaly (mm/day, blue line). Dashed line represents rainfall anomaly of 0. Precipitation data is blended gauge and satellite data for 146.25°E 6.25°S (Adler et al., 2003, Huffman et al., 2009).
Bottom panel: MT7 Ba/Ca record. Shaded areas are peaks in Ba/Ca

Peaks in weekly-resolved Ba/Ca profiles may provide information on the frequency and timing of chlorophyll peaks, inferring productivity over the past 60 ka, and could possibly suggest whether the western Pacific experienced an El Niño or La Niña-like state during the early Holocene and MIS3.

5.6.1 Ba/Ca in Holocene *Tridacna gigas*

The three *T. gigas* all have similar Ba/Ca profiles, with a low background ratio of around 1-2 µmol/mol, punctuated by peaks which reach from 3-12 µmol/mol (Figure 5.21). The number of peaks in each record was calculated by counting those above a threshold individual to each shell (described in 5.3). T73 has a higher number of large peaks per year than T58 or T75, while T75 displays the largest peak value of over 10 µmol/mol.

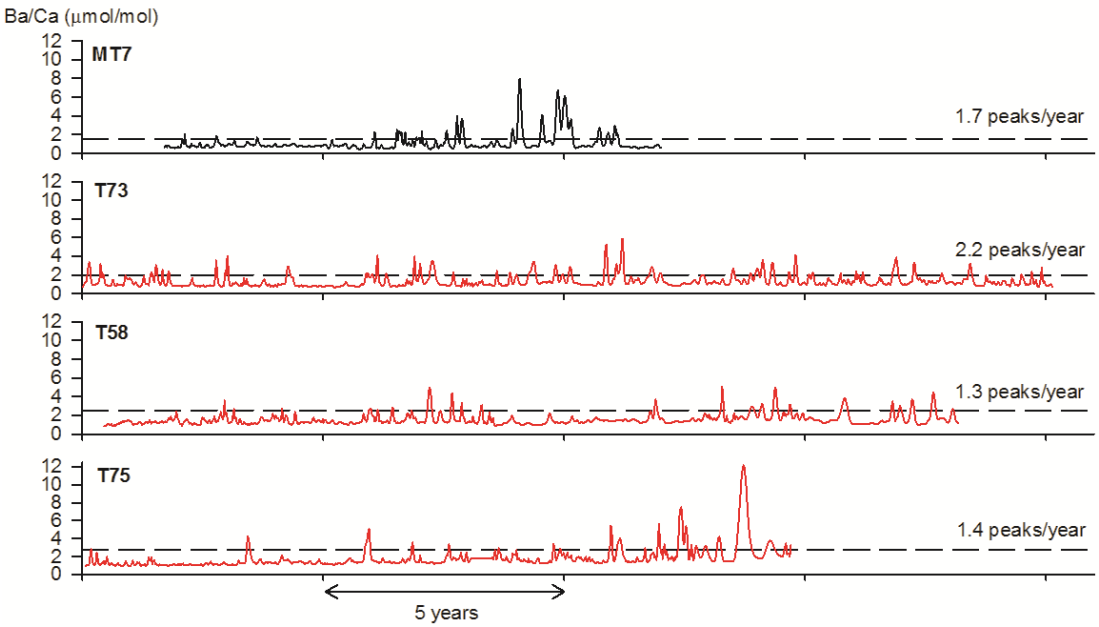

Figure 5.21 Ba/Ca profiles of modern and Holocene *T. gigas* shells. From top to bottom: MT7 (modern); T73 (7.26 ka BP); T58 (7.59 ka BP); T75 (8.76 ka BP). Dashed line shows the value of double the baseline for each shell, which is used as a threshold to classify large peaks in Ba/Ca. Resolution is at 52 samples/year

5.6.2 Ba/Ca in MIS3 *Tridacna* sp.

With the exception of T24, which has a record length of 3.5 years, all the MIS3 *Tridacna* sp. shells show a smaller number of large peaks per year compared to the modern and Holocene *T. gigas*. Peak sizes are also smaller than those recorded in Holocene shells, with the highest peaks of ~8 µmol/mol recorded in T28 (34.1 ka BP) and T18 (52.8 ka BP).

Reef IIa

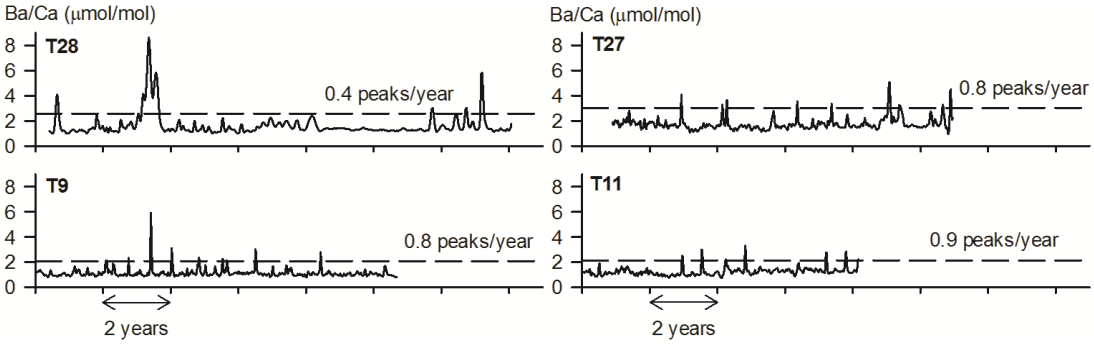

Reef IIIc (lower and upper)

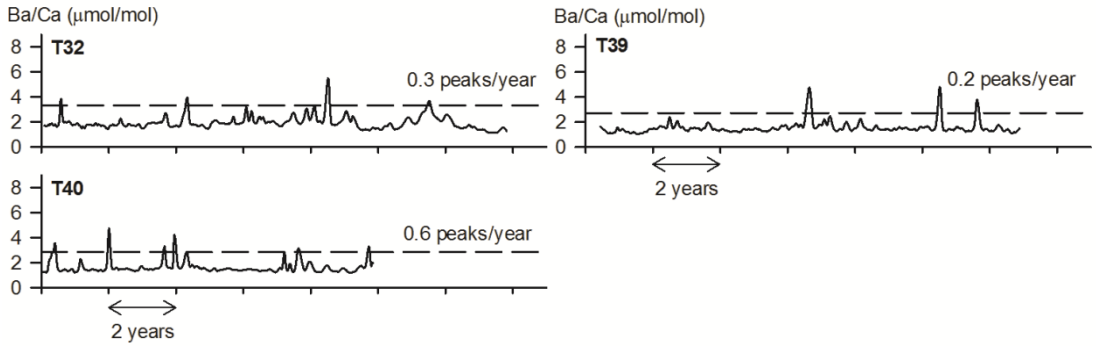

Reef IIIb

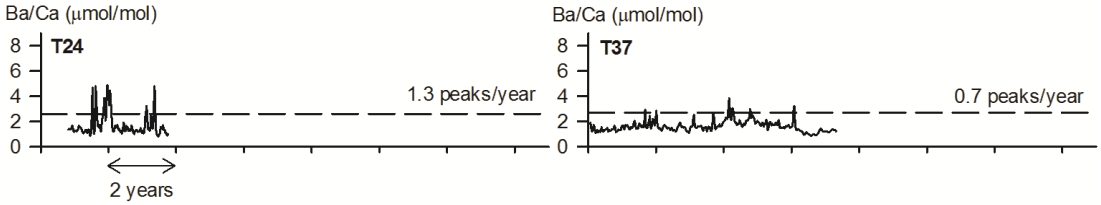

Reef IIIa (lower and middle)

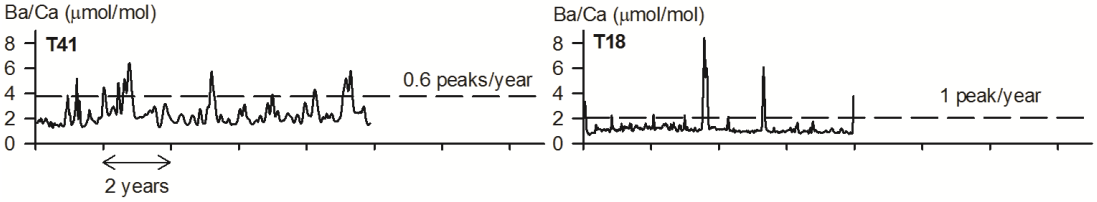

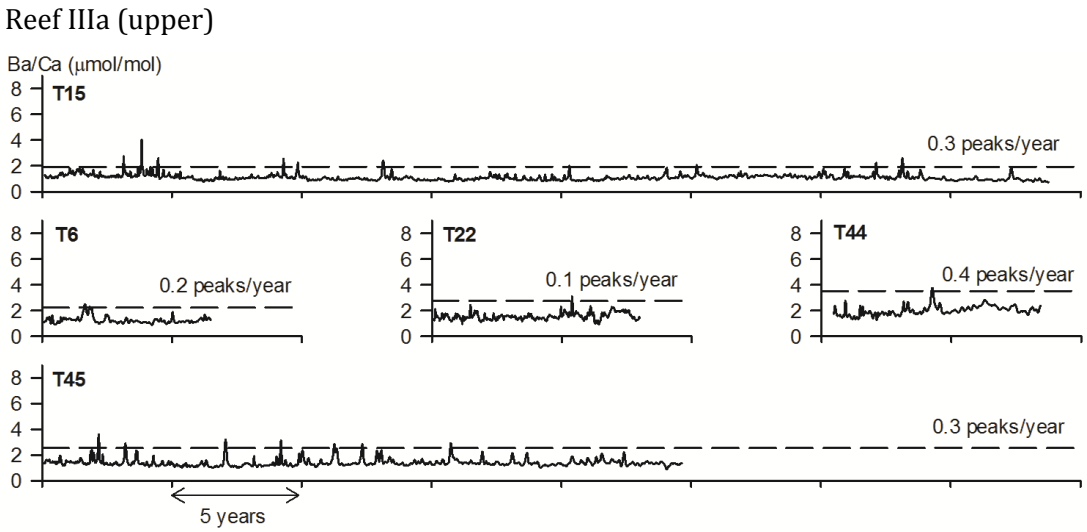

Figure 5.22 Ba/Ca profiles of MIS3 Tridacna sp. Resolution is at 52 samples/year

5.6.3 Ba/Ca over the past 60 ka

Frequency of Ba/Ca peaks

In the modern *T. gigas*, there are 1.7 peaks/year, some of which correspond to peaks in chlorophyll a data (Figure 5.20). In the Holocene *T. gigas*, the number of peaks/year is higher in T73, and lower in T58 and T75 (Figure 5.21). In the MIS3 samples, there are fewer peaks (Holocene = 1.6/year (n=3); MIS3 = 0.5/year (n=17) (Figure 5.22), and those that occur do not reach as high maxima as those in MT7 and the Holocene *T. gigas*. It appears that the frequency of Ba/Ca peaks was reduced during MIS3. To test this, the frequency of peaks was compared to the residual $\delta^{18}O$ (after removal of the ice volume component) (Figure 5.23). Although there is not a strong correlation (r^2=0.4) between the two, there is a trend showing a decreasing number of peaks/year as the $\delta^{18}O$ indicates cooler and/or drier temperatures during MIS3. This could suggest either a decrease in productivity during MIS3 or that other factors affected the uptake of Ba/Ca at this time.

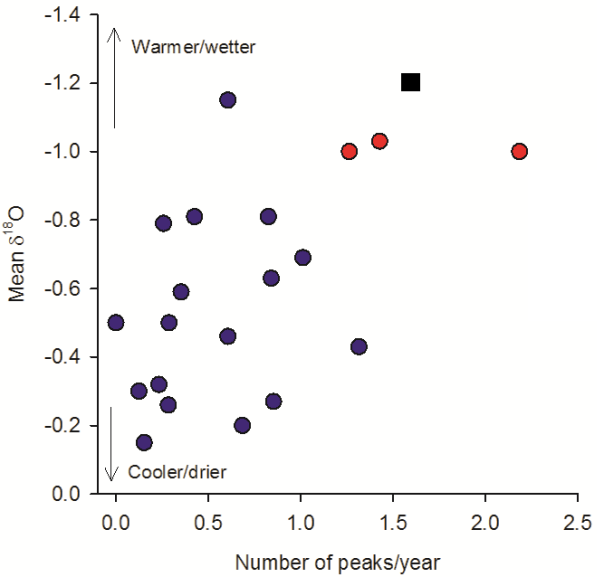

Figure 5.23 Comparison between the number of peaks in Ba/Ca/year and mean *Tridacna* sp. $\delta^{18}O$. Modern *T. gigas* is shown as a square, Holocene shells in red, and MIS3 in blue

Timing of Ba/Ca peaks

The timing of the occurrence of peaks in Ba/Ca can be compared between MT7 and the fossil shells (Figure 5.24). In the modern shell, most peaks occur during Austral spring and summer, and this is also seen in the Holocene shells and those from Reef IIIb. In the remainder of the glacial period, peaks are predominantly during autumn and winter (Reef IIa, Reef IIIa (u)) or they do not occur in a specific season (Reef IIIb, IIIa (lower and middle)). Coincidentally, at present the highest productivity occurs at this site during summer, which coincides with increased rainfall as the ITCZ shifts. Mixed layer depth follows the movement of the ITCZ seasonally (Sprintall and Tomczak, 1992), which also raises the amount of nutrients in surface waters. The data from glacial reefs may suggest higher productivity occurring in autumn/winter during these time periods. However, as the Ba/Ca profiles of MIS3 shells tend to be shorter (8-14 years compared to 14-20 years in Holocene shells) with fewer peaks, it is more likely that all peaks occur during one season.

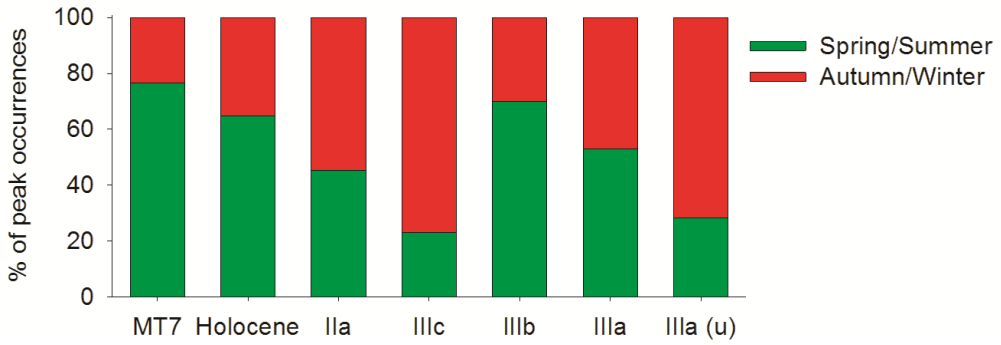

Figure 5.24 Timing of Ba/Ca peaks in modern, Holocene and MIS3 fossil shells, grouped by reef. Austral seasons are used

5.7 Conclusions

The use of trace element concentrations is an established method of reconstructing particular environmental variables in certain biogenic carbonates, such as foraminifera and corals. The relationship in bivalves appears to be less straightforward, and, as shown in this study, there seem to be a number of complications.

The trace element data from the modern and fossil *Tridacna* sp. from Papua New Guinea confirm previous studies using *Tridacna* sp. from other localities which suggest that Mg/Ca and Sr/Ca cannot yet be used to reconstruct SST as in corals and foraminifera. Published Sr/Ca-SST relationships appear to be site specific and cannot be applied to this data set. With additional studies, seasonal oscillations in Mg/Ca from the inner layer of *Tridacna* sp. might reveal changes in seasonality. Removing the biological trend from Mg/Ca time series results in a residual Mg/Ca profile which appears to correspond to SST, but this is only seen in the inner layer modern shell and requires additional calibration studies.

Ba/Ca peaks in modern *Tridacna* sp. seem to be related to chlorophyll a concentrations, suggesting that Ba/Ca could be a proxy for productivity during the past. As shown here, the frequency of peaks was reduced during MIS3, and it can be hypothesised that productivity was decreased during the glacial period. As yet it is not possible to quantify the relationship between Ba/Ca and productivity, and further work is needed with chlorophyll a records and modern *T. gigas* Ba/Ca profiles.

6. Reconstructing ENSO variability from *Tridacna* sp. $\delta^{18}O$ time series

Chapter Abstract

El Niño and La Niña events are typified by temperature and precipitation anomalies within a specified region of the tropical Pacific (described in Chapter 1). Characterising this mode of climate variability prior to the instrumental record relies on historical observations as well as proxy records, which provide reconstructions of sea surface temperature and precipitation, in the core regions affected by ENSO. These records may also contain seasonal and decadal variability which must first be removed in order to extract the portion of the record attributable to ENSO.

In this chapter, different methods ("metrics") for reconstructing overall ENSO variability using stable oxygen isotope ($\delta^{18}O$) time series of modern and fossil *Tridacna* sp. are discussed and compared. Changes in ENSO variability may reflect variations in event frequency, length or intensity. One of the most common methods for reconstructing ENSO variability in fossil coral records, a bandpass filter, cannot be used to draw statistically robust conclusions with records less than ~12 years in length due to the loss of data caused by the width of the filtering window. The average length of the records presented here are 10-15 years, therefore alternative methods are explored in order to examine possible changes in ENSO. The inter-annual anomaly $\delta^{18}O$ time series ($\delta^{18}O_A$) is one such method which can be used with shorter records at seasonal resolution. Although this method does not remove all non-ENSO variability, it produces similar results to a bandpass filter and to a qualitative method of counting El Niño and La Niña events above a threshold. Although this is a qualitative method, the number of El Niño and La Niña events exceeding a threshold was calculated in each fossil record in order to assess whether the quantitative metrics are capturing ENSO variability.

6.1 Introduction

Within the instrumental temperature record, El Niño and La Niña events can be seen when sea surface temperature (SST) anomalies exceed a threshold of ±0.5°C for 5 consecutive months within one of the ENSO index regions (Figure 6.1) (Trenberth, 1997). The frequency of ENSO events and the ratio of El Niño to La Niña events has not remained stable over time, with variability even during the 20th century (Chapter 2). The strength or amplitude of individual El Niño and La Niña events has also varied; with SST anomalies recorded ranging from ±0.5 to ±3°C during events over the last 30 years (Figure 6.1).

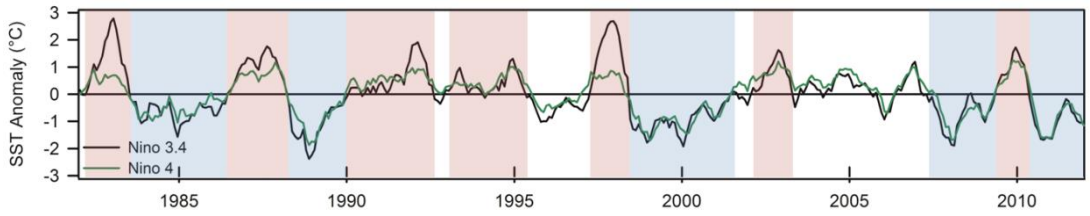

Figure 6.1 Above: Sea surface temperature anomaly in Niño 3.4 and Niño 4 regions of the Pacific (location map of index boxes in Chapter 1). Moderate and strong (exceeding ±1°C) El Niño (red) and La Niña (blue) events are highlighted

Modern ENSO events are well documented and associated with SST or SLP anomalies, but this information is not available for events pre-dating the instrumental record. In order to assess ENSO variance from a $\delta^{18}O$ time series, variability not attributable to ENSO, such as the seasonal cycle, must first be removed. There are several ways of assessing ENSO variance in proxy records. Filters which remove variability outside a specified band (e.g. bandpass filter (Tudhope et al., 2001)) or which are based on a particular length (e.g. Hanning filter (Corrège et al., 2000)) can be used, and these can also be used with lower resolution (seasonal) data. Removing the seasonal trend and examining the residual inter-annual anomalies can be used for higher resolution (e.g. monthly or bi-monthly) data (McGregor and Gagan, 2004). These anomalies can be used in combination with a specified threshold in order to count the number of El Niño or La Niña events occurring during a record (McGregor and Gagan, 2004).

The stable oxygen isotope ($\delta^{18}O$) profiles of *Tridacna* sp. capture changes in SST and local precipitation/evaporation (Aharon, 1991), which in turn are influenced by ENSO at the Huon Peninsula (Figure 6.2 shows the correlation between the Niño 3.4 Index,

Niño 4 Index and HadISST from 1980-present for the region around the Huon Peninsula). Previous studies have demonstrated that the $\delta^{18}O$ profile of modern *Tridacna* sp. from the Huon Peninsula can be used to examine changes in ENSO over time (Welsh et al., 2011).

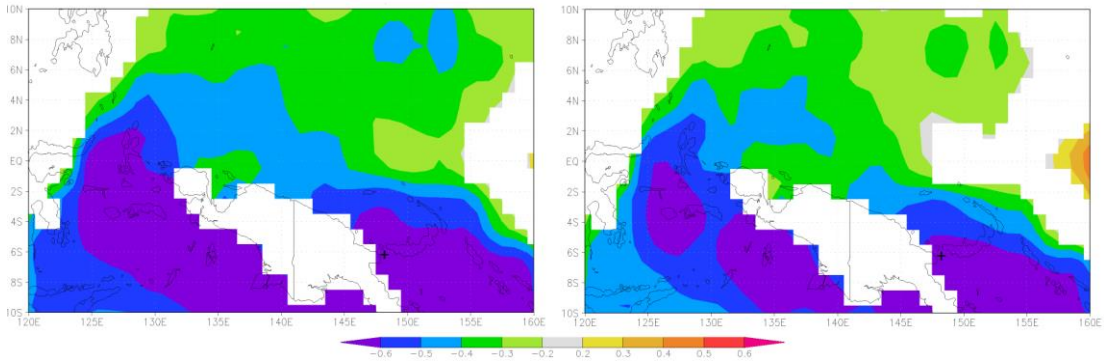

Figure 6.2 Correlation between October SST from HadISST and the Niño 3.4 Index (left) and Niño 4 Index (right) (1980-present) (http://climexp.knmi.nl/). Cross marks the location of the Huon Peninsula. October was chosen as this month has the highest correlation between SST and the two Niño indices. White areas show where data is missing

There are a number of methods which can be used to reconstruct ENSO variability in proxy records. These include:

- the number of El Niño events over a threshold (McGregor and Gagan, 2004);
- the standard deviation or variance of inter-annual variability (Tudhope et al., 2001); and
- the size of El Niño events, and the size of the largest El Niño event.

These three methods have been described and discussed in Brown et al. (2008b). In climate models, ENSO variability has also been estimated using the following methods, which resemble the approach used with proxy data:

- the number of events exceeding an anomaly threshold in one of the core Niño regions (Clement et al., 2000, Braconnot et al., 2012);
- the variance in the ENSO frequency band of the Niño 3.4 SST anomaly power spectrum (Liu et al., 2000);
- the standard deviation of monthly Niño 3 SST anomalies (Otto-Bliesner et al., 2003, Brown et al., 2008a, Zheng et al., 2008);
- the variance of bandpass filtered Niño 3 (Chiang et al., 2009); and
- the "strength" of El Niño (calculated by the number of El Niño events multiplied by the mean Niño 3.4 index) (Bush, 2007).

Comparison of model and fossil coral data with model output has shown that some of these methods have the potential to result in substantially different estimates of the reduction of Holocene El Niño event amplitude (Brown et al., 2008b). In order to extract ENSO variability in fossil *Tridacna* sp. $\delta^{18}O$ records several methods were compared: two filters; counting events over a threshold and calculating inter-annual anomalies ($\delta^{18}O_A$).

6.2 Methods

Seasonally resolved profiles of $\delta^{18}O$ were derived from 17 fossil *Tridacna* sp. shells (Chapter 3), with three dated to the early to mid-Holocene (8.73-7.26 ka BP) and 14 dated to Marine Isotope Stage 3 (MIS3) (60.7-34.1ka BP). $\delta^{18}O$ profiles were transformed from a distance scale to an annual scale based on the modern SST cycle for the Huon Peninsula, with $\delta^{18}O$ maxima (most positive value) being assigned an August date, and were corrected for a sea level effect (Chapter 4). $\delta^{18}O$ time series were interpolated to give 6 samples per year using Analyseries (Paillard et al., 1996). For methods involving the use of a filter, the interpolated time series were used, while calculating inter-annual anomalies required the removal of any possible ontogenetic or biological trends in the data. Several methods were tested, including subtracting the 48 month running average and a first (linear) and second-order polynomial fit, and all gave reasonably reproducible results (see Appendix). All $\delta^{18}O$ time series therefore had a linear trend removed prior to calculating the mean seasonal cycle and inter-annual anomalies.

Estimating 20th century "ENSO" variance using local SST

As there is only one modern *T. gigas* $\delta^{18}O$ record, which has a length of 16 years, and grew through a period of high ENSO variability, the 20th century SST observational record was used as an additional benchmark to compare with *Tridacna* sp. data. In order to use the SST record as a benchmark, the variance within this record had to be scaled to the *T. gigas* variance. The "ENSO" variance of the 20th century was calculated using HadISST (Rayner et al., 2003) for the Huon Peninsula (6.5°S, 147.5°E). The SST was treated in the same way as the *Tridacna* sp. $\delta^{18}O$ data, by removing a linear trend,

calculating mean monthly SST values and removing these from the detrended SST. Following this, several steps were taken, the results of which are shown in Table 6.1:

1. The standard deviation and variance of the residual SST was calculated for the entire 20th century
2. The standard deviation and variance was calculated for SST from 1986-2000
3. The standard deviation and variance of the residual *T. gigas* $\delta^{18}O$ was calculated from 1986-2000
4. The SST standard deviation and variance was scaled to the *T. gigas* standard deviation and variance

The resultant variance can therefore be thought of as the inferred theoretical variance of 20th century $\delta^{18}O$. This is a necessary step as the variance of both SST and $\delta^{18}O$ for 1986-2000 is unusually high (Table 6.1). The 20th century variance will be used in the discussion, Section 6.5.

Table 6.1 Calculations of SST variance for the 20th century from the Huon Peninsula

Variable	Time period	Step	Variance
SST	1900-2000	1	0.146
SST	1986-2000	2	0.221
Tridacna $\delta^{18}O$	1986-2000	3	0.055
Inferred $\delta^{18}O$	1900-2000	4	0.0365

6.3 Methods for reconstructing ENSO variance in proxy climate records

6.3.1 Quantitative methods of calculating inter-annual variability

Bandpass filter

ENSO has a variable period ranging from approximately 2.5-7 years, but tends to be focused on the 3-5 year band (Philander, 1990, Tudhope et al., 2001). A Gaussian bandpass filter can be used to reject frequencies outside a specified band (e.g. 2.5-7 years in the case of ENSO), resulting in a smoothed time series and the removal of variability outside this band. As this includes variability on ENSO timescales, the filtered record can be assumed to contain ENSO variability. Bandpass filters have been used with both modern (Kilbourne et al., 2004) and fossil coral data (Figure 6.3) to characterise ENSO variability during the Holocene and at intervals over the past

130,000 years (Tudhope et al., 2001, McGregor and Gagan, 2004, Duprey et al., 2012, Cobb et al., 2013, McGregor et al., 2013).

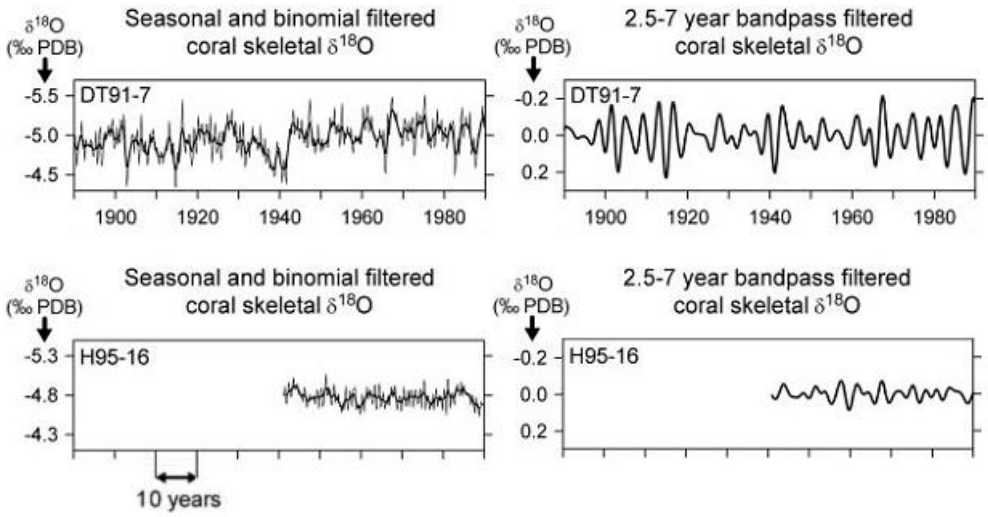

Figure 6.3 Top: Modern coral skeletal $\delta^{18}O$ time series (left) and bandpass filtered $\delta^{18}O$ time series (right);
Below: Mid-Holocene coral skeletal $\delta^{18}O$ time series (left) and bandpass filtered $\delta^{18}O$ time series (right) from Tudhope et al. (2001)

Here a 2.5-7 year bandpass filter (based on Tudhope et al. (2001) and Brown et al. (2008b)) was applied to the bi-monthly resolved $\delta^{18}O$ data. As the filter removes all variability not in the specified band, the $\delta^{18}O$ data requires no other treatment (so any seasonal or ontological trends can be left in the time series). The standard deviation and variance of the bandpass filtered $\delta^{18}O$ can be compared between the modern *T. gigas* shell and the fossil *Tridacna* sp. shells. Tudhope et al. (2001) explored a variety of filter widths (e.g. 2-8 years, 2.5-5 years), and found that their conclusions were not sensitive to the precise definition of ENSO bandwidth.

When using a bandpass filter, the raw $\delta^{18}O$ data is used. However, due to the length of the records, using a filter which loses a minimum of 4 years of data is not appropriate as it is impossible to assess ENSO variability which occurs on a timescale of 2-7 years in a bandpass filtered record which is only 3 or 4 years. Studies which use a bandpass filter tend to focus on coral records which can be decades-centuries long, and at lower resolution (e.g. seasonal), and are therefore able to lose data without drastically influencing the results.

Stable isotope ($\delta^{18}O$) anomaly

The $\delta^{18}O$ anomaly time series ($\delta^{18}O_A$) has been used with coral data, calculated as anomalies relative to a 10-year running mean (e.g McGregor and Gagan (2004), Figure 6.4).

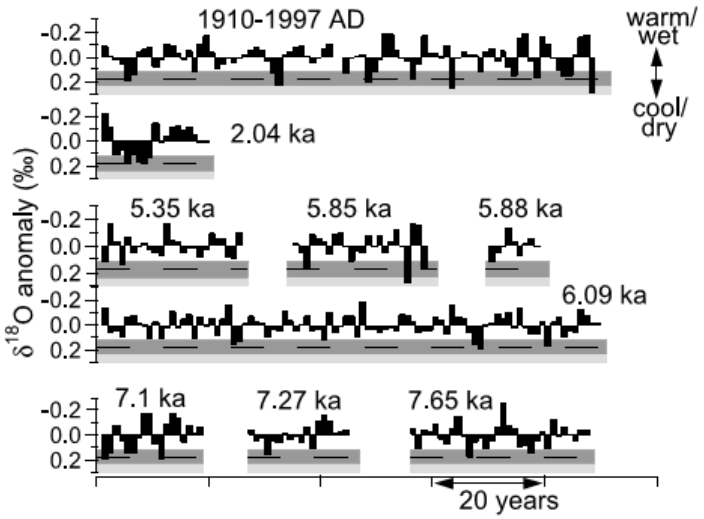

Figure 6.4 Comparison of inter-annual variability in modern and fossil annual coral $\delta^{18}O$ anomalies. Anomalies calculated relative to a 10-year running mean, or in records <20 years, relative to the mean $\delta^{18}O$ value. Dashed lines indicate the average $\delta^{18}O$ anomaly recorded by a modern coral for El Niño events from 1950 to 1997. Anomalies extending in to the dark grey box indicate moderate El Niño; those in the light grey box show strong-very strong El Niños (McGregor and Gagan, 2004)

For the *Tridacna* sp. shells, this method involved removing the mean seasonal cycle, rather than the 10-year running mean, and assuming that the residual $\delta^{18}O$ reflects inter-annual variability attributable to ENSO. After each $\delta^{18}O$ time series was interpolated to give a regular number of samples per year (Chapter 3), a linear fit was calculated and then subtracted from the $\delta^{18}O$ time series, in order to remove any potential trends in the data (Figure 6.5a). The seasonal cycle was calculated by averaging bi-monthly $\delta^{18}O$ values over the entire lifespan of each shell (Figure 6.5b), and was then subtracted from the detrended time series. Once the seasonal cycle is removed, the residual $\delta^{18}O$ (Figure 6.5c) should reflect inter-annual variability (i.e. ENSO), low-frequency variability (i.e. decadal trends), and high frequency variability (i.e. noise) in the record.

When using $\delta^{18}O_A$, the data must have any ontological and seasonal trends removed prior to calculating the residual $\delta^{18}O$. In order to remove potential trends in the

Tridacna sp. data set, a first-order polynomial trend (linear) was fitted to the data and then subtracted. The seasonal cycle was then removed by calculating bi-monthly $\delta^{18}O$ values and subtracting them from the detrended time series.

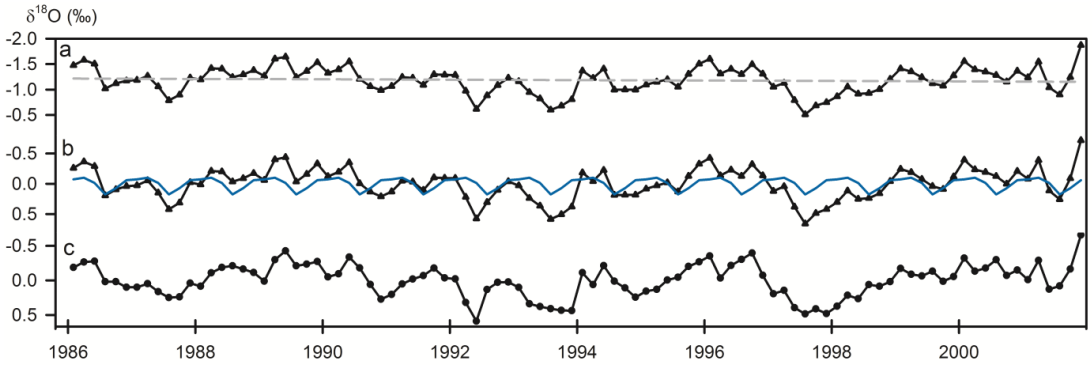

Figure 6.5 Method for calculating the $\delta^{18}O_A$ time series.
a: "raw" $\delta^{18}O$ data interpolated to 6 samples/year. Dashed line shows the linear regression.
b: "detrended" $\delta^{18}O$ time series with the linear regression subtracted from the raw $\delta^{18}O$ data (black line); mean bi-monthly $\delta^{18}O$ values, calculated from entire record (blue line).
c: residual $\delta^{18}O$ ($\delta^{18}O_A$) with the mean bi-monthly $\delta^{18}O$ values subtracted from the detrended $\delta^{18}O$ data. Y axis is inverted

Hanning filter

There are additional methods which can be used to reconstruct ENSO variability in fossil records. Smoothing the data with a 12 or 24 month running average can remove noise but may not necessarily assist with the identification of ENSO events. A Hanning filter (Blackman and Tukey, 1958) is a discrete window function, and is similar to a Gaussian bandpass filter in that it removes low and high frequency variability. Corrège et al. (2000) used a 25-month Hanning filter with fossil coral Sr/Ca data (Figure 6.6) in order to eliminate noise and highlight inter-annual variability.

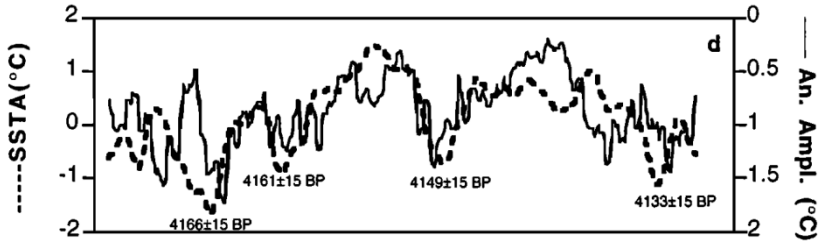

Figure 6.6 Monthly SST anomaly (solid line) calculated from fossil coral Sr/Ca and filtered with a 25 month Hanning filter; 24 month running annual amplitude (dashed line) (Corrège et al., 2000)

Although this method removes high and low frequency variability, the fact that it is centred on one point may mean that ENSO events at higher or lower frequencies are ignored.

6.3.2 Comparison of methods in modern records

The modern coral and *T. gigas* profiles record discrete windows within the past 40 years (Figure 6.7), for which the timing of ENSO events is known. This means that it is possible to tell whether events are captured by the profiles and ENSO extraction methods or "ENSO metrics". All three methods capture ENSO events as positive or negative excursions (Figure 6.7). The bandpass filtered SST record shows that the strength of ENSO variability has not remained constant during the 20th century (e.g. Allan, 2000, Fedorov and Philander, 2000, Tudhope et al., 2001, Juillet-Leclerc et al., 2006, Gergis and Fowler, 2009). Some periods such as 1950-55 and 1970-80 have lower variability of the bandpass filtered record than 1985-2000 (Figure 6.7). The $\delta^{18}O_A$ profile appears "noisy" in all three modern records, due to the fact that only the seasonal cycle is removed, leaving behind background noise (i.e. local climate variability, or longer scale climate variability), but ENSO events can be seen. ENSO events such as the 1986/87 and 1991-1995 El Niño and the 1988/89 La Niña are captured in all three records (Figure 6.7).

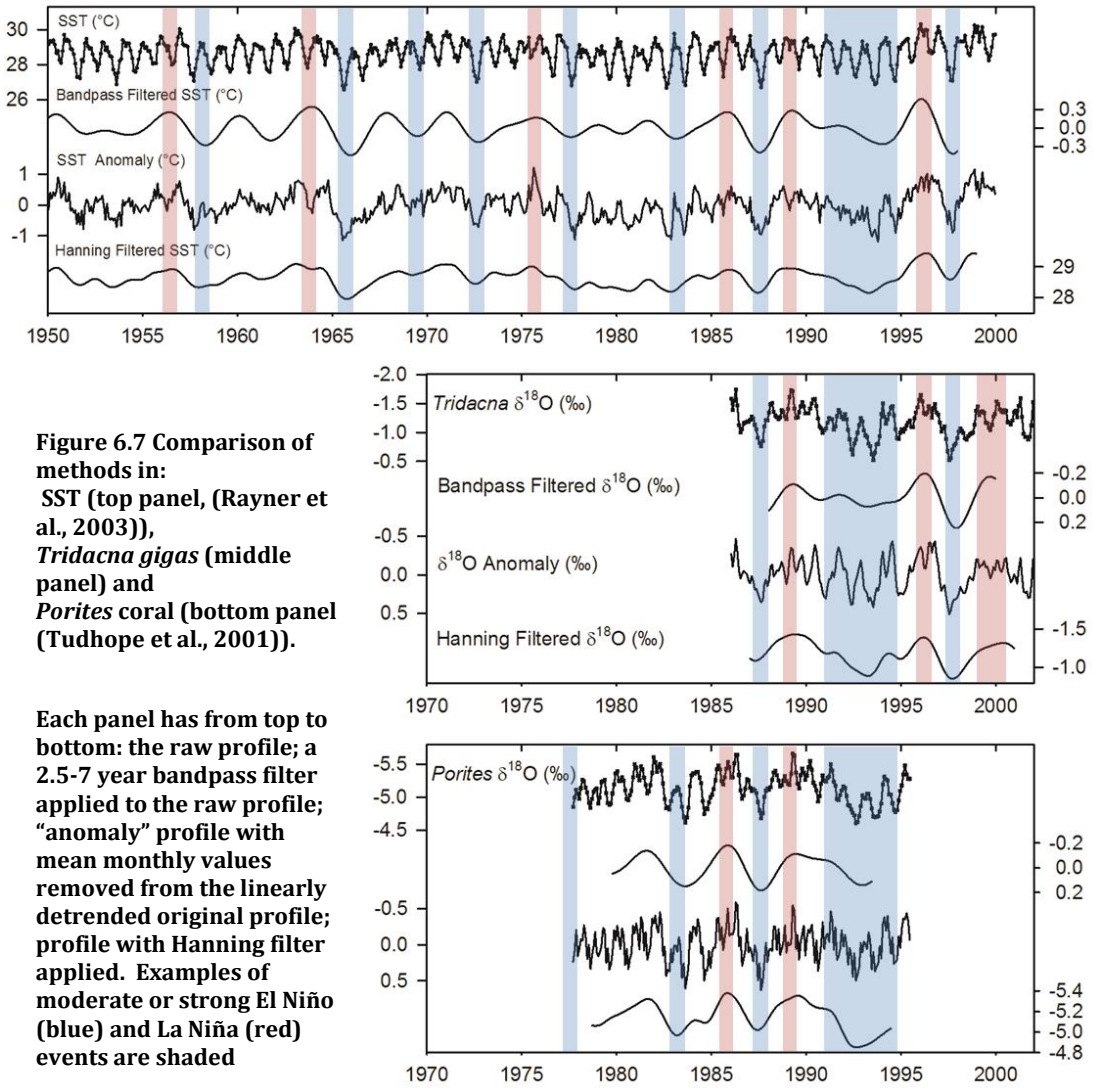

Figure 6.7 Comparison of methods in:
SST (top panel, (Rayner et al., 2003)),
***Tridacna gigas* (middle panel) and**
***Porites* coral (bottom panel (Tudhope et al., 2001)).**

Each panel has from top to bottom: the raw profile; a 2.5-7 year bandpass filter applied to the raw profile; "anomaly" profile with mean monthly values removed from the linearly detrended original profile; profile with Hanning filter applied. Examples of moderate or strong El Niño (blue) and La Niña (red) events are shaded

6.3.3 Calculating events using a threshold

An alternative method for looking at ENSO in modern and fossil time series is to count the number of events characterised by anomalies exceeding a specified threshold. McGregor and Gagan (2004) used this to examine the amplitude and frequency of El Niño events in mid-Holocene corals from the Muschu Islands, Papua New Guinea. The threshold for defining El Niño events in coral $\delta^{18}O$ was calculated based on the average modern El Niño $\delta^{18}O$ anomaly in a Muschu Island coral for 1950-1997, and was found to be an anomaly of +0.12‰. A coral from Madang, Papua New Guinea (Tudhope et al., 2001), required a threshold of +0.14‰ in order to produce the same number of

events/century as the Muschu Island corals (Brown et al., 2008b), suggesting the threshold for the same time period is dependent on region.

The aim of a threshold calibrated with the modern *T. gigas* was to capture accurately all of the El Niño and La Niña events between 1986 and 2002. Following the same strategy as McGregor and Gagan (2004), for the time period covered by MT7, the $\delta^{18}O$ anomaly recorded during El Niño events is 0.23±0.08‰ (1σ). The El Niño threshold, following the calculation of McGregor and Gagan (2004) is 0.15‰ (0.23‰-1σ), or 0.31‰ (+1σ) for strong events. The La Niña anomaly in the modern shell is -0.18±0.03‰ (1σ), which results in a threshold of -0.15‰ or -0.21‰ for strong events (Figure 6.8). The discrepancy between the threshold for strong El Niño and La Niña events is due to the fact that the amplitude of La Niña events recorded in *Tridacna* $\delta^{18}O$ is similar, while El Niño events display greater differences. The 1986-87 El Niño records small anomalies, while the 1997-98 El Niño, which was particularly strong, is recorded by $\delta^{18}O_A$ values between 0.3 and 0.52‰.

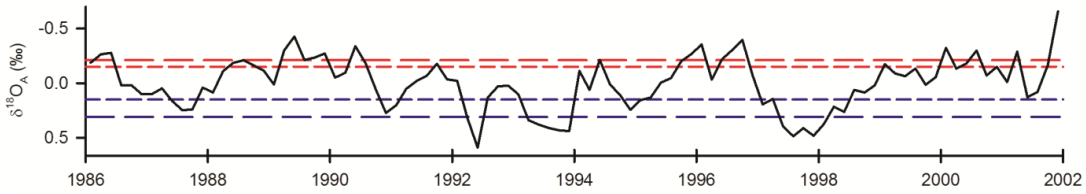

Figure 6.8 MT7 $\delta^{18}O$ anomaly record with El Niño (blue) and La Niña (red) thresholds marked. Short dashed line represents the "normal" threshold for an event, long dashed line represents a strong El Niño or La Niña

6.4 Results: Reconstructing ENSO in modern and fossil *Tridacna* sp.

In the following section a 2.5-7 year bandpass filter, $\delta^{18}O_A$ and the number of events in the modern and fossil *Tridacna* sp. are compared. In shell profiles which are less than 10 years in length, the number of events/10 years is given with the caveat that this number has been extrapolated.

6.4.1 Results from the modern *Tridacna gigas*

The modern *T. gigas* (MT7) $\delta^{18}O$ profile spans 1986 to 2002 (Figure 6.9), and can therefore be compared to instrumental SST and precipitation records for the Huon

Peninsula, as well as indices of ENSO variability such as Niño 3.4 and Niño 4 (e.g. Welsh et al., 2011). From the instrumental record we know that three El Niño and three La Niña events occurred during the growth of MT7, of differing lengths and amplitudes. This period experienced higher ENSO variability than other periods of the 20th century (Figure 6.10). The variance of the anomaly and the bandpass filtered time series therefore represent a time period of abnormally high (for the 20th century) ENSO variability which needs to be kept in mind when comparing modern with fossil *Tridacna* sp. The raw $\delta^{18}O$ data from MT7 can be compared to the Niño 4 index, which represents SST anomalies in the western Pacific (location map in Chapter 1), and which is negatively correlated with the HadISST record around the Huon Peninsula (Figure 6.2).

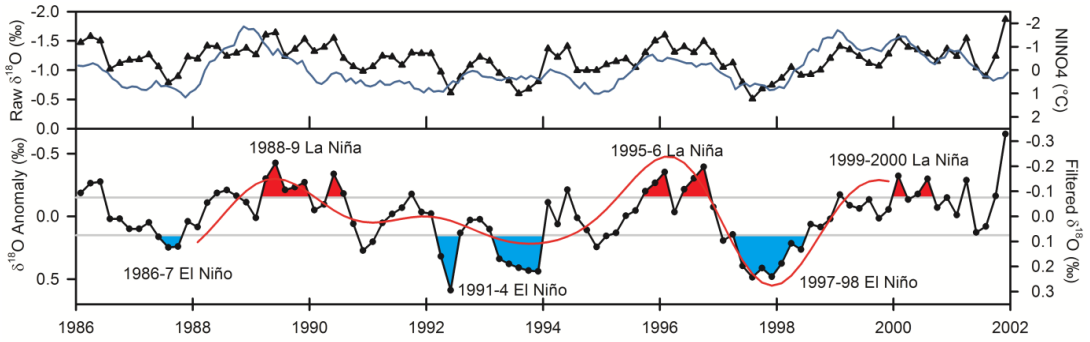

Figure 6.9 Results from MT7. Raw $\delta^{18}O$ interpolated to 6 samples per year (top, triangles), Niño 4 index (blue, top right axis), MT7 $\delta^{18}O_A$ time series (bottom, circles), bandpass filtered $\delta^{18}O$ (bottom, red). Grey lines represent threshold of ±0.15‰ of the anomaly time series, filled areas show El Niño (which involves cool and dry conditions) and La Niña (which involves warm and wet conditions at the Huon Peninsula)

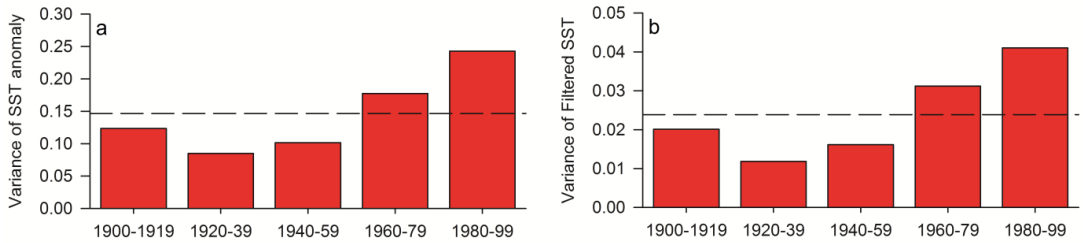

Figure 6.10 Inter-annual variance of HadISST for 147.5°E, 6.5°S (Rayner et al., 2003) for 20 year windows of the 20th century. Dashed line represents the variance of the entire 20th century. Calculated using a: inter-annual anomalies and b: 2.5-7 year bandpass filtered SST

Both the $\delta^{18}O_A$ and the bandpass filtered $\delta^{18}O$ time series show excursions during ENSO events (Figure 6.9). During an El Niño, cool and dry conditions around Papua New Guinea result in a shift towards more positive $\delta^{18}O$ values, while during a La Niña,

warm and wet conditions result in a shift towards more negative $\delta^{18}O$ values. If the threshold of ±0.15‰ (Figure 6.9) is exceeded for six consecutive months, three El Niño and three La Niña events are recorded. The bandpass filtered $\delta^{18}O$ does not capture one El Niño (1986/87) and one La Niña (1999/2000) due to the width of the filtering window.

6.4.2 Reconstructing ENSO variability in Holocene *Tridacna gigas*

$\delta^{18}O$ derived from three fossil *T. gigas* from the early Holocene have record lengths of between 12 and 20 years. The variance of each anomaly time series is similar to the number of events exceeding a threshold of ±0.15‰ when normalised to the modern shell (in T58, $\delta^{18}O_A$ normalised to MT7 is 0.42, the number of events/10 years normalised to MT7 is 0.44) (Table 6.2). This suggests that using the anomaly time series to reconstruct ENSO variability gives a reliable estimate of actual ENSO events as captured by changes in the $\delta^{18}O$ time series. The bandpass filter produces the lowest variance in T73 and T58, but the highest variance in T75. This discrepancy is to be expected as this method loses two years at either end of the time series due to the width of the filtering window, making each record 4 years shorter than the anomaly time series. The $\delta^{18}O_A$ time series and bandpass filtered time series are shown in Figure 6.11 for the three Holocene shells. All three shells show a smaller range in $\delta^{18}O$ values than the modern *T. gigas*, with flatter bandpass filtered $\delta^{18}O$ profiles and an apparent reduction in the number of ENSO events (Driscoll et al., 2014).

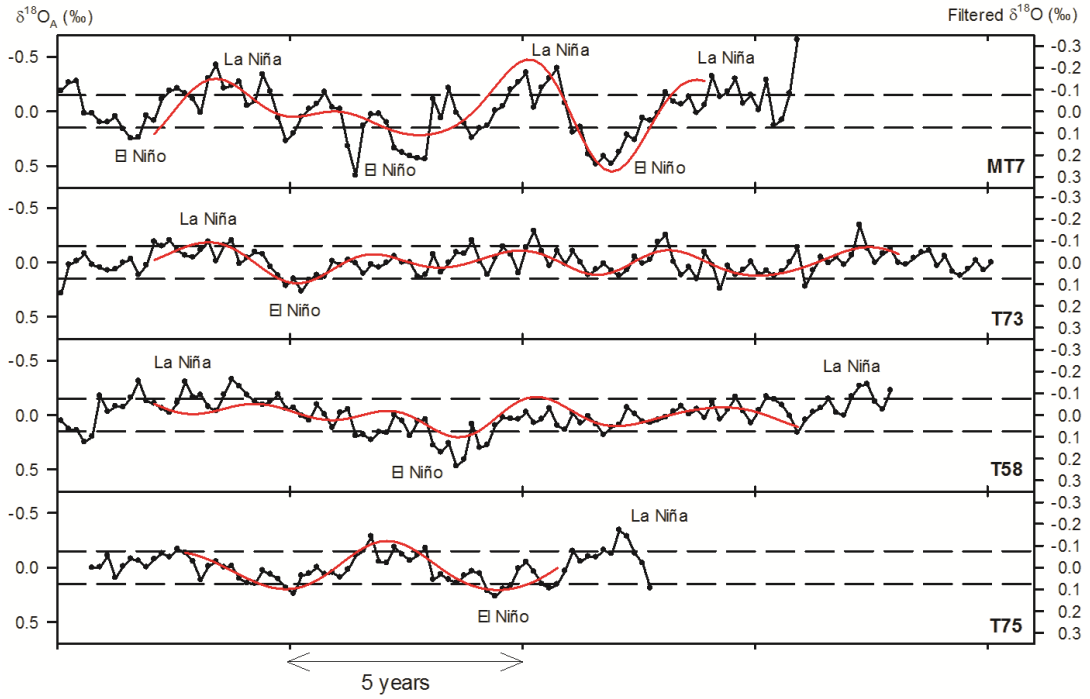

Figure 6.11 Results from MT7 (modern; top panel); T73 (7.26 ka BP; second panel); T58 (7.59 ka BP; third panel) and T75 (8.73 ka BP; bottom panel). Shown are the $\delta^{18}O_A$ and bandpass filtered $\delta^{18}O$ (red line). $\Delta^{18}O_A$ has a linear trend and mean bi-monthly $\delta^{18}O$ values removed from the raw profile. The resolution is at 6 samples/year. Dashed lines show the ±0.15‰ threshold for El Niño and La Niña events

The bandpass filtered $\delta^{18}O$ time series of T73 is less variable than that of MT7. This apparent reduction in variance is also shown in the earlier Holocene shells, with all three demonstrating a reduction in El Niño and La Niña/10 years. In T73, the two ENSO-type events seen in the anomaly time series as exceeding the specified threshold are also seen as excursions exceeding ±0.1‰ in the bandpass filtered $\delta^{18}O$ profile.

There is a trend in the $\delta^{18}O$ profile of T58 between the first and fifth years of growth, which is potentially growth related (see Appendix for individual profiles). The negative excursions in the anomaly time series do not coincide with those in the bandpass filtered $\delta^{18}O$ record as in T73 and MT7, which suggests that these may not be due to ENSO-type climate variability. The positive excursion in the $\delta^{18}O_A$ profile (marked by "El Niño" in Figure 6.11) coincides with an excursion in the bandpass filtered $\delta^{18}O$.

All three Holocene shells exhibit excursions in the $\delta^{18}O_A$ and bandpass filtered $\delta^{18}O$ time series which may be a result of ENSO activity during the period of growth. The variance of the anomaly time series gives a similar result to that produced when using a

threshold to count ENSO events during the lifetime of the shell (Table 6.2). Whichever method is used to reconstruct ENSO variability, a significant increase is seen in the late 20th century compared to the early Holocene. The bandpass filter produces the lowest estimate of variance in T73 and T58, while the $\delta^{18}O_A$ method produces a lower estimate in T75 (Table 6.2).

Table 6.2 Results of ENSO reconstruction methods in Holocene *T. gigas* shells. The variance of bandpass filtered $\delta^{18}O$ and $\delta^{18}O_A$ are normalised to that of MT7, and the number of events/10 years is normalised to that of MT7

Shell	Age (ka BP)	Length (years)	$\delta^{18}O_A$		Bandpass Filter		Threshold	
			Variance	Variance Index	Variance	Variance Index	ENSO/10 years	Normalised to MT7
MT7	0	16	0.055	1	0.015	1	3.75	1
T73	7.26	20	0.012	0.22	0.0023	0.15	1	0.267
T58	7.59	18	0.023	0.42	0.0018	0.11	1.67	0.444
T75	8.73	12	0.017	0.30	0.0053	0.35	1.67	0.444

6.4.3 Reconstructing ENSO variability in MIS3 *Tridacna* sp.

There are 14 *Tridacna* sp. shells from MIS3 dated between 60.7 and 34.1 ka BP, with record lengths of between 5 and 38 years. Table 6.3 compares the variance of the two inter-annual variability calculation methods and the number of ENSO events/10 years above the specified threshold for these 14 shells and the modern *T. gigas*. Profiles from individual shells where ENSO-type events can be seen are shown in Figures 6.12 – 6.15.

Table 6.3 Results of ENSO reconstruction methods in MIS3 *Tridacna* sp. Description in Table 6.2

Shell	Age (ka BP)	Length (years)	$\delta^{18}O_A$		Bandpass Filter		Threshold	
			Variance	Variance Index	Variance	Variance Index	ENSO/10 years	Normalised to MT7
MT7	0	16	0.055	1	0.015	1	3.75	1
T28	34.1	12	0.025	0.45	0.0046	0.3	1.67	0.44
T27	35.4	8	0.0035	0.63	0.00036	0.02	2.5	0.67
T9	36.5	9	0.016	0.29	0.0024	0.15	0	0
T11	37.2	7	0.0081	0.15	0.00055	0.036	0	0
T32	38.6	14	0.022	0.39	0.0037	0.24	2.86	0.76
T39	40.8	13	0.055	0.99	0.016	1.03	3.85	1.02
T40	41.5	10	0.015	0.27	0.0020	0.13	2	0.53
T37	46	7	0.0093	0.17	0.0027	0.18	0	0
T41	50.7	9	0.041	0.74	0.0039	0.26	3.33	0.89
T18	52.8	7	0.018	0.32	0.003	0.19	1.33	0.36
T6	60.7	6	0.02	0.36	0.0039	0.25	0	0
T15	60	38	0.013	0.24	0.0025	0.16	0.526	0.14
T22	60	5	0.0025	0.45	0.0023	0.15	1	0.53
T45	60	18	0.039	0.71	0.0077	0.5	1.67	0.44

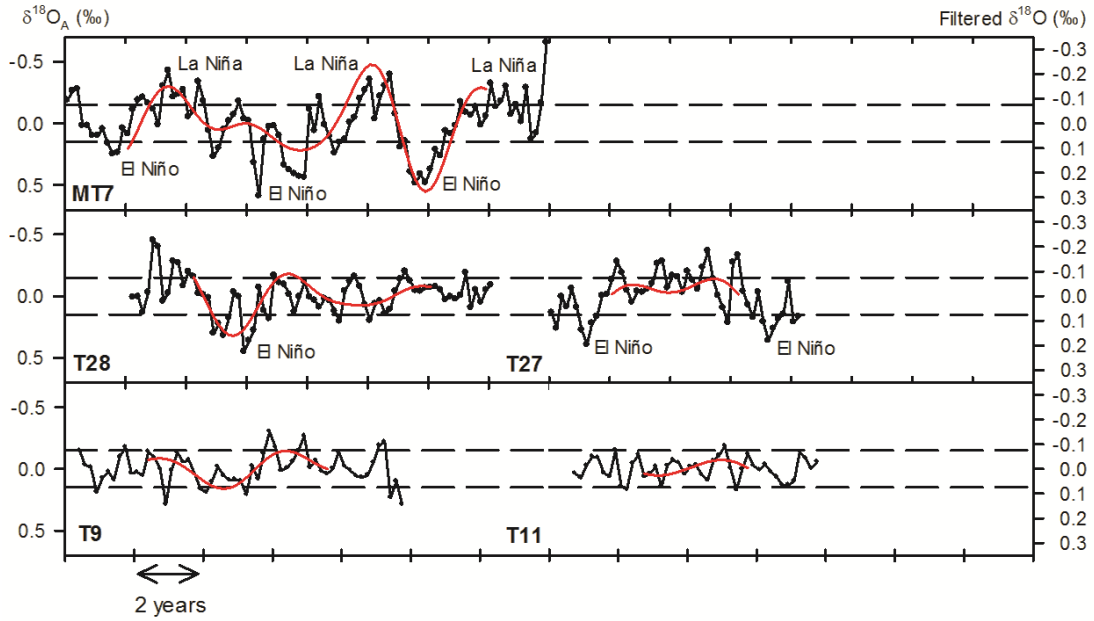

Figure 6.12 MT7 (modern; top panel); IIa Reef results: T28 (34.1 ka BP), T27 (35.4 ka BP), T9 (36.5 ka BP) and T11 (37.2 ka BP). Shown are $\delta^{18}O_A$ and bandpass filtered $\delta^{18}O$ (red line). $\delta^{18}O_A$ has a linear trend and mean bi-monthly $\delta^{18}O$ values removed from the raw profile. Resolution is at 6 samples/year. Dashed lines show the ±0.15‰ threshold for El Niño and La Niña events

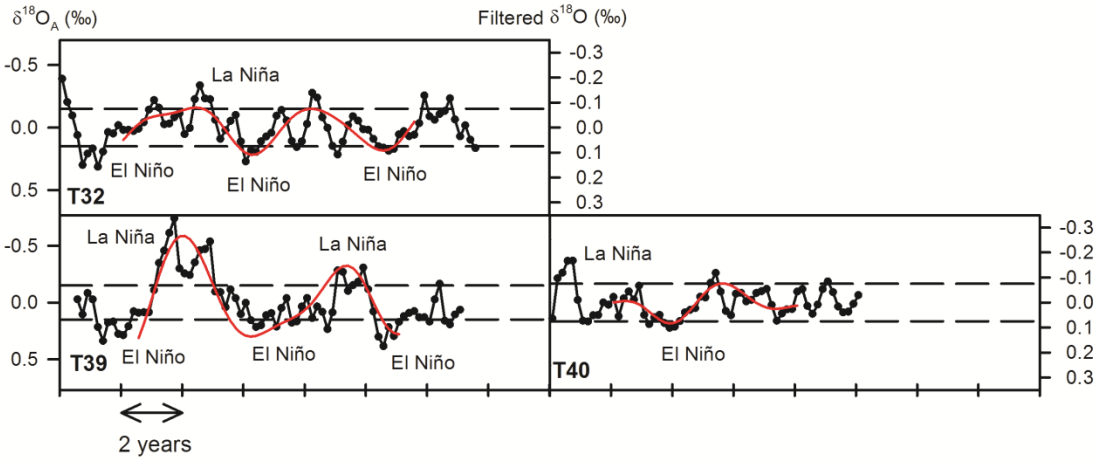

Figure 6.13 IIIc Reef results: T32 (38.6 ka BP); T39 (40.8 ka BP) and T40 (41.5 ka BP). Description the same as Figure 6.12

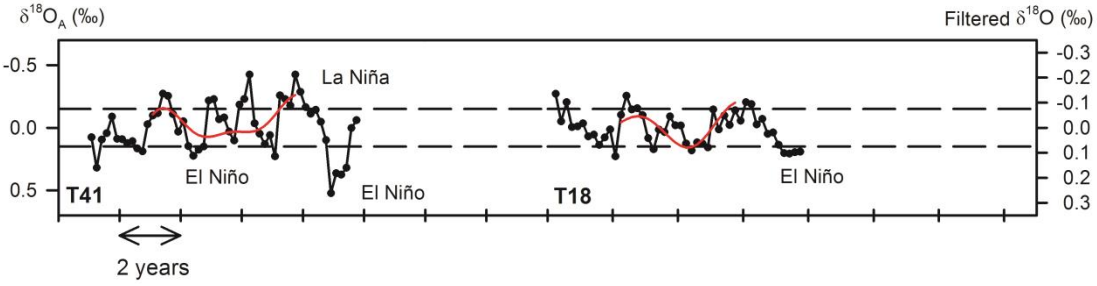

Figure 6.14 IIIa (l) and (m) results: T41 (50.7 ka BP, top panel) and T18 (52.8 ka BP, bottom panel). Description the same as Figure 6.12

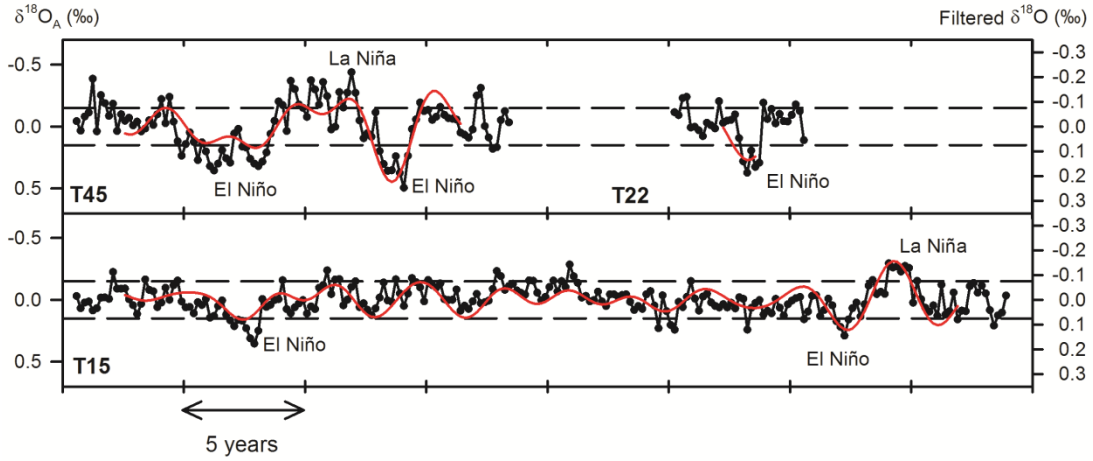

Figure 6.15 IIIa (u) results: T45 (60 ka BP, top left panel); T22 (60 ka BP, top right panel) and T15 (60 ka BP, bottom panel). Description the same as Figure 6.12

Observations from MIS3 Reef Terraces

Reef IIa (38-34 ka BP)

There are four *Tridacna* sp. shells from the IIa reef, dated between 37.2 and 34.1 ka BP, and with record lengths of 7 to 12 years. All four shells show reduced ENSO variance compared to the modern *T. gigas*. In two shells (T9 and T11), no ENSO events can be seen using the threshold of ±0.15‰.

The *Tridacna* sp. shells T28 and T27 (Figure 6.12) both have cool El Niño-like (positive) excursions exceeding the ±0.15‰ threshold, and the variance of the anomaly time series is similar to the number of events/10 years normalised to MT7. These excursions can be seen in both the anomaly and the bandpass filtered $\delta^{18}O$ time series in T28. The El Niño events in T27 occur at the start and end of the record, which is not covered by the bandpass filtered $\delta^{18}O$ time series due to the width of the filtering window.

The earlier two Reef IIa shells (T9 and T11, Figure 6.12) do not show any excursions exceeding the 0.15‰ threshold. They show a reduction in variance of 71% (T9) and 85% (T11) of $\delta^{18}O_A$, and 85% (T9) and 99% (T11) of the bandpass filtered $\delta^{18}O$ compared to the modern shell (Table 6.3). As no ENSO events are seen in the time series, this suggests that this variance is caused by variability not attributable to ENSO.

However, this also may be due to the fact that the threshold used here is based on ENSO events occurring in the late 20th century, which experienced both a high number of events and several particularly strong events.

Reef IIIc (42-38 ka BP)

There are three shells from the IIIc reef (lower and upper) dated between 41.5 and 38.6 ka BP, with record lengths of between 10 and 13 years. T39 (*T. maxima*, Figure 6.13) shows higher variance of the bandpass filtered $\delta^{18}O$, as well as ENSO event frequency and variance of $\delta^{18}O_A$ almost as high as today. This slight discrepancy may be due to the strength of the events seen in the anomaly time series. The other two shells from this reef show reduced variance and a lower number of anomalous events than the modern *T. gigas* (Figure 6.13).

Reef IIIb (46-44 ka BP)

Reef IIIb consists of two shells although, as one of these shells (T24) has a record length of only 3 years, it cannot be used to reconstruct ENSO which runs on a timescale of 2-7 years. T37, dated to ~46 ka BP, shows a reduction in variance of $\delta^{18}O_A$ of 83% and bandpass filtered $\delta^{18}O$ of 82%, and there are no excursions exceeding ±0.15‰.

Reef IIIa (lower and middle: 53-50 ka BP)

There are two shells from Reef IIIa (lower and middle) dated to between 52.8 and 50.7 ka BP. T41 (Figure 6.14) shows a 26% reduction in $\delta^{18}O_A$ variance and a 12% reduction in the number of ENSO events compared to the modern, which suggests more ENSO-type variability than many of the other fossil shells, while T18 shows a 68% reduction in $\delta^{18}O_A$ variance, a 81% reduction in bandpass filtered $\delta^{18}O$ variance and a 64% reduction in the number of events recorded.

Reef IIIa (upper: 62-60 ka BP)

$\delta^{18}O$ profiles were derived from 4 *Tridacna* sp. with two of the longest records (T15, 38 years and T45, 18 years) (Figure 6.15). These shells were collected from the IIIa (u)

reef which has been dated to 62-60 ka BP (Chapter 2). All samples show reduced variance and a reduced number of ENSO events/10 years compared to the modern shell. There is a slight inconsistency between the variance and number of events normalised to MT7 for the two methods involving the anomaly timescale. The two longer records show a reduction in variance of 76% (T15) and 29% (T45) using the $\delta^{18}O_A$ time series, while when counting ENSO events the reduction is increased to 86% (T15) and 56% (T45). If a lower threshold is used (e.g. ±0.12‰), counting ENSO events results in a reduction of 72% (T15) and 40% (T45).

6.5 Discussion

6.5.1 Comparison of ENSO metrics

The three methods: threshold analysis, bandpass filter and inter-annual anomaly ($\delta^{18}O_A$) variance have all been used to reconstruct ENSO variability in different climate proxy records (e.g. Tudhope et al., 2001, McGregor and Gagan, 2004, Cobb et al., 2013, LaVigne et al., 2013, McGregor et al., 2013). As demonstrated by using a threshold based on the modern *T. gigas*, warm and cool anomalies, representing La Niña and El Niño in the modern climate system, can be seen in the fossil shells, although these rarely have as large an amplitude as during the late 20th century. Using a threshold confirms that ENSO events are seen in the $\delta^{18}O_A$ time series, but due to the length of the records, these cannot always be quantified as the number of events per decade/century without extrapolating. While the threshold used is based on a time period which experienced abnormally frequent and strong ENSO events, it still helps to identify ENSO events, and gives weight to the fact that the variance of the two other metrics is actually capturing an aspect of ENSO variability.

In proxy climate data from corals, calculating the standard deviation or variance of the anomaly time series was found to provide a more robust measure of the full ENSO cycle than qualitative measures of El Niño amplitude or the number of events exceeding a threshold (Brown et al., 2008b). In the following sections the three methods for extracting ENSO variance will be compared for two distinct time periods – the early Holocene and MIS3. While ENSO reconstructions from climate archives (particularly

corals) tend to use one of the metrics described here, there are few cases of comparisons of these methods within the literature (e.g. Brown et al., 2008b, Russon et al., 2014).

6.5.2 Comparison of methods in Holocene *T. gigas* samples

The two methods of calculating variance (inter-annual anomalies and the bandpass filter) can be compared to the number of events/10 years, all normalised to that calculated for the modern *T. gigas*, MT7. The variance produced by inter-annual anomalies and counting the number of events tends to agree within each sample, suggesting that the $\delta^{18}O_A$ is capturing variability attributable to ENSO, which is consistent with the findings of Brown et al. (2008b). The variance of the bandpass filtered $\delta^{18}O$ is not in such close agreement as the filtered $\delta^{18}O$ profiles lose 4 years of data. In T73 and T75, the variance of the three methods is very similar, while in T58 there is a significant difference between the $\delta^{18}O_A$, the number of events per decade and the bandpass filtered $\delta^{18}O$ methods when all values are normalised to MT7 (Figure 6.16). Because of the trend during the juvenile portion of the T58 $\delta^{18}O$ profile, the mean bi-monthly $\delta^{18}O$ values may result in a larger range of $\delta^{18}O_A$ measurements. There is also a warm La Niña-type event at the end of the T58 record (Figure 6.11), and this would not be included in the bandpass filtered $\delta^{18}O$ record, which therefore results in higher $\delta^{18}O_A$ variance and more ENSO events. The bandpass filter removes all variability outside the ENSO band, and therefore is less "noisy" than the $\delta^{18}O_A$ record, and consequently tends to have lower variance. Calculating the standard deviation or variance of a bandpass filtered record is the most commonly used method of reconstructing ENSO variability in corals (e.g. Tudhope et al., 2001, Cobb et al., 2003, Cobb et al., 2013), but it appears that using the $\delta^{18}O_A$ record is more accurate at capturing ENSO with the shorter, higher resolution *Tridacna* sp. data presented here.

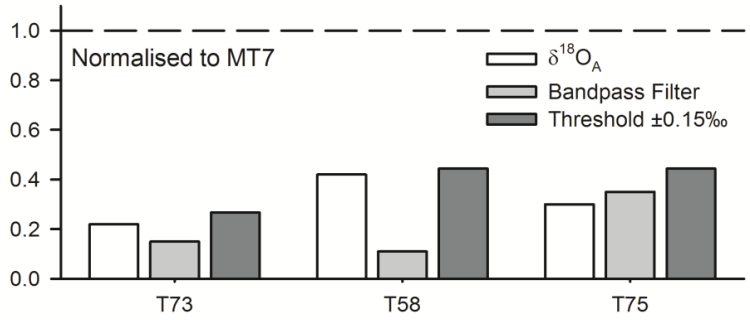

Figure 6.16 Variance of the two quantitative methods normalised to MT7, and the number of ENSO events per 10 years normalised to MT7 in three Holocene shells dated to 8.73 to 7.26 ka BP.

6.5.3 Comparison of methods in MIS3 fossil *Tridacna* sp.

There is more variation between the metrics used to reconstruct ENSO in the fossil data set from MIS3 (Figure 6.17), with four of the MIS3 records showing a large discrepancy between methods. In several of the fossil shells (T9, T11, T37 and T6), no ENSO events are recorded using the threshold of ±0.15‰ in $\delta^{18}O_A$ for 6 months, but the corresponding variance of $\delta^{18}O_A$ or bandpass filtered $\delta^{18}O$ can be between 1 and 35% of the modern shell. There are a number of explanations for this discrepancy. There may be ENSO events occurring which have a lower amplitude than the threshold used here. If a lower threshold of ±0.12‰ is used, El Niño and La Niña events can be seen in T37 and T9, while if a threshold of 0.1‰ is used, El Niño events occur in T11 and T6. These records are all between 6 and 9 years in length, so if ENSO was acting on a different timescale then the records might be too short to capture any events. The anomaly time series contains contamination from non-ENSO related variability (Russon et al., 2014), which cannot be removed without using a filter.

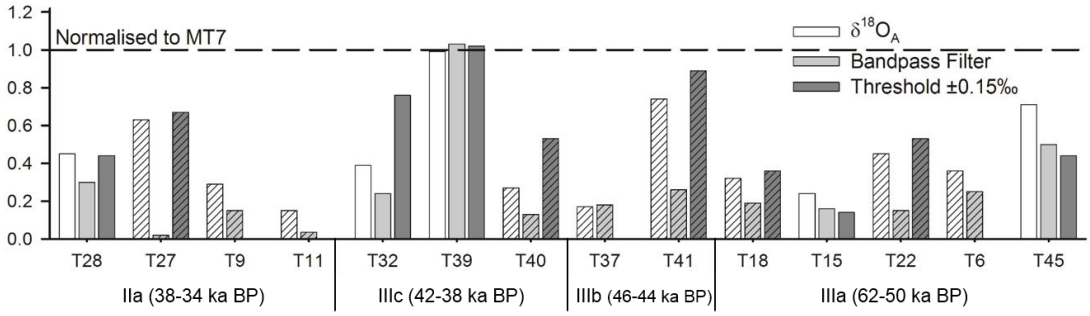

Figure 6.17 Variance of the two quantitative methods normalised to MT7, and the number of ENSO events per 10 years normalised to MT7 in 14 MIS3 shells. Records which are less than 10 years in length are shown by hatched bars, records over 10 years by solid bars

6.5.4 Frequency of El Niño and La Niña recorded by fossils

The number of El Niño and La Niña events exceeding a specified threshold recorded in fossil *Tridacna* sp. shells can be counted in order to calculate the number of events/decade, following the example of McGregor and Gagan (2004). Results from fossil shells can then be compared to the modern *T. gigas* $\delta^{18}O$ record. The number of events recorded in the $\delta^{18}O$ time series is sensitive to the threshold selected (Figure 6.18) (Brown et al., 2008b), which is dependent on the time period used for calibration. Studies have shown that the amplitude of ENSO events was reduced during the Holocene (McGregor and Gagan, 2004), and using an absolute threshold based on modern ENSO may therefore result in fewer events being identified in fossil records (Brown et al., 2008b). While a lower threshold may help with identifying more ENSO events in the past, it may also capture non-ENSO related variability. If, for example, a threshold of ±0.1‰ is used with the modern *T. gigas*, the $\delta^{18}O$ profile would suggest an additional El Niño and La Niña not recorded in the instrumental record.

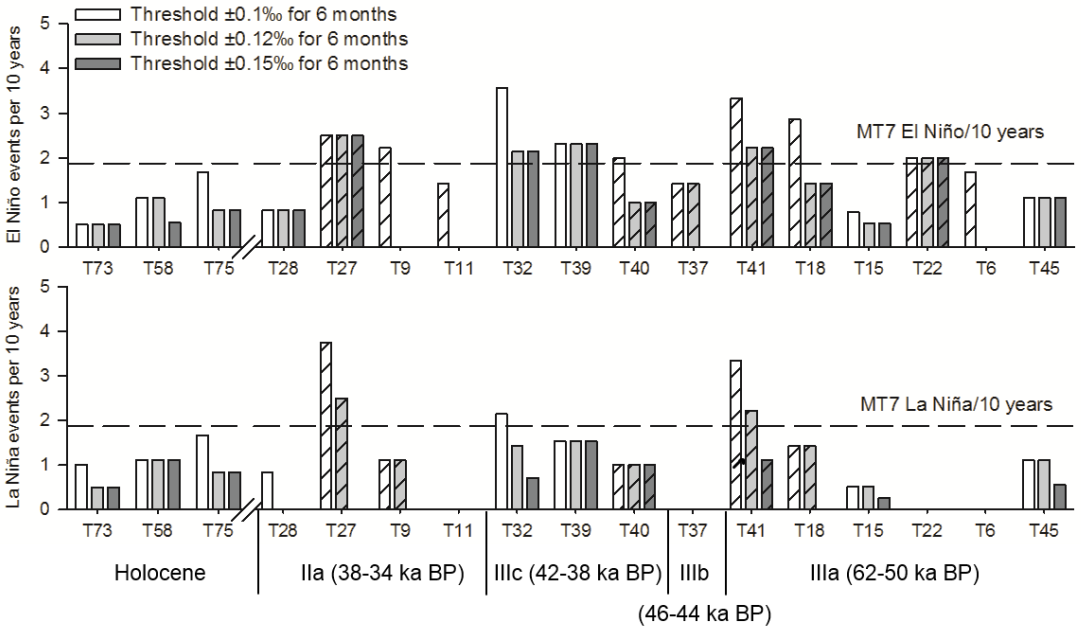

Figure 6.18 Comparison of number of El Niño (top panel) and La Niña (bottom panel). Events calculated per 10 year period using three thresholds – ±0.1‰, an arbitrary threshold, ±0.12‰, the threshold used by McGregor and Gagan (2004), and ±0.15‰, the El Niño and La Niña anomaly seen in the modern *T. gigas*. Break indicates the divide between Holocene and MIS3 shells. Records which are 10 years or less in length are shown by hatched bars, records over 10 years by solid bars. Reef names and ages are shown below the top panel

In six fossil shells, the number of El Niño events remains constant despite changes to the threshold, while in five fossil shells the number of La Niña events remains the same. The three shells which only record El Niño events at the lowest threshold (0.1‰) also show low variance of the quantitative methods (Figure 6.17). When the calculated threshold of ±0.15‰ is used there appears to be a disparity between El Niño and La Niña events (Figure 6.19). Of the 13 shells which record "ENSO" events, all record at least one cold El Niño event, while only 10 record at least one warm La Niña event.

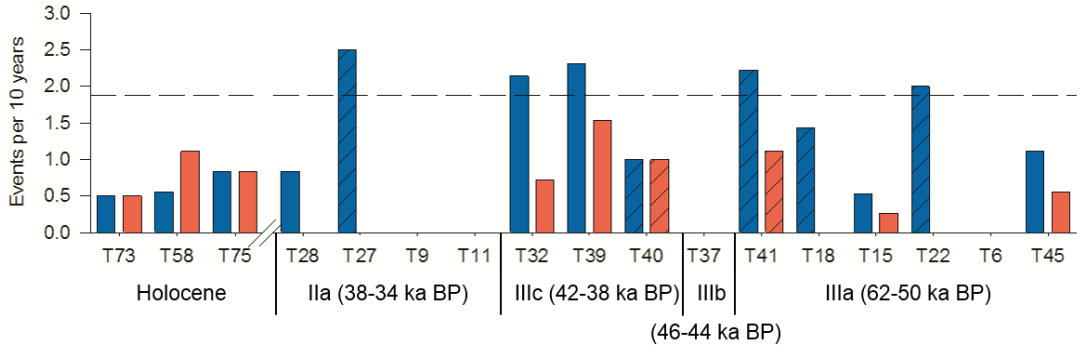

Figure 6.19 Number of El Niño (blue) and La Niña (red) events per 10 years, counted above a threshold of ±0.15‰. Break indicates the divide between Holocene and MIS3 shells. Records which are 10 years or less in length are shown by hatched bars, records over 10 years by solid bars. Reef names and ages are shown below the top panel

6.5.5 Comparison of variance derived from fossil corals, SST and *Tridacna*

It is possible to compare the variance of the bandpass filtered data with that of the $\delta^{18}O_A$ data in order to assess the appropriateness of these two methods for records of different lengths. This can not only be compared in the fossil *Tridacna* sp. data, where records are between 5 and 38 years, but also in fossil *Porites* corals (Tudhope et al., 2001), which have record lengths of up to 95 years, and in the 20th century HadISST SST record (Rayner et al., 2003).

In order to assess the two methods (bandpass filtered data and $\delta^{18}O_A$ data), the variance of each fossil shell and coral was normalised to that of MT7, using the following equation: $\frac{Fossil\ variance}{MT7\ variance}$. The variance of the bandpass filter method was subtracted from that of the $\delta^{18}O_A$ method for each individual shell or coral (Figure 6.20). Positive values indicate that the variance of the $\delta^{18}O_A$ method is higher than the bandpass filter method, and vice versa. The HadISST SST record was divided into

discrete windows, with the variance of each window normalised to that of the entire 20th century for both methods, so that it could be determined if the length of the sampling period had a significant impact.

The difference in variance between the two methods ranges from -0.15 to +0.41 in the *Tridacna* sp. data, -0.2 to +0.43 in the *Porites* data, and -0.38 to 0.38 in the SST data (Figure 6.20). If the $\delta^{18}O_A$ method is used with the long coral records, the variance of this method is far higher than that produced by the bandpass filter method. In three short (>10 years) *Tridacna* records, the variance of the $\delta^{18}O_A$ method is again far higher than that of the bandpass filter method (Figure 6.20).

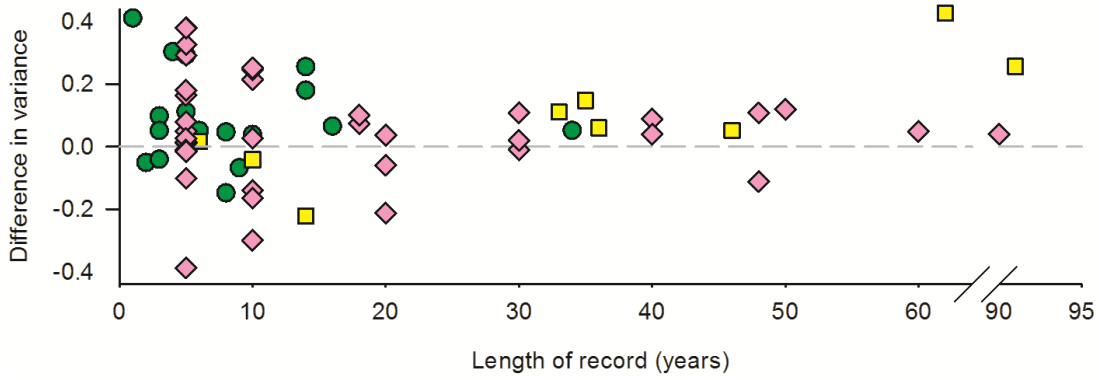

Figure 6.20 Difference between variance of bandpass filtered $\delta^{18}O$ and SST, and that of $\delta^{18}O_A$ and SST_A in *Tridacna* sp. shells (circles), *Porites* corals (Tudhope et al., 2001) (squares) and HadISST for 147.5°E, 6.5°S (Rayner et al., 2003) (diamonds). The variance is calculated for the equal length records, therefore records lose 4 years due to the width of the bandpass filter. The SST record was divided into discrete windows. Positive values indicate higher variance of $\delta^{18}O_A$ or SST_A, negative values indicate higher variance of bandpass filtered $\delta^{18}O$ or SST, normalised to MT7 or 20th century SST. All proxy records normalised to the variance calculated for MT7, all SST records normalised to that calculated for the 20th century

In order to assess the most appropriate method to use with these records, absolute differences were grouped by record length (Figure 6.21).

In the SST record, the difference between the two methods decreases as the window size increases. This also occurs in *Tridacna* sp. In the corals, the greatest difference (average of 0.25, n=2) between the two methods occurs in the long records which span 66 and 95 years (Figure 6.21). This may be because the corals are recording decadal variability within the $\delta^{18}O$ time series, which is not removed using the $\delta^{18}O_A$ method. However, this decadal variability does not appear to affect the SST records, as the 50 year windows show an average difference of 0.05 between the two methods.

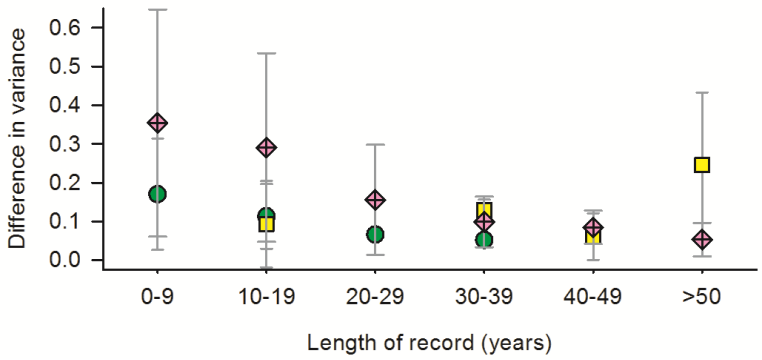

Figure 6.21 Absolute mean difference between grouped bandpass filtered $\delta^{18}O$ and SST variance and $\delta^{18}O_A$ and SST_A variance in modern and fossil *Tridacna* sp. shells (circles), modern and fossil *Porites* corals (Tudhope et al., 2001) (squares) and SST from HadISST (diamonds). Error bars represent 1 s.d. of the grouped data

The variance produced by the $\delta^{18}O_A$ is higher than that produced by the bandpass filter in 13 of the 17 *Tridacna* sp. records. This method may produce an underestimation in the reduction of ENSO variability because only the seasonal cycle is removed, and therefore any other variability is included. In 4 records, ENSO variability would be overestimated by 4-15%, while in 8 records ENSO would be underestimated by 4-11%. In the 2 records with trends in the data, ENSO variability would be overestimated by 25% (T45) and 29% (T58). The remaining 3 shells all have a record length of less than 10 years, resulting in a record of 1-5 years due to the loss of data from edge effect uncertainties (Russon et al., 2014). ENSO variability would be overestimated in these records by 29-41%. Although there are discrepancies, the length of the records in this study makes $\delta^{18}O_A$ the most appropriate method for reconstructing past ENSO variability.

6.5.6 PaleoENSO recorded at the Huon Peninsula

The variance of the $\delta^{18}O_A$ time series can be compared between the fossil *Tridacna* sp. and fossil *Porites* corals from the same region from Tudhope et al. (2001). These have also been shown to capture ENSO events in their $\delta^{18}O$ time series. The inferred variance of 20th century $\delta^{18}O$ can be compared to the fossil *Tridacna* sp. in order to examine whether the ENSO activity of the modern *T. gigas* is unusual for the 20th century, and to see if fossil *Tridacna* sp. experienced ENSO activity similar to that seen in the instrumental record. This comes with the caveat that because SST variance has been scaled to that of MT7 $\delta^{18}O$, inferring 20th century *T. gigas* $\delta^{18}O$ variability, it

assumes the relationship between SST and SSS has remained constant throughout the 20th century. The variance of inferred 20th century $\delta^{18}O$ can therefore only be used as a guide for ENSO variability during the last century.

Fossil corals from the IIa reef show similar variance to the fossil *Tridacna* sp. shells from the same reef (Figure 6.22). There is no published coral data between 60 and 42 ka BP, so it is not possible to compare data further back into MIS3. The mid-Holocene *Porites* shows lower variance than the early Holocene *Tridacna* sp., but this may be due to the fact that there is approximately 1kyr between the time of growth of the *Porites* and the latest *T. gigas* (T73), and there have been a number of studies suggesting that the mid-Holocene experienced particularly supressed ENSO activity (e.g. Tudhope et al., 2001, McGregor and Gagan, 2004, McGregor et al., 2013).

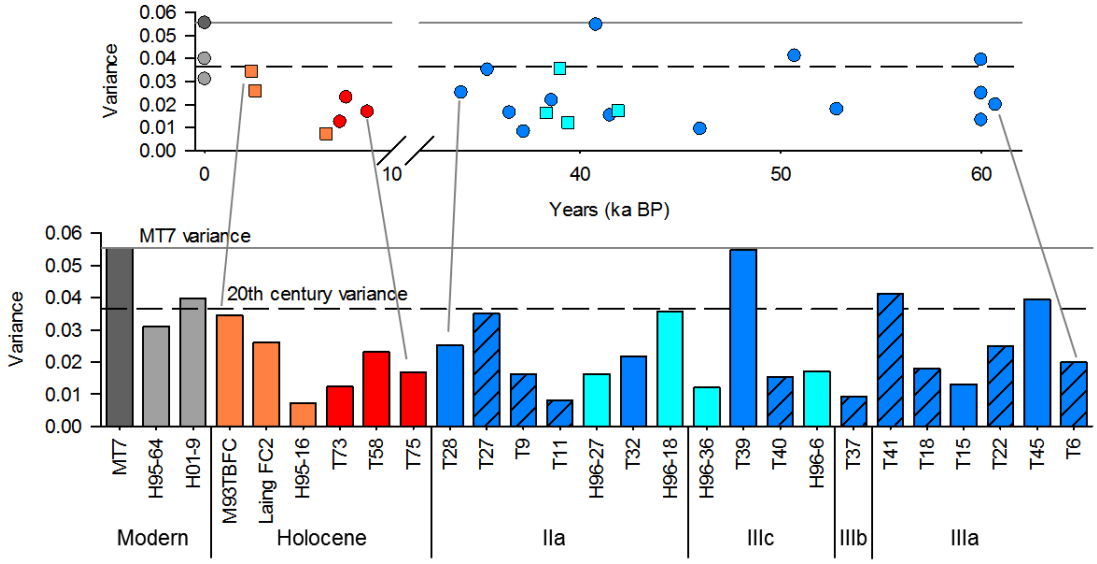

Figure 6.22 Variance of $\delta^{18}O_A$ time series of *Tridacna* sp. shells and *Porites* from Tudhope et al. (2001). Solid line represents the variance of the modern *T. gigas*, while the dashed line represents that calculated for the 20th century. Lighter colours represent *Porites* corals. Grey bars indicate modern corals and *T. gigas*; red bars indicate Holocene fossils; blue bars represent glacial fossils. Hatched bars represent shells which have records which are 10 years or fewer in length

The variance of fossil $\delta^{18}O_A$ has never exceeded that of the modern *T. gigas*, and only exceeds the inferred $\delta^{18}O$ variance of the 20th century in three shells (Figure 6.22). This reduction in ENSO variability could be due to changes in background climate (e.g. Tudhope et al., 2001), orbital forcing (e.g. Clement et al., 1999), or indeed ENSO may

not have impacted this region as greatly in the past. This will be discussed in detail in Chapter 7.

6.6 Conclusions

This chapter has shown several of the methods which are commonly used to reconstruct ENSO variability in $\delta^{18}O$ time series, in both modern and fossil climate proxies. The three main methods - the use of a bandpass filter, the $\delta^{18}O$ anomaly time series, and using a threshold, all produce relatively similar results in fossil shells when the variance is normalised to the modern *Tridacna gigas*. Using a threshold confirms that El Niño and La Niña-type events are present in many of the fossil shells spanning the past 60 ka, and confirms that the variance produced by the quantitative metrics is due to ENSO variability rather than noise or decadal trends in the data. Due to the length of the records and because it is at sufficient resolution to resolve inter-annual anomalies, the variance of the $\delta^{18}O_A$ time series will be used as a metric to reconstruct paleoENSO in further chapters.

7. Changes in Seasonality and ENSO over the past 60 ka

Chapter Abstract

Information derived from climate modelling experiments and proxy data from the Holocene suggest that the early Holocene (~9-6 ka BP) had a similar mean climate to today, and yet that ENSO was supressed in the West Pacific. Marine Isotope Stage 3 (60-30 ka) in the tropics was characterised by cooler mean SSTs and lower seas levels. Mean insolation and patterns of seasonal insolation varied throughout this period.

Three early Holocene (8.7-7.3 ka BP) shells record similar mean values of $\delta^{18}O$ with a smaller range of values, suggesting a stable mean climate, a decrease in seasonal amplitude of $\delta^{18}O$ of approximately 40% compared with the modern shell, and a reduction in recorded ENSO variability of up to ~80%. A reduction in seasonal $\delta^{18}O$, calculated using the mean amplitude of annual $\delta^{18}O$, is consistent with lower seasonal insolation at 6.5°S during the early Holocene. The reduction in ENSO variability, calculated using inter-annual anomalies is consistent with data from western and central Pacific corals during the early Holocene. The number of El Niño and La Niña events, calculated as anomalies exceeding a threshold, is also reduced compared with the modern *T. gigas* (1986-2002) and the 20th century, with a slight preference for warm and wet La Niña-type events.

The amplitude of the annual cycle of $\delta^{18}O$ is the same or lower during MIS3 than the modern *T. gigas* shell, and does not seem to be solely influenced by changes in solar insolation. ENSO, as reconstructed using inter-annual $\delta^{18}O$ anomalies ($\delta^{18}O_A$), appears to have been suppressed compared with the period covered by the modern *T. gigas*. Individual *Tridacna* sp. shells show variance comparable to that calculated for the 20th century using the modern SST record. This suggests that ENSO was present and active throughout the last glacial period, although events appear to have been less frequent and generally smaller in amplitude than in the present day.

Chapter 7

7.1 Introduction

Fluctuations in mean climate over the past 60 ka (Chapter 4) are likely to have been accompanied by changes in local seasonality and the El Niño Southern Oscillation, in response to both the background state and external forcings such as solar insolation (e.g. Tudhope et al., 2001, McGregor et al., 2013, Sadekov et al., 2013). The timing of maximum and minimum insolation, and the seasonal amplitude of insolation varied over the past 60 ka (Laskar et al., 2004) (Figure 7.1), and may have affected local seasonality in temperature and precipitation, which is recorded in the $\delta^{18}O$ of *Tridacna* sp. carbonate shells.

Changes in overall ENSO variability (Chapter 6) may be related to fluctuations in the amplitude or strength of events, i.e. the size of SST/precipitation anomalies recorded by proxies during El Niño or La Niña, or to changes in the frequency of events, or the ratio of El Niño to La Niña occurrences.

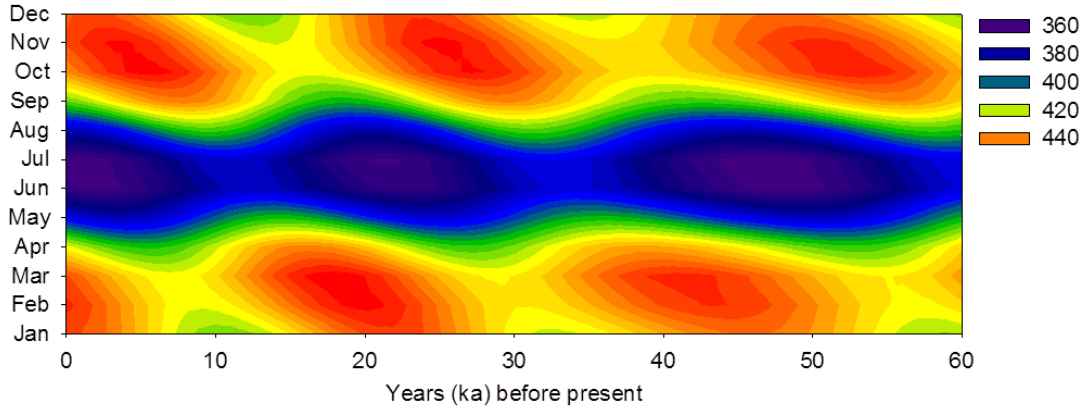

Figure 7.1 Mean monthly insolation (W/m²) for 6.5°S over the past 60 ka (Laskar et al., 2004)

Models run for the early to mid-Holocene, ranging in complexity from the Zebiak-Cane model, which uses solar insolation as the only forcing (Clement et al., 2000), to general circulation models which include atmospheric and ocean components (Liu et al., 2000, Otto-Bliesner et al., 2003, Brown et al., 2006) have suggested a reduction in ENSO amplitude and frequency during this period. Information on the behaviour of ENSO during glacial periods comes predominantly from modelling experiments, proxy data from low-resolution records such as foraminifera (Stott et al., 2002, Leduc et al., 2007,

Leduc et al., 2009, Li et al., 2011), or from outside the tropical Pacific (Merkel et al., 2010).

Due to the abundance of data, and modelling studies of Holocene climate, there are certain expectations of the $\delta^{18}O$ records derived from *Tridacna* sp. during this period. SSTs during the early to mid-Holocene (e.g. 10-6 ka BP) in the west Pacific are thought to have been reasonably similar to today (e.g. Lea et al., 2000, Stott et al., 2002, Stott et al., 2004, de Garidel-Thoron et al., 2007 and references within Chapter 4). Due to changes in insolation (e.g. Figure 7.1) and the timing of perihelion, the strength of the seasonal cycle was enhanced in the northern and reduced in the southern hemisphere (Berger, 1978, Laskar et al., 2004). It has been proposed that this configuration caused a suppression of the development of ENSO events, either through direct changes in the strength of the seasonal cycle (Clement et al., 2000, McGregor et al., 2013), or through orbitally driven changes in the Asian monsoon (Liu et al., 2000, Abram et al., 2009). Although many models find a reduction in ENSO variability during the early to mid-Holocene, there is no clear consensus as to what led to this suppression and reduction in variability.

Charcoal records from Papua New Guinea (Haberle et al., 2001) and pollen records from Australia (Shulmeister and Lees, 1995, Turney et al., 2004) suggest that drought and fires were reduced during the early Holocene (~9 – 6 ka BP) due to a relatively stable climate. Seasonally resolved $\delta^{18}O$ records from tropical Pacific corals (Tudhope et al., 2001, Cobb et al., 2003, McGregor and Gagan, 2004, Duprey et al., 2012, McGregor et al., 2013, Cobb et al., 2013), sediment cores from Indonesia (Brijker et al., 2007), Peru (Rein et al., 2005), the Galapagos (Koutavas et al., 2002, Koutavas et al., 2006, Koutavas and Joanides, 2012), and several locations across the equatorial Pacific (Sadekov et al., 2013); and lake sediments from the Galapagos (Koutavas et al., 2002, Conroy et al., 2008) and Ecuador (Rodbell et al., 1999) have been used to reconstruct changes in SST or precipitation which can be attributed to ENSO variability during the Holocene. These data tend to suggest a reduction in ENSO variability during the early Holocene, with an increase in events towards the present day.

While the mean background state or climate of the early to mid-Holocene has been reconstructed using low-resolution data from foraminifera, higher resolution data is

required in order to look at seasonality and ENSO variability. High resolution data from corals and bivalves is less abundant than low resolution foraminifera data, and this study adds to the published tropical Pacific data covering the last 60 ka BP. Bivalve $\delta^{18}O$ from Peru (Carré et al., 2005) and coral $\delta^{18}O$ from the central Pacific (McGregor et al., 2013) provide information on changes in seasonality during the Holocene. Coral data from the Holocene tend to suggest a reduction in the amplitude and frequency of ENSO events during the early to mid-Holocene, with ENSO frequency and strength increasing towards the late Holocene (e.g. Tudhope et al., 2001, Cobb et al., 2013). The reduction in ENSO variability seen in published data ranges in value, and is dependent on the method used for calculating ENSO variability (Brown et al., 2008b) (see Chapter 6 for details). The data in this chapter will be processed using the methods described in Chapter 6.

Modelling studies of glacial ENSO tend to focus on the Last Glacial Maximum (LGM, ~21 ka BP), when ice sheets were at their maximum extent, producing a severe impact on the global climate. LGM studies disagree as to whether the frequency, strength or amplitude of events was enhanced (Otto-Bliesner et al., 2003, An et al., 2004, Peltier and Solheim, 2004, Leduc et al., 2009, Merkel et al., 2010), or reduced (Otto-Bliesner et al., 2006). Studies using the Zebiak-Cane model suggest more frequent and intense cool (in the east Pacific) La Niña events, dictated by the precessional cycle, during glacial periods compared with the modern period (Clement et al., 1999). There are very few (Tudhope et al., 2001) high resolution glacial proxy studies from the tropical Pacific, and no published seasonally resolved $\delta^{18}O$ profiles between 60 and 42 ka BP, as well preserved corals are rare prior to the Holocene.

The data set of *Tridacna* sp. collected from the raised coral reef terraces at the Huon Peninsula provide information about changes in seasonality and ENSO during a relatively stable period (early Holocene) and a highly variable period (MIS3).

7.2 Methods

Most of the methods used are presented in previous chapters. Thin sections of *Tridacna* sp. were sampled and geochemical profiles were converted from a distance

scale to an annual scale (Chapter 3). The data was thereafter corrected for an ice volume effect (Chapter 4). The length of the Holocene *T. gigas* $\delta^{18}O$ time series was between 12 and 20 years. Resolution was between 12 and 15 samples a year for the first 8-13 years of growth, with growth slowing significantly thereafter, resulting in a temporal resolution of 6 to 12 samples/year. In samples of *Tridacna* sp. from MIS3 reefs, records were between 3 and 38 years, with a temporal resolution of 6 to 12 samples/year. Profiles were therefore interpolated linearly to give 6 samples/year using Analyseries (Paillard et al., 1996). Using the modern mean SST as a guide to building individual shell chronologies results in $\delta^{18}O$ maxima being matched to August SST minima. This assumption may result in an error of ±1 month on the chronology of each shell (Chapter 3).

Calculating seasonality in Tridacna sp. $\delta^{18}O$ profiles

Estimates of the amplitude of the seasonal cycle are affected by the observed reduction in growth over the bivalve's lifespan. Therefore, seasonality recorded in *Tridacna* sp. $\delta^{18}O$ was examined in two ways. In the Holocene samples, monthly mean $\delta^{18}O$ values were calculated from the first 8-10 years of each profile, where the sampling resolution was above 12 samples per year. From this information, a mean seasonal cycle for each shell was derived (e.g. Figure 7.2). This is referred to in the discussion as the "mean seasonal cycle". In the MIS3 samples, mean bi-monthly $\delta^{18}O$ values were calculated using the entire record.

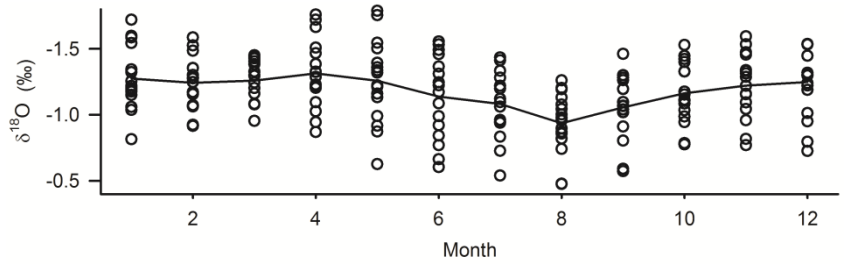

Figure 7.2 Measurements of $\delta^{18}O$ recorded by MT7 during each month. The solid line shows the mean $\delta^{18}O$ for each month and corresponds to the calculated mean seasonal cycle for the modern shell

A second method was used to calculate the amplitude of the seasonal cycle for each year of growth. This was calculated from the entire $\delta^{18}O$ profile of each *Tridacna* sp. sample, interpolated to 6 samples/year, by subtracting the minimum from the

maximum $\delta^{18}O$ within each year (maximum $\delta^{18}O$ shown circled in red in Figure 7.3). The "seasonal" amplitude discussed in the following sections is therefore an average of that of all of the years of record, given with one standard deviation (1σ). This will be referred to in the discussion as the "mean annual/seasonal amplitude of $\delta^{18}O$".

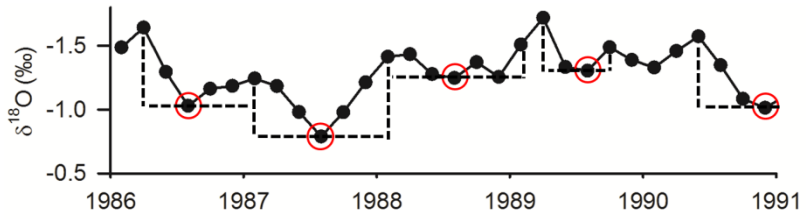

Figure 7.3 Example of the calculation of seasonal/annual $\delta^{18}O$ amplitude in modern shell, MT7. The most positive $\delta^{18}O$ values in each year are shown in red circles.

7.3 Results

7.3.1 Seasonally resolved profiles of *T. gigas* $\delta^{18}O$ during the Early Holocene

The three Holocene *T. gigas* discussed in this chapter (ages in Table 7.1) have similar mean $\delta^{18}O$ values (calculated at bi-monthly resolution). The difference in mean values between Holocene samples is up to 0.04‰ (within instrumental error), and the samples have a similar range of $\delta^{18}O$ measurements (Figure 7.4). The range of individual $\delta^{18}O$ measurements from three Holocene *T. gigas* is within the maximum and minimum $\delta^{18}O$ recorded by MT7 (Figure 7.4), despite mean $\delta^{18}O$ of the fossil shells being more positive by 0.19‰ (n=3).

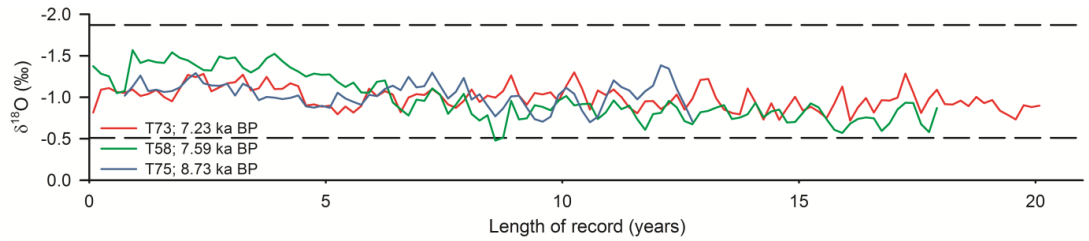

Figure 7.4 $\delta^{18}O$ profiles of three Holocene *T. gigas* shells. Dashed lines represent the maximum and minimum $\delta^{18}O$ of the modern *T. gigas* shell. The $\delta^{18}O$ has been corrected for ice volume effects (described in Chapter 4). Resolution is at 6 samples/year

The range of variability of individual $\delta^{18}O$ measurements is smaller than in the modern *T. gigas* in all three samples - MT7 $\delta^{18}O$ spans 1.4‰, while the fossil *T. gigas* $\delta^{18}O$

values are 0.6‰ (T73), 1.1‰ (T58) and 0.7‰ (T75) (Table 7.1). If the first five years of the $\delta^{18}O$ record of T58 are excluded because of the trend in the data, the range of $\delta^{18}O$ values decreases to 0.8‰.

Table 7.1 Modern and Holocene *T. gigas* ages, mean $\delta^{18}O$, range in $\delta^{18}O$ (maximum – minimum $\delta^{18}O$) and mean amplitude of annual $\delta^{18}O$ cycle (±1 s.d.). Values have been corrected for an ice volume effect (Chapter 4)

Shell	Age (ka BP)	Length of record (years)	Mean $\delta^{18}O$ (‰)	Range (‰)	% Change from MT7	Amplitude (±1 s.d.) (‰)	% Change from MT7
MT7		16	-1.2	1.4		0.36±0.16	
T73	7.26	20	-1.0	0.6	-60	0.22±0.09	-39
T58	7.59	18	-1.0	1.1	-21	0.23±0.09	-36
T75	8.73	12	-1.0	0.7	-51	0.24±0.11	-33

The amplitude of the seasonal cycle in $\delta^{18}O$ can be calculated for each sample, as described in the methods section, while mean monthly $\delta^{18}O$ values can be calculated from portions of the $\delta^{18}O$ record where the resolution exceeds 12 samples per year (Figure 7.5).

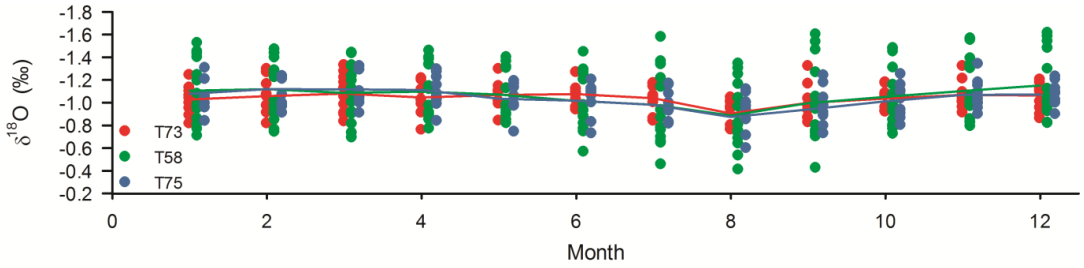

Figure 7.5 Holocene *T. gigas* measurements of $\delta^{18}O$ by month. Solid lines show the mean $\delta^{18}O$ for each month

The mean monthly $\delta^{18}O$ values of the early Holocene samples, calculated from the first 9-13 years of each record are all more positive than those from modern sample MT7 (Figure 7.6, left), while the mean seasonal cycle annual amplitude derived from the fossil samples are less than that of MT7 (Figure 7.6, right). The mean annual amplitude of the modern *T. gigas* is 0.36±0.16‰, with fossil Holocene *T. gigas* amplitudes of 0.22±0.09‰ (T73, 7.26 ka BP), 0.23±0.09‰ (T58, 7.59 ka BP) and 0.24±0.11‰ (T75, 8.73 ka BP).

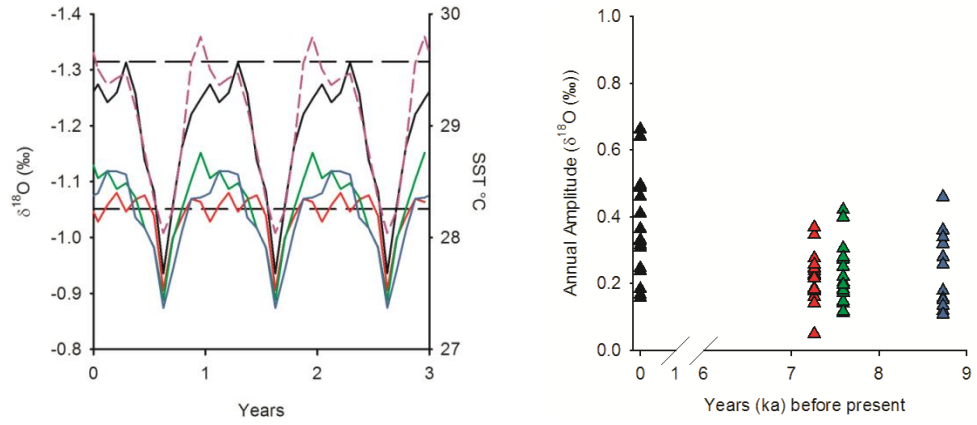

Figure 7.6 Left: Mean monthly values of $\delta^{18}O$ for three Holocene samples (T73 – red, T58 – green, T75 - blue). Dashed lines represent the minimum and maximum $\delta^{18}O$ values for MT7, and solid black line shows the mean monthly $\delta^{18}O$ values for MT7. Right axis and dashed purple line represent the mean SST cycle calculated for 1986-2002 using IGOSS SST for 147.5°E, 6.5°S (Reynolds et al., 2002).
Right: Annual amplitudes of $\delta^{18}O$ for three Holocene samples compared with MT7 (black)

7.3.2 Seasonally resolved $\delta^{18}O$ profiles of MIS3 *Tridacna* sp.

The seasonally resolved profiles of $\delta^{18}O$ derived from MIS3 *Tridacna* sp. are more positive than the modern *T. gigas* (Figure 7.7 and Table 7.2), and generally show a decrease in the range of $\delta^{18}O$ measurements, as well as a reduction in the mean amplitude of annual $\delta^{18}O$. The following sections describe the results divided into the MIS3 reefs described in Chapter 2.

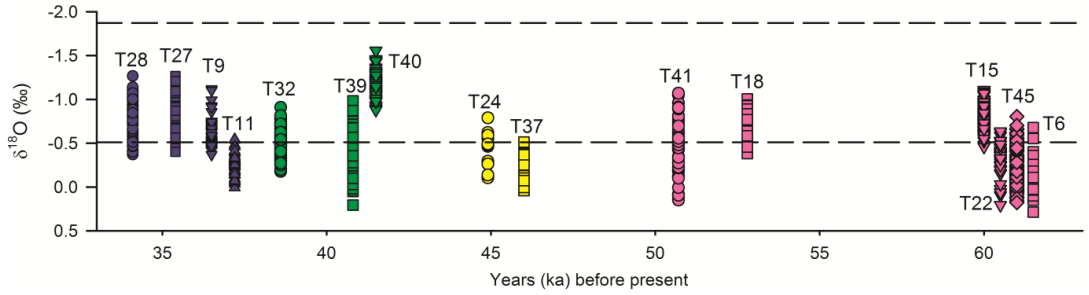

Figure 7.7 Spread of $\delta^{18}O$ results (corrected for ice volume effect, Chapter 4) for MIS3 fossil *Tridacna* sp. shells, interpolated to 6 samples/year. Dashed lines represent the maximum and minimum $\delta^{18}O$ values recorded by the modern shell, MT7. Colours indicate different reefs – IIa (blue); IIIc (green); IIIb (yellow); IIIa (pink). Individual $\delta^{18}O$ profiles are shown in the Appendix

Table 7.2 MIS3 *Tridacna* sp. ages, mean $\delta^{18}O$, range in $\delta^{18}O$ (maximum – minimum $\delta^{18}O$) and mean amplitude of annual $\delta^{18}O$ cycle (±1 s.d.)

Shell	Reef	Age (ka BP)	Length of record (years)	Mean $\delta^{18}O$ (‰)	Range (‰)	% Change from MT7	Amplitude (±1 s.d.) (‰)	% Change from MT7
MT7	Modern	0	16	-1.2	1.4		0.36±0.16	
T28	IIa	34.1	12	-0.81	0.9	-36	0.35±0.15	-4
T27	IIa	35.4	8	-0.81	0.86	-39	0.32±0.13	-11
T9	IIa	36.5	9	-0.63	0.75	-46	0.27±0.12	-25
T11	IIa	37.2	7	-0.27	0.55	-61	0.21±0.08	-41
T32	IIIc (l)	38.6	14	-0.50	0.73	-48	0.23±0.09	-36
T39	IIIc (u)	40.8	13	-0.32	1.2	-14	0.33±0.15	-10
T40	IIIc (u)	41.5	10	-1.15	0.68	-51	0.23±0.08	-36
T24	IIIb	44.9	2	-0.43	0.68	-51	0.25±0.11	-30
T37	IIIb	46	7	-0.20	0.55	-61	0.27±0.10	-28
T41	IIIa (l)	50.7	9	-0.46	1.2	-14	0.39±0.18	9
T18	IIIa (m)	52.8	7	-0.69	0.62	-56	0.23±0.07	-37
T15	IIIa (u)	60	38	-0.79	0.65	-54	0.20±0.08	-45
T22	IIIa (u)	60	5	-0.30	0.84	-40	0.24±0.13	-34
T45	IIIa (u)	60	18	-0.26	0.98	-30	0.23±0.09	-36
T6	IIIa (u)	60.7	6	-0.15	0.96	-31	0.36±0.16	-1

Observations from MIS3 Reef Terraces

Reef IIa (38-34 ka BP)

The $\delta^{18}O$ measurements of the four *Tridacna* sp. from the IIa reef are partially within the range recorded by the modern *T. gigas* (Figure 7.7) after being corrected for ice volume. Sample T11, the oldest shell from this reef, has more positive values than MT7. The T11 $\delta^{18}O$ values suggest cooler and/or drier conditions at 37.2 ka BP than between 36.5 – 34.1 ka BP. When compared with MT7, the mean $\delta^{18}O$ of the IIa samples equates to a reduction in temperature of 2.7°C, an increase in salinity of 2.1‰ p.s.u., or a combination of the two (Chapter 4). The range of $\delta^{18}O$ values is lower by 36 to 61% than in MT7 (Table 7.2), while the mean annual amplitude of $\delta^{18}O$ is lower by 4 to 41%. Mean bi-monthly values of $\delta^{18}O$ are more positive than MT7 (Figure 7.8).

Reef IIIc (42-38 ka BP)

The $\delta^{18}O$ measurements of two of the three *Tridacna* sp. from the IIIc (lower and upper) reefs are more positive than the modern *T. gigas*, while one sample (T40) has $\delta^{18}O$ measurements which are similar to modern day values (Figure 7.7). The mean $\delta^{18}O$ values of the three IIIc *Tridacna* sp. equate to a reduction in temperature of 2.6°C, an increase in salinity of 2‰ p.s.u., or a combination of the two. The range of $\delta^{18}O$

values is lower (by 14-51%) in the IIIc samples than in MT7, and the mean annual amplitude is lower by 10-36% (Table 7.2). Mean bi-monthly values of $\delta^{18}O$ are more positive in T32 and T39 than in MT7, while T40 records mean bi-monthly values which are within the range of MT7 (Figure 7.8).

Reef IIIb (46-44 ka BP)

The $\delta^{18}O$ profiles of the two IIIb reef *Tridacna* sp. are more positive than the modern *T. gigas* (Figure 7.7). The mean $\delta^{18}O$ values of the two IIIb samples equate to a reduction in temperature of 4.2°C, an increase in salinity of 3.3‰ p.s.u., or a combination of the two (Chapter 4). The range of $\delta^{18}O$ values is lower in all the IIIb shells than in MT7 (Table 7.2). The mean annual amplitude of $\delta^{18}O$ of these samples is smaller than the modern shell (Table 7.2), with an amplitude of 0.25±0.11‰ (T24) and 0.27±0.1‰ (T37). Mean bi-monthly values of $\delta^{18}O$ are more positive than MT7 (Figure 7.8).

Reef IIIa (62-50 ka BP)

The two samples from the IIIa (lower and middle) reefs have $\delta^{18}O$ measurements which are towards the more positive end of values recorded by the modern *T. gigas* (Figure 7.7). There is a trend in the $\delta^{18}O$ time series in sample T41, with more negative $\delta^{18}O$ measurements recorded towards the adult phase of growth (see Appendix for T41 time series). This is the only *T. crocea* shell with a record over 5 years used in this study and the only shell with a clear linear trend in $\delta^{18}O$, which could signify a species specific effect. The mean $\delta^{18}O$ values derived from the two samples from reef IIIa (l and m) equate to a reduction in temperature of 2.9°C, an increase in salinity of 2.3‰ p.s.u., or a combination of the two. The range of $\delta^{18}O$ values is lower in these records than in MT7. The mean annual amplitude in $\delta^{18}O$ is higher by 9% in sample T41, potentially due to the ontogenetic effect, while in sample T18 it is 37% lower than in modern sample.

Three of the four samples from the IIIa (upper) reef have $\delta^{18}O$ measurements which are more positive than those recorded by the modern shell, while the profile of sample T15 is within the range of MT7 (Figure 7.7). The mean $\delta^{18}O$ values of the 4 shell samples derived from reef IIIa (u) equate to a reduction in temperature of 3.6°C, an increase in

salinity of 3‰ p.s.u., or a combination of the two. The range of $\delta^{18}O$ values is lower in the IIIa (u) samples than in MT7.

Overall, the mean $\delta^{18}O$ values of the six IIIa *Tridacna* sp. equate to a reduction in temperature of 3.4°C, an increase in salinity of 2.8‰ p.s.u., or a combination of the two. The mean annual amplitude of the IIIa(u) reef samples is lower than that of MT7 by between 1 and 45% (Table 7.2). Mean bi-monthly values of $\delta^{18}O$ are more positive than MT7 (Figure 7.8).

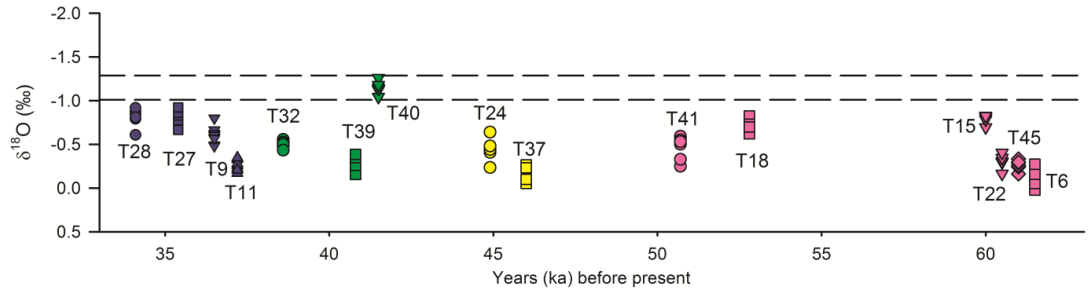

Figure 7.8 Mean bi-monthly $\delta^{18}O$ values for fossil MIS3 samples (6 measurements per sample). Dashed lines represent the maximum (recorded in July/August) and minimum (recorded in March/April) mean bi-monthly values of $\delta^{18}O$ in MT7

The amplitude of the seasonal cycle in $\delta^{18}O$ in the MIS3 samples fluctuates between an equivalent SST cycle of 1-2°C (Figure 7.9). A number of profiles show a double peak in $\delta^{18}O$ throughout the year (Figure 7.11), despite only $\delta^{18}O$ maxima being matched to SST minima when the chronology of the samples was constructed. In the modern climate at Huon, there is a double peak in the SST due to the movement of the ITCZ over the WPWP (Figure 7.10), and this seems to be recorded in several of the glacial samples.

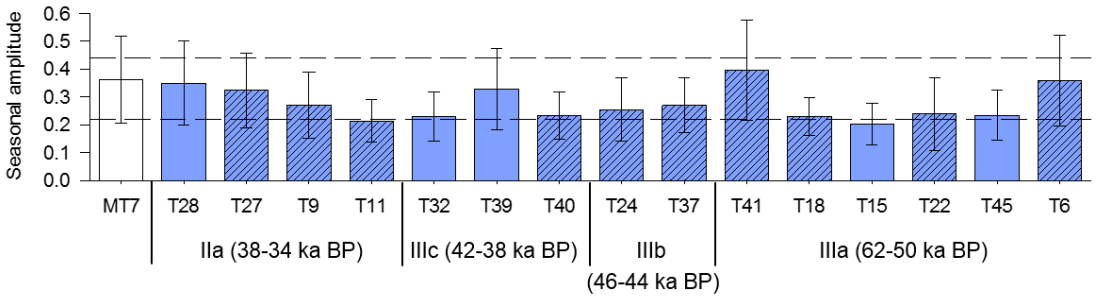

Figure 7.9 Mean amplitude of annual cycle of $\delta^{18}O$ in MIS3 samples. Dashed lines represent the amplitude in $\delta^{18}O$ which would represent a 1°C and 2°C seasonal cycle in SST. Hatched bars indicate shells which have a record length of 10 years or less. Samples are divided into reefs

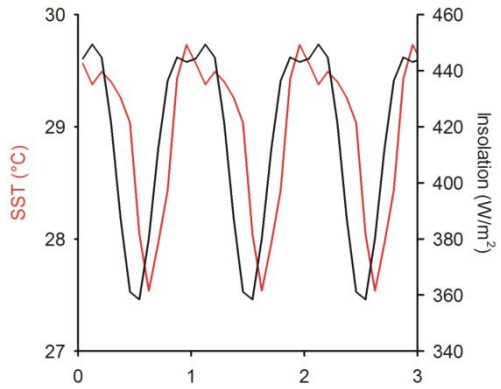

Figure 7.10 Mean SST for 1986-2002 from IGOSS for 147.5°E, 6.5°S (Reynolds et al., 2002) (left axis), with mean modern insolation for 6.5°S (right axis). Y axis shows three cycles representing three years

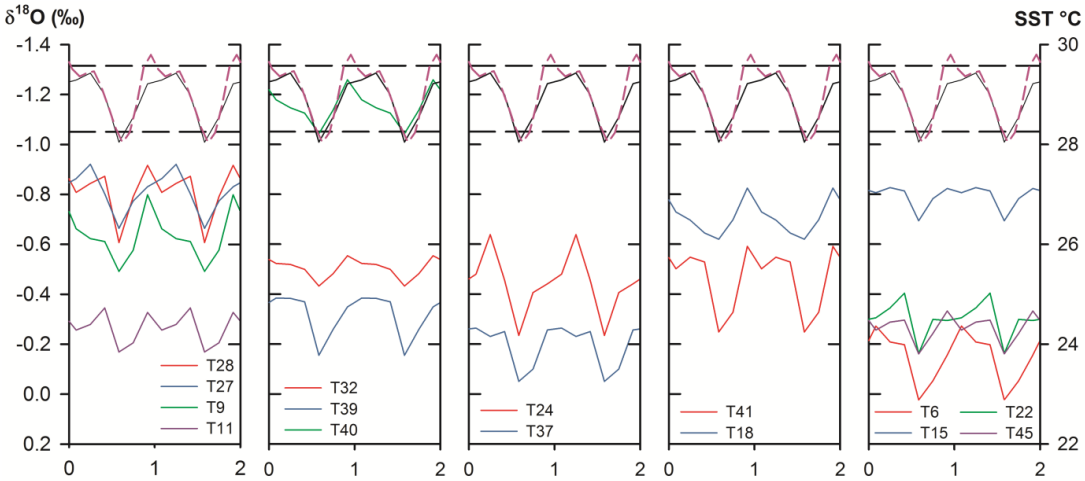

Figure 7.11 Mean bi-monthly profiles of $\delta^{18}O$ in Reef IIa, IIIc (lower and upper), Reef IIIb and Reef IIIa (lower, middle and upper); MT7 (black line), and the mean SST cycle calculated using IGOSS for 147.5°E, 6.5°S (Reynolds et al., 2002) from 1986-2002 (purple dashed line). Y axis shows two full cycles representing two years for each reef

ENSO Reconstructions from MIS3 Reef Tridacna sp.

The variability of ENSO during MIS3 was compared between fossil *Tridacna* sp. and the modern *T. gigas*. The number of anomalous events exceeding a threshold based on El Niño and La Niña in the modern *T. gigas* $\delta^{18}O$ record (±0.15‰) was also counted in order to examine the frequency of events during MIS3 (Figures 7.12 – 7.16).

Observations from MIS3 Reef Terraces

Reef IIa (38-34 ka BP)

All the IIa reef *Tridacna* show a reduced variability of the $\delta^{18}O_A$ time series compared to MT7, as well as fewer events which exceed the specified anomaly threshold of ±0.15‰ (Figure 7.12). Despite the short length of the records, positive anomalies, indicating cooler or drier conditions which are recorded during El Niño events in the modern *T. gigas* profile, can be seen in two samples. There are no negative events exceeding the threshold in any of the IIa reef samples, which indicate warmer and wetter conditions during La Niña.

Reef IIIc (42-38 ka BP)

One IIIc (u) sample (T39) shows as high variance as the modern *T. gigas*, while all three show El Niño and La Niña-type events in their anomaly time series (Figure 7.13). Each sample shows at least one warm and one cool episode, and as with the IIa reef, there is a preference for cool anomalous events which currently represent El Niño. The high variance recorded in T39 is likely due to the strong La Niña-type event occurring between 3 and 5 years in the record, which slightly exceeds the anomalies recorded by the modern shell during any La Niña between 1986 and 2002.

Reef IIIb (46-44 ka BP)

The $\delta^{18}O$ profile of T24 is too short to reconstruct ENSO variability, and T37 contains no El Niño or La Niña events above the 0.15‰ threshold in the $\delta^{18}O_A$ profile (Figure 7.14).

Reef IIIa (62-50 ka BP)

All the *Tridacna* sp. collected from the IIIa reef show reduced variance of the $\delta^{18}O_A$ time series compared to MT7. Warm and cold anomalous episodes can be seen in five of the six profiles, with a tendency towards more cool (El Niño) – there are eight El Niño and three La Niña events. None captured in the $\delta^{18}O_A$ profile of the IIIa *Tridacna* sp. exceed

the anomalies recorded by MT7 during modern El Niño or La Niñas, suggesting that those which occurred during this period were less intense, or recorded lower SST and precipitation anomalies than the modern *T. gigas* (Figures 7.15 and 7.16).

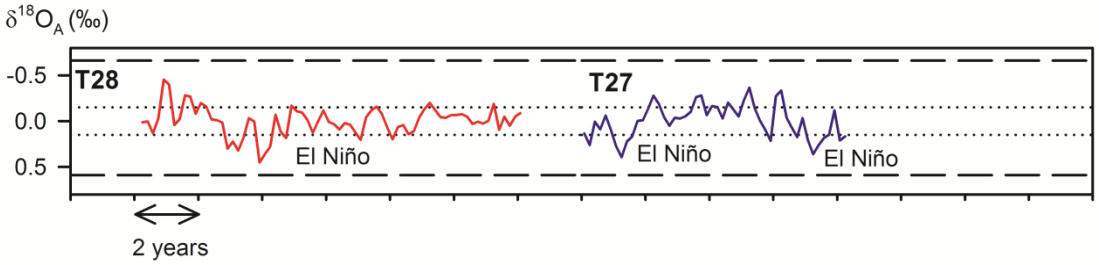

Figure 7.12 $\delta^{18}O_A$ profiles of two IIa reef samples which include ENSO-type events. El Niño and La Niña events, where a threshold of ±0.15‰ (dotted line) is exceeded for at least 6 consecutive months, are marked on each profile. Dashed line represents anomalies recorded in MT7

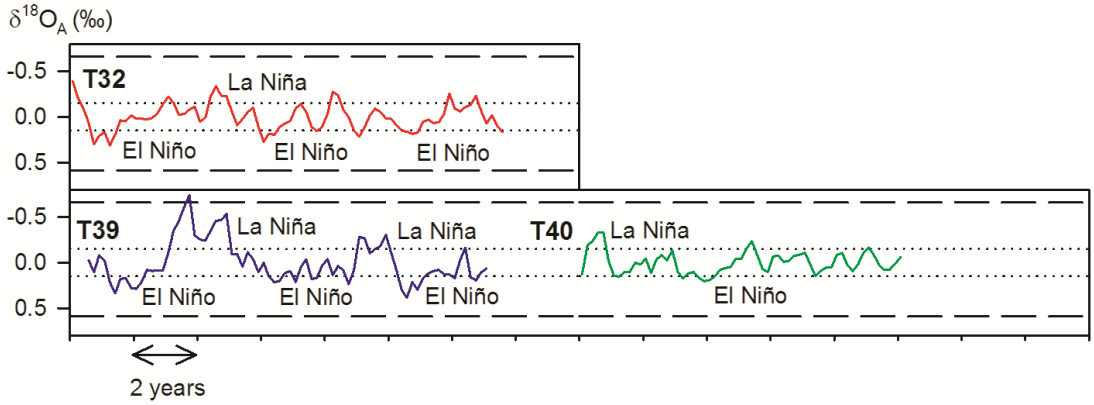

Figure 7.13 $\delta^{18}O_A$ profiles of three IIIc reef samples. Description the same as for Figure 7.12

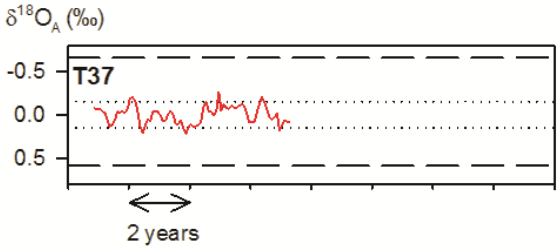

Figure 7.14 $\delta^{18}O_A$ profile of T37 from the IIIb reef. Description the same as for Figure 7.11

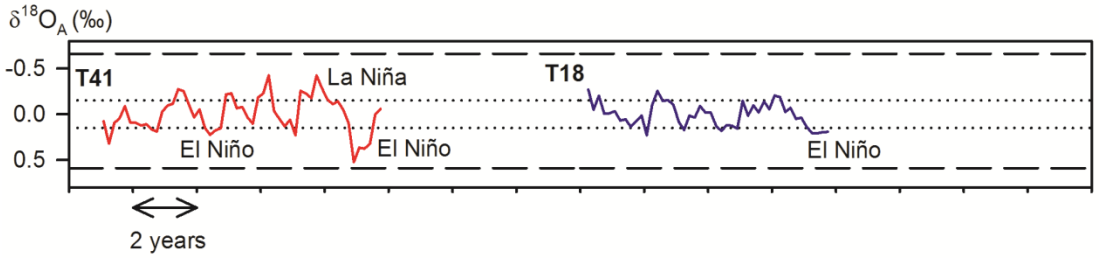

Figure 7.15 $\delta^{18}O_A$ profiles of T41 from the IIIa (l) reef and T18 from the IIIa (m) reef. Description the same as for Figure 7.12

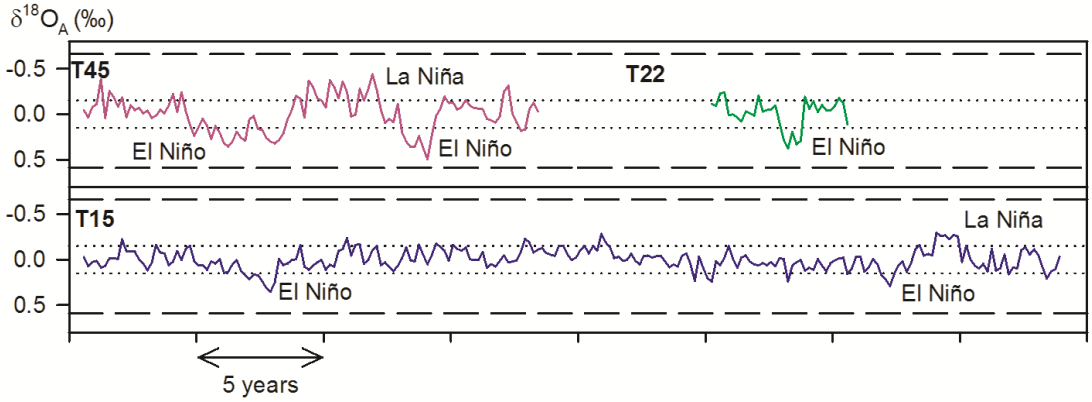

Figure 7.16 $\delta^{18}O_A$ profiles of three IIIa (u) reef samples. Description the same as for Figure 7.12

7.4 Discussion

7.4.1 Seasonality recorded in early Holocene *T. gigas*

The amplitude of seasonal $\delta^{18}O$ (Section 7.3.1) for the Holocene *Tridacna gigas* show a reduction of between 33 and 39% compared to the modern *T. gigas,* suggesting a reduction in the seasonal cycle in SST or salinity compared to the modern day. The three Holocene samples produce similar results, suggesting that any changes in seasonality between 8.73 and 7.26 ka BP were small.

Although both the $\delta^{18}O$ time series and the seasonal cycles of fossil samples are more positive than those of the modern shell, the difference between the two is variable (Figure 7.17). The data suggest that the cooling recorded in Holocene *T. gigas* $\delta^{18}O$ is not uniform throughout the year compared to MT7. The greatest cooling occurs between November and May, with the least between June and October (Figure 7.18). This non-uniformity suggests that the western Pacific cooled more during boreal winter than summer in the early Holocene, which might be related to changes in seasonality caused by insolation. This result confirms model simulations of the early Holocene climate which propose that tropical Pacific SSTs were cooler in winter and warmer in summer (Luan et al., 2012), consistent with changes in insolation (Berger, 1978, Laskar et al., 2004).

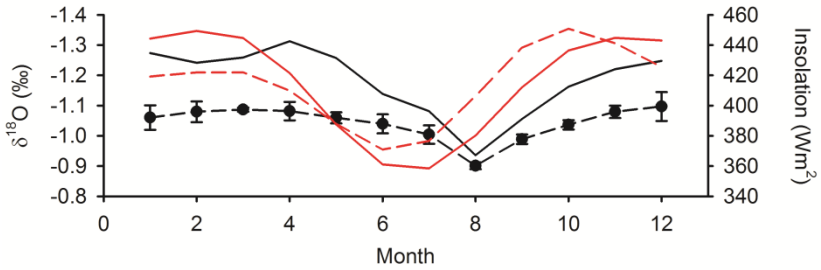

Figure 7.17 Monthly values of $\delta^{18}O$ for MT7 (solid black line) and the three Holocene *T. gigas* shells (dashed black line), compared to monthly insolation for 6.5°S at present (solid red line) and averaged at 7 and 8 ka BP (dashed red line) (Laskar et al., 2004). Error bars represent 1 s.d. of Holocene $\delta^{18}O$ measurements

In the three Holocene samples, mean monthly values of $\delta^{18}O$ are 0.14‰ more positive than the mean monthly values of $\delta^{18}O$ of MT7 in the juvenile portion of the shell. This reduction ranges between 0.08‰ and 0.23‰ depending on the month (Figure 7.18). If this were attributable only to SST, it would suggest a cooling of 0.2°C during boreal summer, compared to a cooling of 1°C during boreal winter.

The insolation curve for 6.5°S shows that there was greater insolation between May and October at 8-7 ka BP than at present, and vice versa between November and April (Figure 7.18). It appears that in months where there are the greatest absolute insolation differences, the Holocene *T. gigas* samples record greater absolute differences in $\delta^{18}O$ compared to the modern *T. gigas* (r^2=0.66).

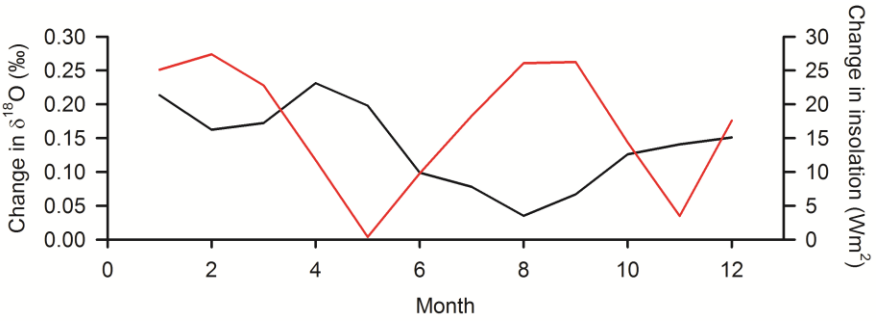

Figure 7.18 Difference between mean Holocene $\delta^{18}O$ monthly values and MT7 (black line) (described in Section 7.2) and absolute difference between insolation for 6.5°S at present and averaged at 7 and 8 ka BP (red line) (Laskar et al., 2004)

Mean monthly values of SST (°C) and precipitation (mm/day) during El Niño and La Niña can be compared to the modern $\delta^{18}O$ record (Figure 7.19). There is a cooling/drying during El Niño events, with the coolest/driest conditions occurring in June, and the warmest/wettest in February. During a La Niña event, the coolest/driest

conditions occur in August and the warmest/wettest in January, which is the same timing as the mean annual cycle of MT7 $\delta^{18}O$ and the instrumental SST record. This suggests that La Niña events are an enhancement of normal conditions in this region. La Niña events capture an enhanced mean seasonal cycle of $\delta^{18}O$, compared to El Niño and non-ENSO years. In the SST record, La Niña events exhibit a reduced cycle, and El Niño events an enhanced seasonal cycle (Figure 7.19).

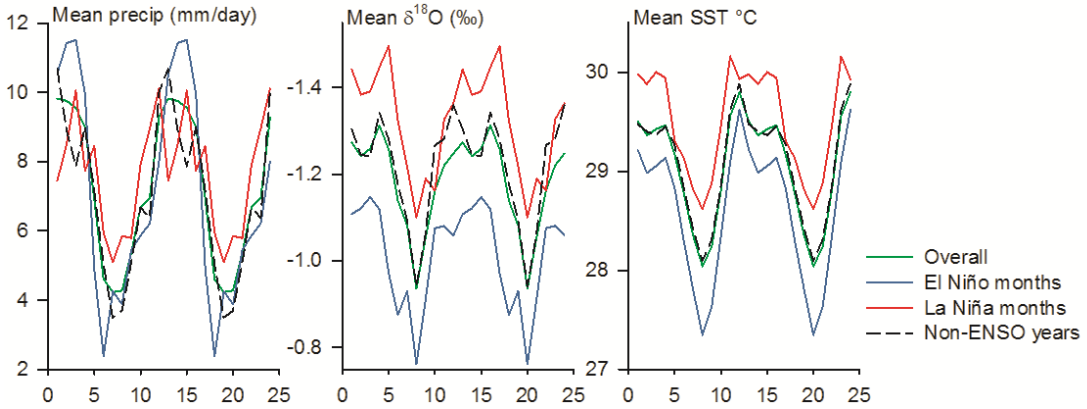

Figure 7.19 Mean seasonal $\delta^{18}O$ in MT7 during El Niño and La Niña months, compared to non-ENSO months and the overall mean seasonal cycle over the length of the record. Mean seasonal cycle of SST from IGOSS for 147.5°E, 6.5°S (Reynolds et al., 2002) during El Niño, La Niña and non-ENSO months, and the overall mean seasonal cycle from 1986-2002. Mean seasonal cycle of precipitation (mm/day) during El Niño and La Niña months (blended satellite and gauge data for 146.25°E, 6.25°S (Adler et al., 2003, Huffman et al., 2009)), compared to non-ENSO months and the overall amplitude from 1986-2002

$\delta^{18}O$ data from Holocene *T. gigas* suggest reduced seasonality during the early Holocene compared to the modern period. The three *T. gigas* show a reduction in seasonality of between 33 and 39%. This is consistent with a decrease in the annual insolation at 6.5°S during the early Holocene.

Comparison with published records of early Holocene seasonality

The seasonal cycles (using annual amplitude) obtained from the modern and early Holocene *T. gigas* suggest that the mean amplitude of the annual/seasonal cycle was up to 40% higher in the modern compared to Holocene *T. gigas* specimens. The timing of the seasonal cycle, i.e. the warmest and coolest months, and the double peak in $\delta^{18}O$ minima due to the passing over of the ITCZ, is the same as in the modern shell but this is in part due to August SST minima being used to construct the age model. Data from charcoal deposits from Papua New Guinea suggest reduced seasonality during the early

Holocene (Haberle et al., 2001), which is reflected here in the $\delta^{18}O$ data. There is no evidence for a stronger seasonal cycle as seen in the eastern Pacific (Carré et al., 2005). Early Holocene *Porites* corals from Papua New Guinea show seasonal fluctuations of 1°C and occasionally 2°C (McCulloch et al., 1996), which is consistent with the *T. gigas* data. In order to examine seasonality, high resolution records, ideally at monthly resolution, are needed from proxy records. Many coral records from the Holocene have a resolution of 4 samples/year, which is not ideal, and there are few published high resolution records to which the seasonality of *Tridacna* sp. $\delta^{18}O$ can be compared. General circulation models (GCMs) run for 9 ka BP and 6 ka BP have suggested greater seasonality during the early to mid-Holocene, due to increased obliquity and precession-driven changes in the timing of perihelion (Bush, 2007). However, this is not consistent in all models, and Braconnot et al. (2012) found a reduction in the magnitude of the seasonal cycle in the Niño 3 box of 64% at 6 ka BP and 26% at 9.5 ka BP, compared to the pre-industrial climate. The reduction in the annual amplitude, representing the seasonal cycle, is consistent with that of annual insolation for 6.5°S, as well as with the reduction found by Braconnot et al. (2012).

Inter-annual variability is higher in the modern *T. gigas* than within the early Holcoene *T. gigas* specimens, which is perhaps due to the suppression of strong anomalous events during the early Holocene. Conversely, fossil bivalve shells from Peru showed higher inter-annual variability during the early Holocene between 9 and 7.9 ka BP than during the modern period (Carré et al., 2005), suggesting stronger seasonality and a stronger ENSO at this period in the eastern equatorial Pacific. However, the *Mesodesma donacium* bivalves sampled by Carré et al. (2005) had short (3-5 year) record lengths, and the authors assumed that because each shell recorded a warm event, the probability was that such events were frequent. As the length of the records is short, the frequency of events cannot be extrapolated, and it could just be coincidence that warm events were recorded in each of the three shells.

Reconstructed seasonality from *T. gigas* $\delta^{18}O$ is consistent with published records from the western Pacific (e.g. Lorenz et al., 2006, Koutavas and Joanides, 2012) and models (e.g. Brown et al., 2008a, Braconnot et al., 2012, Luan et al., 2012) , which suggest reduced seasonality during the early Holocene.

7.4.2 Seasonality recorded in MIS3 *Tridacna* sp. $\delta^{18}O$

In the tropics, local seasonality is affected by changes in the seasonal cycle of insolation, particularly in response to precession and obliquity (Luan et al., 2012). *Tridacna* sp. samples which grew when the seasonal cycle of insolation was reduced compared to the present day would be expected to have a reduced seasonal cycle. The Holocene *T. gigas* show a reduction in mean annual amplitude $\delta^{18}O$ consistent with a decrease in seasonal insolation during the early Holocene, but this is not recorded in the MIS3 samples (Figure 7.20). The modern *T. gigas* shows higher mean amplitude than all but one fossil *Tridacna*.

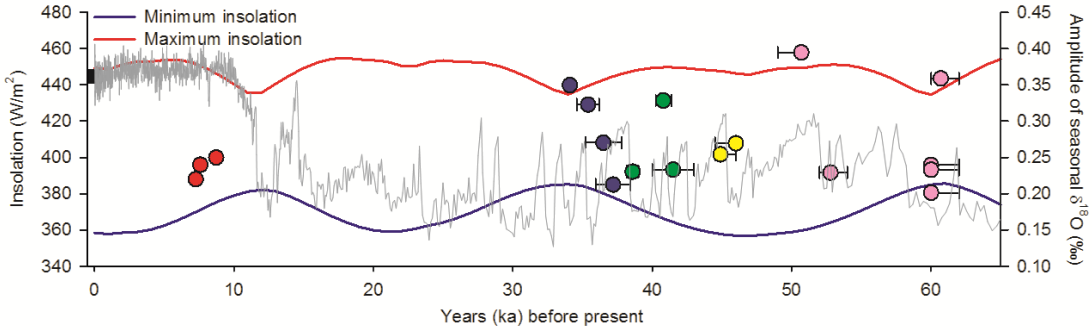

Figure 7.20 Maximum and minimum insolation for 6.5°S (Laskar et al., 2004), and amplitude of fossil *Tridacna* sp. mean annual $\delta^{18}O$. Samples are separated into reefs – modern (black square); Holocene (red); IIa (blue), IIIc (green), IIIb (yellow), IIIa (pink). Grey line shows the GISP2 $\delta^{18}O$ record (Grootes et al., 1993)

To test the significance of the change in annual amplitude of $\delta^{18}O$ between MT7 and fossil *T. gigas*, a Mann Whitney U Test was performed on both individual fossil samples, and those grouped into their separate reefs (Tables 7.3 and 7.4). Seven of the 15 individual samples show a statistically significant reduction in the amplitude of annual $\delta^{18}O$. When samples are grouped by reefs, the seasonal amplitude derived from fossil *Tridacna* sp. of three reefs show a statistically significant reduction (Table 7.4)

Table 7.3 Results of the Mann Whitney U Test for individual MIS3 *Tridacna* sp.

Shell	Reef	Age (ka BP)	Length of record (years)	Annual amplitude	Significant?	*p* value
T28	IIa	34.1	12	0.35±0.15	No	0.94
T27	IIa	35.4	8	0.32±0.13	No	0.69
T9	IIa	36.5	9	0.27±0.12	No	0.16
T11	IIa	37.2	7	0.21±0.08	Yes	0.035
T32	IIIc (l)	38.6	14	0.23±0.09	Yes	0.015
T39	IIIc (u)	40.8	13	0.33±0.15	No	0.66
T40	IIIc (u)	41.5	10	0.23±0.08	Yes	0.042
T24	IIIb	44.9	2	0.25±0.11	No	0.29
T37	IIIb	46	7	0.27±0.10	No	0.25
T41	IIIa (l)	50.7	9	0.39±0.18	No	0.76
T18	IIIa (m)	52.8	7	0.23±0.07	Yes	0.035
T15	IIIa (u)	60	38	0.20±0.08	Yes	<0.001
T22	IIIa (u)	60	5	0.24±0.13	No	0.083
T45	IIIa (u)	60	18	0.23±0.09	Yes	0.01
T6	IIIa (u)	60.7	6	0.36±0.16	No	0.91

Table 7.4 Results of the Mann Whitney U Test for samples grouped into their respective reefs

Reef	Length of record (years)	Annual amplitude	Significant?	*p* value
IIa	36	0.29±0.12	No	0.19
IIIc (l)	14	0.23±0.09	Yes	0.015
IIIc (u)	23	0.29±0.13	No	0.15
IIIb	9	0.26±0.10	No	0.15
IIIa (l)	9	0.39±0.18	No	0.76
IIIa (m)	7	0.23±0.07	Yes	0.035
IIIa (u)	67	0.23±0.10	Yes	<0.001

There is no published data from the tropical Pacific during MIS3 at sufficient resolution to compare to the bi-monthly *Tridacna* sp. $\delta^{18}O$ data. Stott et al. (2002) reconstructed summer and winter temperatures in the tropical Pacific using foraminifera Mg/Ca. Their work shows evidence that there were periods where the difference between summer and winter temperatures was greater, and less. However, these SST reconstructions come from two species of foraminifera thought to be representative of summer and winter temperatures. These data cannot be used to create a "seasonal amplitude" in temperature to compare to the *Tridacna* sp. $\delta^{18}O$ for a number of reasons. The resolution of the summer foraminifera (*G. ruber*) is at one measurement per 100-200 years, while the resolution of the winter foraminifera (*G. sacculifer*) is at one measurement per 200-2,000 years. Because of this disparity, there are very few occasions where both foraminifera species have been dated to the same short window as the *Tridacna* sp. samples. Additionally, while both species are surface-dwelling, there may be differences in habitat or growth which would add great uncertainties to a seasonal amplitude calculated, and to do so would assume that the two species were recording the same monthly values as the present day. While samples from the same

species of foraminifera have been used to reconstruct paleoseasonality (Evans et al., 2013), it is not possible to reconstruct a comparable seasonal amplitude to the *Tridacna* sp. data set using the Stott et al. (2002) time series.

While the data from Holocene *T. gigas* samples shows a reduction in $\delta^{18}O$ seasonality which coincides with a reduction in seasonal insolation, the seasonality recorded in MIS3 samples does not appear to be strongly correlated. This may be as a result of other factors such as high latitude processes (e.g. Heinrich events), shifts in the ITCZ (e.g. Ivanochko et al., 2005) or to changes in ocean circulation patterns (e.g. Timmermann et al., 2005a, Timmermann et al., 2005b).

7.4.3 Reduced ENSO variability recorded in Holocene *T. gigas* $\delta^{18}O$ profiles

The methods/metrics used to reconstruct ENSO variability in $\delta^{18}O$ time series were described in Chapter 6. In this section, the variance of the anomaly time series ($\delta^{18}O_A$, representing inter-annual variability attributable to ENSO) is used to quantify changes in ENSO variability. The number of events/10 years exceeding a $\delta^{18}O$ anomaly threshold of ±0.15‰ is also discussed in order to discuss changes in ENSO frequency through time. All results are compared to both 20th century ENSO variance and 1986-2002 ENSO variance (Figure 7.23).

The three *T. gigas* samples from the early Holocene all show a smaller range in $\delta^{18}O_A$, translating into smaller variance of the $\delta^{18}O_A$ time series (Figures 7.21 and 7.23). The reduction in variance compared with MT7, is approximately 78% (T73), 58% (T58) and 70% (T75). Each of the Holocene samples therefore shows at least a 50% reduction in variance compared to the modern *T. gigas*. There are no excursions in the $\delta^{18}O_A$ profile as large as those found in MT7, suggesting that there are no recorded events of greater amplitude to those seen in the modern shell. The significance of changes in variance was calculated using an *F* test approach, and the differences between all three fossil samples and the modern shell were found to be significant (one-tailed confidence levels – T58 and T75=95%, T73=99%). The three Holocene *T. gigas* profiles can be grouped together to create a 50 year record in a 1.8 ka window (Figure 7.22), and the difference in the inter-annual variance can be compared with both MT7 and the inferred $\delta^{18}O$ variance of the 20th century (Chapter 6). These results

show that there is a significant reduction in inter-annual variance (99% confidence level) between the grouped early Holocene samples and the modern *T. gigas* (69%), and the 20th century (53%).

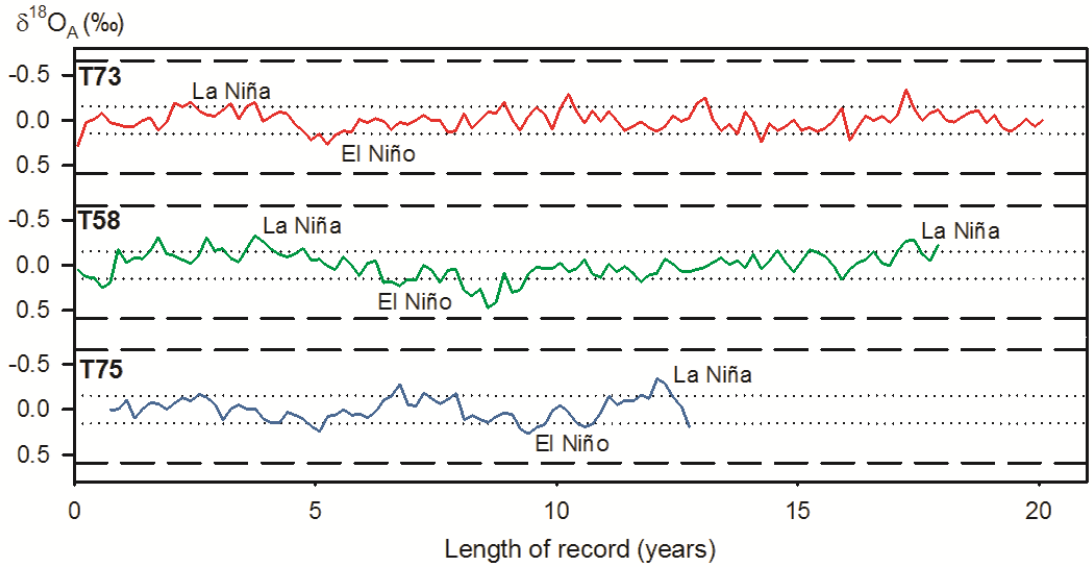

Figure 7.21 $\delta^{18}O_A$ profiles of three *T. gigas* samples. El Niño and La Niña events, where a threshold of ±0.15‰ (indicated by dotted line) is exceeded for at least 6 months, are marked on each profile. Dashed lines represent the maximum and minimum values of $\delta^{18}O_A$ in MT7

Using a threshold of ±0.15‰ to categorise events results in the following number of El Niño/10 years and La Niña/10 years: 0.5 El Niño in T73, 0.6 in T58 and 0.8 in T75, and 0.5 La Niña in T73, 1.1 in T58 and 0.8 in T75. With the exception of La Niña in T58, this a reduction of over 50% in the Holocene samples, compared with the 1.88 El Niño and 1.88 La Niña events/10 years seen in the modern *T. gigas* (Figure 7.23).

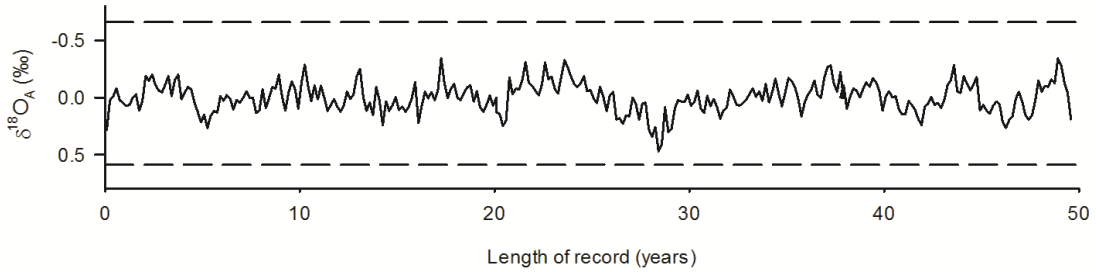

Figure 7.22 Combined $\delta^{18}O_A$ profile of T73, T58 and T75. Dashed lines represent the maximum and minimum values of $\delta^{18}O_A$ in MT7

There is also a reduction in the number of "strong" ENSO events, using a threshold of 0.31‰ for El Niño and 0.21‰ for La Niña (Chapter 6). In the modern record, two El

Niño and La Niña events, giving a ratio of 1.25 events/10 years, are seen (Figure 7.21). In the Holocene samples, only T58 records a cool (El Niño) event exceeding this threshold, and resulting in a ratio of 0.5 El Niño events/10 years.

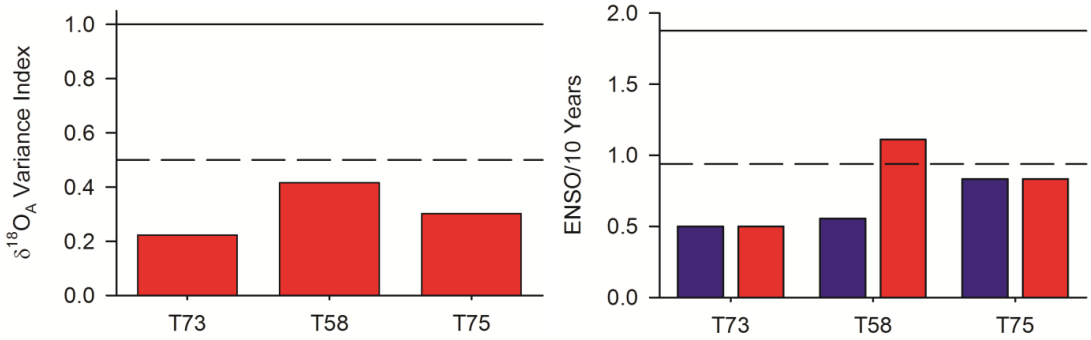

Figure 7.23 Comparison of variance of $\delta^{18}O_A$ in three Holocene samples, normalised to MT7 (left), and number of El Niño (blue) and La Niña (red) events per 10 years (right), calculated using a threshold of ±0.15‰. In both graphs, solid line represents value of MT7 and dashed line represents 50% of MT7

The fact that all three samples show a reduction in both inter-annual variability as well as a reduction in the frequency of anomalous "ENSO" events suggests that ENSO events were reduced between 9-7 ka BP. Although the records are for 20 years or less, the $\delta^{18}O_A$ profiles capture anomalous episodes which appear to be similar to modern day El Niño and La Niña. The number of events/10 years and the variance of $\delta^{18}O_A$ is reduced by over 40% in each shell, suggesting that both the frequency and amplitude of ENSO events was reduced in the early Holocene, and strong events were rare.

Comparison with other paleoclimate records of ENSO variability

The reduction in ENSO frequency and amplitude in Holocene *T. gigas* is consistent with coral data from the early/mid Holocene in the western Pacific (Figure 7.24). McGregor and Gagan (2004) found a reduction in El Niño amplitude of 15% and a reduction in El Niño frequency from 19 events/century for 1950-1997 to 12 events/century from corals dated between 7.6-7.1 ka BP from Papua New Guinea. Although *Tridacna* sp. records are shorter and require extrapolation to quantify the number of events per century, there would be an increase from 6 events/century in the three Holocene samples to 18 El Niño events/century using MT7 (1986-2002). Tudhope et al. (2001) found ENSO variance was lower during the mid-Holocene (6.5ka) than the late Holocene and present day using the standard deviation of bandpass filtered coral $\delta^{18}O$

records from Papua New Guinea. Other studies based on the $\delta^{18}O$ recorded by planktonic foraminifera also show a reduction in variance for this period. Results derived from deep sea sediment cores from the Seram Trough, eastern Indonesia have suggested that during the early Holocene (10-6 ka BP) high-frequency variability was lower than during the mid-late Holocene (6-2 ka BP) (Brijker et al., 2007).

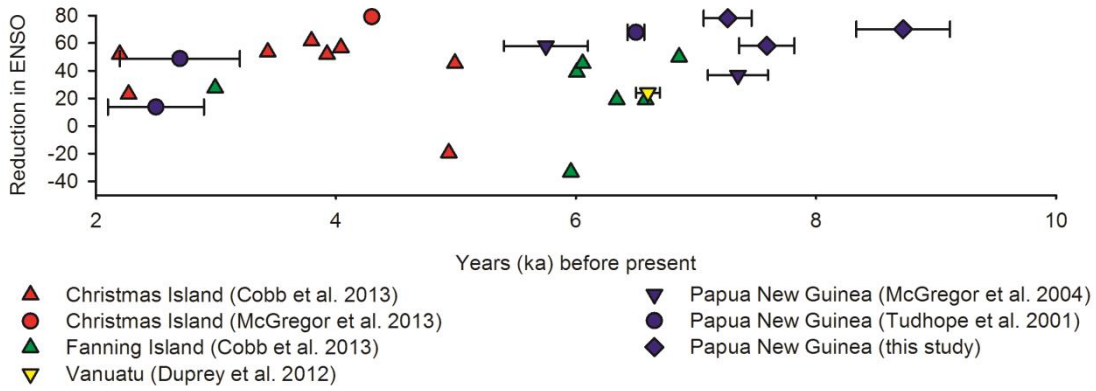

Figure 7.24 Published high resolution records of ENSO from Pacific corals. ENSO calculated using the bandpass filtered records of coral $\delta^{18}O$ and the frequency of events (McGregor and Gagan, 2004). Christmas and Fanning islands are in the central Pacific and Vanuatu is in the southern Pacific (see Figure 4.1)

Although ENSO variability appears to have been reduced during the early to mid-Holocene, this reduction was not sustained throughout the entire Holocene. Cobb et al. (2013) found highly variable ENSO throughout the Holocene in Pacific coral $\delta^{18}O$ (e.g. Figure 7.24). This study focuses on the central Pacific and covers the past 7,000 years (some corals shown in Figure 7.24). ENSO variance has been found to be higher during the late Holocene (~ 3-1 ka BP) than the mid-Holocene (Tudhope et al., 2001). The oldest coral from the Cobb et al. (2013) study shows a ~40% reduction in ENSO variability, calculated using the standard deviation of bandpass filtered coral $\delta^{18}O$. Additionally, Corrège et al. (2000) found that inter-annual SST anomalies were 2-3 times higher at ~4.2 ka BP than present, using Sr/Ca measured in a *Porties* coral.

The concentration of fine-grained lithic fragments, eroded by intense runoff and washed onto the shelf via local rivers, have been measured in sediment cores and used as a proxy for El Niño flood events (e.g. Rein et al., 2004, Rein et al., 2005). Lithic peaks in eastern Pacific marine sediments indicate strong El Niño floods between 5-1 and 12-10 ka BP, with reduced flooding between 9-6 ka BP (Rein et al., 2005). Koutavas et al.

(2006) found that the variance of $\delta^{18}O$ in individual foraminifera from the eastern Pacific was 50% lower during the mid-Holocene (7-5 ka BP) than modern. ENSO reconstructions from the early to mid-Holocene show a variety of responses to background changes across the Pacific. In the central and southern Pacific there is more variability over time (Figure 7.24), while in the western Pacific there is a consistent reduction in variance. This is consistent with the early to mid-Holocene data presented here, which shows a reduction in ENSO variance. However, this may also be a result of site sampling bias, with many records from the Line Islands (central Pacific) and around Papua New Guinea, due to the availability of fossil corals and bivalves.

Comparison with modelling studies of Holocene ENSO variability

While the data from this study cannot confirm the mechanisms causing the reduction in ENSO during the early to mid-Holocene, it can be compared to modelling studies covering the same time period. The mid-Holocene climate is often simulated using climate models (Table 7.5), partly because background conditions were similar to today (with similar SSTs, sea level and ice sheet cover). However, there were differences in orbital parameters leading to changes in seasonality. Models run for the mid-Holocene tend to suggest a suppression in ENSO variability, generally attributed to changes in insolation. Bush (2007) found that simulations of the climate at 9 ka BP and 6 ka BP exhibited a La Niña-like mean climate which they proposed was due to stronger easterly winds and a steeper tilt to the thermocline. Brown et al. (2006) found a 12% reduction in ENSO amplitude at 6 ka BP, due to changes in the timing of perihelion and the seasonal cycle of insolation. Otto-Bliesner et al. (2003) found a statistically significant reduction in inter-annual variability at 8.5 and 6 ka BP compared to modern, which they attributed to changes in zonal and vertical gradients of ocean temperature, and to seasonal insolation variations. Results from these climate models are compiled in Table 7.5.

Table 7.5 Change in Niño3 variance reported in modelling studies of the early/mid Holocene and modern day simulations. Modified after Roberts et al. (2014)

Model (reference)	Time (ka BP)	Change in Niño3 Variance	Hypothesis/Findings
Zebiak-Cane (Clement et al., 2000)	Past 12 ka	Smaller amplitude, less frequent warm and cold events	Decreased instability in ENSO mode due to enhanced trade winds and changed seasonality
FOAM (Liu et al. 2000)	11, 6	-20%	Increased stability of ENSO mode due to weakened thermocline. Intensity reduced by intensified Asian summer monsoon.
CSM1.4 (Otto-Bliesner et al., 2003)	11, 8.5	-22% and -28%	Increased stability in ENSO mode due to weakened thermocline.
HadCM3 (Brown et al., 2006)	6	-12% in ENSO amplitude	Increased stability in ENSO mode due to enhanced trade winds and changed seasonality.
GDFL, MOM2 (Bush, 2007)	9, 6	-47% and -35% reduction in El Niño strength (Niño 3.4)	Changes in orbital forcing regulate the strength of climatological easterlies.
HadCM3 (Brown et al., 2008a)		-24%	Increased stability in ENSO mode due to enhanced trade winds and changed seasonality.
PMIP2 (Zheng et al., 2008)	6	+3.3 to -22.5%	Increased stability in ENSO mode due to enhanced trade winds and changed seasonality.
CAM+RGO (Chiang et al., 2009)	6	-38%	Reduction in amplitude of stochastic forcing from the extratropics.
IPSL-CM4 (Braconnot et al., 2012)	9.5, 6	Fewer warm and cold events	Increased stability in the ENSO mode due to enhanced trade winds.
KCM (Salau et al., 2012)	9.5, 6	5% and 6% reduction in ENSO amplitude	ENSO amplitude increases linearly with SSTs in the tropical Pacific and with an increased west-east equatorial SST gradient.

7.4.4 Potential mechanisms on Early Holocene ENSO

Modelling studies (e.g. Table 7.5) have suggested that changes in insolation caused the reduction in ENSO during the early to mid-Holocene, but there is little consensus on the processes responsible (Roberts et al., 2014). There are three hypotheses:

1) Proposed by Clement et al. (2000). ENSO variance is reduced as changes in the climatological mean state of the tropical Pacific ocean-atmosphere system render the ENSO eigenmode less unstable than in the modern climate. Using the Zebiak-Cane model, they found that the most important changes were enhanced trade winds and changed seasonality.

2) Liu et al. (2000) suggested that changes in the mean state of the thermocline along the equator stabilise the ENSO mode, which they hypothesised was the likely source of reduced ENSO in the CSM1.4 model.

3) A third hypothesis proposed by Chiang et al. (2009) and Chiang and Fang (2010) suggests that reduced ENSO variability was due to a change in the weather in the extra-tropical northern hemisphere which supplies the noise forcing that excites ENSO in their model (Roberts et al., 2014). The data presented within this thesis are consistent with a reduction in ENSO during the early to mid-Holocene found in modelling studies.

Insolation

The reduction in ENSO variability during the early to mid-Holocene has been suggested to have been a result of changes in solar forcing. Models suggest that changes to insolation and the timing of perihelion led to a reduction of ENSO amplitude and variability compared to the 20th century. In the modern climate, perihelion, the point earth is closest to the sun, occurs in boreal winter. In the early and mid-Holocene, perihelion occurred during boreal summer. This increased incoming solar radiation at the top of the atmosphere by about 5% during summer compared to today (Cane et al., 2006). During the mid-Holocene, there was therefore greater heating in summer and lower heating in winter, altering the seasonal cycle and suppressing the development of El Niño events by stronger trade winds and a cooling in the eastern Pacific.

The Zebiak-Cane model, used by Clement et al. (2000) uses solar insolation as the only forcing and demonstrates that orbitally driven changes in the seasonal cycle can alone alter ENSO behaviour in a way that is consistent with data. The difference between maximum and minimum monthly insolation for 6.5°S over the past 10 ka can be compared to the variance of $\delta^{18}O_A$ of *T. gigas*, as well as three Holocene corals from Papua New Guinea (Tudhope et al., 2001) (Figure 7.25). ENSO variance is higher in the late Holocene *Porites* corals than the early or mid-Holocene samples. The late Holocene *Porites* grew during a period with higher mean summer insolation during austral summer than both today, and the early and mid-Holocene. The late Holocene *Porites* shows almost as high variance as the 20th century (Figure 7.25), but not as high as MT7.

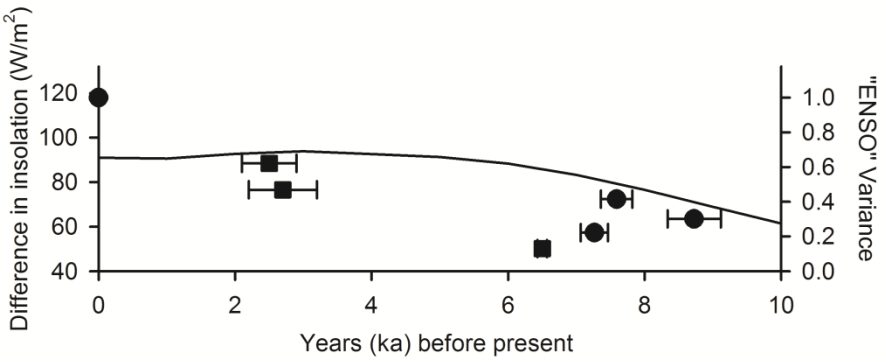

Figure 7.25 Difference between maximum and minimum monthly insolation for 6.5°S (Laskar et al., 2004), and variance of $\delta^{18}O_A$ of Holocene *T. gigas* (circles), and *Porites* corals from Papua New Guinea (Tudhope et al., 2001) normalised to MT7

The data from this study is therefore in agreement with the reduction in ENSO predicted by models detailed in Table 7.5. At this moment it is not possible to resolve the reasons for this reduction with the available data.

7.4.5 Variable ENSO during MIS3

Between 40 and 34 ka BP, all five *Tridacna* show a reduction in inter-annual variance, relative to the modern, of between 37 and 85%, (significant in T28 at the 90% confidence level, T9 and T32 at the 95% confidence level, T11 at the 99% confidence level using the *F* test approach, non-significant in T27) (Figure 7.26). The *Tridacna* sp. can be compared to *Porites* coral records published from the same location (Tudhope et al., 2001). If the corals undergo the same data processing, they show a reduction in variance of between 36 and 87% (Figure 7.29). The range of variance for the shells and corals is similar, and they do not exceed that recorded by the modern *T. gigas*, or that calculated for the 20th century using HadISST. This is consistent with a simulation of 35 ka BP using the CCSM3 climate model, which found a non-significant reduction in ENSO variability (Merkel et al., 2010).

The samples dated between 60 and 40 ka BP show a large range of reduction in variance compared to the modern *T. gigas*, of between 1 and 83%. The Tudhope et al. (2001) coral dated to 41.9 ka BP and the *T. maxima* (T40) dated to 41.2±3 ka BP show a significant (99% confidence level for coral, 95% confidence level for *Tridacna* sp.) reduction of 73% and 69% relative to the modern shell. The *Tridacna* sp. from the IIIa (u) reef demonstrate a reduction of between 29% (T45, not significant) and 76% (T15,

significant at the 99% confidence level). Thermocline reconstructions from foraminifera from the eastern equatorial Pacific suggest higher "ENSO" variability at 52.1 ka BP than between 39.6 and 38.9 ka BP (Leduc et al., 2009). Although there is only one sample dated to ~50 ka BP (T41), it shows higher variance than any of the seven *Tridacna* sp. and corals dated between 40-34 ka BP, as well as those dating back to ~60 ka BP.

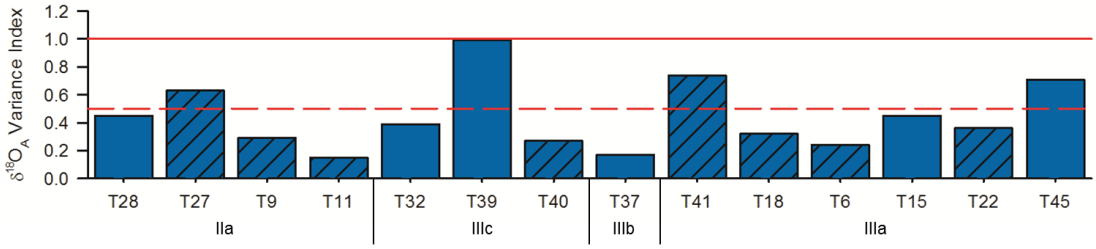

Figure 7.26 Variance of $\delta^{18}O_A$ time series of MIS3 *Tridacna* sp., normalised to MT7 variance. Red line represents MT7 variance and dashed line represents 50% of MT7 variance. Hatched bars represent shells with a record length of 10 years or less. Samples are separated into reefs

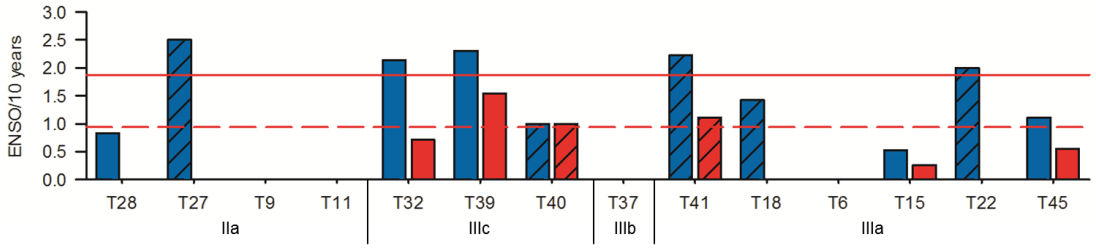

Figure 7.27 Number of El Niño (blue) and La Niña (red) events per 10 years in MIS3 *Tridacna* sp. shells. Red line represents MT7 with 1.9 El Niño and 1.9 La Niña events per 10 years, and dashed line represents 50% of MT7. Hatched bars represent shells with a record length of 10 years or less. Samples are separated into reefs

If the MIS3 *Tridacna* sp. are grouped together, the difference in the grouped inter-annual variance can be compared with the modern *T. gigas* (MT7) and the variance of ENSO metrics in the 20th century. There is a significant reduction (35%) in variance (99% confidence level) compared to that of the 20th century, as well as a significant reduction (57%) compared to the modern *T. gigas* which represents the late 20th century. The fourteen MIS3 shells show a 28% increase in variance (90% confidence level) compared to the three Holocene shells. Due to the fact that the compiled records cover ~160 years in a 25,000 year period, or approximately 0.005% of the time that they span, it cannot be assumed that ENSO was consistently significantly reduced over the entire glacial period. Individual *Tridacna* sp. have higher variance than that calculated for the 20th century (Figure 7.27), which suggests that the events seen in the

instrumental record over the past ~100 years are not unprecedented in glacial fossil shells. The number of El Niño events/century can be calculated and there is a reduction from 18 events/century using MT7 to 11 events/century during MIS3; while the number of La Niña events/century is reduced to 4 events/century.

The ratio of warm to cold events is approximately 1:1 in both MT7 and between 1950 and 2011 (Figure 7.28), while in the Holocene data there is a very slight preference for warm La Niña events. In the MIS3 data, there is a stronger preference for El Niño events, which involve cooler and drier conditions than usual at the Huon Peninsula.

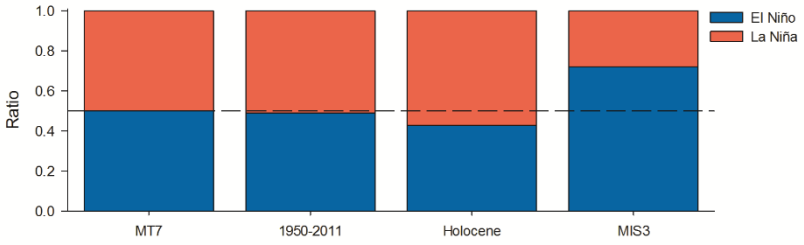

Figure 7.28 Ratio of El Niño to La Niña events in MT7, the instrumental record from 1950-2011, the three Holocene *T. gigas* shells and the MIS3 *Tridacna* sp. shells

Clement et al. (1999) suggested that cool events would be more frequent and intense during glacial periods as a result of insolation forcing. Although the MIS3 data does not show more frequent or intense El Niño events than today, there is clearly a preference for cool events during the glacial period.

7.4.6 Potential mechanisms acting on MIS3 ENSO

Insolation

During the Holocene, a suppression of ENSO has been proposed as a response to changes in solar insolation, either directly through the timing of the seasons or due to changes in the monsoon cycle, which strengthened the trade winds in the Pacific, leading to a suppression of El Niño events (Cane et al., 2006). During MIS3 (Figure 7.29), there does not appear to be a relationship between seasonal insolation (i.e. the difference between maximum and minimum monthly insolation) for 6.5°S, and the variance of fossil *Tridacna* $\delta^{18}O_A$.

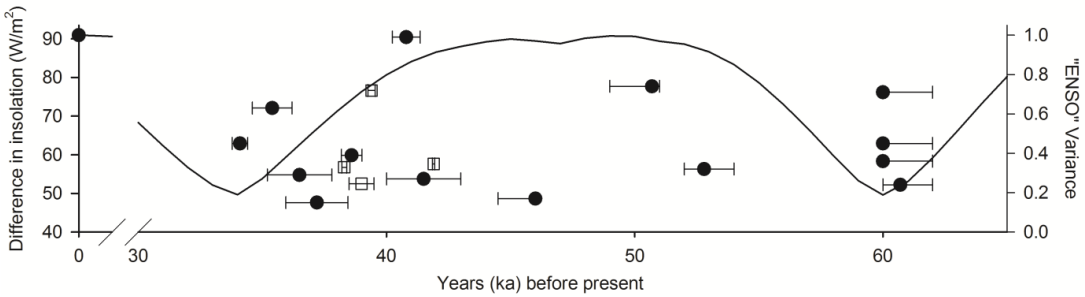

Figure 7.29 Difference between maximum and minimum monthly insolation for 6.5°S (Laskar et al., 2004), and variance of $\delta^{18}O_A$ of MIS3 *Tridacna* sp. shells (circles), normalised to MT7. Squares indicate the variance of $\delta^{18}O_A$ of *Porites* corals from Papua New Guinea (Tudhope et al., 2001) normalised to MT7.

A reduction in the variance of bandpass filtered coral $\delta^{18}O$, used as a metric for ENSO in paleoclimate data during MIS3 has been attributed to glacial dampening (Tudhope et al., 2001), while an increase in ENSO (defined as the 500 year average Niño 3 index, Figure 7.30) seen in models during MIS3 has been attributed to extreme strengths of the seasonal cycle on a semi-precessional cycle – e.g. when perihelion is in either boreal spring or autumn (Clement et al., 1999). Although the fossil *T. maxima* with the highest variance (T39) possibly grew during a period when perihelion occurred during boreal spring, other *Tridacna* sp. from a similar time period show significantly reduced variance. Most models tend to focus on the LGM, rather than spanning the whole of MIS3. There are few published studies to compare the *Tridacna* sp. data to, and few model outputs which could suggest changes to ENSO during this time period (Table 7.6).

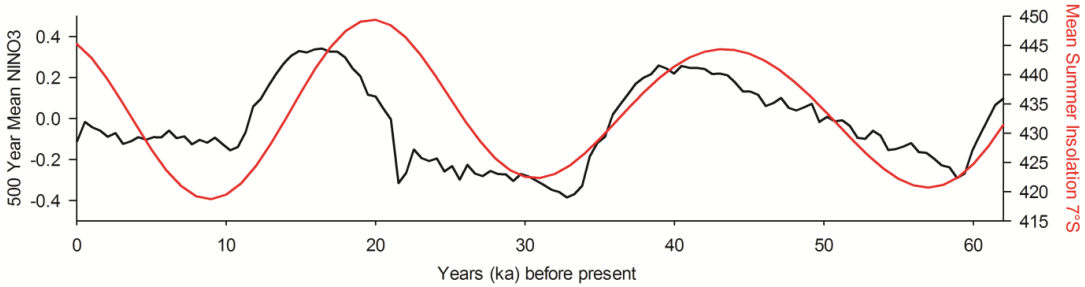

Figure 7.30 Result of Zebiak-Cane model from Clement et al. (1999) for 500 year mean Niño3, and mean Austral summer insolation on right axis.

The predicted ENSO variance from the Zebiak-Cane model can be compared to that of $\delta^{18}O_A$ from the MIS3 fossil shells, normalised to MT7 (Figure 7.31). If insolation was the only forcing on ENSO during MIS3, then the Zebiak-Cane model predicts that there would be periods of higher and lower ENSO variance than the modern period. The data

from MIS3 *Tridacna* sp. does not support this, as only one shell shows as high a variance as the modern shell, and most shells show statistically significantly reduced variance.

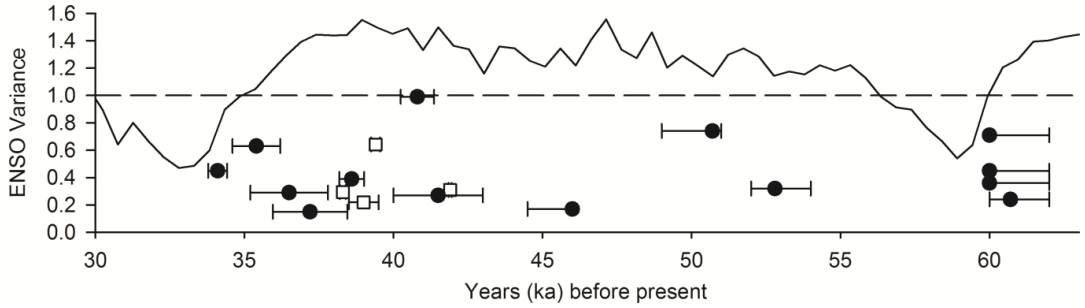

Figure 7.31 ENSO Variance from Zebiak-Cane model (1999) and MIS3 *Tridacna* sp. $\delta^{18}O_A$ (circles) and *Porites* $\delta^{18}O_A$ variance (squares) normalised to MT7

Table 7.6 Model findings for ENSO during glacial periods

Model (reference)	Time period	Findings
Zebiak-Cane (Clement et al., 1999)	Past 150 ka	Warm periods occur when perihelion is in Jan-June, cold periods when July-Dec.
		Cold event frequency and amplitude is larger in cold periods.
NCAR CCSM (Peltier and Solheim, 2004)	LGM	El Niño considerably more intense under full glacial conditions.
ECHO-G (Timmermann et al., 2007)	142 ka	If annual cycle amplitude is large, ENSO activity is weak.
		Orbital ENSO modulations are strongly controlled by annual cycle.
CCSM3 (Merkel et al., 2010)	MIS3	HS1 – Increase of ENSO variability despite an overall deepening of the thermocline.
		LGM conditions produce a larger number of moderate La Niña events.
CGCM (Brandefelt et al., 2011)	30-60 ka	Glacial boundary conditions induce modulations to ENSO.
		Amplitude of sea level pressure anomalies associated with ENSO in the NA are significantly reduced in glacial climates.

Additional Mechanisms

The *Tridacna* sp. used in this study were collected from a tectonically active region, and it has been suggested that volcanic activity can be recorded in corals (Crowley et al., 1997), and that explosive volcanoes can trigger El Niño events (Adams et al., 2003). A Holocene fossil coral from Vanuatu (Corrège et al., 2000) recorded a cooling which the authors linked to a volcanic eruption recorded in the GISP $\delta^{18}O$ record. While there may be a transient response to volcanic activity within the tropical Pacific, it is impossible at present to link this to the data within this study.

7.4.7 Relationship between ENSO and seasonality

Timmermann et al. (2007) suggested that ENSO activity is strongly controlled by the annual cycle in short-wave radiation, due to changes in precession, obliquity and eccentricity. The modern mean SST cycle at 6.5°S has been shown to mirror the seasonal cycle of insolation for 6.5°S (Figure 7.10) and it seems likely that this relationship occurred during the last glacial period. The mean amplitude of the annual cycle of $\delta^{18}O$, calculated as described in 6.1, can be compared to reconstructed ENSO variability, calculated as the variance of the anomaly time series ($\delta^{18}O_A$) (Figure 7.32). Although there is not a direct linear relationship between the annual cycle of $\delta^{18}O$ and ENSO variability, there is a positive correlation between the two (r^2=0.38). This suggests that when the amplitude of the annual cycle is large, ENSO variability is increased. This may be in part due to the fact that if there are El Niño and La Niña events recorded in *Tridacna* sp. $\delta^{18}O$ time series, they will cause an enhanced annual cycle. This is not consistent with Timmermann et al. (2007), who found that orbital modulations of ENSO were strongly controlled by the strength of the annual cycle, resulting in weak ENSO activity when the equatorial annual cycle was large (Table 7.6). They attributed this to the precessional cycle modifying meridional asymmetry and the strength of cross-equatorial winds, which drive changes in the strength of the annual cycle on the equator. However, the model used by Timmermann et al. (2007) also did not find the early to mid-Holocene ENSO suppression, which has been recorded in corals, sediment cores and *Tridacna* sp. from across the Pacific.

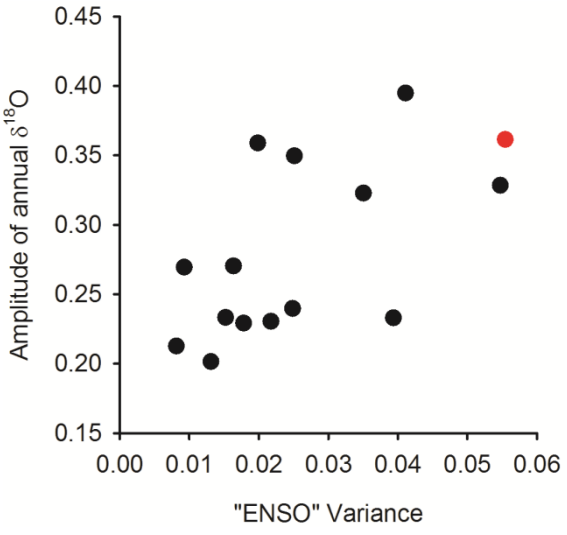

Figure 7.32 Relationship between ENSO variance, calculated from the $\delta^{18}O_A$ time series, and the mean amplitude of annual $\delta^{18}O$, calculated as described in the Methods section. Red circle shows the modern *T. gigas*, MT7

7.5 Conclusions

Three *T. gigas* from the Huon Peninsula, dated between 8.76 and 7.23 ka BP record changes in temperature and evaporation/precipitation during the early Holocene. Monthly $\delta^{18}O$, averaged over each individual shell profile, suggest a monthly seasonal cycle with a similar amplitude to the modern *T. gigas*, and monthly cycles are reproducible between the three Holocene samples. The mean annual amplitude of Holocene *T. gigas* $\delta^{18}O$ is reduced by up to 40% compared to modern, while the variance of ENSO in the three Holocene shells is at least 50% less than in the modern *T. gigas* from the Huon Peninsula.

The $\delta^{18}O$ profiles of 14 *Tridacna* sp. shells collected from the MIS3 reefs reveal information about local seasonality and ENSO at discrete intervals during the last glacial period. Most shells show a reduced mean amplitude of annual $\delta^{18}O$, used here to gather information about the seasonal cycle in SST and salinity at the Huon Peninsula. Unlike the *T. gigas* from the Holocene, the reduction in seasonality is not consistent with changes in solar insolation over MIS3, suggesting that other forces affected local seasonality during the last glacial period. The variability of ENSO appears to have been generally suppressed during MIS3. However, individual shells still record El Niño and La Niña events, with a tendency for more cool/dry El Niño events. The reduction in ENSO variability recorded in these $\delta^{18}O$ profiles may suggest that ENSO was reduced globally during this time period, possibly due to glacial dampening, or it could suggest that ENSO was still operating as usual, but the signal was reduced in the west Pacific, meaning that fewer events were captured by the *Tridacna* sp. $\delta^{18}O$.

8. Conclusions and Future Work

The aim of this project was to use a paleoclimate archive to study variability in seasonality and the El Niño Southern Oscillation (ENSO) during the early Holocene and last Glacial (MIS3) periods. The archive has the potential to be used for local climate reconstruction during periods where usual paleoclimate archives such as corals are unavailable or have undergone diagenesis. While much paleoclimate data is available for the Holocene, there are fewer studies on glacial timescales, particularly with high resolution records which are needed to reconstruct seasonality.

The study site where modern and fossil samples were collected has a small seasonal cycle in SST, with large changes in evaporation/precipitation throughout the year. It is within the core ENSO region and is influenced by inter-annual variability due to ENSO. Geochemical profiles of samples from this site are therefore influenced by ENSO.

8.1 General conclusions

Geochemical profiles derived from *Tridacna* sp. have been shown to be faithful recorders of climate (e.g. Aharon, 1991, Elliot et al., 2009), while the stable oxygen isotope ($\delta^{18}O$) record of a modern *T. gigas* has been shown to record accurately El Niño and La Niña events at the Huon Peninsula (Welsh et al., 2011). This modern *T. gigas* was used as a benchmark against which to test geochemical profiles derived from four Holocene *T. gigas*, and 17 MIS3 *Tridacna* sp.

The $\delta^{18}O$ derived from *T. gigas* samples collected from Holocene reefs suggest a theoretical reduction in mean SST of ~0.5°C, which is within estimates of mean climate from around the tropical Pacific, and a slight increase in salinity. As this assumes that SST and evaporation/precipitation (inferring salinity) contribute equally to *T. gigas* $\delta^{18}O$, the evidence from these samples could suggest a similar temperature to today, with a larger increase in salinity, if evaporation/precipitation contributed more to the $\delta^{18}O$ signal during the Holocene.

During MIS3, $\delta^{18}O$ derived from fossil samples provides evidence of a possible decrease in temperature of 0-2.5°C, or an increase in salinity of 0-2‰. There are fewer SST

reconstructions for MIS3, but those available record a decrease in temperature of anywhere between 0 and 4°C. If the SST signal was more dominant than evaporation/precipitation during MIS3, $\delta^{18}O$ from MIS *Tridacna* sp. could infer theoretical decreases in temperature towards the higher end of these reconstructions.

In order to examine changes in variability of ENSO over the past 60 ka, a number of methods were tested in order to reconstruct ENSO in the $\delta^{18}O$ profile of modern and fossil *Tridacna* sp. The variance of inter-annual anomalies ($\delta^{18}O_A$) gave reasonably similar results to that of bandpass filtered $\delta^{18}O$, which is used with longer coral records to reconstruct variability within the ENSO band. In turn, the variance of these two metrics was comparable to the number of El Niño or La Niña/decade calculated using the $\delta^{18}O_A$ profile. This adds weight to the assumption that these metrics accurately capture some change in ENSO. The *T. gigas* from the Holocene show over 50% reduction in variance of both metrics, with a significant decrease in the number of events/decade, as well as the number of strong events. Previous work, from both paleoclimate data and climate models, have suggested a suppression in ENSO during the early to mid-Holocene, and the data presented in this study are in agreement with the suppression. During MIS3, although most *Tridacna* sp. show a reduction in both variance of the quantitative metrics and the frequency of events/decade, there is one shell which shows as high variance as the modern *T. gigas*. The data suggest that ENSO variability was reduced during the glacial period, but ENSO was not completely absent and strong events, although rare, did occur.

Due to the resolution of the *Tridacna* sp. geochemical profiles, it was possible to reconstruct seasonality in the fossil data set. During the early Holocene, seasonality was reduced by up to 40%, consistent with a reduction in seasonal insolation during this time period. During MIS3, a general reduction in seasonality is not consistent with insolation, which was not consistently reduced compared to today.

8.2 Further work

The trace element profiles derived from *Tridacna* sp. samples appear to provide indirect information about environmental parameters including SST and productivity. Unfortunately, this information remains qualitative rather than quantitative. The

relationship between Ba/Ca and chlorophyll a data shows promise in the modern *T. gigas* shell, and could be taken further with more modern specimens. The availability of chlorophyll a data is poor, and may only have implications for assessing local productivity.

Due to the size of the data set and uncertainties in dating, it was not possible to make strong conclusions regarding the effect of rapid climate change at high latitudes on temperature and evaporation/precipitation in the tropics. Additional *Tridacna* sp. shells from Heinrich equivalent reefs with better constrained ages might provide supplementary information regarding changes in the tropics as a result of Heinrich events.

References

Abram, N. J., McGregor, H. V., Gagan, M. K., Hantoro, W. S. & Suwargadi, B. W. 2009. Oscillations in the southern extent of the Indo-Pacific Warm Pool during the mid-Holocene. *Quaternary Science Reviews,* 28**,** 2794-2803.

Accordi, G., Brilli, M., Carbone, F. & Voltaggio, M. 2010. The raised coral reef complex of the Kenyan coast: *Tridacna gigas* U-series dates and geological implications. *Journal of African Earth Sciences,* 58**,** 97-114.

Adams, J. B., Mann, M. E. & Ammann, C. M. 2003. Proxy evidence for an El Niño-like response to volcanic forcing. *Nature,* 426**,** 274-278.

Adler, R. F., Huffman, G. J., Chang, A., Ferraro, R., Xie, P. P., Janowiak, J., Rudolf, B., Schneider, U., Curtis, S., Bolvin, D., Gruber, A., Susskind, J., Arkin, P. & Nelkin, E. 2003. The version-2 global precipitation climatology project (GPCP) monthly precipitation analysis (1979-present). *Journal of Hydrometeorology,* 4**,** 1147-1167.

Aharon, P. 1983. 140,000-Yr Isotope Climatic Record from Raised Coral Reefs in New-Guinea. *Nature,* 304**,** 720-723.

Aharon, P. Carbon isotope record of late quaternary coral reefs: Possible index of sea surface paleoproductivity. The carbon cycle and atmospheric CO2: Natural variations archean to present; Proceedings of the Chapman Conference on Natural Variations in Carbon Dioxide and the Carbon Cycle, 9-13 Jan. 1984 1985 Tarpon Springs, FL: United States. 343-355.

Aharon, P. 1991. Recorders of reef environment histories: stable isotopes in corals, giant clams and calcareous algae. *Coral Reefs,* 10**,** 71-90.

Aharon, P. & Chappell, J. 1986. Oxygen isotopes, sea level changes and the temperature history of a coral reef environment in New Guinea over the last 105 years. *Palaeogeography, Palaeoclimatology, Palaeoecology,* 56**,** 337-379.

Aharon, P., Chappell, J. & Compston, W. 1980. Stable Isotope and Sea Level Data from New Guinea Supports Antarctic Ice-Surge Theory of Ice Ages. *Nature,* 283**,** 649-651.

Alibert, C. & Kinsley, L. 2008. A 170-year Sr/Ca and Ba/Ca coral record from the western Pacific warm pool: 1. What can we learn from an unusual coral record? *Journal of Geophysical Research-Oceans,* 113.

Alibert, C. & McCulloch, M. T. 1997. Strontium/calcium ratios in modern Porites corals from the Great Barrier Reef as a proxy for sea surface temperature: Calibration of the thermometer and monitoring of ENSO. *Paleoceanography,* 12**,** 345-363.

Allan, R. 2000. ENSO and climatic variability in the past 150 years. *In:* Diaz, H. F. & Markgraf, V. (eds.) *El Niño and the Southern Oscillation – Multiscale variability and global and regional impacts.* Cambridge: Cambridge University Press.

Allison, N., Finch, A. A., Webster, J. M. & Clague, D. A. 2007. Palaeoenvironmental records from fossil corals: The effects of submarine diagenesis on temperature and climate estimates. *Geochimica Et Cosmochimica Acta,* 71**,** 4693-4703.

An, S. I., Timmermann, A., Bejarano, L., Jin, F. F., Justino, F., Liu, Z. & Tudhope, A. W. 2004. Modeling evidence for enhanced El Niño-Southern Oscillation amplitude during the Last Glacial Maximum. *Paleoceanography,* 19**,** 18.

Antonov, J. I., Seidov, D., Boyer, T. P., Locarnini, R. A., Mishonov, A. V., Garcia, H. E., Baranova, O. K., Zweng, M. M. & Johnson, D. R. 2010. World Ocean Atlas 2009, Volume 2: Salinity. *In:* Levitus, S. (ed.) *NOAA Atlas NESDIS 69.* Washington, D.C.: U.S. Government Printing Office.

Arz, H. W., Lamy, F., Ganopolski, A., Nowaczyk, N. & Paetzold, J. 2007. Dominant Northern Hemisphere climate control over millennial-scale glacial sea-level variability. *Quaternary Science Reviews,* 26**,** 312-321.

Ayliffe, L. K., Bird, M. I., Gagan, M. K., Isdale, P. J., Scott-Gagan, H., Parker, B., Griffin, D., Nongkas, M. & McCulloch, M. T. 2004. Geochemistry of coral from Papua New Guinea as a proxy for ENSO ocean-atmosphere interactions in the Pacific Warm Pool. *Continental Shelf Research,* 24**,** 2343-2356.

Barats, A., Amouroux, D., Chauvaud, L., Pécheyran, C., Lorrain, A., Thébault, J., Church, T. M. & Donard, O. F. X. 2009. High frequency Barium profiles in shells of the Great Scallop *Pecten maximus*: a methodical long-term and multi-site survey in Western Europe. *Biogeosciences,* 6**,** 157-170.

Batenburg, S. J., Reichart, G. J., Jilbert, T., Janse, M., Wesselingh, F. P. & Renema, W. 2011. Interannual climate variability in the Miocene: High resolution trace element and stable isotope ratios in giant clams. *Palaeogeography, Palaeoclimatology, Palaeoecology,* 306**,** 75-81.

Bathurst, R. G. C. 1975. *Carbonate Sediments and Their Diagenesis,* Amsterdam, Elsevier.

Beck, J. W., Edwards, R. L., Ito, E., Taylor, F. W., Recy, J., Rougerie, F., Joannot, P. & Henin, C. 1992. Sea surface temperature from coral skeletal strontium calcium ratios. *Science,* 257**,** 644-647.

Behrenfeld, M. J., O'Malley, R. T., Siegel, D. A., McClain, C. R., Sarmiento, J. L., Feldman, G. C., Milligan, A. J., Falkowski, P. G., Letelier, R. M. & Boss, E. S. 2006. Climate-driven trends in contemporary ocean productivity. *Nature,* 444**,** 752-755.

Berger, A. 1988. Milankovitch Theory and Climate. *Reviews of Geophysics,* 26**,** 624-657.

Berger, A. & Loutre, M. F. 1991. Insolation Values for the Climate of the Last 10,000,000 Years. *Quaternary Science Reviews,* 10**,** 297-317.

Berger, A. L. 1978. Long-term Variations of Daily Insolation and Quaternary Climatic Changes. *Journal of the Atmospheric Sciences,* 35**,** 2362-2367.

bin Othman, A. S., Goh, G. H. S. & Todd, P. A. 2010. The distribution and status of giant clams (Family Tridacnidae) - A short review. *Raffles Bulletin of Zoology,* 58**,** 103-111.

Bjerknes, J. 1969. Atmospheric Teleconnections from the Equatorial Pacific. *Monthly Weather Review,* 97**,** 163-&.

Blackman, R. & Tukey, J. 1958. *The Measurement of Power Spectra*, Dover, Mineola, N.Y.

Bloom, A. L., Broecker, W. S., Chappell, J. M., Matthews, R. K. & Mesolell.Kj 1974. Quaternary sea level fluctuations on a tectonic coast - New Th-230 U-234 dates from Huon Peninsula, Papua New Guinea. *Quaternary Research,* 4**,** 185-205.

Bohm, F., Joachimski, M. M., Lehnert, H., Morgenroth, G., Kretschmer, W., Vacelet, J. & Dullo, W. C. 1996. Carbon isotope records from extant Caribbean and south Pacific sponges: Evolution of $\delta^{13}C$ in surface water DIC. *Earth and Planetary Science Letters,* 139**,** 291-303.

Bond, G., Broecker, W., Johnsen, S., McManus, J., Labeyrie, L., Jouzel, J. & Bonani, G. 1993. Correlations between Climate Records from North Atlantic Sediments and Greenland Ice. *Nature,* 365**,** 143-147.

Bond, G. C. & Lotti, R. 1995. Iceberg Discharges into the North Atlantic on Millennial Timescales during the Last Glaciation. *Science,* 267**,** 1005-1010.

Bonham, K. 1965. Growth Rate of Giant Clam *Tridacna gigas* at Bikini Atoll as revealed by radioautography. *Science,* 149**,** 300-&.

Braconnot, P., Luan, Y., Brewer, S. & Zheng, W. 2012. Impact of Earth's orbit and freshwater fluxes on Holocene climate mean seasonal cycle and ENSO characteristics. *Climate Dynamics,* 38.

Brandefelt, J., Kjellstrom, E., Naslund, J. O., Strandberg, G., Voelker, A. H. L. & Wohlfarth, B. 2011. A coupled climate model simulation of Marine Isotope Stage 3 stadial climate. *Climate of the Past,* 7**,** 649-670.

Brijker, J. M., Jung, S. J. A., Ganssen, G. M., Bickert, T. & Kroon, D. 2007. ENSO related decadal scale climate variability from the Indo-Pacific Warm Pool. *Earth and Planetary Science Letters,* 253**,** 67-82.

Broeker, W. S. 1965. Isotope Geochemistry and the Pleistocene Climatic Record. *In:* Wright, H. E. & Frey, D. G. (eds.) *The Quaternary of the United States.* Princeton, N.J.: Princeton University Press.

Brown, J., Collins, M. & Tudhope, A. 2006. Coupled model simulations of mid-Holocene ENSO and comparisons with coral oxygen isotope records. *Advances in Geosciences,* 6**,** 29-33.

Brown, J., Collins, M., Tudhope, A. W. & Toniazzo, T. 2008a. Modelling mid-Holocene tropical climate and ENSO variability: towards constraining predictions of future change with palaeo-data. *Climate Dynamics,* 30**,** 19-36.

Brown, J., Tudhope, A. W., Collins, M. & McGregor, H. V. 2008b. Mid-Holocene ENSO: Issues in quantitative model-proxy data comparisons. *Paleoceanography,* 23.

Bruland, K. W. & Lohan, M. C. 2003. Controls of trace metals in seawater. *In:* Elderfield, H. (ed.) *The Oceans and Marine Geochemistry.* Oxford: Elsevier-Pergamon.

Bush, A. B. G. 2007. Extratropical influences on the El Niño-Southern Oscillation through the late Quaternary. *Journal of Climate,* 20**,** 788-800.

Butler, P. G., Richardson, C. A., Scourse, J. D., Wanamaker, A. D., Jr., Shammon, T. M. & Bennell, J. D. 2010. Marine climate in the Irish Sea: analysis of a 489-year marine master chronology derived from growth increments in the shell of the clam Arctica islandica. *Quaternary Science Reviews,* 29**,** 1614-1632.

Cai, W., Borlace, S., Lengaigne, M., van Rensch, P., Collins, M., Vecchi, G., Timmermann, A., Santoso, A., McPhaden, M. J., Wu, L., England, M. H., Wang, G., Guilyardi, E. & Jin, F.-F. 2014. Increasing frequency of extreme El Niño events due to greenhouse warming. *Nature Climate Change,* 4**,** 111-116.

Cane, M. A. 1986. El Niño. *Annual Review of Earth and Planetary Sciences,* 14**,** 43-70.

Cane, M. A. 2005. The evolution of El Niño, past and future. *Earth and Planetary Science Letters,* 230**,** 227-240.

Cane, M. A., Braconnot, P., Clement, A., Gildor, H., Joussaume, S., Kageyama, M., Khodri, M., Paillard, D., Tett, S. & Zorita, E. 2006. Progress in paleoclimate modeling. *Journal of Climate,* 19**,** 5031-5057.

Cane, M. A., Clement, A., Gagan, M. K., Ayliffe, L. K. & Tudhope, A. 2000. ENSO Through the Holocene, Depicted in Corals and a Model Simulation. *PAGES Newsletter,* 8**,** 3-7.

Carré, M., Bentaleb, I., Bruguier, O., Ordinola, E., Barrett, N. T. & Fontugne, M. 2006. Calcification rate influence on trace element concentrations in aragonitic bivalve shells: Evidences and mechanisms. *Geochimica Et Cosmochimica Acta,* 70**,** 4906-4920.

Carré, M., Bentaleb, I., Fontugne, M. & Lavallee, D. 2005. Strong El Niño events during the early Holocene: stable isotope evidence from Peruvian sea shells. *Holocene,* 15**,** 42-47.

Chappell, J. 1974. Geology of coral terraces, Huon-Peninsula, New Guinea - Study of Quaternary tectonic movements and sea-level changes. *Geological Society of America Bulletin,* 85**,** 553-570.

Chappell, J. 2002. Sea level changes forced ice breakouts in the Last Glacial cycle: new results from coral terraces. *Quaternary Science Reviews,* 21**,** 1229-1240.

Chappell, J., Omura, A., Esat, T., McCulloch, M., Pandolfi, J., Ota, Y. & Pillans, B. 1996a. Reconciliation of late Quaternary sea levels derived from coral terraces at Huon Peninsula with deep sea oxygen isotope records. *Earth and Planetary Science Letters,* 141**,** 227-236.

Chappell, J., Ota, Y. & Berryman, K. 1996b. Late Quaternary coseismic uplift history of Huon Peninsula, Papua New Guinea. *Quaternary Science Reviews,* 15**,** 7-22.

Chappell, J. & Polach, H. 1991. Postglacial Sea-Level Rise From a Coral Record at Huon Peninsula, Papua New Guinea. *Nature,* 349**,** 147-149.

Chappell, J. & Polach, H. A. 1976. Holocene sea level change and coral reef growth at Huon Peninsula, Papua New Guinea. *Geological Society of America Bulletin,* 87**,** 235-240.

Chappell, J. & Shackleton, N. J. 1986. Oxygen isotopes and sea level. *Nature,* 324**,** 137-140.

Chauvaud, L., Lorrain, A., Dunbar, R. B., Paulet, Y. M., Thouzeau, G., Jean, F., Guarini, J. M. & Mucciarone, D. 2005. Shell of the Great Scallop *Pecten maximus* as a high-frequency archive of paleoenvironmental changes. *Geochemistry, Geophysics, Geosystems,* 6.

Chauvaud, L., Thouzeau, G. & Paulet, Y. M. 1998. Effects of environmental factors on the daily growth rate of *Pecten maximus* juveniles in the Bay of Brest (France). *Journal of Experimental Marine Biology and Ecology,* 227.

Chen, M. H., Li, Q. Y., Zheng, F., Tan, X. Z., Xiang, R. & Jian, Z. M. 2005. Variations of the Last Glacial Warm Pool: Sea surface temperature contrasts between the open western Pacific and South China Sea. *Paleoceanography,* 20.

Chiang, J. C. H. 2009. The Tropics in Paleoclimate. *Annual Review of Earth and Planetary Sciences,* 37**,** 263-297.

Chiang, J. C. H. & Fang, Y. 2010. Was the North Pacific Wintertime Climate Less Stormy during the Mid-Holocene? *Journal of Climate,* 23**,** 4025-4037.

Chiang, J. C. H., Fang, Y. & Chang, P. 2009. Pacific Climate Change and ENSO Activity in the Mid-Holocene. *Journal of Climate,* 22**,** 923-939.

Clark, P. U., Hostetler, S. W., Pisias, N. G., Schmittner, A. & Meisner, K. J. 2007. Mechanisms for an ~7-kyr climate and sea-level oscillation during marine isotope stage 3. *In:* Schmittner, A., Chiang, J. & Hemming, S. (eds.) *Ocean Circulation: Mechanisms and Impacts.* American Geophysical Union.

Clement, A. C., Seager, R. & Cane, M. A. 1999. Orbital controls on the El Niño/Southern Oscillation and the tropical climate. *Paleoceanography,* 14**,** 441-456.

Clement, A. C., Seager, R. & Cane, M. A. 2000. Suppression of El Niño during the mid-Holocene by changes in the Earth's orbit. *Paleoceanography,* 15**,** 731-737.

Cobb, K. M., Charles, C. D., Cheng, H. & Edwards, R. L. 2003. El Niño/Southern Oscillation and tropical Pacific climate during the last millennium. *Nature,* 424**,** 271-276.

Cobb, K. M., Westphal, N., Sayani, H. R., Watson, J. T., Di Lorenzo, E., Cheng, H., Edwards, R. L. & Charles, C. D. 2013. Highly Variable El Niño-Southern Oscillation Throughout the Holocene. *Science,* 339**,** 67-70.

Collins, M. 2000. The El Niño-Southern Oscillation in the second Hadley Centre coupled model and its response to greenhouse warming. *Journal of Climate,* 13**,** 1299-1312.

Collins, M. 2005. El Niño- or La Niña-like climate change? *Climate Dynamics,* 24**,** 89-104.

Collins, M., An, S. I., Cai, W. J., Ganachaud, A., Guilyardi, E., Jin, F. F., Jochum, M., Lengaigne, M., Power, S., Timmermann, A., Vecchi, G. & Wittenberg, A. 2010. The impact of global warming on the tropical Pacific ocean and El Niño. *Nature Geoscience,* 3**,** 391-397.

Conroy, J. L., Overpeck, J. T., Cole, J. E., Shanahan, T. M. & Steinitz-Kannan, M. 2008. Holocene changes in eastern tropical Pacific climate inferred from a Galapagos lake sediment record. *Quaternary Science Reviews,* 27**,** 1166-1180.

Corrège, T. 2006. Sea surface temperature and salinity reconstruction from coral geochemical tracers. *Palaeogeography, Palaeoclimatology, Palaeoecology,* 232**,** 408-428.

Corrège, T., Delcroix, T., Recy, J., Beck, W., Cabioch, G. & Le Cornec, F. 2000. Evidence for stronger El Niño-Southern Oscillation (ENSO) events in a mid-Holocene massive coral. *Paleoceanography,* 15**,** 465-470.

Cresswell, G. R. 2000. Coastal currents of northern Papua New Guinea, and the Sepik River outflow. *Marine and Freshwater Research,* 51**,** 553-564.

Crowley, T. J., Quinn, T. M., Taylor, F. W., Henin, C. & Joannot, P. 1997. Evidence for a volcanic cooling signal in a 335-year coral record from New Caledonia. *Paleoceanography,* 12**,** 633-639.

Dannenmann, S., Linsley, B. K., Oppo, D. W., Rosenthal, Y. & Beaufort, L. 2003. East Asian monsoon forcing of suborbital variability in the Sulu Sea during Marine Isotope Stage 3: Link to Northern Hemisphere climate. *Geochemistry Geophysics Geosystems,* 4.

de Brauwere, A., De Ridder, F., Pintelon, R., Schoukens, J. & Dehairs, F. 2009. A comparative study of methods to reconstruct a periodic time series from an environmental proxy record. *Earth-Science Reviews,* 95.

de Garidel-Thoron, T., Rosenthal, Y., Bassinot, F. & Beaufort, L. 2005. Stable sea surface temperatures in the western Pacific warm pool over the past 1.75 million years. *Nature,* 433**,** 294-298.

de Garidel-Thoron, T., Rosenthal, Y., Beaufort, L., Bard, E., Sonzogni, C. & Mix, A. C. 2007. A multiproxy assessment of the western equatorial Pacific hydrography during the last 30 kyr. *Paleoceanography,* 22.

Delcroix, T., Gourdeau, L. & Henin, C. 1998. Sea surface salinity changes along the Fiji-Japan shipping track during the 1996 La Niña and 1997 El Niño period. *Geophysical Research Letters,* 25**,** 3169-3172.

Diaz, H. F. & Kiladis, G. N. 1992. Atmospheric teleconnections associated with the extreme phases of the Southern Oscillation. *In:* Diaz, H. F. & Markgraf, V. (eds.) *El Niño – Historical and Paleoclimatic aspects of the Southern Oscillation.* Cambridge University Press.

Dodd, J. R. 1965. Environmental Control of Strontium and Magnesium in *Mytilus*. *Geochimica Et Cosmochimica Acta,* 29.

Donders, T. H., Wagner-Cremer, F. & Visscher, H. 2008. Integration of proxy data and model scenarios for the mid-Holocene onset of modern ENSO variability. *Quaternary Science Reviews,* 27**,** 571-579.

Driscoll, R., Elliot, M., Russon, T., Welsh, K., Yokoyama, Y. & Tudhope, A. 2014. ENSO reconstructions over the past 60 ka using giant clams (*Tridacna* sp.) from Papua New Guinea. *Geophysical Research Letters,* 41**,** 6819-6825.

Druffel, E. R. M. & Benavides, L. M. 1986. Input of Excess CO_2 to the Surface Ocean Based on C^{13}/C^{12} Ratios in a Banded Jamaican Sclerosponge. *Nature,* 321**,** 58-61.

Duprey, N. 2012. *Variabilité climatique de deux périodes clés de l'Holocène, c. 7000-6000 et 3500-2500 années BP, dans le Pacifique Sud-Ouest à partir de l'analyse d'archives biocarbonatées. .* Université Pierre et Marie Curie.

Duprey, N., Galipaud, J.-C., Cabioch, G. & Lazareth, C. E. 2014. Isotopic records from archeological giant clams reveal a variable climate during the southwestern

Pacific colonization ca. 3.0 ka BP. *Palaeogeography, Palaeoclimatology, Palaeoecology,* 404**,** 97-108.
Duprey, N., Lazareth, C. E., Corrège, T., Le Cornec, F., Maes, C., Pujol, N., Madeng-Yogo, M., Caquineau, S., Derome, C. S. & Cabioch, G. 2012. Early mid-Holocene SST variability and surface-ocean water balance in the southwest Pacific. *Paleoceanography,* 27.
Dyez, K. A. & Ravelo, A. C. 2013. Late Pleistocene tropical Pacific temperature sensitivity to radiative greenhouse gas forcing. *Geology,* 41**,** 23-26.
Dymond, J. & Collier, R. 1996. Particulate barium fluxes and their relationships to biological productivity. *Deep-Sea Research Part Ii-Topical Studies in Oceanography,* 43**,** 1283-&.
Edinger, E. N., Burr, G. S., Pandolfi, J. M. & Ortiz, J. C. 2007. Age accuracy and resolution of Quaternary corals used as proxies for sea level. *Earth and Planetary Science Letters,* 253**,** 37-49.
Edwards, R. L., Beck, J. W., Burr, G. S., Donahue, D. J., Chappell, J. M. A., Bloom, A. L., Druffel, E. R. M. & Taylor, F. W. 1993. A large drop in atmospheric C-14/C-12 and reduced melting in the Younger Dryas, documented with Th-230 ages of corals. *Science,* 260**,** 962-968.
Elderfield, H. & Ganssen, G. 2000. Past temperature and $\delta^{18}O$ of surface ocean waters inferred from foraminiferal Mg/Ca ratios. *Nature,* 405.
Elderfield, H., Vautravers, M. & Cooper, M. 2002. The relationship between shell size and Mg/Ca, Sr/Ca, $\delta^{18}O$, and $\delta^{13}C$ of species of planktonic foraminifera. *Geochemistry, Geophysics, Geosystems,* 3.
Elliot, M., deMenocal, P. B., Linsley, B. K. & Howe, S. S. 2003. Environmental controls on the stable isotopic composition of *Mercenaria mercenaria*: Potential application to paleoenvironmental studies. *Geochemistry, Geophysics, Geosystems,* 4**,** 16.
Elliot, M., Labeyrie, L., Bond, G., Cortijo, E., Turon, J. L., Tisnerat, N. & Duplessy, J. C. 1998. Millennial-scale iceberg discharges in the Irminger Basin during the last glacial period: Relationship with the Heinrich events and environmental settings. *Paleoceanography,* 13**,** 433-446.
Elliot, M., Labeyrie, L. & Duplessy, J. C. 2002. Changes in North Atlantic deep-water formation associated with the Dansgaard-Oeschger temperature oscillations (60-10 ka). *Quaternary Science Reviews,* 21**,** 1153-1165.
Elliot, M., Welsh, K., Chilcott, C., McCulloch, M., Chappell, J. & Ayling, B. 2009. Profiles of trace elements and stable isotopes derived from giant long-lived *Tridacna gigas* bivalves: Potential applications in paleoclimate studies. *Palaeogeography, Palaeoclimatology, Palaeoecology,* 280**,** 132-142.
Epstein, S., Buchsbaum, R., Lowenstam, H. & H.C, U. 1951. Carbonate-water isotopic temperature scale. *Bulletin of the Geological Society of America,* 52**,** 417-426.
Epstein, S., Buchsbaum, R., Lowenstam, H. A. & Urey, H. C. 1953. Revised carbonate-water isotopic temperature scale. *Geological Society of America Bulletin,* 64**,** 1315-1325.
Esat, T. M. & Yokoyama, Y. 2006. Growth patterns of the last ice age coral terraces at Huon Peninsula. *Global and Planetary Change,* 54**,** 216-224.
Evans, D., Mueller, W., Oron, S. & Renema, W. 2013. Eocene seasonality and seawater alkaline earth reconstruction using shallow-dwelling large benthic foraminifera. *Earth and Planetary Science Letters,* 381**,** 104-115.
Fairbanks, R. G., Evans, M. N., Rubenstone, J. L., Mortlock, R. A., Broad, K., Moore, M. D. & Charles, C. D. 1997. Evaluating climate indices and their geochemical proxies measured in corals. *Coral Reefs,* 16**,** S93-S100.

Fairbridge, R. W. 1960. The Changing Level of the Sea. *Scientific American,* 202**,** 70-79.
Faylona, M. G. P. G., Lazareth, C. E., Semah, A.-M., Caquineau, S., Boucher, H. & Ronquillo, W. P. 2011. Preliminary Study on the Preservation of Giant Clam (*Tridacnidae*) Shells from the Balobok Rockshelter Archaeological Site, South Philippines. *Geoarchaeology-an International Journal,* 26**,** 888-901.
Fedorov, A. V. & Philander, S. G. 2000. Is El Niño changing? *Science,* 288**,** 1997-2002.
Fine, R. A., Lukas, R., Bingham, F. M., Warner, M. J. & Gammon, R. H. 1994. The western equatorial Pacific: A water mass crossroads. *Journal of Geophysical Research: Oceans,* 99**,** 25063-25080.
Ford, H. L., Schellenberg, S. A., Becker, B. J., Deutschman, D. L., Dyck, K. A. & Koch, P. L. 2010. Evaluating the skeletal chemistry of *Mytilus californianus* as a temperature proxy: Effects of microenvironment and ontogeny. *Paleoceanography,* 25.
Freitas, P., Clarke, L. J., Kennedy, H., Richardson, C. & Abrantes, F. 2005. Mg/Ca, Sr/Ca, and stable-isotope ($\delta^{18}O$ and $\delta^{13}C$) ratio profiles from the fan mussel *Pinna nobilis*: Seasonal records and temperature relationships. *Geochemistry, Geophysics, Geosystems,* 6.
Freitas, P. S., Clarke, L. J., Kennedy, H., Richardson, C. A. & Abrantes, F. 2006. Environmental and biological controls on elemental (Mg/Ca, Sr/Ca and Mn/Ca) ratios in shells of the king scallop *Pecten maximus*. *Geochimica Et Cosmochimica Acta,* 70.
Freitas, P. S., Clarke, L. J., Kennedy, H. A. & Richardson, C. A. 2008. Inter- and intra-specimen variability masks reliable temperature control on shell Mg/Ca ratios in laboratory- and field-cultured *Mytilus edulis* and *Pecten maximus* (bivalvia). *Biogeosciences,* 5.
Gagan, M. K., Hendy, E. J., Haberle, S. G. & Hantoro, W. S. 2004. Post-glacial evolution of the Indo-Pacific Warm Pool and El Niño-Southern Oscillation. *Quaternary International,* 118**,** 127-143.
Galeotti, S., von der Heydt, A., Huber, M., Bice, D., Dijkstra, H., Jilbert, T., Lanci, L. & Reichart, G.-J. 2010. Evidence for active El Niño Southern Oscillation variability in the Late Miocene greenhouse climate. *Geology,* 38**,** 419-422.
Gates, D. M. 1993. *Climate change and its biological consequences*, Sinauer Associates, Inc.
Gergis, J. L. & Fowler, A. M. 2009. A history of ENSO events since AD 1525: implications for future climate change. *Climatic Change,* 92**,** 343-387.
Gillikin, D. P., De Ridder, F., Ulens, H., Elskens, M., Keppens, E., Baeyens, W. & Dehairs, F. 2005a. Assessing the reproducibility and reliability of estuarine bivalve shells (*Saxidomus giganteus*) for sea surface temperature reconstruction: Implications for paleoclimate studies. *Palaeogeography, Palaeoclimatology, Palaeoecology,* 228**,** 70-85.
Gillikin, D. P., Dehairs, F., Lorrain, A., Steenmans, D., Baeyens, W. & Andre, L. 2006. Barium uptake into the shells of the common mussel (*Mytilus edulis*) and the potential for estuarine paleo-chemistry reconstruction. *Geochimica Et Cosmochimica Acta,* 70**,** 395-407.
Gillikin, D. P., Lorrain, A., Navez, J., Taylor, J. W., Keppens, E., Baeyens, W. & Dehairs, F. 2005b. Strong biological controls on Sr/Ca ratios in aragonitic marine bivalve shells. *Geochemistry, Geophysics, Geosystems,* 6.
Gillikin, D. P., Lorrain, A., Paulet, Y. M., Andre, L. & Dehairs, F. 2008. Synchronous barium peaks in high-resolution profiles of calcite and aragonite marine bivalve shells. *Geo-Marine Letters,* 28**,** 351-358.

Goewert, A. E. & Surge, D. 2008. Seasonality and growth patterns using isotope sclerochronology in shells of the Pliocene scallop *Chesapecten madisonius*. *Geo-Marine Letters,* 28.
Goodwin, D. H., Schone, B. R. & Dettman, D. L. 2003. Resolution and fidelity of oxygen isotopes as paleotemperature proxies in bivalve mollusk shells: Models and observations. *Palaios,* 18**,** 110-125.
Greer, L. & Swart, P. K. 2006. Decadal cyclicity of regional mid-Holocene precipitation: Evidence from Dominican coral proxies. *Paleoceanography,* 21.
Grootes, P. M., Stuiver, M., White, J. W. C., Johnsen, S. & Jouzel, J. 1993. Comparison of Oxygen Isotope Records from the GISP2 and GRIP Greenland Ice Cores. *Nature,* 366**,** 552-554.
Haberle, S. G., Hope, G. S. & van der Kaars, S. 2001. Biomass burning in Indonesia and Papua New Guinea: natural and human induced fire events in the fossil record. *Palaeogeography, Palaeoclimatology, Palaeoecology,* 171**,** 259-268.
Hallmann, N., Burchell, M., Schoene, B. R., Irvine, G. V. & Maxwell, D. 2009. High-resolution sclerochronological analysis of the bivalve mollusk *Saxidomus gigantea* from Alaska and British Columbia: techniques for revealing environmental archives and archaeological seasonality. *Journal of Archaeological Science,* 36.
Hanley, D. E., Bourassa, M. A., O'Brien, J. J., Smith, S. R. & Spade, E. R. 2003. A quantitative evaluation of ENSO indices. *Journal of Climate,* 16**,** 1249-1258.
Hart, A. M., Bell, J. D. & Foyle, T. P. 1998. Growth and survival of the giant clams, *Tridacna derasa*, *T-Maxima* and *T-Crocea*, at village farms in the Solomon Islands. *Aquaculture,* 165**,** 203-220.
Hean, R. L. & Cacho, O. J. 2003. A growth model for giant clams *Tridacna crocea* and *T-derasa*. *Ecological Modelling,* 163**,** 87-100.
Heinrich, H. 1988. Origin and consequences of cyclic ice rafting in the Northeast Atlantic Ocean during the past 134,000 years. *Quaternary Research,* 29**,** 142-152.
Hernandez, A., Giralt, S., Bao, R., Saez, A., Leng, M. J. & Barker, P. A. 2010. ENSO and solar activity signals from oxygen isotopes in diatom silica during late glacial-Holocene transition in Central Andes (18°S). *Journal of Paleolimnology,* 44**,** 413-429.
Hippler, D., Buhl, D., Witbaard, R., Richter, D. K. & Immenhauser, A. 2009. Towards a better understanding of magnesium-isotope ratios from marine skeletal carbonates. *Geochimica Et Cosmochimica Acta,* 73.
Holmgren, M., Scheffer, M., Ezcurra, E., Gutierrez, J. R. & Mohren, G. M. J. 2001. El Niño effects on the dynamics of terrestrial ecosystems. *Trends in Ecology & Evolution,* 16**,** 89-94.
Horel, J. D. & Wallace, J. M. 1981. Planetary-scale atmospheric phenomena associated with the Southern Oscillation. *Monthly Weather Review,* 109**,** 813-829.
Huber, M. & Caballero, R. 2003. Eocene El Niño: Evidence for robust tropical dynamics in the "hothouse". *Science,* 299**,** 877-881.
Huffman, G. J., Adler, R. F., Bolvin, D. T. & Gu, G. 2009. Improving the global precipitation record: GPCP Version 2.1. *Geophysical Research Letters,* 36.
Hughen, K. A., Schrag, D. P., Jacobsen, S. B. & Hantoro, W. 1999. El Niño during the last interglacial period recorded by a fossil coral from Indonesia. *Geophysical Research Letters,* 26**,** 3129-3132.
IRI. 2007. *Overview of the ENSO system* [Online]. Available: http://iri.columbia.edu/climate/ENSO/background/basics.html 2011].

Ivanochko, T. S., Ganeshram, R. S., Brummer, G. J. A., Ganssen, G., Jung, S. J. A., Moreton, S. G. & Kroon, D. 2005. Variations in tropical convection as an amplifier of global climate change at the millennial scale. *Earth and Planetary Science Letters,* 235**,** 302-314.

Ivany, L. C., Brey, T., Huber, M., Buick, D. P. & Schoene, B. R. 2011. El Niño in the Eocene greenhouse recorded by fossil bivalves and wood from Antarctica. *Geophysical Research Letters,* 38.

Jin, F. F., An, S. I., Timmermann, A. & Zhao, J. X. 2003. Strong El Niño events and nonlinear dynamical heating. *Geophysical Research Letters,* 30.

Jones, D. S., Williams, D. F. & Romanek, C. S. 1986. Life-History of Symbiont-Bearing Giant Clams from Stable Isotope Profiles. *Science,* 231**,** 46-48.

Juillet-Leclerc, A., Thiria, S., Naveau, P., Delcroix, T., Le Bec, N., Blamart, D. & Corrège, T. 2006. SPCZ migration and ENSO events during the 20th century as revealed by climate proxies from a Fiji coral. *Geophysical Research Letters,* 33.

Kennedy, H., Richardson, C. A., Duarte, C. M. & Kennedy, D. P. 2001. Oxygen and carbon stable isotopic profiles of the fan mussel, Pinna nobilis, and reconstruction of sea surface temperatures in the Mediterranean. *Marine Biology,* 139**,** 1115-1124.

Kilbourne, K. H., Quinn, T. M., Taylor, F. W., Delcroix, T. & Gouriou, Y. 2004. El Niño-Southern Oscillation-related salinity variations recorded in the skeletal geochemistry of a Porites coral from Espiritu Santo, Vanuatu. *Paleoceanography,* 19.

Kim, S. T. & Yu, J.-Y. 2012. The two types of ENSO in CMIP5 models. *Geophysical Research Letters,* 39.

Kitzberger, T., Swetnam, T. W. & Veblen, T. T. 2001. Inter-hemispheric synchrony of forest fires and the El Niño-Southern Oscillation. *Global Ecology and Biogeography,* 10**,** 315-326.

Klein, R. T., Lohmann, K. C. & Thayer, C. W. 1996. Bivalve skeletons record sea-surface temperature and $\delta^{18}O$ via Mg/Ca and $^{18}O/^{16}O$ ratios. *Geology,* 24**,** 415-418.

Klumpp, D. W. & Griffith, C. L. 1994. Contributions of Phototropic and Heterotrophic Nutrition to the Metabolic and Growth Requirements of 4 Species of Giant Clam (*Tridacnidae*). *Marine Ecology-Progress Series,* 115**,** 103-115.

Kobayashi, I. 1969. Internal Microstructure of Shell of Bivalve Molluscs. *American Zoologist,* 9.

Koutavas, A., Demenocal, P. B., Olive, G. C. & Lynch-Stieglitz, J. 2006. Mid-Holocene El Niño-Southern Oscillation (ENSO) attenuation revealed by individual foraminifera in eastern tropical Pacific sediments. *Geology,* 34**,** 993-996.

Koutavas, A. & Joanides, S. 2012. El Niño-Southern Oscillation extrema in the Holocene and Last Glacial Maximum. *Paleoceanography,* 27.

Koutavas, A., Lynch-Stieglitz, J., Marchitto, T. M. & Sachs, J. P. 2002. El Niño-like pattern in ice age tropical Pacific sea surface temperature. *Science,* 297**,** 226-230.

Kuroda, Y. 2000. Variability of Currents off the Northern Coast of New Guinea. *Journal of Oceanography,* 56**,** 103-116.

Lacan, F. & Jeandel, C. 2001. Tracing Papua New Guinea imprint on the central Equatorial Pacific Ocean using neodymium isotopic compositions and Rare Earth Element patterns. *Earth and Planetary Science Letters,* 186**,** 497-512.

Lartaud, F., Chauvaud, L., Richard, J., Toulot, A., Bollinger, C., Testut, L. & Paulet, Y. M. 2010. Experimental growth pattern calibration of Antarctic scallop shells (*Adamussium colbecki*, Smith 1902) to provide a biogenic archive of high-

resolution records of environmental and climatic changes. *Journal of Experimental Marine Biology and Ecology,* 393**,** 158-167.
Laskar, J., Robutel, P., Joutel, F., Gastineau, M., Correia, A. C. M. & Levrard, B. 2004. A long-term numerical solution for the insolation quantities of the Earth. *Astronomy & Astrophysics,* 428.
LaVigne, M., Nurhati, I. S., Cobb, K. M., McGregor, H. V., Sinclair, D. & Sherrell, R. M. 2013. Systematic ENSO-driven nutrient variability recorded by central equatorial Pacific corals. *Geophysical Research Letters,* 40**,** 3956-3961.
Lazareth, C. E., Vander Putten, E., Andre, L. & Dehairs, F. 2003. High-resolution trace element profiles in shells of the mangrove bivalve *Isognomon ephippium*: a record of environmental spatio-temporal variations? *Estuarine Coastal and Shelf Science,* 57.
Lea, D. W. 2003. Elemental and isotopic proxies of past ocean temperatures. *In:* Elderfield, H. (ed.) *The Oceans and Marine Geochemistry.* Oxford: Elsevier-Pergamon.
Lea, D. W., Mashiotta, T. A. & Spero, H. J. 1999. Controls on magnesium and strontium uptake in planktonic foraminifera determined by live culturing. *Geochimica Et Cosmochimica Acta,* 63**,** 2369-2379.
Lea, D. W., Pak, D. K. & Spero, H. J. 2000. Climate impact of late quaternary equatorial Pacific sea surface temperature variations. *Science,* 289**,** 1719-1724.
Lea, D. W., Shen, G. T. & Boyle, E. A. 1989. Coralline barium records temporal variability in equatorial Pacific upwelling. *Nature,* 340**,** 373-376.
Leder, J. J., Swart, P. K., Szmant, A. M. & Dodge, R. E. 1996. The origin of variations in the isotopic record of scleractinian corals .1. Oxygen. *Geochimica Et Cosmochimica Acta,* 60**,** 2857-2870.
Leduc, G., Vidal, L., Cartapanis, O. & Bard, E. 2009. Modes of eastern equatorial Pacific thermocline variability: Implications for ENSO dynamics over the last glacial period. *Paleoceanography,* 24**,** 14.
Leduc, G., Vidal, L., Tachikawa, K., Rostek, F., Sonzogni, C., Beaufort, L. & Bard, E. 2007. Moisture transport across Central America as a positive feedback on abrupt climatic changes. *Nature,* 445**,** 908-911.
Lee, S., Klein, A. & Over, T. 2004. Effects of the El Niño-Southern Oscillation on temperature, precipitation, snow water equivalent and resulting streamflow in the Upper Rio Grande river basin. *Hydrological Processes,* 18**,** 1053-1071.
Levi, C., Labeyrie, L., Bassinot, F., Guichard, F., Cortijo, E., Waelbroeck, C., Caillon, N., Duprat, J., de Garidel-Thoron, T. & Elderfield, H. 2007. Low-latitude hydrological cycle and rapid climate changes during the last deglaciation. *Geochemistry Geophysics Geosystems,* 8.
Li, T. G., Zhao, J. T., Nan, Q. Y., Sun, R. T. & Yu, X. K. 2011. Palaeoproductivity evolution in the centre of the western Pacific warm pool during the last 250 ka. *Journal of Quaternary Science,* 26**,** 478-484.
Lin, A. Y. M., Meyers, M. A. & Vecchio, K. S. 2006. Mechanical properties and structure of *Strombus gigas*, *Tridacna gigas*, and *Haliotis rufescens* sea shells: A comparative study. *Materials Science & Engineering C-Biomimetic and Supramolecular Systems,* 26.
Liu, Z. Y., Kutzbach, J. & Wu, L. X. 2000. Modeling climate shift of El Niño variability in the Holocene. *Geophysical Research Letters,* 27**,** 2265-2268.
Lorens, R. B. 1981. Sr, Cd, Mn and Co distribution coefficients in calcite as a function of calcite precipitation rate. *Geochimica Et Cosmochimica Acta,* 45**,** 553-561.

Lorens, R. B. & Bender, M. L. 1977. Physiological Exclusion of Magnesium from *Mytilus edulis* calcite. *Nature,* 269.
Lorenz, S. J., Kim, J. H., Rimbu, N., Schneider, R. R. & Lohmann, G. 2006. Orbitally driven insolation forcing on Holocene climate trends: Evidence from alkenone data and climate modeling. *Paleoceanography,* 21.
Lorrain, A., Gillikin, D. P., Paulet, Y. M., Chauvaud, L., Le Mercier, A., Navez, J. & Andre, L. 2005. Strong kinetic effects on Sr/Ca ratios in the calcitic bivalve *Pecten maximus*. *Geology,* 33.
Lorrain, A., Paulet, Y. M., Chauvaud, L., Savoye, N., Nezan, E. & Guerin, L. 2000. Growth anomalies in *Pecten maximus* from coastal waters (Bay of Brest, France): relationship with diatom blooms. *Journal of the Marine Biological Association of the United Kingdom,* 80**,** 667-673.
Luan, Y., Braconnot, P., Yu, Y., Zheng, W. & Marti, O. 2012. Early and mid-Holocene climate in the tropical Pacific: seasonal cycle and interannual variability induced by insolation changes. *Climate of the Past,* 8.
Luthi, D., Kawamura, K., Stocker, T. F., Le Floch, M., Bereiter, B., Blunier, T., Barnola, J. M., Siegenthaler, U., Raynaud, D., Jouzel, J. & Fischer, H. 2008. EPICA Dome C - 800KYr CO2 Data. *NOAA Paleoclimatology*.
Makou, M. C., Eglinton, T. I., Oppo, D. W. & Hughen, K. A. 2010. Postglacial changes in El Niño and La Niña behavior. *Geology,* 38**,** 43-46.
Mann, M. E., Cane, M. A., Zebiak, S. E. & Clement, A. 2005. Volcanic and solar forcing of the tropical Pacific over the past 1000 years. *Journal of Climate,* 18**,** 447-456.
Mantyla, A. W., Venrick, E. L. & Hayward, T. L. 1995. Primary production and chlorophyll relationships, derived from ten years of CalCOFI measurements. *California Cooperative Oceanic Fisheries Investigations Reports,* 36**,** 159-166.
Marchitto, T. M., Muscheler, R., Ortiz, J. D., Carriquiry, J. D. & van Geen, A. 2010. Dynamical response of the tropical Pacific Ocean to solar forcing during the early Holocene. *Science,* 330**,** 1378-81.
Martin, P. A., Lea, D. W., Mashiotta, T. A., Papenfuss, T. & Sarnthein, M. 1999. Variation of foraminiferal Sr/Ca over Quaternary glacial-interglacial cycles: Evidence for changes in mean ocean Sr/Ca? *Geochemistry Geophysics Geosystems,* 1.
McConnaughey, T. A. & Gillikin, D. P. 2008. Carbon isotopes in mollusk shell carbonates. *Geo-Marine Letters,* 28**,** 287-299.
McCulloch, M., Fallon, S., Wyndham, T., Hendy, E., Lough, J. & Barnes, D. 2003. Coral record of increased sediment flux to the inner Great Barrier Reef since European settlement. *Nature,* 421**,** 727-730.
McCulloch, M., Mortimer, G., Esat, T., Li, X. H., Pillans, B. & Chappell, J. 1996. High resolution windows into early Holocene climate: Sr/Ca coral records from the Huon Peninsula. *Earth and Planetary Science Letters,* 138**,** 169-178.
McCulloch, M. T., Gagan, M. K., Mortimer, G. E., Chivas, A. R. & Isdale, P. J. 1994. A high-resolution Sr/Ca and $\delta^{18}O$ coral record from the Great Barrier Reef, Australia, and the 1982-1983 El Niño. *Geochimica Et Cosmochimica Acta,* 58**,** 2747-2754.
McGregor, H. V., Fischer, M. J., Gagan, M. K., Fink, D., Phipps, S. J., Wong, H. & Woodroffe, C. D. 2013. A weak El Niño/Southern Oscillation with delayed seasonal growth around 4,300 years ago. *Nature Geoscience*.
McGregor, H. V. & Gagan, M. K. 2003. Diagenesis and geochemistry of Porites corals from Papua New Guinea: Implications for paleoclimate reconstruction. *Geochimica Et Cosmochimica Acta,* 67**,** 2147-2156.

McGregor, H. V. & Gagan, M. K. 2004. Western Pacific coral $\delta^{18}O$ records of anomalous Holocene variability in the El Niño-Southern Oscillation. *Geophysical Research Letters,* 31.
Merkel, U., Prange, M. & Schulz, M. 2010. ENSO variability and teleconnections during glacial climates. *Quaternary Science Reviews,* 29**,** 86-100.
Merlis, T. M., Schneider, T., Bordoni, S. & Eisenman, I. 2013. The Tropical Precipitation Response to Orbital Precession. *Journal of Climate,* 26**,** 2010-2021.
Merryfield, W. J. 2006. Changes to ENSO under CO_2 doubling in a multimodel ensemble. *Journal of Climate,* 19**,** 4009-4027.
Milankovitch, M. 1941. Canon of insolation and the ice-age problem (Kanon der Erdbestrahlung und seine Anwendung auf das Eiszeitenproblem). R. Serb. Acad., Belgrade.
Mix, A. C. & Ruddiman, W. F. 1984. Oxygen isotope analyses and Pleistocene ice volumes. *Quaternary Research,* 21**,** 1-20.
Mohtadi, M., Lueckge, A., Steinke, S., Groeneveld, J., Hebbeln, D. & Westphal, N. 2010. Late Pleistocene surface and thermocline conditions of the eastern tropical Indian Ocean. *Quaternary Science Reviews,* 29**,** 887-896.
Moir, B. G. 1989. A Review of Tridacnid Ecology and Some Possible Implications for Archaeological Research . *Asian Perspectives,* 27**,** 95-121.
Molnar, P. & Cane, M. A. 2007. Early pliocene (pre-Ice Age) El Niño-like global climate: Which El Niño? *Geosphere,* 3**,** 337-365.
Mook, W. G. & Vogel, J. C. 1968. Isotopic Equilibrium between Shells and their Environment. *Science,* 159**,** 874-&.
Müller, W., Shelley, M., Miller, P. & Broude, S. 2009. Initial performance metrics of a new custom-designed ArF excimer LA-ICPMS system coupled to a two-volume laser-ablation cell. *Journal of Analytical Atomic Spectrometry,* 24**,** 209-214.
Neumann, A. C. & Macintyre, I. Reef response to sea level rise: keep-up, catch-up or give-up *In:* Gabrie, C., Toffart, J. L. & Salvat, B., eds. Proceedings Of The Fifth International Coral Reef Congress, 27 May -1 June 1985 1985 Tahiti. 105-110.
Norrish, R. G. W. & Smith, R. R. 1936. Biology of *Tridacna* and its relatives. *Nature,* 138**,** 473-474.
Ohno, T. 1985. Experimental analyses concerning the rhythm of shell growth in some bivalves and its paleobiological implications. *Palaeontographica Abteilung A Palaeozoologie-Stratigraphie,* 189**,** 63-123.
Ota, Y. & Chappell, J. 1999. Holocene sea-level rise and coral reef growth on a tectonically rising coast, Huon Peninsula, Papua New Guinea. *Quaternary International,* 55**,** 51-59.
Ota, Y., Chappell, J., Kelley, R., Yonekura, N., Matsumoto, E., Nishimura, T. & Head, J. 1993. Holocene coral-reef terraces and coseismic uplift of Huon Peninsula, Papua-New-Guinea. *Quaternary Research,* 40**,** 177-188.
Otto-Bliesner, B. L., Brady, E. C., Clauzet, G., Tomas, R., Levis, S. & Kothavala, Z. 2006. Last Glacial Maximum and Holocene climate in CCSM3. *Journal of Climate,* 19**,** 2526-2544.
Otto-Bliesner, B. L., Brady, E. C., Shin, S. I., Liu, Z. Y. & Shields, C. 2003. Modeling El Niño and its tropical teleconnections during the last glacial-interglacial cycle. *Geophysical Research Letters,* 30**,** 4.
Paillard, D., Labeyrie, L. & Yiou, P. 1996. Macintosh Program performs time-series analysis. *Eos,* 77**,** 379.
Pandolfi, J. & Chappell, J. 1994. Stratigraphy and relative sea level changes at the Kanzarua and Bobongara sections, Huon Peninsula, Papua New Guinea. *In:* Ota,

Y. (ed.) *Study on coral reef terraces of the Huon Peninsula, Papua New Guinea: Establishment of Quaternary Sea Level and Tectonic History.*
Pandolfi, J. M. 1996. Limited membership in Pleistocene reef coral assemblages from the Huon Peninsula, Papua New Guinea: Constancy during global change. *Paleobiology,* 22**,** 152-176.
Pannella, G. & Macclintock, C. 1968. Biological and Environmental Rhythms Reflected in Molluscan Shell Growth. *Journal of Paleontology,* 42**,** 64-80.
Paytan, A. & Kastner, M. 1996. Benthic Ba fluxes in the central Equatorial Pacific, implications for the oceanic Ba cycle. *Earth and Planetary Science Letters,* 142**,** 439-450.
Peltier, W. R. & Solheim, L. P. 2004. The climate of the Earth at Last Glacial Maximum: statistical equilibrium state and a mode of internal variability. *Quaternary Science Reviews,* 23**,** 335-357.
Philander, S. G. 1990. *El Niño, La Niña, and the Southern Oscillation*, Academic Press, Inc.
Picaut, J., Ioualalen, M., Menkes, C., Delcroix, T. & McPhaden, M. J. 1996. Mechanism of the zonal displacements of the Pacific warm pool: Implications for ENSO. *Science,* 274**,** 1486-1489.
Pätzold, J., Heinrichs, J. P., Wolschendorf, K. & Wefer, G. 1991. Correlation of Stable Oxygen Isotope Temperature Record with Light Attenuation Profiles in Reef-Dwelling *Tridacna* shells. *Coral Reefs,* 10**,** 65-69.
Quinn, T. M., Taylor, F. W. & Crowley, T. J. 2006. Coral-based climate variability in the Western Pacific Warm Pool since 1867. *Journal of Geophysical Research-Oceans,* 111**,** 11.
Rahmstorf, S. 2002. Ocean circulation and climate during the past 120,000 years. *Nature,* 419**,** 207-214.
Rayner, N. A., Parker, D. E., Horton, E. B., Folland, C. K., Alexander, L. V., Rowell, D. P., Kent, E. C. & Kaplan, A. 2003. Global analyses of sea surface temperature, sea ice, and night marine air temperature since the late nineteenth century. *Journal of Geophysical Research-Atmospheres,* 108.
Rein, B., Luckge, A., Reinhardt, L., Sirocko, F., Wolf, A. & Dullo, W. C. 2005. El Niño variability off Peru during the last 20,000 years. *Paleoceanography,* 20**,** 18.
Rein, B., Luckge, A. & Sirocko, F. 2004. A major Holocene ENSO anomaly during the Medieval period. *Geophysical Research Letters,* 31**,** 4.
Revelle, R. & Suess, H. E. 1957. Carbon dioxide exchange between atmosphere and ocean and the question of an increase of atmospheric CO_2 during the past decades. *Tellus,* 9**,** 18-27.
Reynolds, R. W., Rayner, N. A., Smith, T. M., Stokes, D. C. & Wang, W. Q. 2002. An improved in situ and satellite SST analysis for climate. *Journal of Climate,* 15**,** 1609-1625.
Richardson, C. A. 1987. Microgrowth Patterns in the Shell of the Malaysian Cockle *Anadara granosa* (L) and their Use in Age Determination. *Journal of Experimental Marine Biology and Ecology,* 111**,** 77-98.
Richardson, C. A., Peharda, M., Kennedy, H., Kennedy, P. & Onofri, V. 2004. Age, growth rate and season of recruitment of *Pinna nobilis* (L) in the Croatian Adriatic determined from Mg/Ca and Sr/Ca shell profiles. *Journal of Experimental Marine Biology and Ecology,* 299.
Rimbu, N., Lohmann, G., Felis, T. & Patzold, J. 2003. Shift in ENSO teleconnections recorded by a northern Red Sea coral. *Journal of Climate,* 16**,** 1414-1422.

Rimbu, N., Lohmann, G., Lorenz, S. J., Kim, J. H. & Schneider, R. R. 2004. Holocene climate variability as derived from alkenone sea surface temperature and coupled ocean-atmosphere model experiments. *Climate Dynamics,* 23**,** 215-227.
Roberts, W. H. G., Battisti, D. S. & Tudhope, A. W. 2014. ENSO in the Mid-Holocene according to CSM and HadCM3. *Journal of Climate,* 27**,** 1223-1242.
Rodbell, D. T., Seltzer, G. O., Anderson, D. M., Abbott, M. B., Enfield, D. B. & Newman, J. H. 1999. An ~ 15,000-year record of El Niño-driven alluviation in southwestern Ecuador. *Science,* 283**,** 516-520.
Romanek, C. S. & Grossman, E. L. 1989. Stable isotope profiles of *Tridacna maxima* as environmental indicators. *Palaios,* 4**,** 402-413.
Romanek, C. S., Jones, D. S., Williams, D. F., Krantz, D. E. & Radtke, R. 1987. Stable isotopic investigation of physiological and environmental changes recorded in shell carbonate from the giant clam *Tridacna maxima*. *Marine Biology,* 94**,** 385-393.
Roopnarine, P. D., Fitzgerald, P., Byars, G. & Kilb, K. 1998. Coincident boron profiles of bivalves from the gulf of California: Implications for the calculation of paleosalinities. *Palaios,* 13**,** 395-400.
Rosewater, J. 1965. The family Tridacnidae in the Indo-Pacific. *Indo Pacific Mollusca,* 1**,** 347-396.
Russon, T., Tudhope, A. W., Hegerl, G. C., Schurer, A. & Collins, M. 2014. Assessing the Significance of Changes in ENSO Amplitude Using Variance Metrics. *Journal of Climate,* 27**,** 4911-4922.
Sadekov, A. Y., Ganeshram, R., Pichevin, L., Berdin, R., McClymont, E., Elderfield, H. & Tudhope, A. W. 2013. Palaeoclimate reconstructions reveal a strong link between El Niño-Southern Oscillation and Tropical Pacific mean state. *Nature Communications,* 4.
Saikku, R., Stott, L. & Thunell, R. 2009. A bi-polar signal recorded in the western tropical Pacific: Northern and Southern Hemisphere climate records from the Pacific warm pool during the last Ice Age. *Quaternary Science Reviews,* 28**,** 2374-2385.
Salau, O. R., Schneider, B., Park, W., Khon, V. & Latif, M. 2012. Modeling the ENSO impact of orbitally induced mean state climate changes. *Journal of Geophysical Research-Oceans,* 117.
Sandweiss, D. H., Maasch, K. A., Burger, R. L., Richardson, J. B., Rollins, H. B. & Clement, A. 2001. Variation in Holocene El Niño frequencies: Climate records and cultural consequences in ancient Peru. *Geology,* 29**,** 603-606.
Sandweiss, D. H., Richardson, J. B., Reitz, E. J., Rollins, H. B. & Maasch, K. A. 1996. Geoarchaeological evidence from Peru for a 5000 years BP onset of El Niño. *Science,* 273**,** 1531-1533.
Sano, Y., Kobayashi, S., Shirai, K., Takahata, N., Matsumoto, K., Watanabe, T., Sowa, K. & Iwai, K. 2012. Past daily light cycle recorded in the strontium/calcium ratios of giant clam shells. *Nature Communications,* 3.
Schmidt, G. A. 1999. Error analysis of paleosalinity calculations. *Paleoceanography,* 14**,** 422-429.
Schwartzmann, C., Durrieu, G., Sow, M., Ciret, P., Lazareth, C. E. & Massabuau, J.-C. 2011. In situ giant clam growth rate behavior in relation to temperature: A one-year coupled study of high-frequency noninvasive valvometry and sclerochronology. *Limnology and Oceanography,* 56.
Schöne, B. R. 2008. The curse of physiology - challenges and opportunities in the interpretation of geochemical data from mollusk shells. *Geo-Marine Letters,* 28.

Schöne, B. R., Dunca, E., Fiebig, J. & Pfeiffer, M. 2005. Mutvei's solution: An ideal agent for resolving microgrowth structures of biogenic carbonates. *Palaeogeography, Palaeoclimatology, Palaeoecology,* 228.

Schöne, B. R., Zhang, Z., Jacob, D., Gillikin, D. P., Tutken, T., Garbe-Schonberg, D., McConnaughey, T. & Soldati, A. 2010. Effect of organic matrices on the determination of the trace element chemistry (Mg, Sr, Mg/Ca, Sr/Ca) of aragonitic bivalve shells (*Arctica islandica*)-Comparison of ICP-OES and LA-ICP-MS data. *Geochemical Journal,* 44.

Schöne, B. R., Zhang, Z., Radermacher, P., Thébault, J., Jacob, D. E., Nunn, E. V. & Maurer, A.-F. 2011. Sr/Ca and Mg/Ca ratios of ontogenetically old, long-lived bivalve shells (*Arctica islandica*) and their function as paleotemperature proxies. *Palaeogeography, Palaeoclimatology, Palaeoecology,* 302.

Shackleton, N. 1967. Oxygen isotope analyses and Pleistocene temperatures re-assessed. *Nature,* 215**,** 15-&.

Shiau, L.-J., Chen, M.-T., Huh, C.-A., Yamamoto, M. & Yokoyama, Y. 2012. Insolation and cross-hemispheric controls on Australian monsoon variability over the past 180 ka: new evidence from offshore southeastern Papua New Guinea. *Journal of Quaternary Science,* 27**,** 911-920.

Shiau, L. J., Chen, M. T., Clemens, S. C., Huh, C. A., Yamamoto, M. & Yokoyama, Y. 2011. Warm pool hydrological and terrestrial variability near southern Papua New Guinea over the past 50k. *Geophysical Research Letters,* 38.

Shulmeister, J. & Lees, B. G. 1995. Pollen evidence from tropical Australia for the onset of an ENSO-dominated climate at C 4000 BP. *Holocene,* 5**,** 10-18.

Siddall, M., Rohling, E. J., Almogi-Labin, A., Hemleben, C., Meischner, D., Schmelzer, I. & Smeed, D. A. 2003. Sea-level fluctuations during the last glacial cycle. *Nature,* 423**,** 853-858.

Sinclair, D. J., Kinsley, L. P. J. & McCulloch, M. T. 1998. High resolution analysis of trace elements in corals by laser ablation ICP-MS. *Geochimica Et Cosmochimica Acta,* 62.

Sinclair, D. J. & McCulloch, M. T. 2004. Corals record low mobile barium concentrations in the Burdekin River during the 1974 flood: evidence for limited Ba supply to rivers? *Palaeogeography, Palaeoclimatology, Palaeoecology,* 214.

Smith, S. V., Buddemeier, R. W., Redalje, R. C. & Houck, J. E. 1979. Strontium-calcium thermometry in coral skeletons. *Science,* 204**,** 404-407.

Sprintall, J. & Tomczak, M. 1992. Evidence of the Barrier Layer in the Surface Layer of the Tropics. *Journal of Geophysical Research-Oceans,* 97**,** 7305-7316.

Stecher, H. A., Krantz, D. E., Lord, C. J., Luther, G. W. & Bock, K. W. 1996. Profiles of strontium and barium in Mercenaria mercenaria and Spisula solidissima shells. *Geochimica Et Cosmochimica Acta,* 60**,** 3445-3456.

Stoll, H. M. & Schrag, D. P. 1998. Effects of Quaternary sea level cycles on strontium in seawater. *Geochimica Et Cosmochimica Acta,* 62**,** 1107-1118.

Stoll, H. M., Schrag, D. P. & Clemens, S. C. 1999. Are seawater Sr/Ca variations preserved in Quaternary foraminifera? *Geochimica Et Cosmochimica Acta,* 63**,** 3535-3547.

Stott, L., Cannariato, K., Thunell, R., Haug, G. H., Koutavas, A. & Lund, S. 2004. Decline of surface temperature and salinity in the western tropical Pacific Ocean in the Holocene epoch. *Nature,* 431**,** 56-59.

Stott, L., Poulsen, C., Lund, S. & Thunell, R. 2002. Super ENSO and global climate oscillations at millennial time scales. *Science,* 297**,** 222-226.

Stuiver, M. & Reimer, P. J. 1993. Extended ^{14}C Database and Revised CALIB 3.0 ^{14}C Age Calibration Program. *Radiocarbon,* 35**,** 215-230.

Swart, P. K., Greer, L., Rosenheim, B. E., Moses, C. S., Waite, A. J., Winter, A., Dodge, R. E. & Helmle, K. 2010. The ^{13}C Suess effect in scleractinian corals mirror changes in the anthropogenic CO_2 inventory of the surface oceans. *Geophysical Research Letters,* 37.

Takesue, R. K., Bacon, C. R. & Thompson, J. K. 2008. Influences of organic matter and calcification rate on trace elements in aragonitic estuarine bivalve shells. *Geochimica Et Cosmochimica Acta,* 72**,** 5431-5445.

Takesue, R. K. & Van Geen, A. 2004. Mg/Ca, Sr/Ca, and stable isotopes in modern and holocene *Protothaca staminea* shells from a northern California coastal upwelling region. *Geochimica Et Cosmochimica Acta,* 68**,** 3845-3861.

Thompson, W. G. & Goldstein, S. L. 2006. A radiometric calibration of the SPECMAP timescale. *Quaternary Science Reviews,* 25**,** 3207-3215.

Timmermann, A., An, S. I., Krebs, U. & Goosse, H. 2005a. ENSO suppression due to weakening of the North Atlantic thermohaline circulation. *Journal of Climate,* 18**,** 3122-3139.

Timmermann, A., Krebs, U., Justino, F., Goosse, H. & Ivanochko, T. 2005b. Mechanisms for millennial-scale global synchronization during the last glacial period. *Paleoceanography,* 20.

Timmermann, A., Lorenz, S. J., An, S. I., Clement, A. & Xie, S. P. 2007. The effect of orbital forcing on the mean climate and variability of the tropical Pacific. *Journal of Climate,* 20**,** 4147-4159.

Toland, H., Perkins, B., Pearce, N., Keenan, F. & Leng, M. J. 2000. A study of sclerochronology by laser ablation ICP-MS. *Journal of Analytical Atomic Spectrometry,* 15**,** 1143-1148.

Trenberth, K. E. 1997. The definition of El Niño. *Bulletin of the American Meteorological Society,* 78**,** 2771-2777.

Tsonis, A. A., Hunt, A. G. & Elsner, J. B. 2003. On the relation between ENSO and global climate change. *Meteorology and Atmospheric Physics,* 84**,** 229-242.

Tudhope, A. W., Chilcott, C. P., McCulloch, M. T., Cook, E. R., Chappell, J., Ellam, R. M., Lea, D. W., Lough, J. M. & Shimmield, G. B. 2001. Variability in the El Niño - Southern oscillation through a glacial-interglacial cycle. *Science,* 291**,** 1511-1517.

Turney, C. S. M., Kershaw, A. P., Clemens, S. C., Branch, N., Moss, P. T. & Fifield, L. K. 2004. Millennial and orbital variations of El Niño/Southern Oscillation and high-latitude climate in the last glacial period. *Nature,* 428**,** 306-310.

Vander Putten, E., Dehairs, F., Keppens, E. & Baeyens, W. 2000. High resolution distribution of trace elements in the calcite shell layer of modern *Mytilus edulis*: Environmental and biological controls. *Geochimica Et Cosmochimica Acta,* 64**,** 997-1011.

Vecchi, G. A. & Wittenberg, A. T. 2010. El Niño and our future climate: where do we stand? *Wiley Interdisciplinary Reviews-Climate Change,* 1**,** 260-270.

Wanamaker, A. D., Kreutz, K. J., Wilson, T., Borns, H. W., Introne, D. S. & Feindel, S. 2008. Experimentally determined Mg/Ca and Sr/Ca ratios in juvenile bivalve calcite for *Mytilus edulis*: implications for paleotemperature reconstructions. *Geo-Marine Letters,* 28**,** 359-368.

Watanabe, T., Suzuki, A., Kawahata, H., Kan, H. & Ogawa, S. 2004. A 60-year isotopic record from a mid-Holocene fossil giant clam (Tridacna gigas) in the Ryukyu Islands: physiological and paleoclimatic implications. *Palaeogeography, Palaeoclimatology, Palaeoecology,* 212**,** 343-354.

Welsh, K. 2009. *Reconstructing the climate of the Western Warm Pool of the tropical Pacific using oxygen isotopes from the long-lived bivalves, Tridacna sp.*, University of Edinburgh.
Welsh, K., Elliot, M., Tudhope, A., Ayling, B. & Chappell, J. 2011. Giant bivalves (*Tridacna gigas*) as recorders of ENSO variability. *Earth and Planetary Science Letters,* 307**,** 266-270.
Wilson, C. & Adamec, D. 2001. Correlations between surface chlorophyll and sea surface height in the tropical Pacific during the 1997-1999 El Niño-Southern Oscillation event. *Journal of Geophysical Research-Oceans,* 106**,** 31175-31188.
Wyrtki, K. 1975. El Niño - Dynamic Response of Equatorial Pacific Ocean to Atmospheric Forcing. *Journal of Physical Oceanography,* 5**,** 572-584.
Yan, H., Shao, D., Wang, Y. & Sun, L. 2013. Sr/Ca profile of long-lived Tridacna gigas bivalves from South China Sea: A new high-resolution SST proxy. *Geochimica Et Cosmochimica Acta,* 112**,** 52-65.
Yokoyama, Y., Esat, T. M. & Lambeck, K. 2001. Coupled climate and sea-level changes deduced from Huon Peninsula coral terraces of the last ice age. *Earth and Planetary Science Letters,* 193**,** 579-587.
Yokoyama, Y., Esat, T. M., Lambeck, K. & Fifield, L. K. 2000. Last ice age millennial scale climate changes recorded in Huon Peninsula corals. *Radiocarbon,* 42**,** 383-401.
Yokoyama, Y., Esat, T. M., McCulloch, M. T., Mortimer, G. E., Chappell, J. & Lambeck, K. 2003. Large sea-level excursions during the Marine Isotope Stages 4 and 3 obtained from Huon Peninsula uplifted coral terraces. *Geochimica Et Cosmochimica Acta,* 67**,** A568-A568.
Zelle, H., Van Oldenborgh, G. J., Burgers, G. & Dijkstra, H. 2005. El Niño and Greenhouse warming: Results from ensemble simulations with the NCAR CCSM. *Journal of Climate,* 18**,** 4669-4683.
Zheng, W., Braconnot, P., Guilyardi, E., Merkel, U. & Yu, Y. 2008. ENSO at 6ka and 21ka from ocean-atmosphere coupled model simulations. *Climate Dynamics,* 30**,** 745-762.

Appendix

Contents

1. Geochemical profiles derived from Holocene *T. gigas* 1
T73 1
T58 2
T75 4
T66 – Anomalous Holocene shell? 5
2. Geochemical profiles derived from MIS3 *Tridacna* sp. 9
2.1 Reef IIa 9
T28 9
T27 10
T9 12
T11 13
2.2 Reef IIIc (lower): T32 15
2.3 Reef IIIc (upper) 16
T39 16
T40 17
2.4 Reef IIIb 19
T24 19
T37 20
2.5 Reef IIIa (lower): T41 21
2.6 Reef IIIa (middle): T18 23
2.7 Reef IIIa (upper) 24
T6 24
T15 26
T22 27
T45 29
Shells sampled for trace elements only 30
T38 30
T44 31
3. Comparison of bulk and mean results 33
4. Comparison of detrending methods 33
48 month running average 33
References 35

Appendix

1. Geochemical profiles derived from Holocene *T. gigas*

Methods are described in Chapter 3. All carbonate values are given in units per mille (‰) relative to a standard reference PDB. All trace elements are given in mmol/mol and have been smoothed using a 9-point running average. Temporal resolution is at 6 samples/year for $\delta^{18}O$ and $\delta^{13}C$ and 52 samples/year for trace elements.

T73

T73 is a *T. gigas* from Salonteron Beach, Huon Peninsula, dated to 7.28 ±0.12 ka. Two thin sections measuring 88 mm from the hinge were sampled. Profiles are ~20 years.

	Species	Length of record	Radiocarbon age	Calibrated age (ka BP)	Mean $\delta^{18}O$ (‰)	Mean $\delta^{13}C$ (‰)
T73	*T. gigas*	20	7129±27	7.26	-0.96	2.8

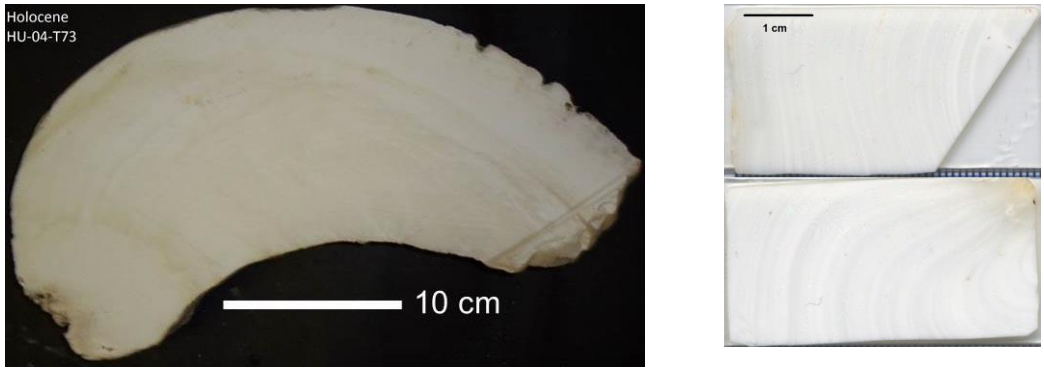

Figure A1.1 Slab of Holocene *Tridacna gigas* shell, T73 (left) and thin sections made from the hinge

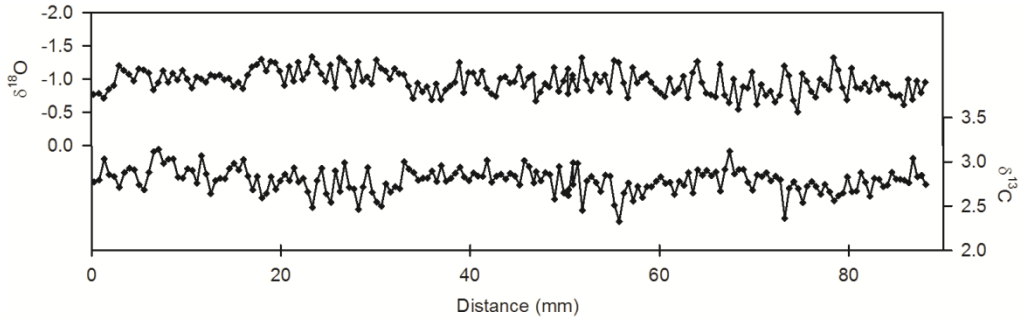

Figure A1.2 $\delta^{18}O$ (above) and $\delta^{13}C$ (below) raw profiles of T73 on a distance scale. Y axis is inverted for $\delta^{18}O$. Shell growth is from left to right, with the juvenile portion of the shell at 0mm

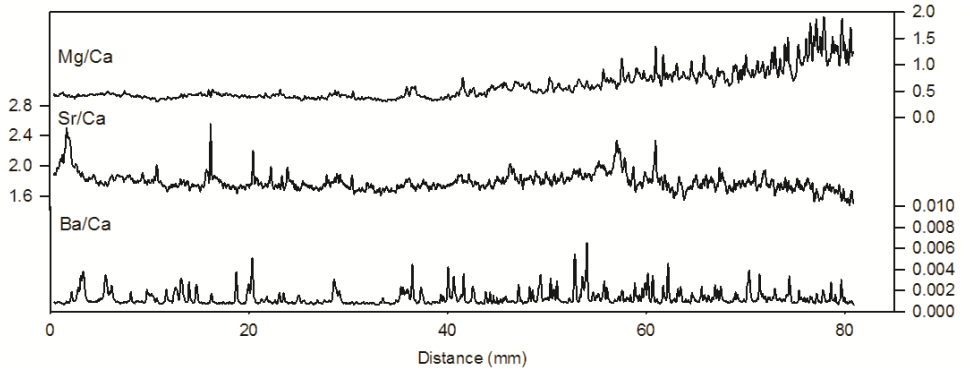

Figure A1.3 Trace element profiles of Mg/Ca, Sr/Ca and Ba/Ca on a distance scale, smoothed with a 9-point running average. All trace element measurements are in mmol/mol. Shell growth is from left to right

Appendix

Converting from a distance to an annual scale

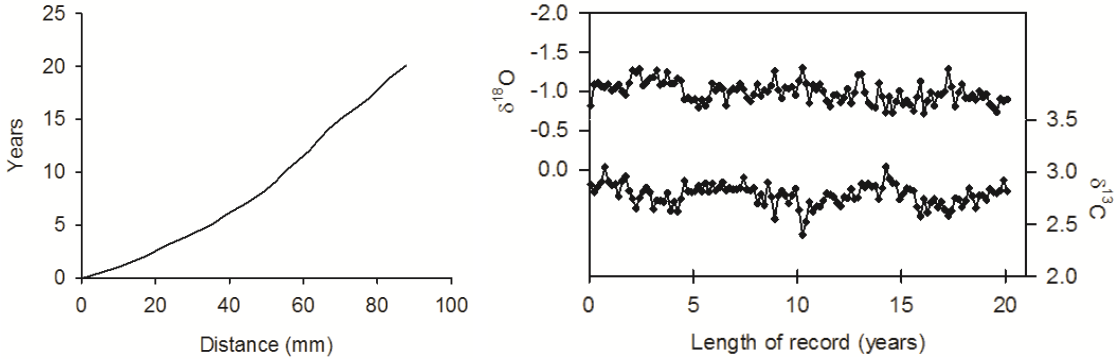

Figure A1.4 Left: Growth curve of T73, calculated using the stable isotope profile
Right: $\delta^{18}O$ (above) and $\delta^{13}C$ (below) profiles of T73 on an annual scale. $\delta^{18}O$ has been corrected for a sea level effect, described in Chapter 4. Resolution is at 6 samples/year.

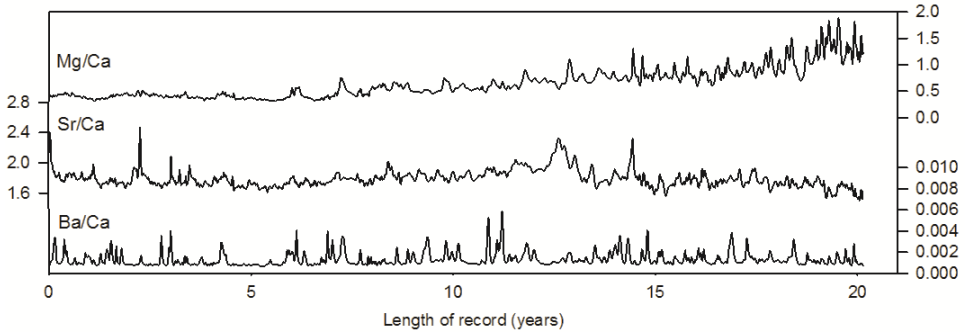

Figure A1.5 Trace element profiles of Mg/Ca, Sr/Ca and Ba/Ca on an annual scale, smoothed with a 9-point running average. Resolution is at 52 samples/year. All measurements are in mmol/mol

T58

T58 was collected from Kwambu Point, Huon Peninsula. T58 is a *T. gigas* shell dated to 7.59 ±0.1ka. Two thin sections measuring 88 mm from the inner layer were sampled. The stable isotope profile is approximately 18 years.

	Species	Length of record	Radiocarbon age	Calibrated age (ka BP)	Mean $\delta^{18}O$ (‰)	Mean $\delta^{13}C$ (‰)
T58	*T. gigas*	18	7527±26	7.59	-0.96	2.7

Figure A1.6 Slab of Holocene *T. gigas* shell, T58 (left), thin sections made from the hinge (right)

Appendix

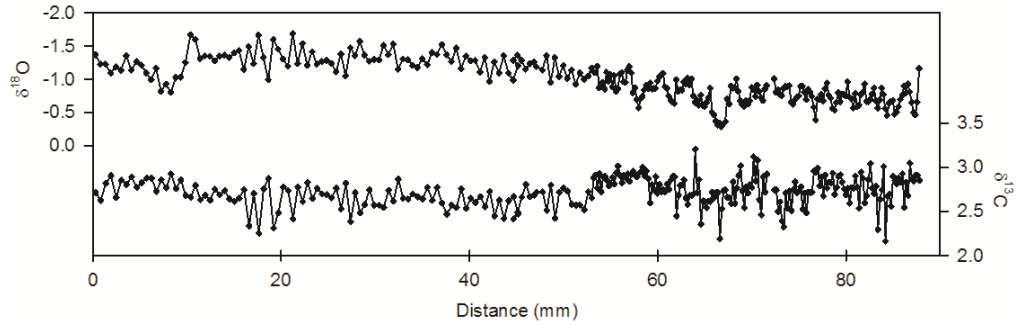

Figure A1.7 $\delta^{18}O$ (above) and $\delta^{13}C$ (below) raw profiles of T58 on a distance scale. Details in Figure A1.2

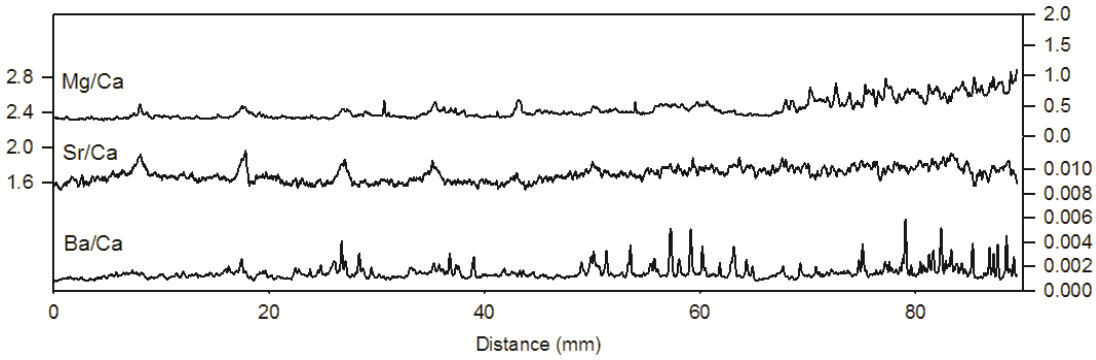

Figure A1.8 Trace element profiles of Mg/Ca, Sr/Ca and Ba/Ca on a distance scale. Details in Figure A1.3

Converting from a distance to an annual scale

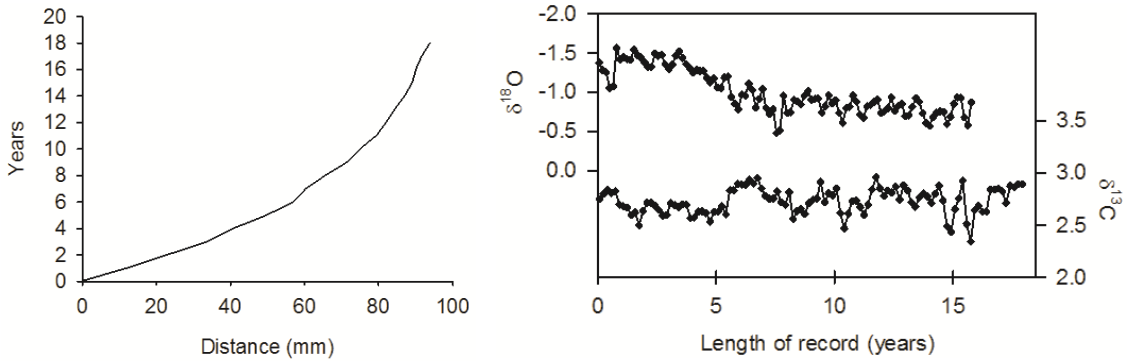

Figure A1.9 Left: Growth curve of T58, calculated using the stable isotope profile
Right: $\delta^{18}O$ (above) and $\delta^{13}C$ (below) profiles of T58 converted to an annual scale. Details in Figure A1.4

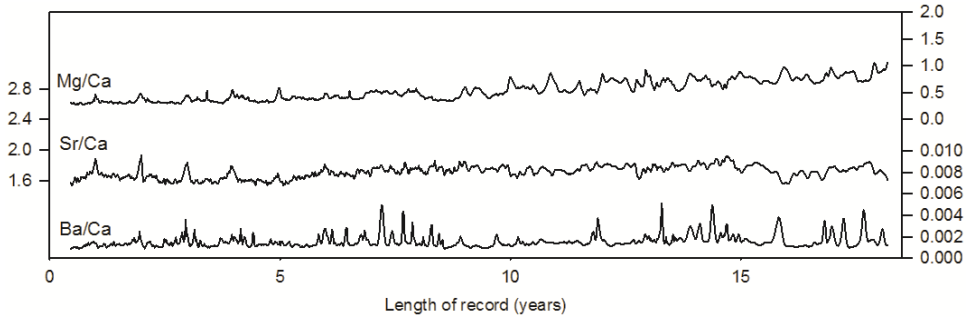

Figure A1.10 Trace element profiles of Mg/Ca, Sr/Ca and Ba/Ca on an annual scale. Details in Figure A1.5

Appendix

T75

T75 is a *T. gigas* collected from Hubegong, Huon Peninsula, and is dated to 8.72±0.19ka. Two thin sections measuring 64mm from the hinge were sampled. The stable isotope profile is approximately 12 years, and the trace element profile is approximately 15 years. This discrepancy is due to borings towards the edge of the shell, which the laser was able to avoid, but was unsuitable for sampling with the MicroMill.

	Species	Length of record	Radiocarbon age	Calibrated age (ka BP)	Mean $\delta^{18}O$ (‰)	Mean $\delta^{13}C$ (‰)
T75	*T. gigas*	12/15	8592±29	8.72	-0.92	2.6

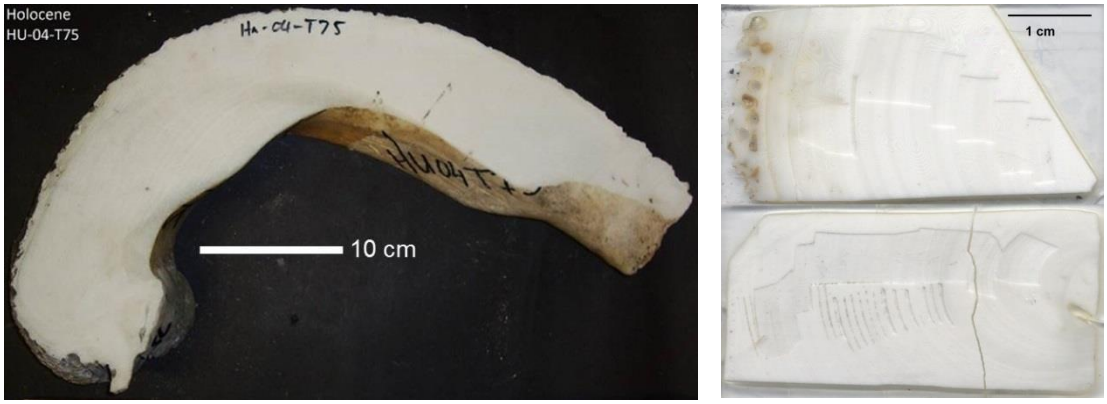

Figure A1.11 Slab of Holocene *Tridacna gigas* shell, T75 (left), thin sections made from the hinge area (right)

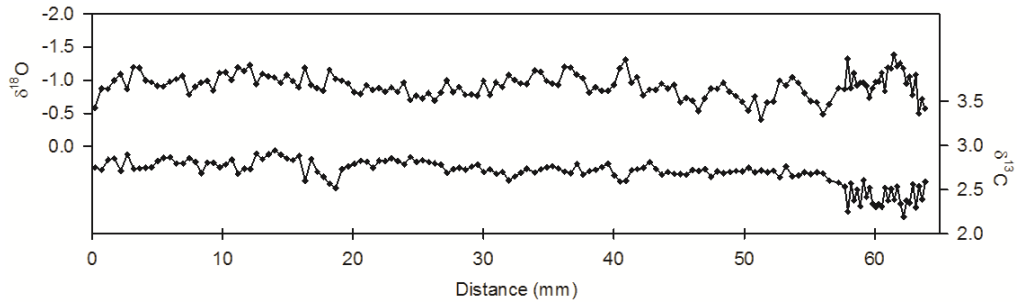

Figure A1.12 $\delta^{18}O$ (above) and $\delta^{13}C$ (below) raw profiles of T75 on a distance scale. Details in Figure A1.2

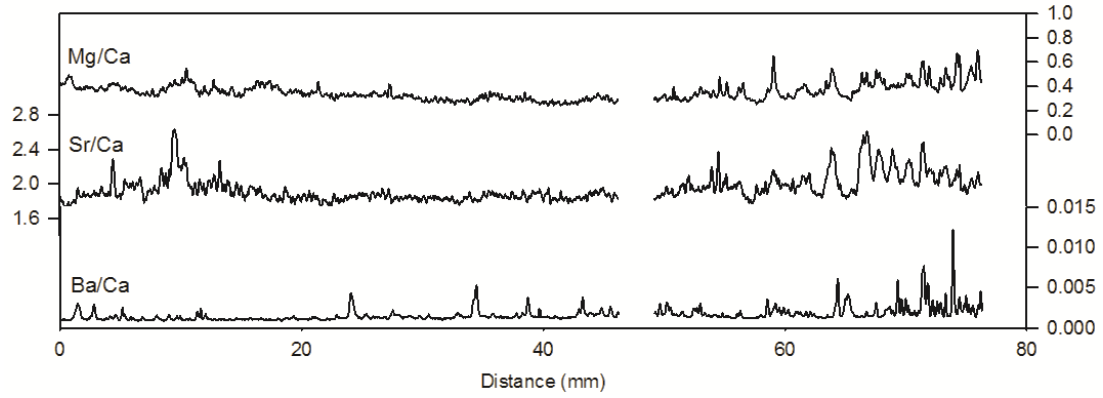

Figure A1.13 Trace element profiles of Mg/Ca, Sr/Ca and Ba/Ca on a distance scale. Details in Figure A1.3

Appendix

Converting from a distance to an annual scale

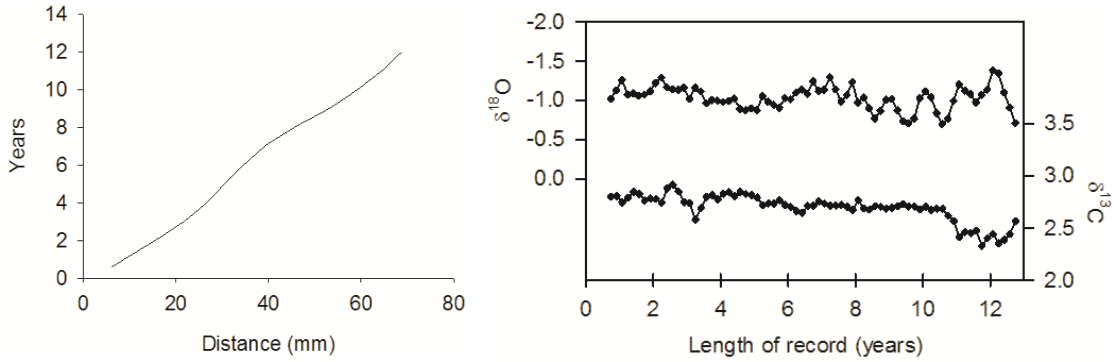

Figure A1.14 Left: Growth curve of T75, calculated using the stable isotope profile
Right: $\delta^{18}O$ (above) and $\delta^{13}C$ (below) profiles of T75 converted to an annual scale. Details in Figure A1.4

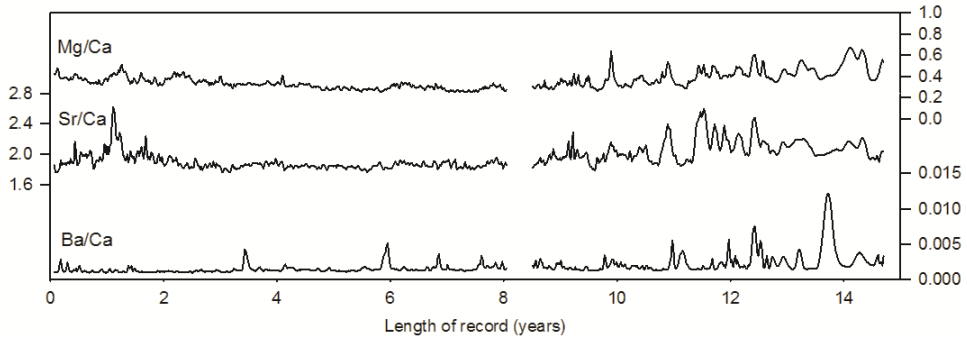

Figure A1.15 Trace element profiles of Mg/Ca, Sr/Ca and Ba/Ca on an annual scale. Details in Figure A1.5

T66 – Anomalous Holocene shell?

T66 is a *T. gigas* shell collected from the Bobongara Lagoon at Huon Peninsula and dated to 6.49 ±0.37 ka. Two thin sections measuring 74mm from the inner layer were sampled. The stable isotope profile is approximately 6 years.

	Species	Length of record	Radiocarbon age	Calibrated age (ka BP)	Mean $\delta^{18}O$ (‰)	Mean $\delta^{13}C$ (‰)
T66	*T. gigas*	6	6480±40	6.49	-1.8	2.9

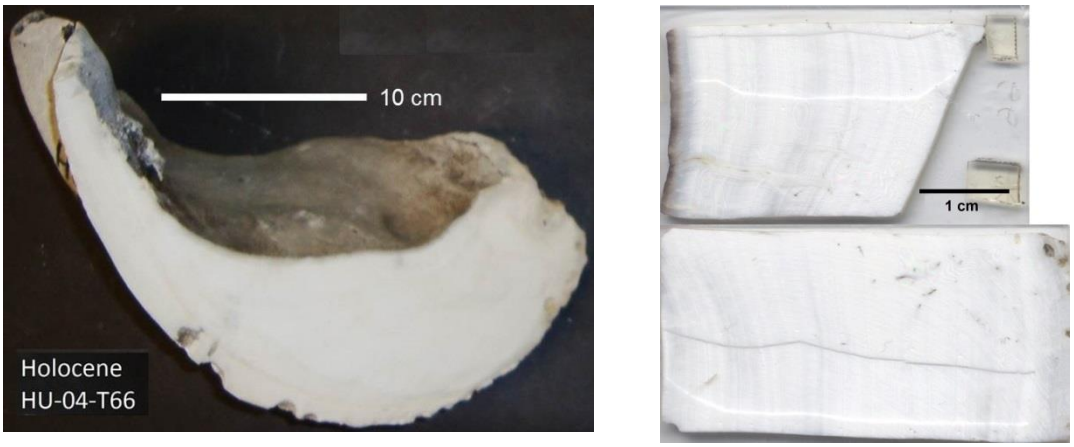

Figure A1.16 Slab of Holocene *T. gigas* shell, T66 (left) and thin sections made from the inner layer (right)

Appendix

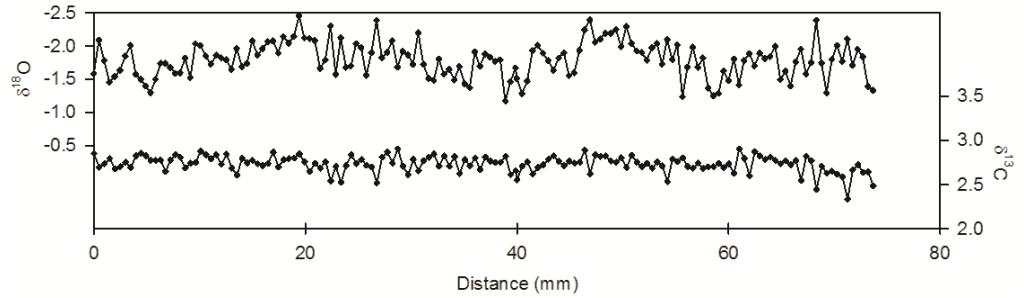

Figure A1.17 $\delta^{18}O$ (above) and $\delta^{13}C$ (below) raw profiles of T66 on a distance scale. Details in Figure A1.2

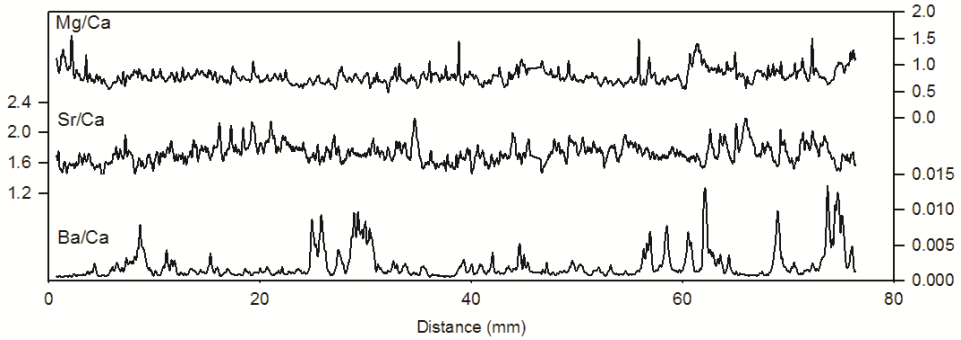

Figure A1.18 Trace element profiles of Mg/Ca, Sr/Ca and Ba/Ca on a distance scale. Details in Figure A1.3

Converting from a distance to an annual scale

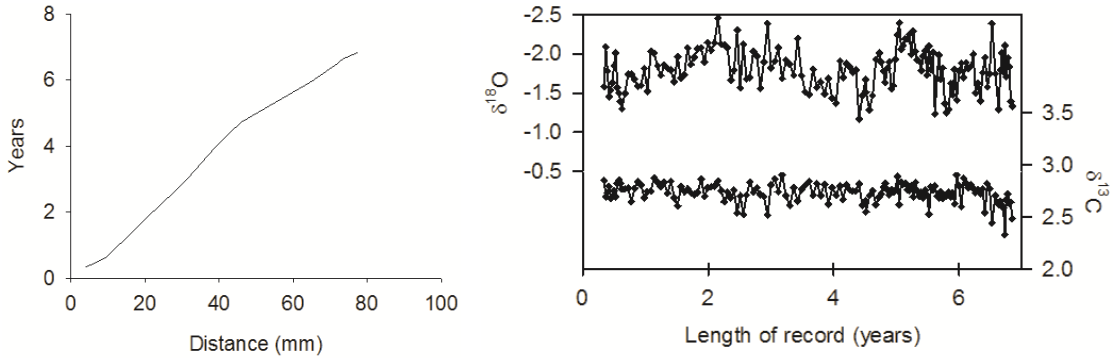

Figure A1.19 Left: Growth curve of T66, calculated using the stable isotope profile
Right: $\delta^{18}O$ (above) and $\delta^{13}C$ (below) profiles of T66 converted to an annual scale. Details in Figure A1.4

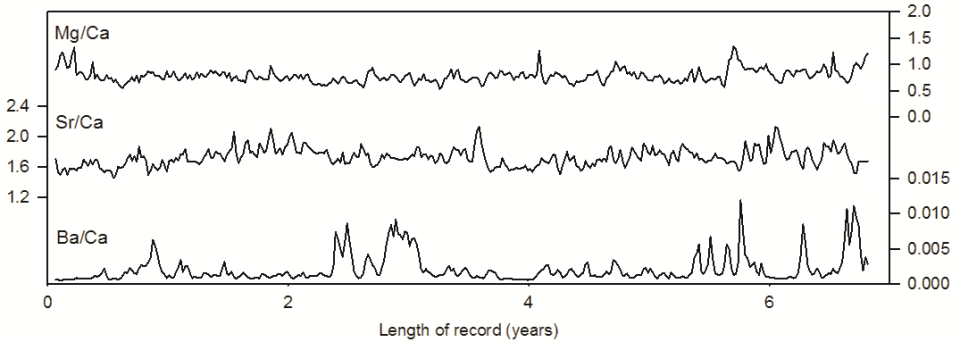

Figure A1.20 Trace element profiles of Mg/Ca, Sr/Ca and Ba/Ca on an annual scale. Details in Figure A1.5

T66 differs from the other Holocene *T. gigas* shells in terms of the $\delta^{18}O$ profile and microstructure growth banding.

Appendix

Growth banding

The day/night banding in this shell is distinctly different to that of the other Holocene samples. In the samples used in this study (Figure A1.21), the width of bands decreases from the juvenile stage of growth to adult. Watanabe et al. (2004) found that juvenile bands measured 40-70µm, while adult bands measured 2-25µm in a Holocene *T. gigas*. In the three Holocene *T. gigas* from the Huon Peninsula, juvenile bands tend to measure 16-33µm, while adult bands measure 4-10 µm. In a modern *T. gigas* from the western Pacific, microstructure growth bands measure 10-50µm in the inner layer (Pätzold et al., 1991).

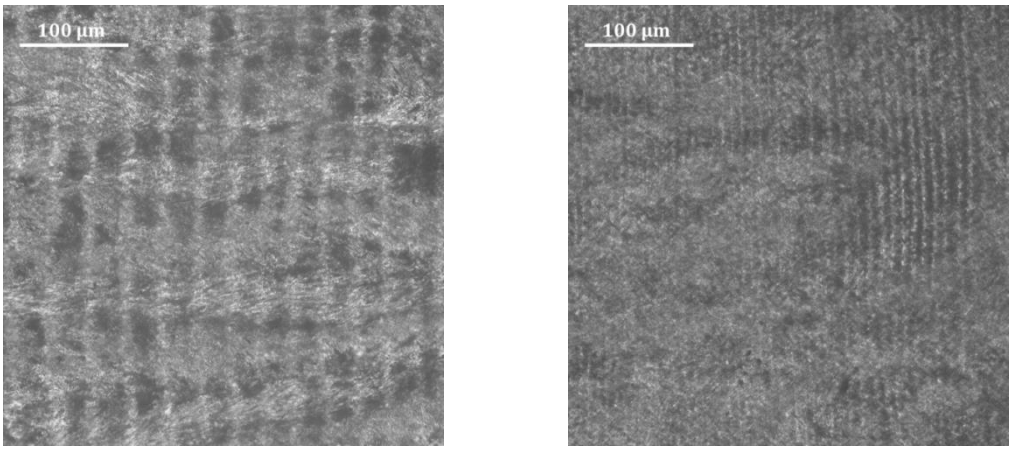

Figure A1.21 Growth banding of T73 under 20x magnification in the juvenile (left) and adult (right) phases

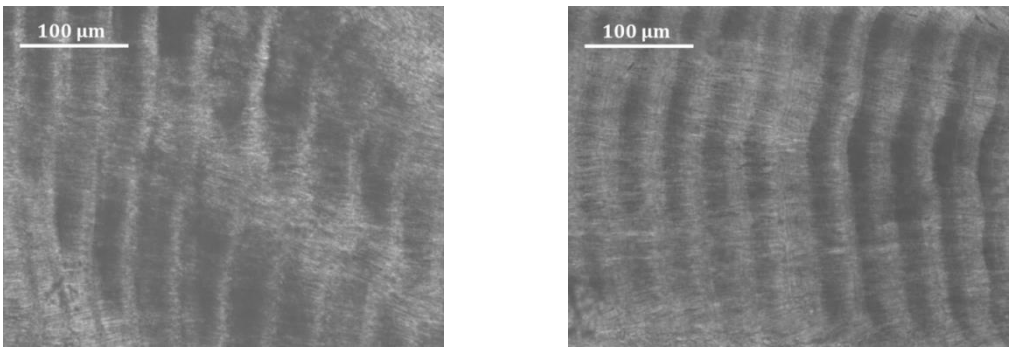

Figure A1.22 Growth banding of T66 under 20x magnification in the juvenile (left) and adult (right) phase

In T66, the growth banding is wide throughout the lifetime of the shell (Figure A1.22), measuring approximately 50µm in the juvenile phase, and 25µm in the adult phase. The size of the growth banding in this shell suggests that growth was more rapid than in the other Holocene *T. gigas*.

Growth curves

The number of pairs of day/night bands can be extrapolated to calculate the growth per year in *Tridacna* sp. samples (Chapter 3). While for three shells, growth is initially rapid before slowing, in T66 the growth rate suggested by the day/night bands is rapid throughout the life of the shell (Figure A1.23). In modern and fossil *T. gigas*, growth rates vary from 16 mm/year during the juvenile phase to 5 mm/year (Aharon, 1991), 2 mm/year (Welsh et al., 2011) and 1 mm/year (Watanabe et al., 2001).

Appendix

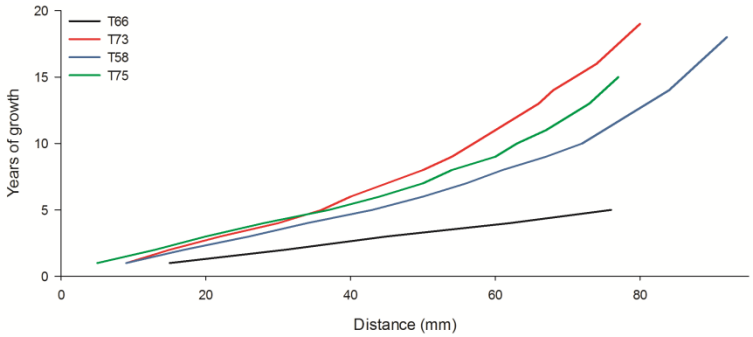

Figure A1.23 Growth curves for Holocene *T. gigas* shells produced using the day/night band counts (described in Chapter 3)

Once explanation for the discrepancy between growth rates in the Holocene *T. gigas* shells could be due to the fact that for T73, T58 and T75, the hinge was sampled, while in T66 the inner layer was sampled. However, the growth rates in the hinge and inner layers of a modern *T. gigas* are very similar (Elliot et al., 2009). It is unlikely that the difference in shell area sampled is alone in causing the difference in growth rate.

$\delta^{18}O$

The $\delta^{18}O$ profile of T66 is more negative than the modern *T. gigas* MT7 and the three Holocene shells, T73, T58 and T75 (Figure A1.17). The mean $\delta^{18}O$ value recorded by T66 is -1.79‰, which would suggest a temperature increase of 2.7°C, or a decrease in salinity of 2.2‰ p.s.u. compared to MT7. Additionally, this would suggest a temperature increase of 3.6°C or decreased in salinity of 2.8‰ p.s.u. compared to the three early Holocene shells. The three early Holocene shells are dated to between 7.26 to 8.73 ka BP, which is a period of 1.47 ka. The latest early Holocene shell, T73, dated to 7.26 ka is 0.77 ka older than T66, and has a mean $\delta^{18}O$ value which is 0.8‰ more positive than T66. It seems very unlikely that the tropical Pacific climate changed so rapidly between 7.26 and 6.49 ka, when the difference between values recorded in 8.73 and 7.26 ka are 0.04‰.

It seems very unlikely that T66 is simply recording warmer SSTs at 6.49 ka than the early Holocene shells. The fast growth and negative $\delta^{18}O$ values recorded in T66 suggest warmer or wetter conditions at this shells time of growth, or a combination of the two. Pugh and Rayner (1981) found an increase of 2°C in lagoonal waters compared to that in the open ocean in cloud free windless weather in Indian Ocean atolls. If it assumed that T66 is recording lagoonal conditions which are 2°C warmer than the open ocean, then it would suggest that conditions at 6.49 ka BP were 1.6°C warmer than between 8.73-7.26 ka BP, and 0.7°C warmer than the present day.

Appendix

2. Geochemical profiles derived from MIS3 *Tridacna* sp.

All the *Tridacna* sp. shells dated to Marine Isotope Stage III were collected from the MIS3 raised coral terraces at Bobongara, Huon Peninsula.

2.1 Reef IIa

T28

T28 is a *Tridacna maxima* shell dated to 34.1 ±0.7 ka. One thin section measuring 16mm from the inner layer was sampled. The stable isotope profile is approximately 12 years long, while the trace element profile is approximately 14 years long. This discrepancy is due to the lack of visible lines at the edge of the shell. Due to the way in which the shell was MicroMilled, samples could not be taken from an area where growth lines were not visible under transmitted or reflected light – however it was possible to ablate this region of the shell.

	Species	Length of record	Radiocarbon age	Calibrated age (ka BP)	Mean $\delta^{18}O$ (‰)	Mean $\delta^{13}C$ (‰)
T28	*T. maxima*	12/14	30,450 ±150	34.13	-0.24	2.4

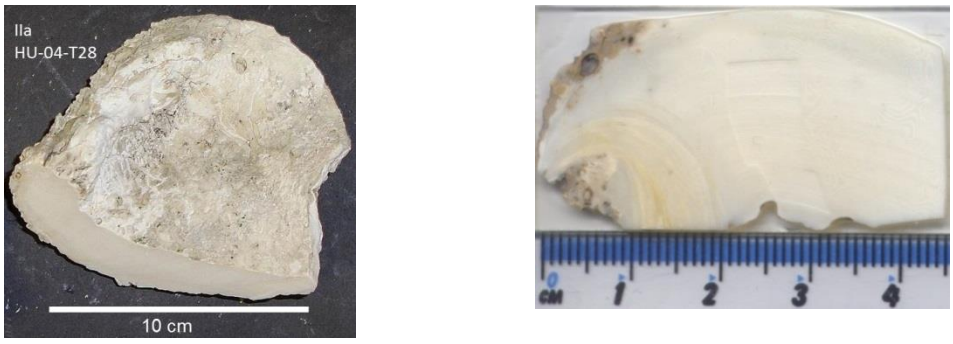

Figure A2.1 Section of Reef IIa *T. maxima* T28 (left) and thin section made from the inner layer (right)

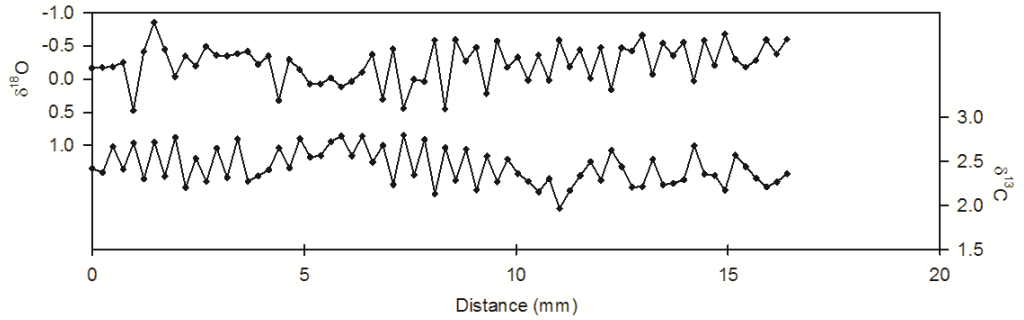

Figure A2.2 $\delta^{18}O$ (above) and $\delta^{13}C$ (below) raw profiles of T28 on a distance scale. Y axis is inverted for $\delta^{18}O$. Shell growth is from left to right, with the juvenile portion of the shell at 0mm

Appendix

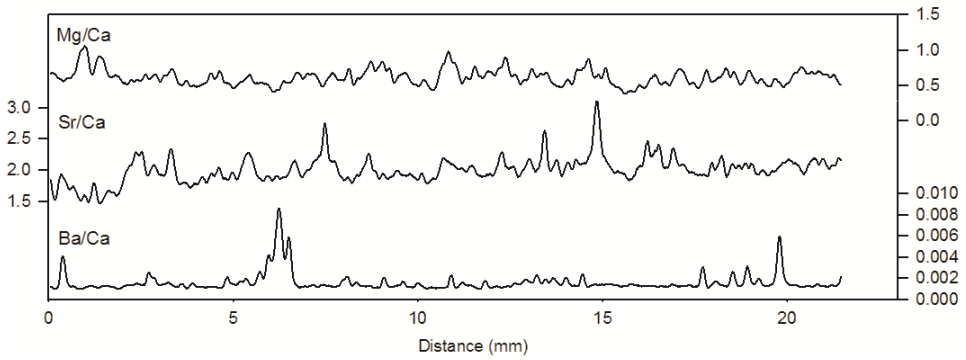

Figure A2.3 Trace element profiles of Mg/Ca, Sr/Ca and Ba/Ca on a distance scale, smoothed with a 9-point running average. All measurements are in mmol/mol. Shell growth is from left to right, with the juvenile portion of the shell at 0mm

Converting from a distance to an annual scale

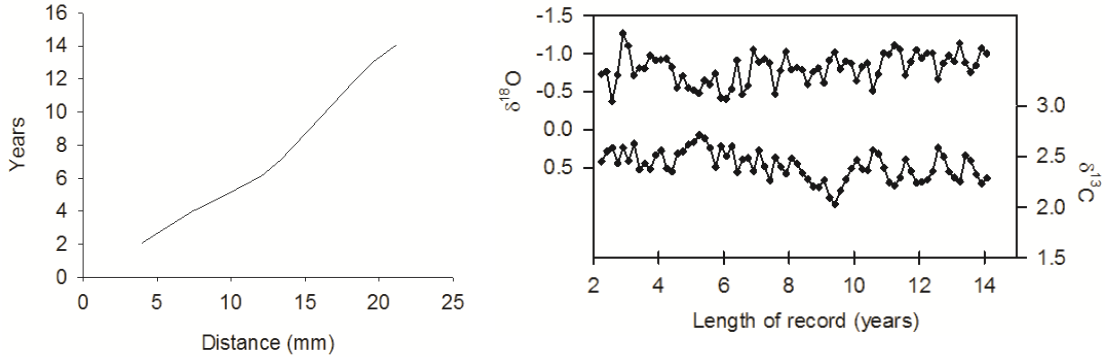

Figure A2.4 Left: Growth curve of T28, calculated using the stable isotope profile
Right: $\delta^{18}O$ (above) and $\delta^{13}C$ (below) profiles of T28 converted to an annual scale. $\delta^{18}O$ has been corrected for an ice volume level effect, described in Chapter 4. Resolution is at 6 samples/year

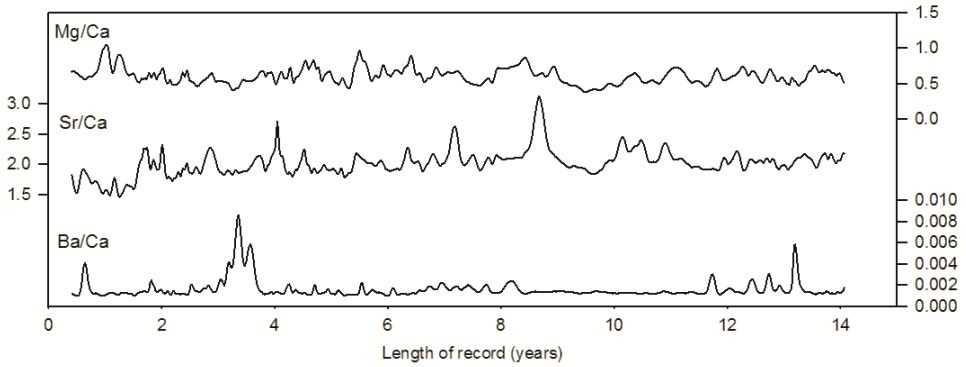

Figure A2.5 Trace element profiles of Mg/Ca, Sr/Ca and Ba/Ca on an annual scale, smoothed with a 9-point running average. Resolution is at 52 samples/year. All measurements in mmol/mol

T27

T27 is a *T. maxima* shell dated to 35.5 ±1.9 ka. One thin section measuring 40 mm from the inner layer was sampled. The stable isotope profile is approximately 8 years.

	Species	Length of record	Radiocarbon age	Calibrated age (ka BP)	Mean $\delta^{18}O$ (‰)	Mean $\delta^{13}C$ (‰)
T27	*T. maxima*	8	31820±425	35.5	-0.24	2.4

Appendix

Figure A2.6 Section of Reef IIa *T. maxima* T27 (left) and thin section made from the inner layer (right)

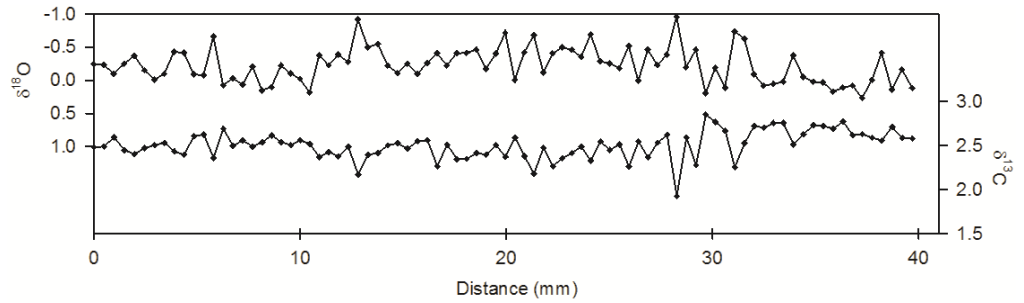

Figure A2.7 $\delta^{18}O$ (above) and $\delta^{13}C$ (below) raw profiles of T27 on a distance scale. Details in Figure A2.2

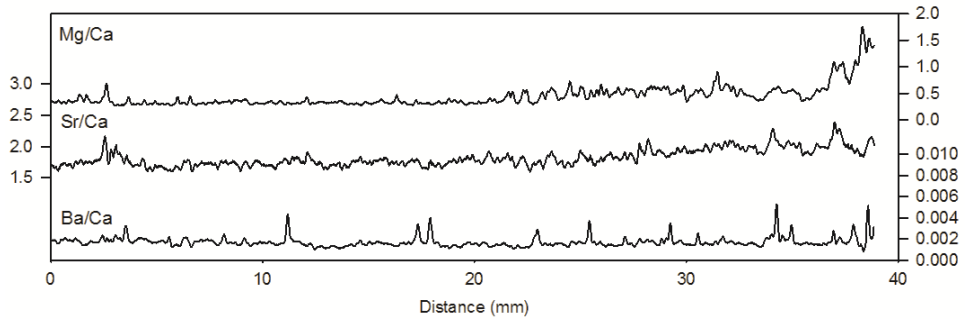

Figure A2.8 Trace element profiles of Mg/Ca, Sr/Ca and Ba/Ca on a distance scale. Details in Figure A2.3

Converting from a distance to an annual scale

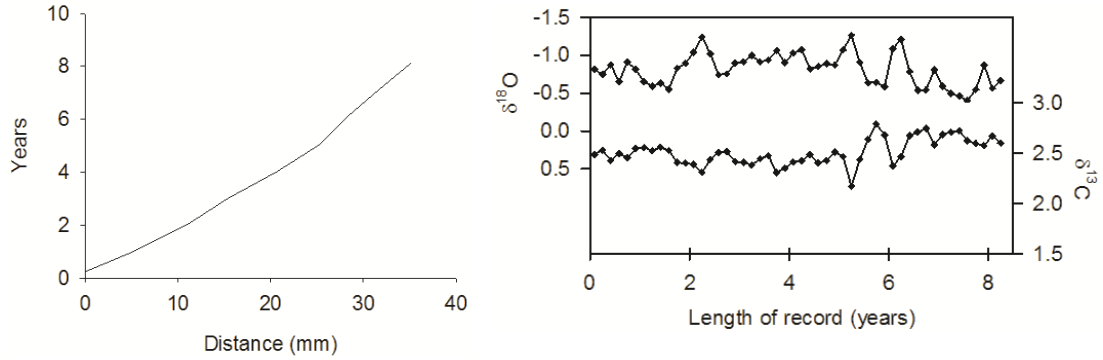

Figure A2.9 Right: Growth curve of T27, calculated using the stable isotope profile
Left: $\delta^{18}O$ (above) and $\delta^{13}C$ (below) profiles of T27 converted to an annual scale. Details in Figure A2.4

Appendix

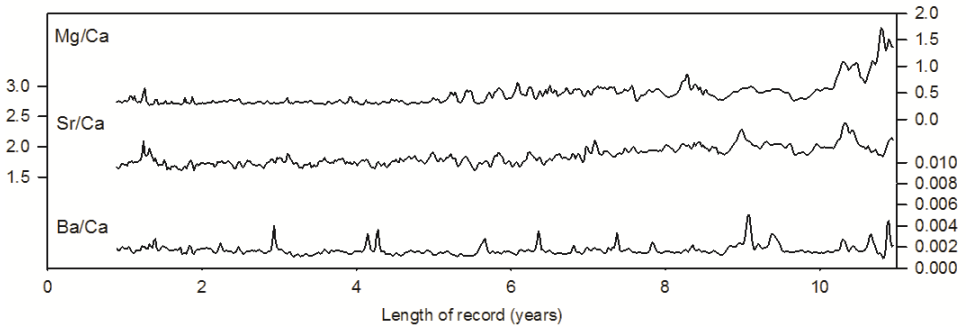

Figure A2.10 Trace element profiles of Mg/Ca, Sr/Ca and Ba/Ca on an annual scale. Details in Figure A2.5

T9

T9 is a *T. gigas* shell dated to 36.7 ± 1.6 ka. One thin section measuring 45mm from the inner layer was sampled. The stable isotope profile is approximately 10 years.

	Species	Length of record	Radiocarbon age	Calibrated age (ka BP)	Mean $\delta^{18}O$ (‰)	Mean $\delta^{13}C$ (‰)
T9	*T. gigas*	10	32794±479	36.74	0.045	2.7

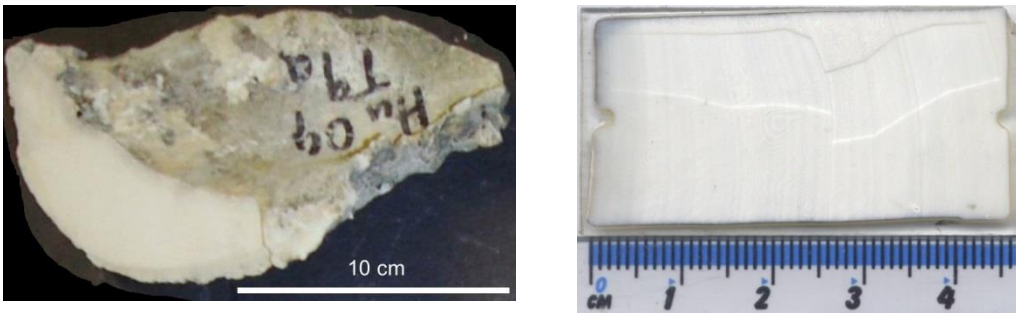

Figure A2.11 Section of Reef IIa *T. gigas* T9 (left) and thin section made from the inner layer (right)

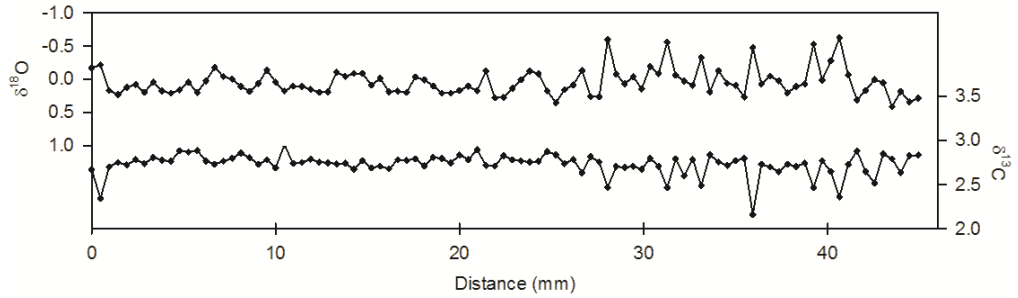

Figure A2.12 $\delta^{18}O$ (above) and $\delta^{13}C$ (below) raw profiles of T9 on a distance scale. Details in Figure A2.2

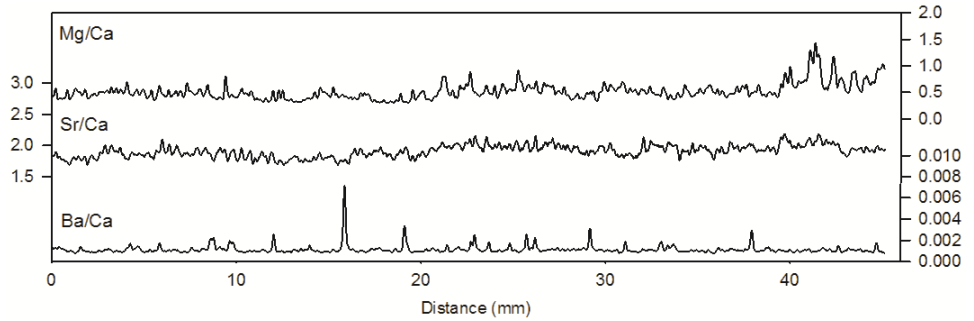

Figure A2.13 Trace element profiles of Mg/Ca, Sr/Ca and Ba/Ca on a distance scale. Details in Figure A2.3

Appendix

Converting from a distance to an annual scale

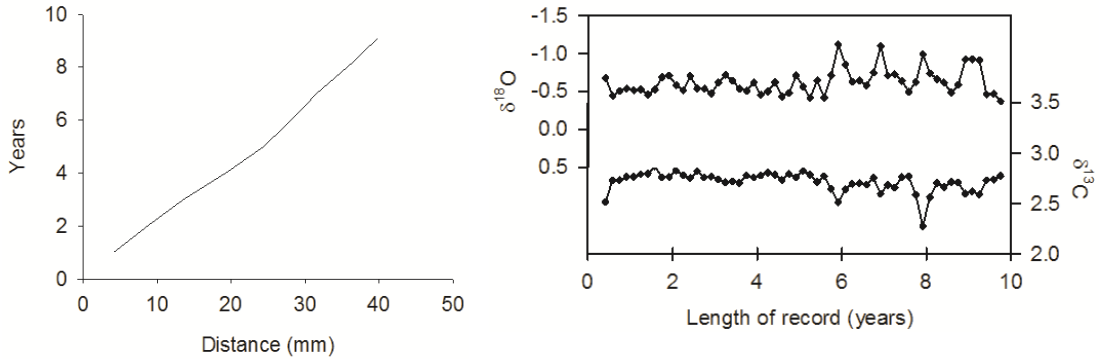

Figure A2.14 Left: Growth curve of T9, calculated using the stable isotope profile
Right: $\delta^{18}O$ (above) and $\delta^{13}C$ (below) profiles of T9 converted to an annual scale. Details in Figure A2.4

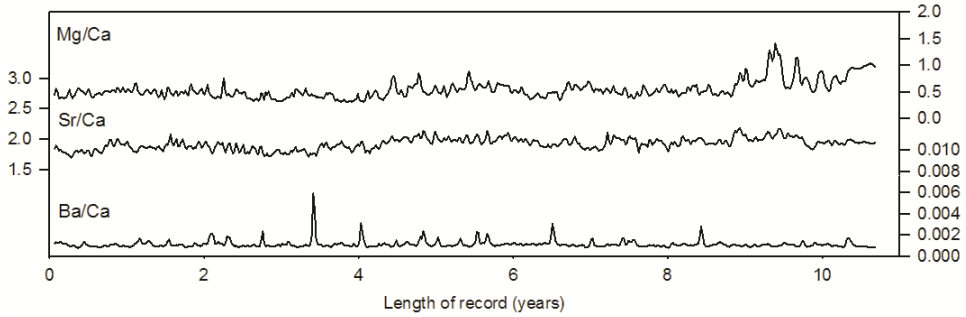

Figure A2.15 Trace element profiles of Mg/Ca, Sr/Ca and Ba/Ca on an annual scale. Details in Figure A2.5

T11

T11 is a *T. squamosa* shell dated to 37.3 ±2.3 ka. One thin section measuring 41mm from the inner layer was sampled. The stable isotope profile is approximately 7 years.

	Species	Length of record	Radiocarbon age	Calibrated age (ka BP)	Mean $\delta^{18}O$ (‰)	Mean $\delta^{13}C$ (‰)
T11	*T. squamosa*	7	31,820±425	37.3	0.38	2.8

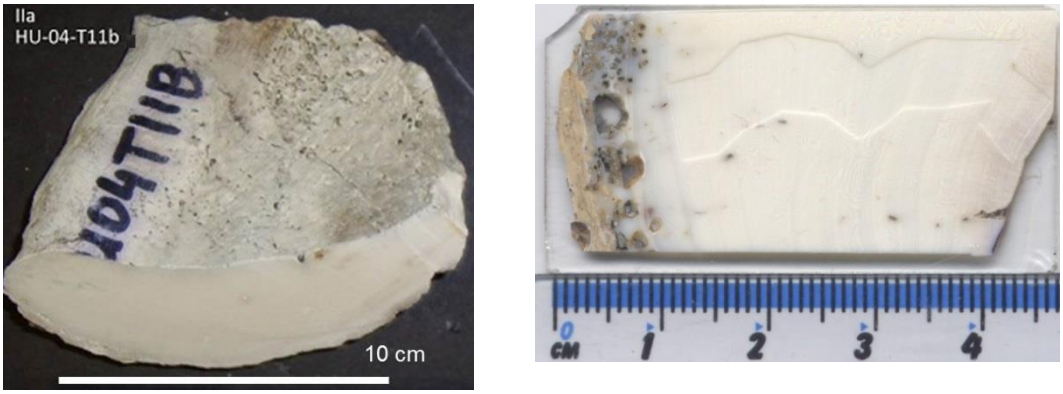

Figure A2.16 Section of Reef IIa *T. squamosa* T11 (left) and thin section made from the inner layer (right)

Appendix

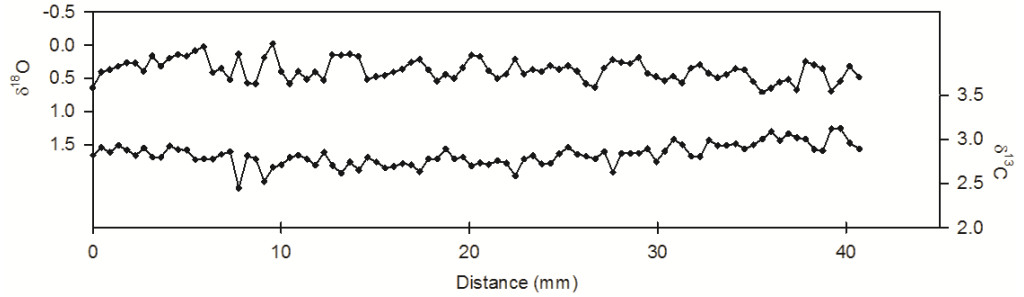

Figure A2.17 $\delta^{18}O$ (above) and $\delta^{13}C$ (below) raw profiles of T11 on a distance scale. Details in Figure A2.2

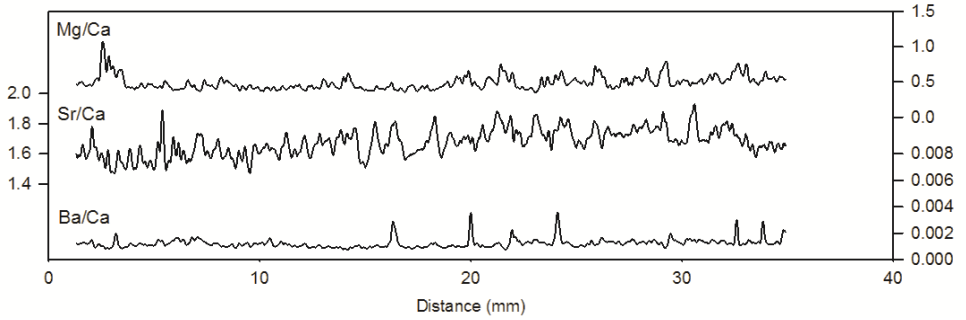

Figure A2.18 Trace element profiles of Mg/Ca, Sr/Ca and Ba/Ca on a distance scale. Details in Figure A2.3

Converting from a distance to an annual scale

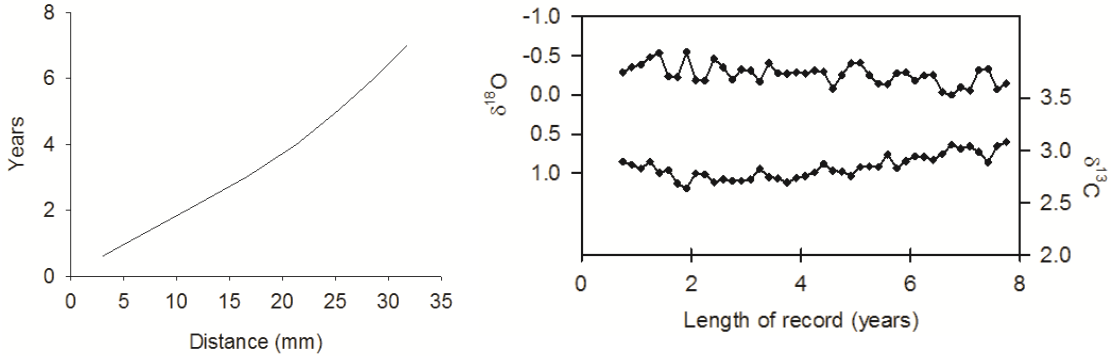

Figure A2.19 Left: Growth curve of T11, calculated using the stable isotope profile
Right: $\delta^{18}O$ (above) and $\delta^{13}C$ (below) profiles of T11 converted to an annual scale. Details in Figure A2.4

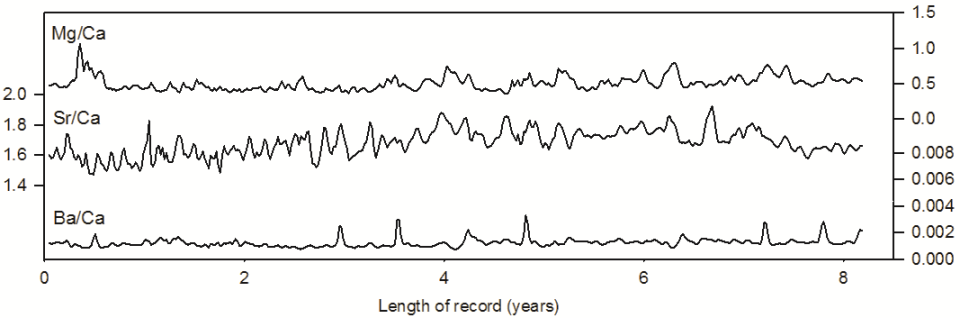

Figure A2.20 Trace element profiles of Mg/Ca, Sr/Ca and Ba/Ca on an annual scale. Details in Figure A2.5

2.2 Reef IIIc (lower): T32

T32 is a *T. maxima* shell dated to 38.4 ±1.2 ka. One thin section measuring 22mm from the hinge was sampled. The stable isotope profile is approximately 15 years.

	Species	Length of record	Radiocarbon age	Calibrated age (ka BP)	Mean $\delta^{18}O$ (‰)	Mean $\delta^{13}C$ (‰)
T32	*T. maxima*	15	34,520±190	38.38	-0.03	2.4

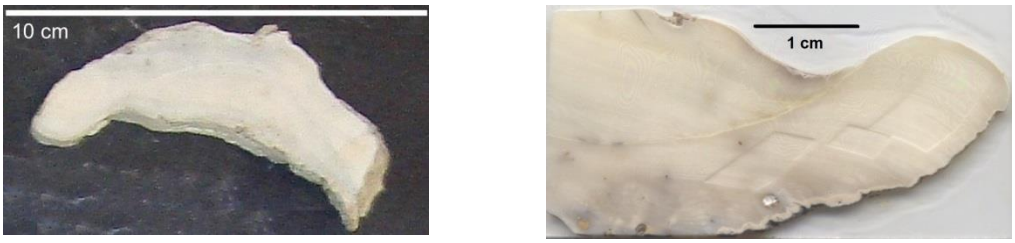

Figure A2.21 Reef IIIc (l) *T. maxima* T32 (left) and thin section made from the hinge and inner layer (right)

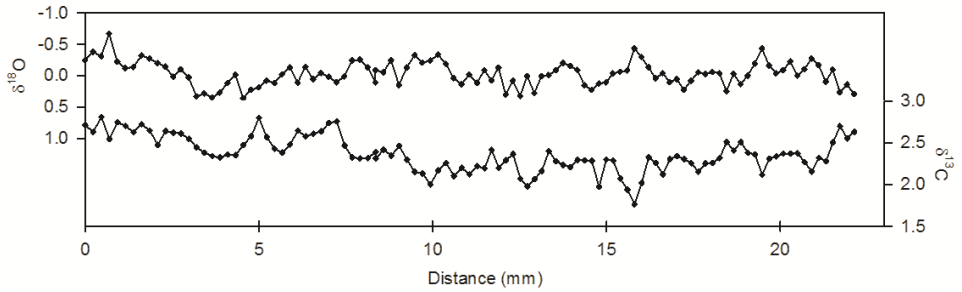

Figure A2.22 $\delta^{18}O$ (above) and $\delta^{13}C$ (below) raw profiles of T32 on a distance scale. Details in Figure A2.2

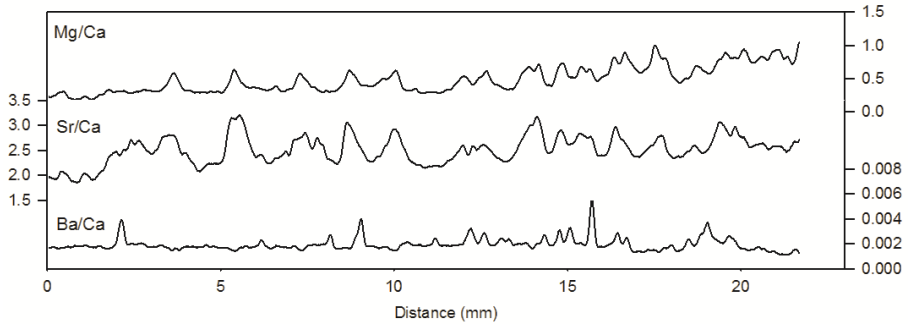

Figure A2.23 Trace element profiles of Mg/Ca, Sr/Ca and Ba/Ca on a distance scale. Details in Figure A2.3

Converting from a distance to an annual scale

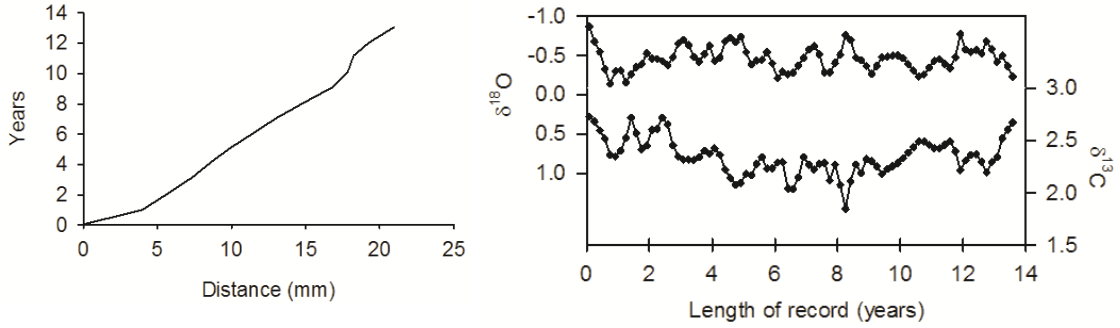

Figure A2.24 Left: growth curve of T32, calculated using the stable isotope profile
Right: $\delta^{18}O$ (above) and $\delta^{13}C$ (below) profiles of T32 converted to an annual scale. Details in Figure A2.4

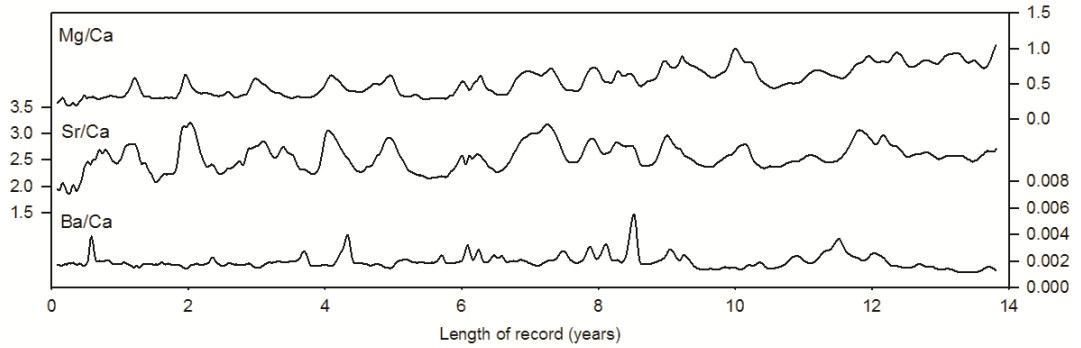

Figure A2.25 Trace element profiles of Mg/Ca, Sr/Ca and Ba/Ca on an annual scale. Details in Figure A2.5

2.3 Reef IIIc (upper)

T39

T39 is a *T. maxima* shell dated to 40.7 ± 1ka. One thin section measuring 24mm from the inner layer was sampled. The stable isotope profile is approximately 13 years.

	Species	Length of record	Radiocarbon age	Calibrated age (ka BP)	Mean $\delta^{18}O$ (‰)	Mean $\delta^{13}C$ (‰)
T39	*T. maxima*	13	36,550±230	40.67	0.32	2.6

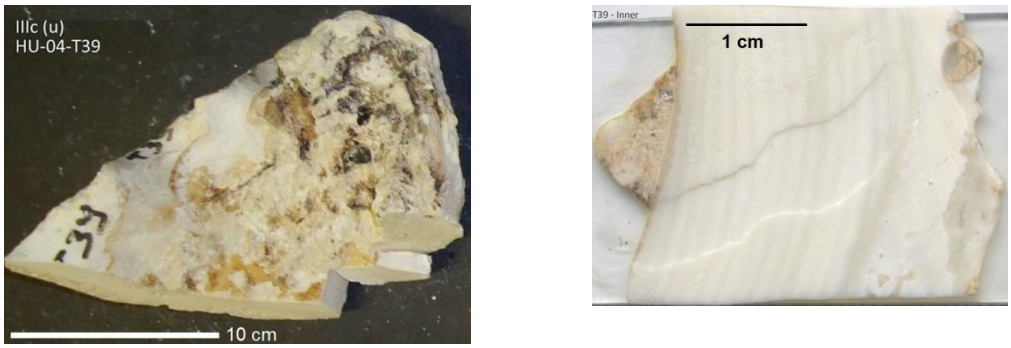

Figure A2.26 Section of Reef IIIc (u) *T. maxima* T39 (left) and thin section made from the inner layer (right)

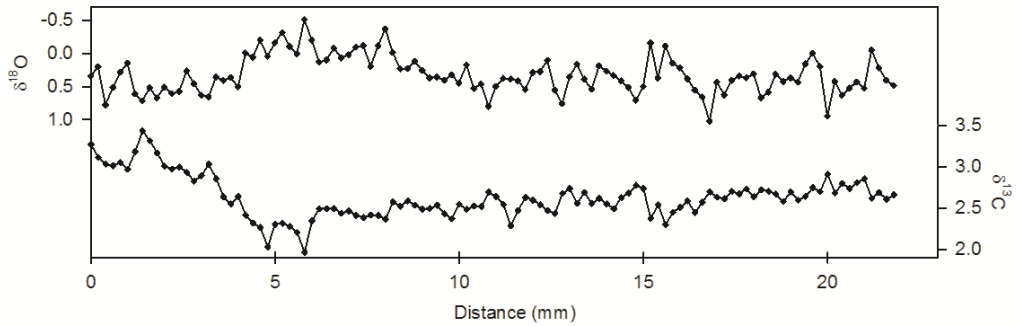

Figure A2.27 $\delta^{18}O$ (above) and $\delta^{13}C$ (below) raw profiles of T39 on a distance scale. Details in Figure A2.2

Appendix

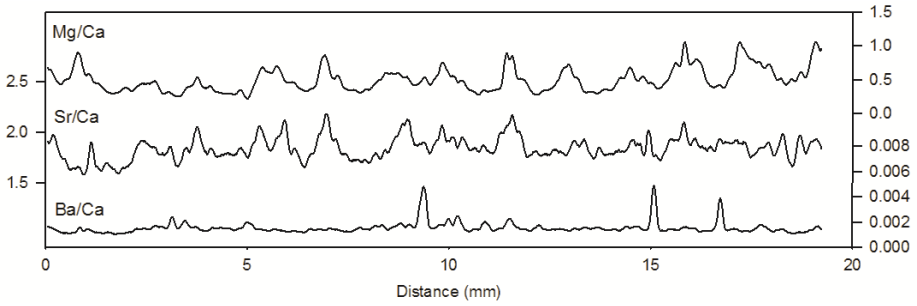

Figure A2.28 Trace element profiles of Mg/Ca, Sr/Ca and Ba/Ca on a distance scale. Details in Figure A2.3

Converting from a distance to an annual scale

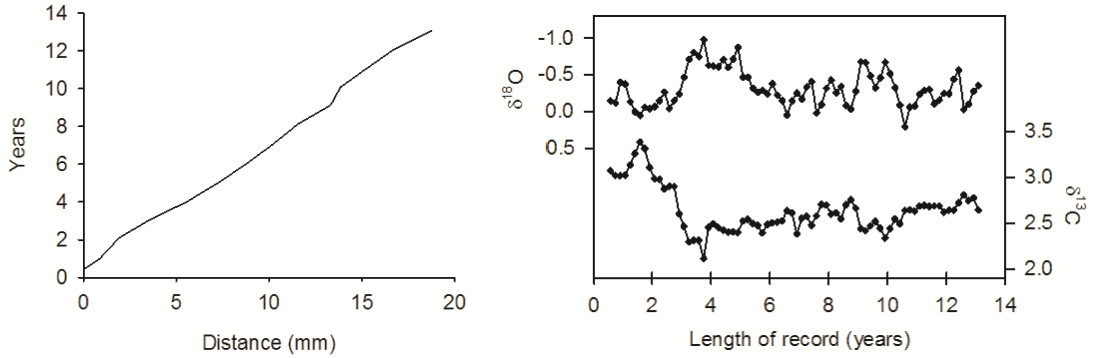

Figure A2.29 Left: Growth curve of T39, calculated using the stable isotope profile
Right: $\delta^{18}O$ (above) and $\delta^{13}C$ (below) profiles of T39 converted to an annual scale. Details in Figure A2.4

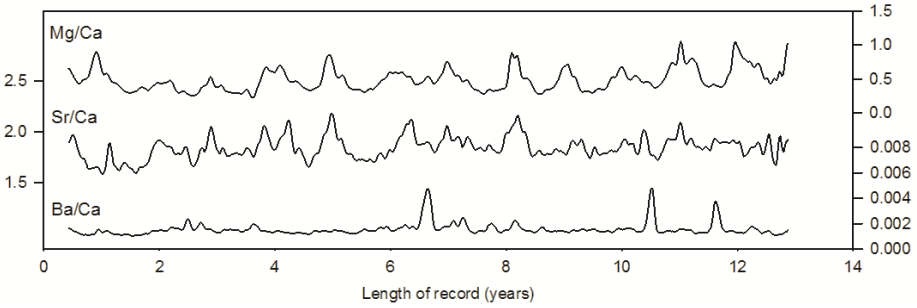

Figure A2.30 Trace element profiles of g/Ca, Sr/Ca and Ba/Ca on an annual scale. Details in Figure A2.5

T40

T40 is a *T. maxima* shell dated to 41.2 ±3 ka. One thin section measuring 11mm from the hinge was sampled. The stable isotope profile is approximately 10 years.

	Species	Length of record	Radiocarbon age	Calibrated age (ka BP)	Mean $\delta^{18}O$ (‰)	Mean $\delta^{13}C$ (‰)
T40	*T. maxima*	10	37,758±912	41.18	-0.48	1.9

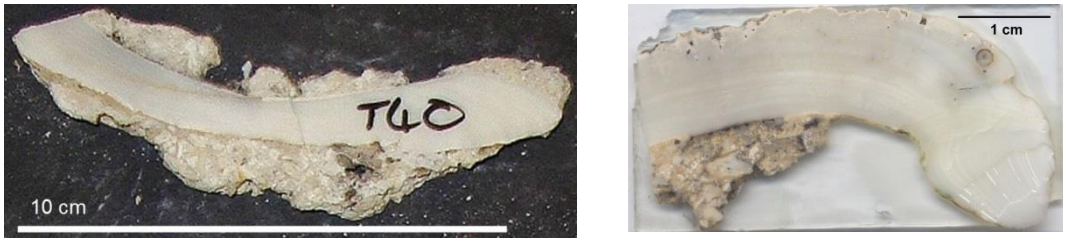

Figure A2.31 Sections *T. maxima* T40 (left) and thin section made from the hinge/inner layer (right)

Appendix

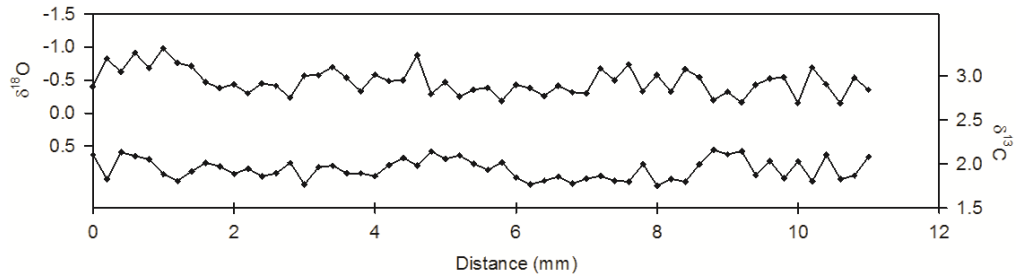

Figure A2.32 $\delta^{18}O$ (above) and $\delta^{13}C$ (below) raw profiles of T40 on a distance scale. Details in Figure A2.2

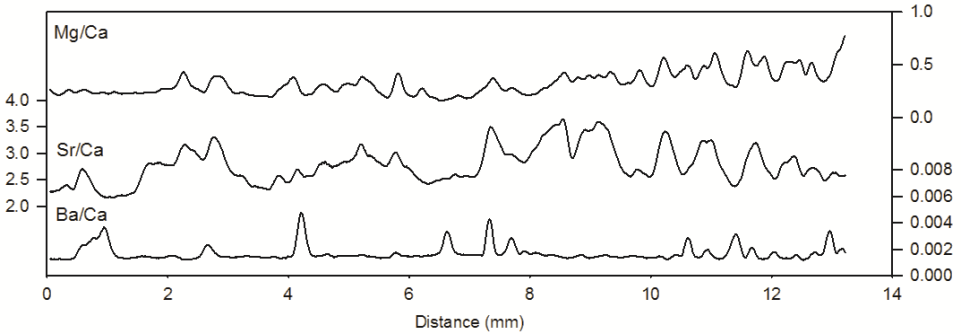

Figure A2.33 Trace element profiles of Mg/Ca, Sr/Ca and Ba/Ca on a distance scale. Details in Figure A2.3

Converting from a distance to an annual scale

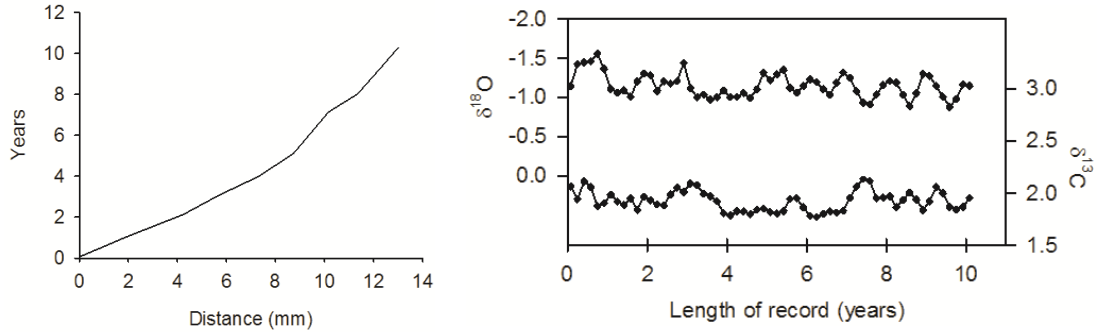

Figure A2.34 Left: Growth curve of T40, calculated using the stable isotope profile
Right: $\delta^{18}O$ (above) and $\delta^{13}C$ (below) profiles of T40 converted to an annual scale. Details in Figure A2.4

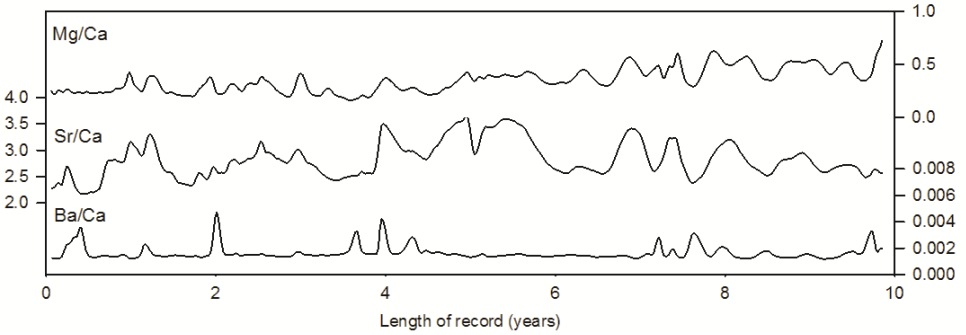

Figure A2.35 Trace element profiles of Mg/Ca, Sr/Ca and Ba/Ca on an annual scale. Details in Figure A2.5

2.4 Reef IIIb

T24

T24 is a *T. crocea* shell dated to 44.9 ka. One thin section measuring 21mm from the inner layer was sampled. The stable isotope profile is approximately 3.5 years.

	Species	Length of record	Reef Age (ka)	Extrapolated Age (ka)	Mean $\delta^{18}O$ (‰)	Mean $\delta^{13}C$ (‰)
T24	*T. crocea*	3.5	44.5-46	44.9	0.085	2.8

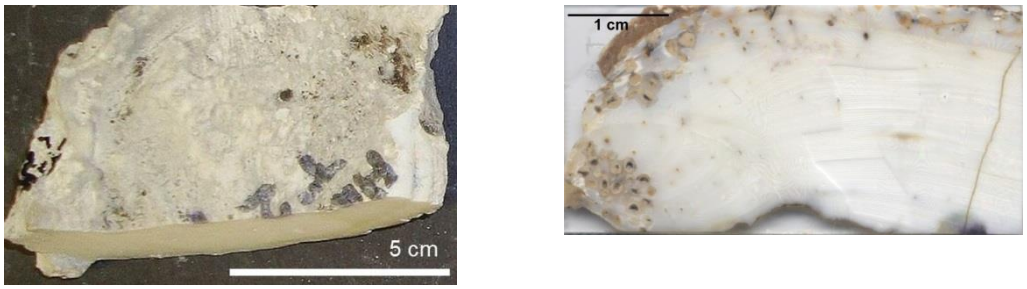

Figure A2.36 Section of Reef IIIb *T. crocea* T24 (left) and thin section made from the hinge/ inner layer (right)

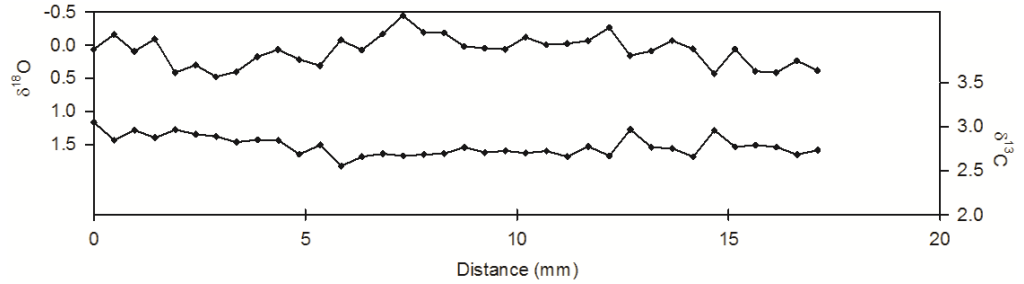

Figure A2.37 $\delta^{18}O$ (above) and $\delta^{13}C$ (below) raw profiles of T24 on a distance scale. Details in Figure A2.2

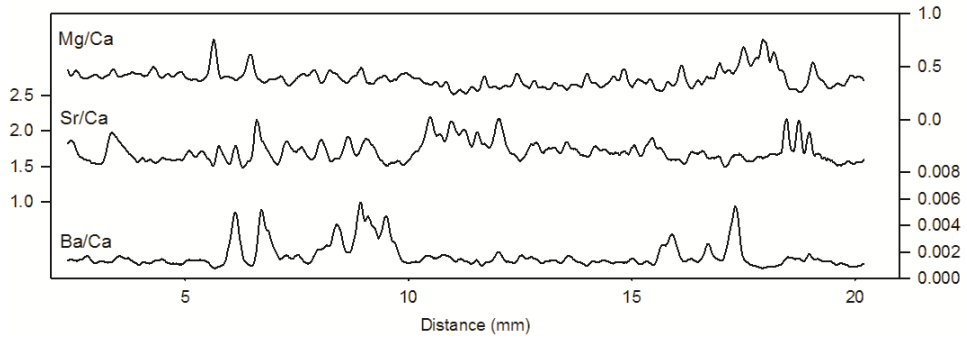

Figure A2.38 Trace element profiles of Mg/Ca, Sr/Ca and Ba/Ca on a distance scale. Details in Figure A2.3

Appendix

Converting from a distance to an annual scale

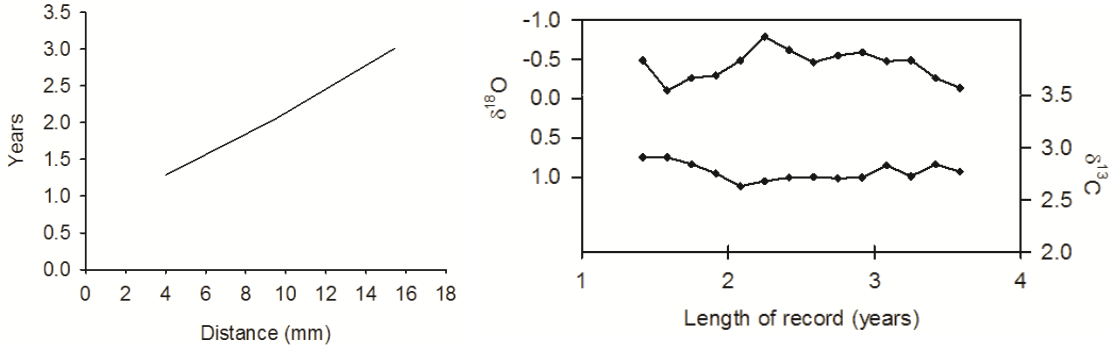

Figure A2.39 Left: Growth curve of T24, calculated using the stable isotope profile
Right: $\delta^{18}O$ (above) and $\delta^{13}C$ (below) profiles of T24 converted to an annual scale. Details in Figure A2.4

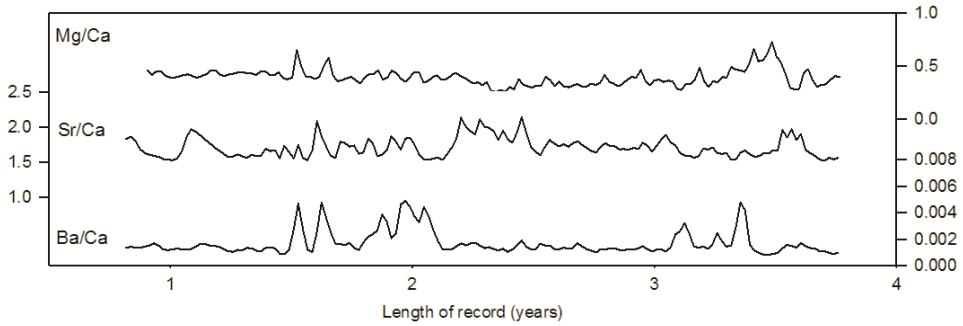

Figure A2.40 Trace element profiles of Mg/Ca, Sr/Ca and Ba/Ca on an annual scale. Details in Figure A2.5

T37

T37 is a *T. maxima* shell dated to 46 ka. One thin section measuring 32mm from the inner layer was sampled. The stable isotope profile is approximately 8 years.

	Species	Length of record	Reef Age (ka)	Extrapolated Age (ka)	Mean $\delta^{18}O$ (‰)	Mean $\delta^{13}C$ (‰)
T37	*T. maxima*	8	44.5-46	46	0.37	3

Figure A2.41 Section of Reef IIIb *T. maxima* T37 (left) and thin section made from the inner layer (right)

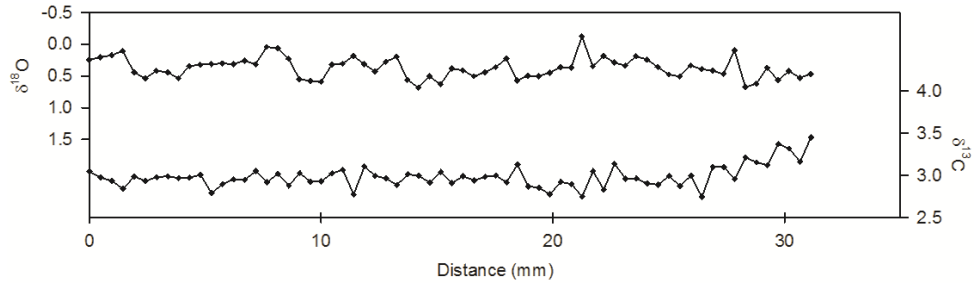

Figure A2.42 $\delta^{18}O$ (above) and $\delta^{13}C$ (below) raw profiles of T37 on a distance scale. Details in Figure A2.2

Appendix

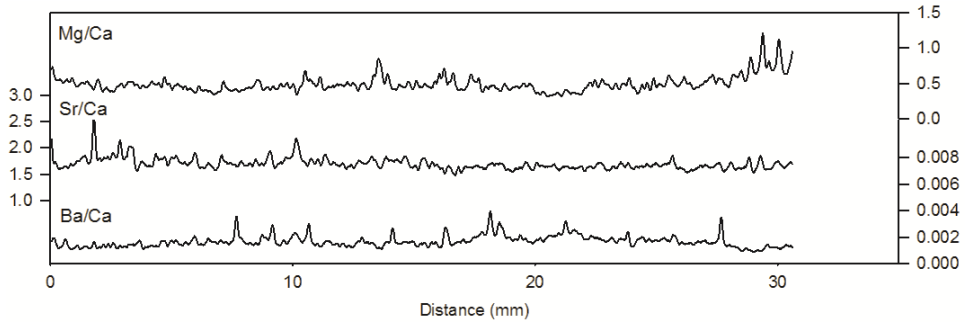

Figure A2.43 Trace element profiles of Mg/Ca, Sr/Ca and Ba/Ca on a distance scale. Details in Figure A2.3

Converting from a distance to an annual scale

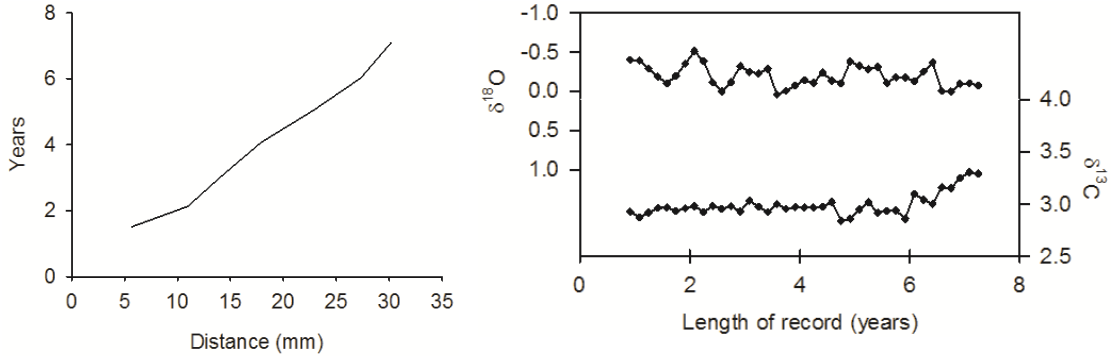

Figure A2.44 Left: Growth curve of T37, calculated using the stable isotope profile
Right: $\delta^{18}O$ (above) and $\delta^{13}C$ (below) profiles of T37 converted to an annual scale. Details in Figure A2.4

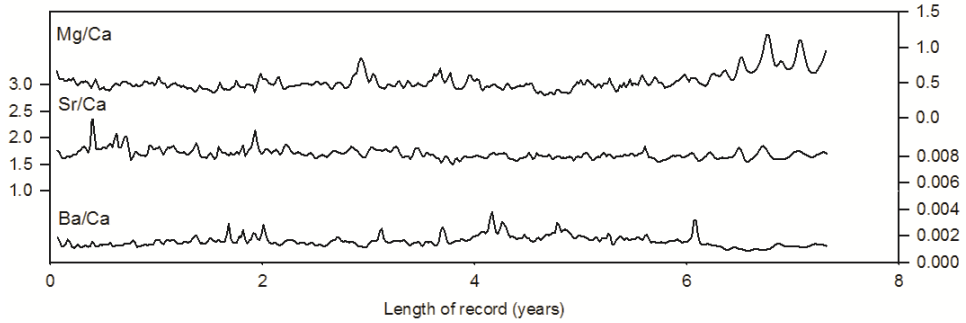

Figure A2.45 Trace element profiles of Mg/Ca, Sr/Ca and Ba/Ca on an annual scale. Details in Figure A2.5

2.5 Reef IIIa (lower): T41

T41 is a *Tridacn crocea* shell dated to 50.7 ka. One thin section measuring 16mm from the inner layer was sampled. The stable isotope profile is approximately 10 years.

	Species	Length of record	Reef Age (ka)	Extrapolated Age (ka)	Mean $\delta^{18}O$ (‰)	Mean $\delta^{13}C$ (‰)
T40	*T. crocea*	10	49-51	50.7	0.06	2.5

Appendix

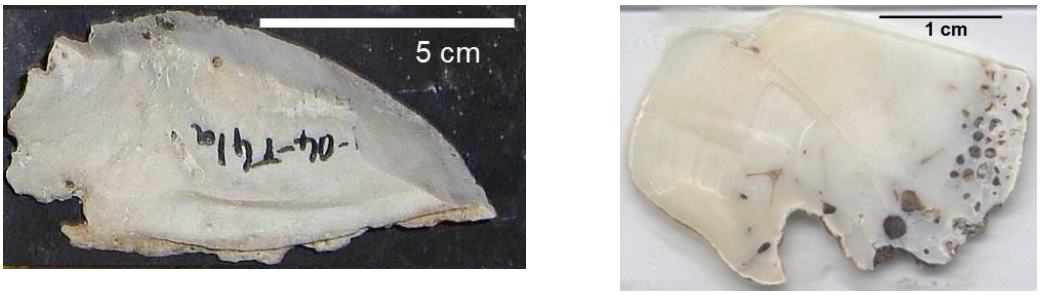

Figure A2.46 Section of Reef IIIa (l) *T. crocea* T41 (left) and thin section made from the hinge (right)

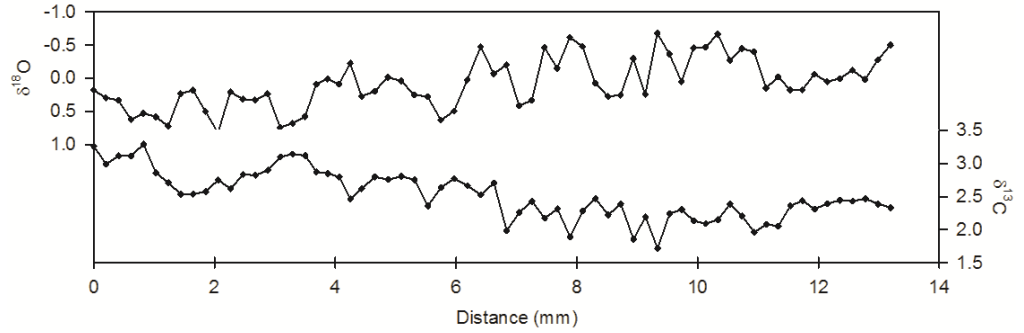

Figure A2.47 $\delta^{18}O$ (above) and $\delta^{13}C$ (below) raw profiles of T41 on a distance scale. Details in Figure A2.2

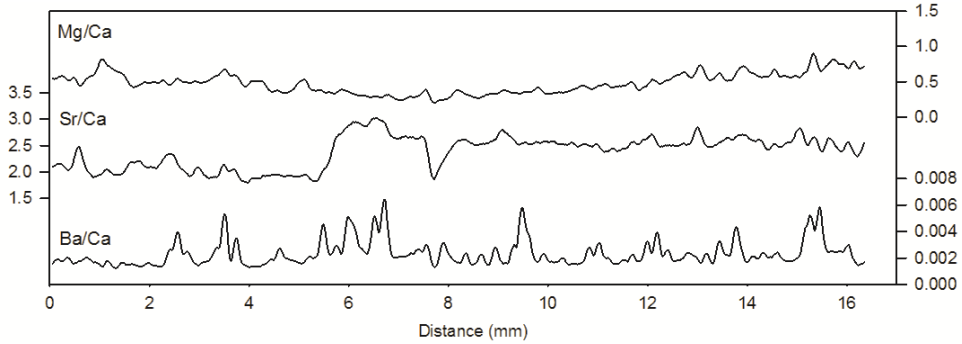

Figure A2.48 Trace element profiles of Mg/Ca, Sr/Ca and Ba/Ca on a distance scale. Details in Figure A2.3

Converting from a distance to an annual scale

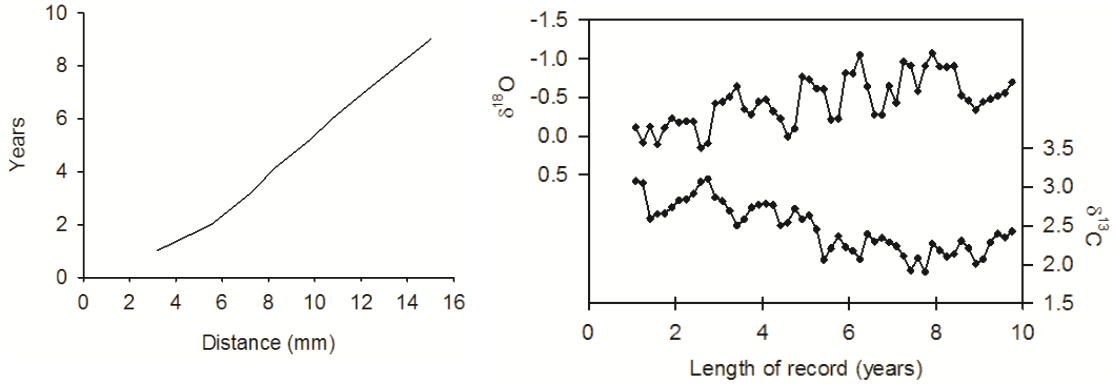

Figure A2.49 Left: Growth curve of T41, calculated using the stable isotope profile
Right: $\delta^{18}O$ (above) and $\delta^{13}C$ (below) profiles of T41 converted to an annual scale. Details in Figure A2.4

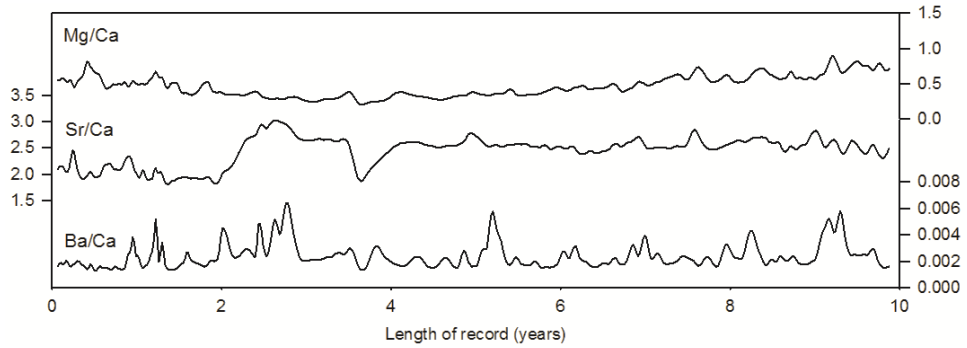

Figure A2.50 Trace element profiles of Mg/Ca, Sr/Ca and Ba/Ca on an annual scale. Details in Figure A2.5

2.6 Reef IIIa (middle): T18

T18 is a *T. gigas* dated to 52.8 ka. Two thin sections measuring 44mm from the inner layer were sampled. The stable isotope profile is approximately 8 years.

	Species	Length of record	Reef Age (ka)	Extrapolated Age (ka)	Mean $\delta^{18}O$ (‰)	Mean $\delta^{13}C$ (‰)
T18	*T. gigas*	8	52-54	52.8	-0.24	2.4

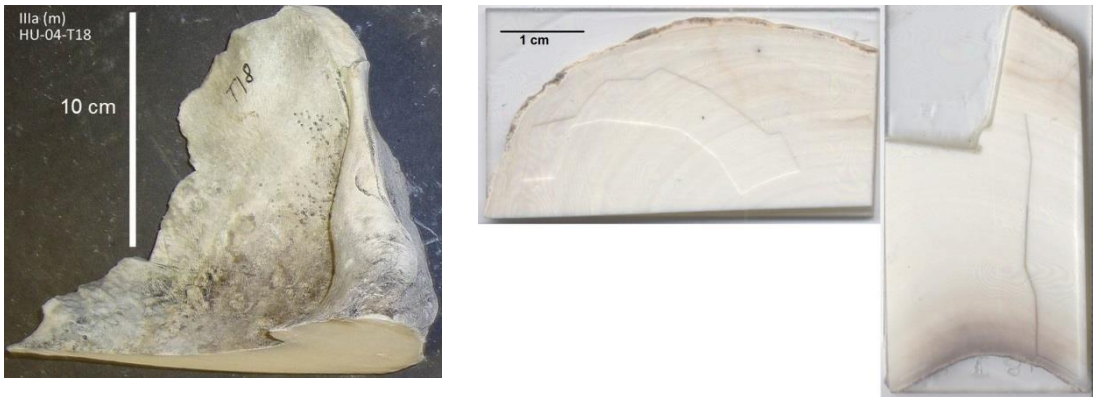

Figure A2.51 Section of Reef IIIa (m) *T. gigas* T18 (left) and thin section made from the inner layer (right)

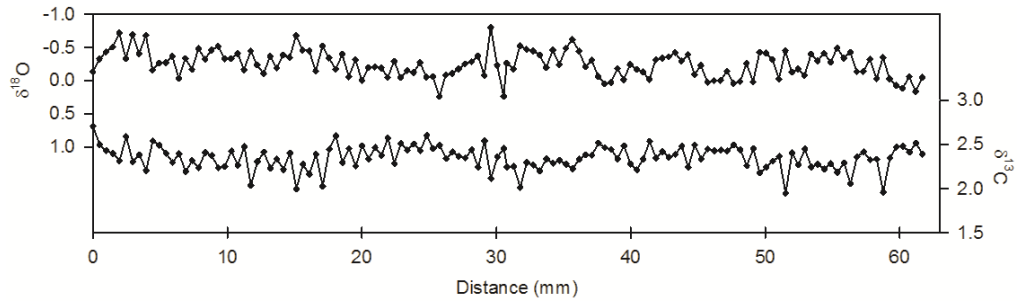

Figure A2.52 $\delta^{18}O$ (above) and $\delta^{13}C$ (below) raw profiles of T18 on a distance scale. Details in Figure A2.2

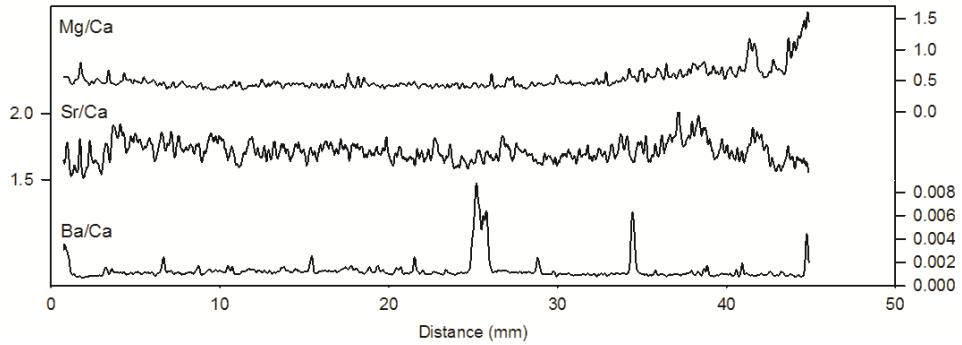

Figure A2.53 Trace element profiles of Mg/Ca, Sr/Ca and Ba/Ca on a distance scale. Details in Figure A2.3

Converting from a distance to an annual scale

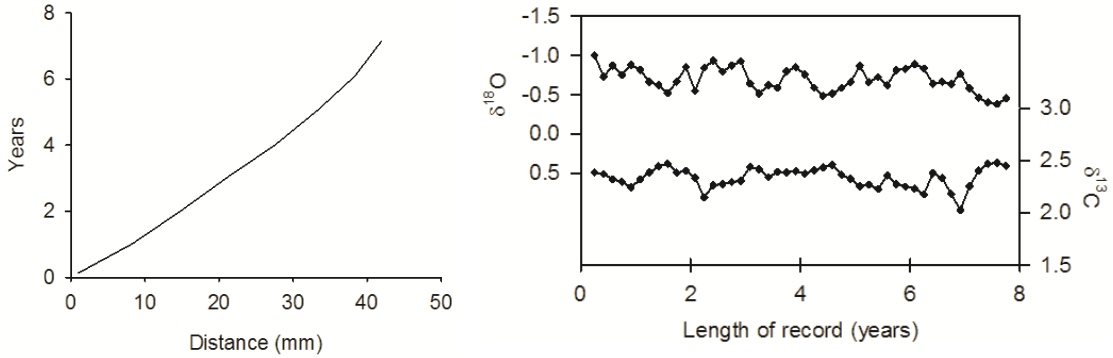

Figure A2.54 Left: Growth curve of T18, calculated using the stable isotope profile
Right: $\delta^{18}O$ (above) and $\delta^{13}C$ (below) profiles of T18 converted to an annual scale. Details in Figure A2.4

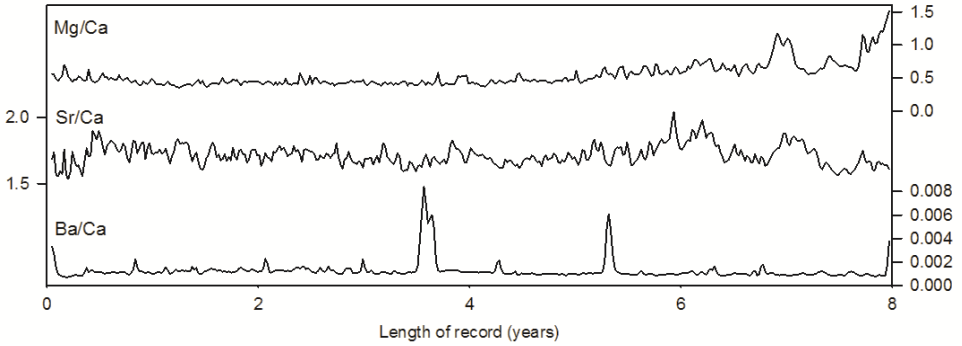

Figure A2.55 Trace element profiles of Mg/Ca, Sr/Ca and Ba/Ca on an annual scale. Details in Figure A2.5

2.7 Reef IIIa (upper)

T6

T6 is a *T. squamosa* dated to 60.7 ka. One thin section measuring approximately 16mm from the inner layer was sampled. The stable isotope profile is approximately 6 years.

	Species	Length of record	Reef Age (ka)	Extrapolated Age (ka)	Mean $\delta^{18}O$ (‰)	Mean $\delta^{13}C$ (‰)
T6	*T. squamosa*	6	60-62	60.7	0.33	3

Appendix

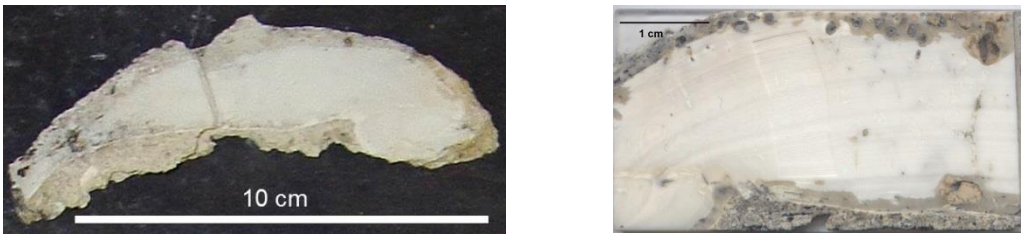

Figure A2.56 Section of Reef IIIa (u) *T. squamosa* T6 (left) and thin section made from the inner layer (right)

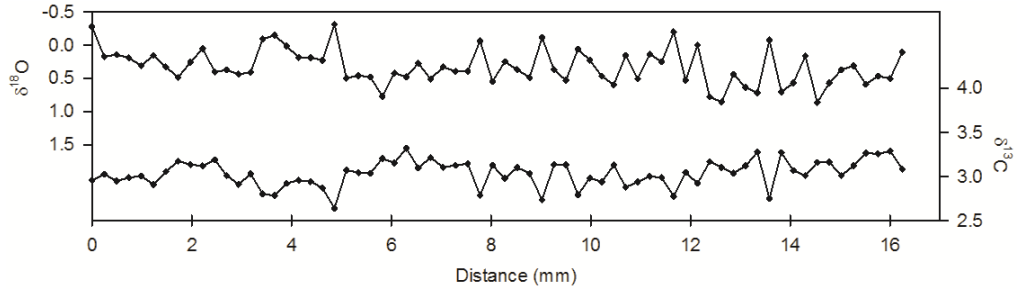

Figure A2.57 $\delta^{18}O$ (above) and $\delta^{13}C$ (below) raw profiles of T6 on a distance scale. Details in Figure A2.2

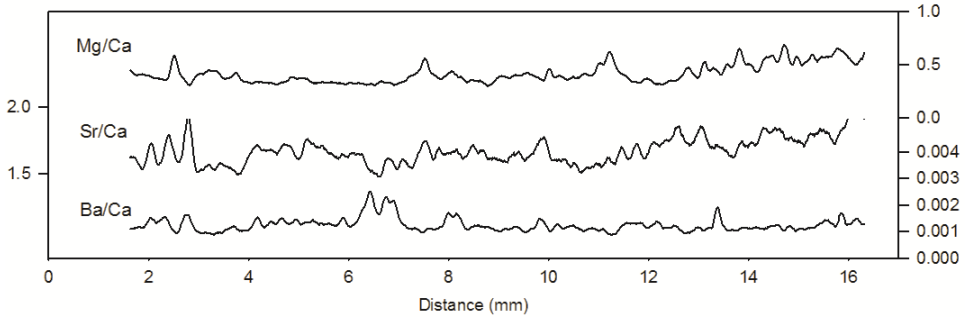

Figure A2.58 Trace element profiles of Mg/Ca, Sr/Ca and Ba/Ca on a distance scale. Details in Figure A2.3

Converting from a distance to an annual scale

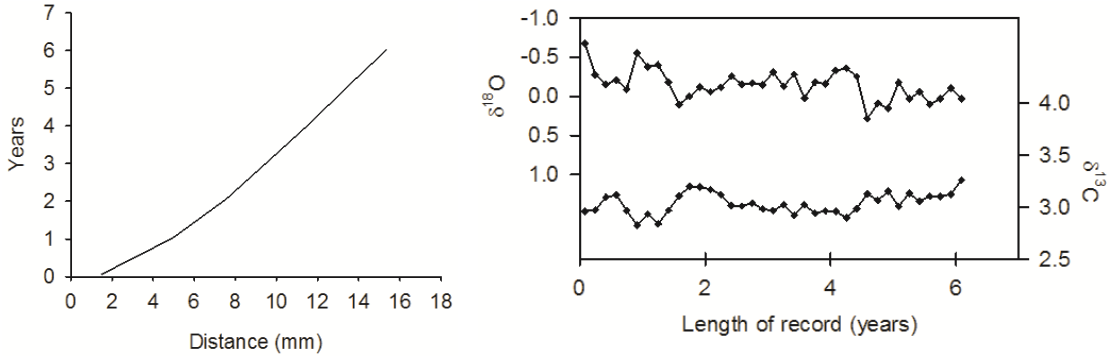

Figure A2.59 Left: Growth curve of T6, calculated using the stable isotope profile
Right: $\delta^{18}O$ (above) and $\delta^{13}C$ (below) profiles of T6 converted to an annual scale. Details in Figure A2.4

Appendix

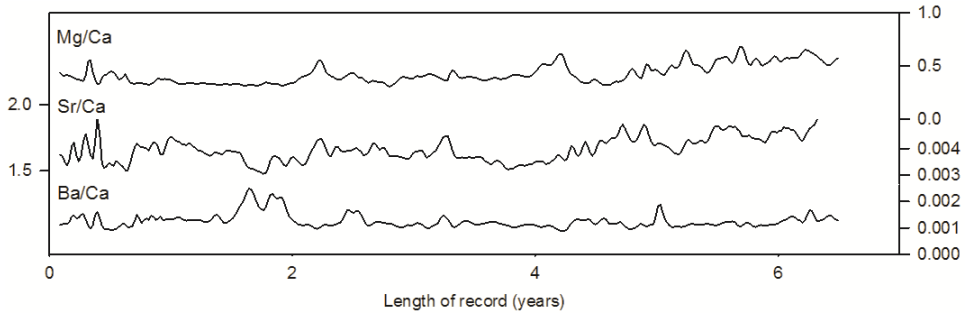

Figure A2.60 Trace element profiles of Mg/Ca, Sr/Ca and Ba/Ca on an annual scale. Details in Figure A2.5

T15

T15 is a *T. gigas* dated to 60 ka. Three thin sections measuring approximately 115mm from the hinge were sampled. The stable isotope profile is approximately 38 years.

	Species	Length of record	Reef Age (ka)	Extrapolated Age (ka)	Mean $\delta^{18}O$ (‰)	Mean $\delta^{13}C$ (‰)
T15	*T. gigas*	38	60-62	60	-0.35	2.5

Figure A2.61 Section of Reef IIIa (u) *T. gigas* T15 (left) and thin sections made from the hinge (above)

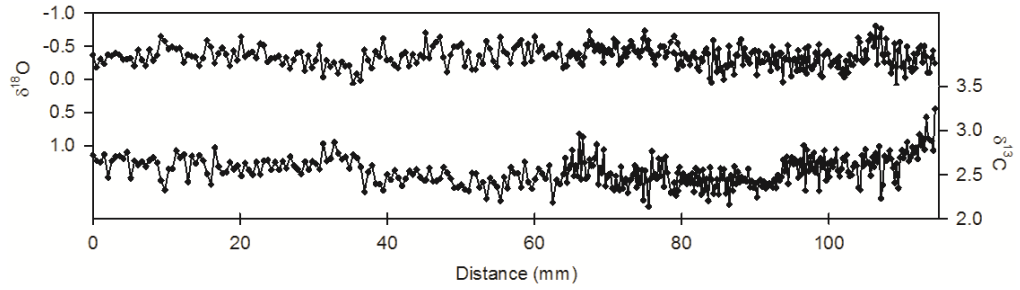

Figure A2.62 $\delta^{18}O$ (above) and $\delta^{13}C$ (below) raw profiles of T15 on a distance scale. Details in Figure A2.2

Appendix

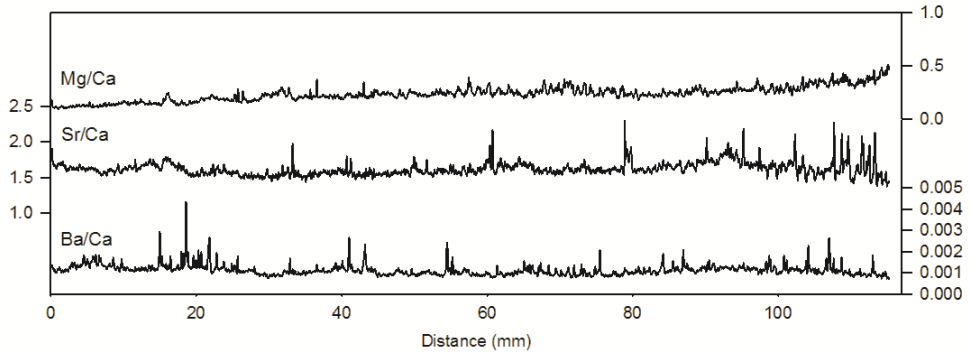

Figure A2.63 Trace element profiles of Mg/Ca, Sr/Ca and Ba/Ca on a distance scale. Details in Figure A2.3

Converting from a distance to an annual scale

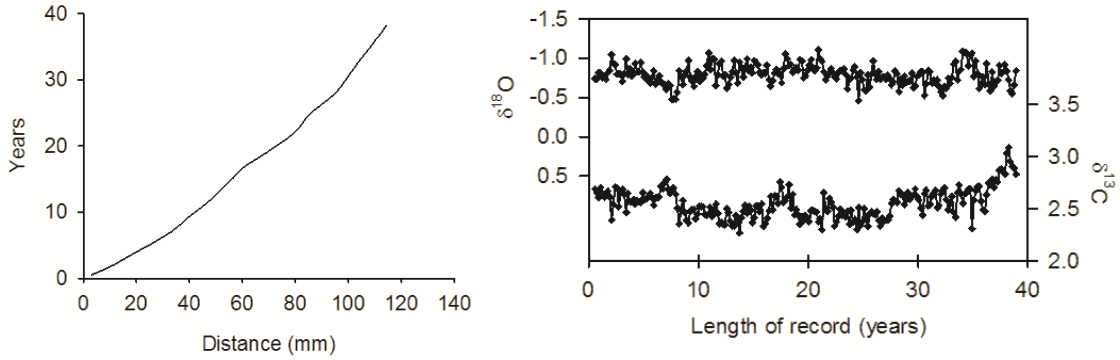

Figure A2.64 Left: Growth curve of T15, calculated using the stable isotope profile
Right: $\delta^{18}O$ (above) and $\delta^{13}C$ (below) profiles of T15 converted to an annual scale. Details in Figure A2.4

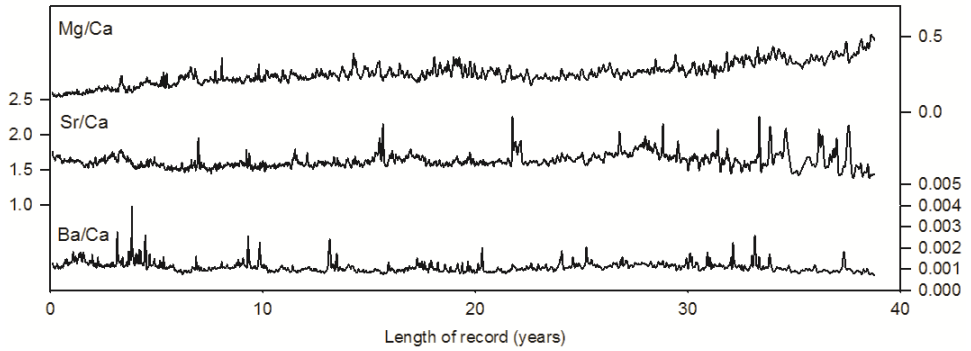

Figure A2.65 Trace element profiles of Mg/Ca, Sr/Ca and Ba/Ca on an annual scale. Details in Figure A2.5

T22

T22 is a *T. gigas* dated to 60 ka. One thin section measuring approximately 36mm (isotope sampling) or 43mm (trace element sampling) from the inner layer was sampled. The stable isotope profile is approximately 6 years.

	Species	Length of record	Reef Age (ka)	Extrapolated Age (ka)	Mean $\delta^{18}O$ (‰)	Mean $\delta^{13}C$ (‰)
T22	*T. gigas*	6	60-62	60	0.13	3

Appendix

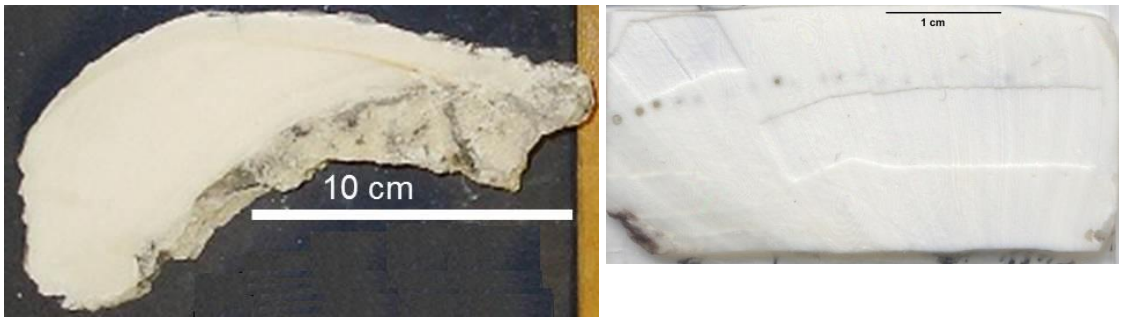

Figure A2.66 Section of Reef IIIa (u) *T. gigas* T22 (left) and thin section made from the inner layer (right)

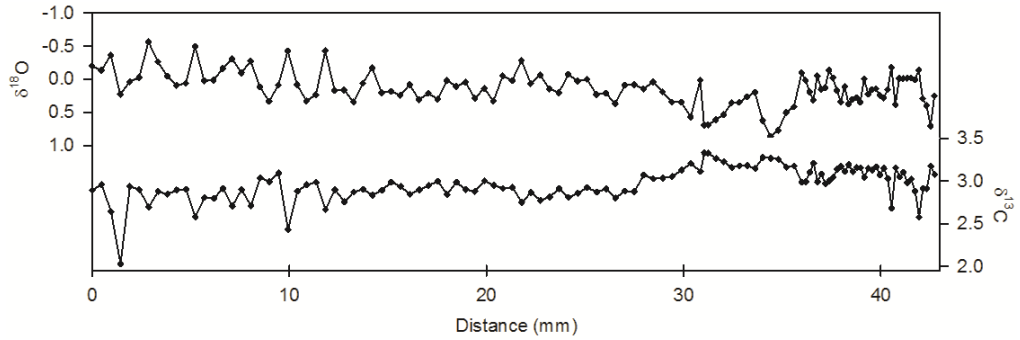

Figure A2.67 $\delta^{18}O$ (above) and $\delta^{13}C$ (below) raw profiles of T22 on a distance scale. Details in Figure A2.2

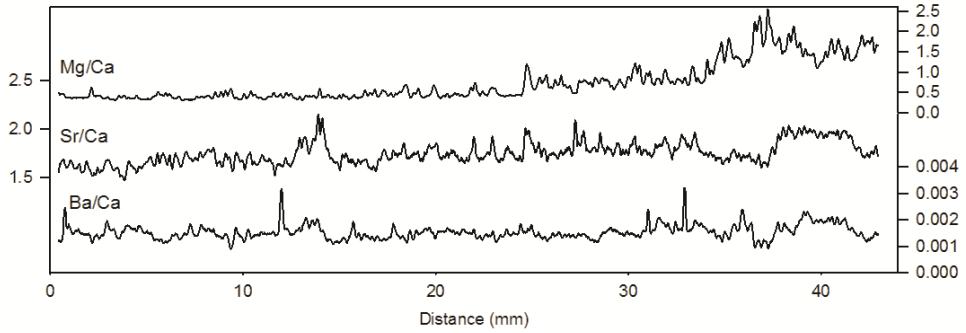

Figure A2.68 Trace element profiles of Mg/Ca, Sr/Ca and Ba/Ca on a distance scale. Details in Figure A2.3

Converting from a distance to an annual scale

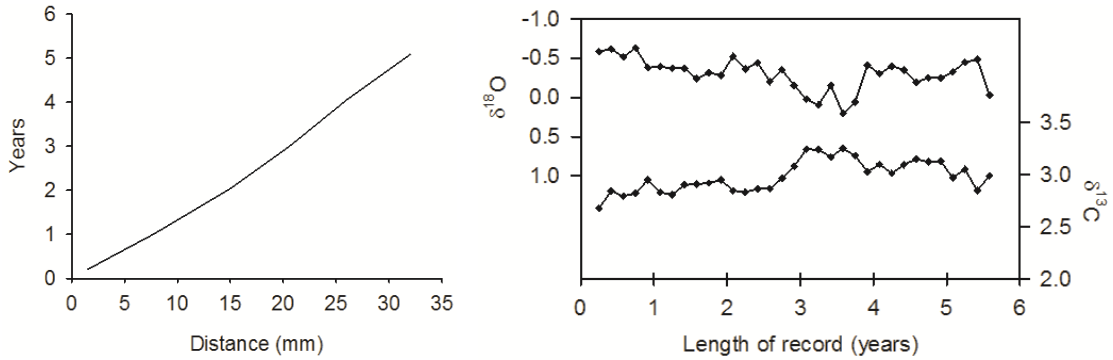

Figure A2.69 Left: Growth curve of T22, calculated using the stable isotope profile
Right: $\delta^{18}O$ (above) and $\delta^{13}C$ (below) profiles of T22 converted to an annual scale. Details in Figure A2.4

Appendix

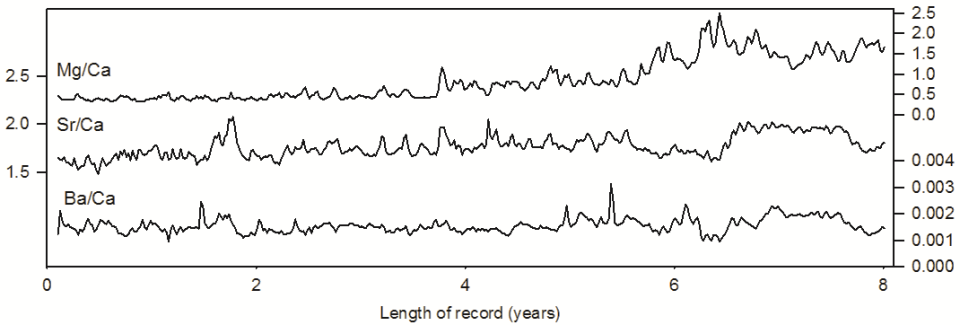

Figure A2.70 Trace element profiles of Mg/Ca, Sr/Ca and Ba/Ca on an annual scale. Details in Figure A2.5

T45

T45 is a *T. gigas* dated to 60 ka. One thin section measuring approximately 38mm from the hinge was sampled for isotopes, two measuring ~59mm were sampled for trace elements. The stable isotope profile is approximately 19 years and trace element profile is ~24 years.

	Species	Length of record	Reef Age (ka)	Extrapolated Age (ka)	Mean $\delta^{18}O$ (‰)	Mean $\delta^{13}C$ (‰)
T60	*T. gigas*	19/24	60-62	60	0.19	2.9

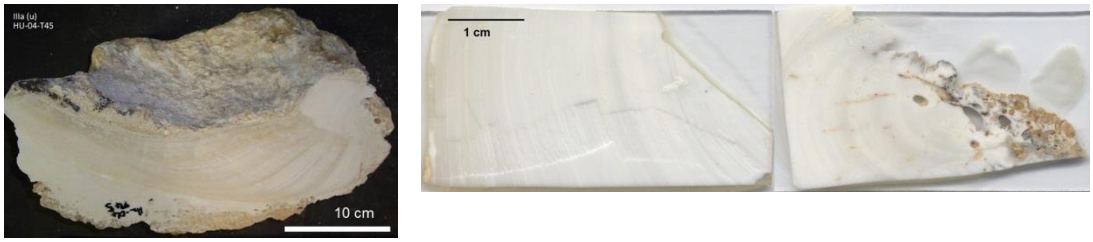

Figure A2.71 Section of Reef IIIa (u) *T. gigas* T45 (left) and thin section made from the hinge (right)

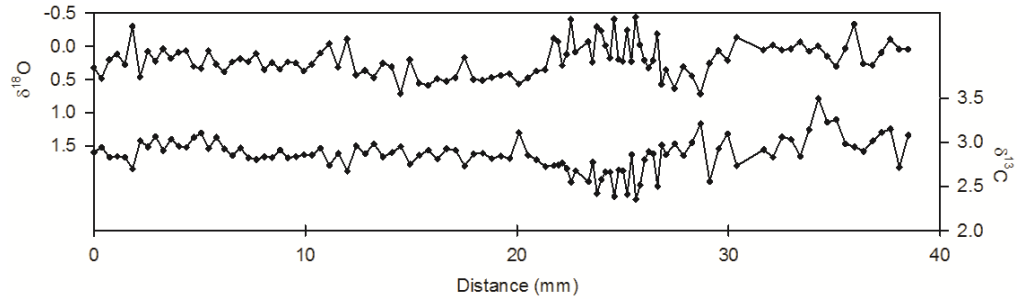

Figure A2.72 $\delta^{18}O$ (above) and $\delta^{13}C$ (below) raw profiles of T45 on a distance scale. Details in Figure A2.2

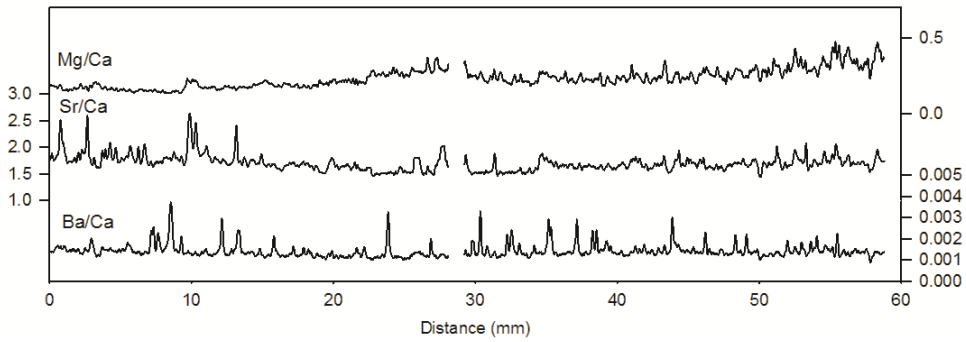

Figure A2.73 Trace element profiles of Mg/Ca, Sr/Ca and Ba/Ca on a distance scale. Details in Figure A2.3

Appendix

Converting from a distance to an annual scale

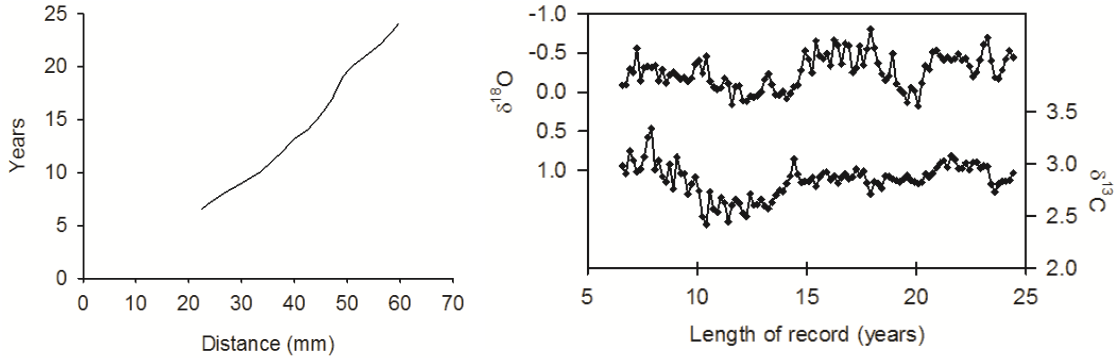

Figure A2.74 Left: Growth curve of T45, calculated using the stable isotope profile
Right: $\delta^{18}O$ (above) and $\delta^{13}C$ (below) profiles of T45 converted to an annual scale. Details in Figure A2.4

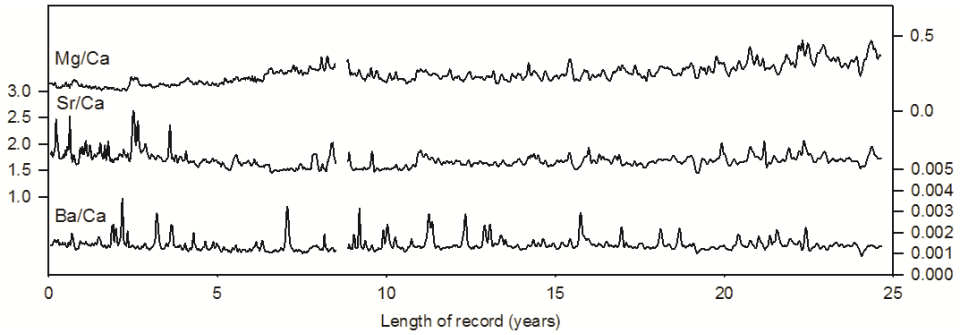

Figure A2.75 Trace element profiles of Mg/Ca, Sr/Ca and Ba/Ca on an annual scale. Details in Figure A2.5

Shells sampled for trace elements only

T38

T38 is a *T. crocea* dated to 60.9 ka. One thin section measuring approximately 16mm from the inner layer was sampled. The trace element profile is approximately 9 years.

	Species	Length of record	Reef Age (ka)	Extrapolated Age (ka)	Bulk $\delta^{18}O$ (‰)
T38	*T. crocea*	9	60-62	60.9	0

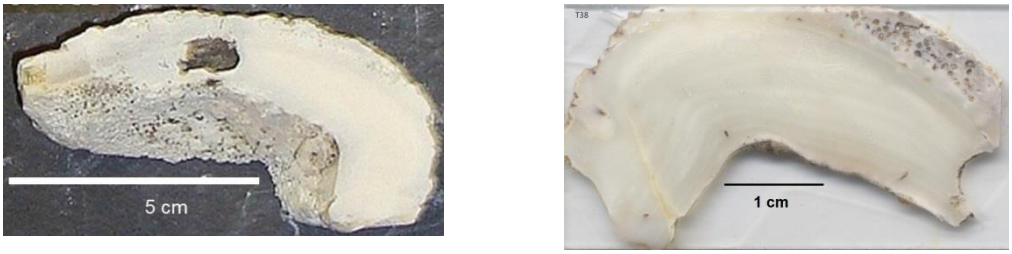

Figure A2.76 Section of Reef IIIa (u) *T. crocea* T38 (left), thin section made from hinge and inner layer (right)

Appendix

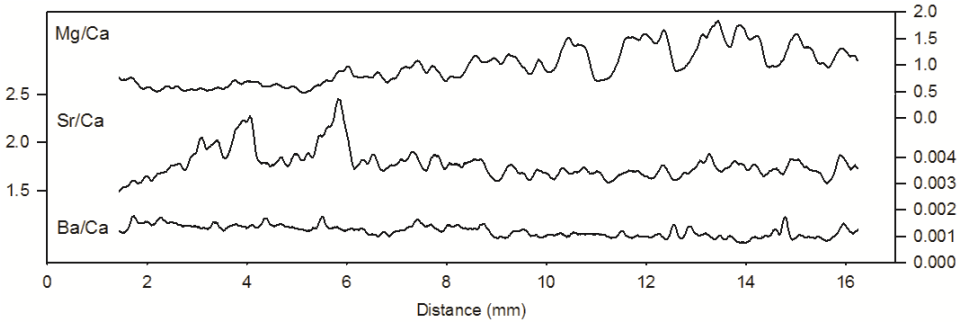

Figure A2.77 Trace element profiles of Mg/Ca, Sr/Ca and Ba/Ca on a distance scale. Details in Figure A2.3

Converting from a distance to an annual scale

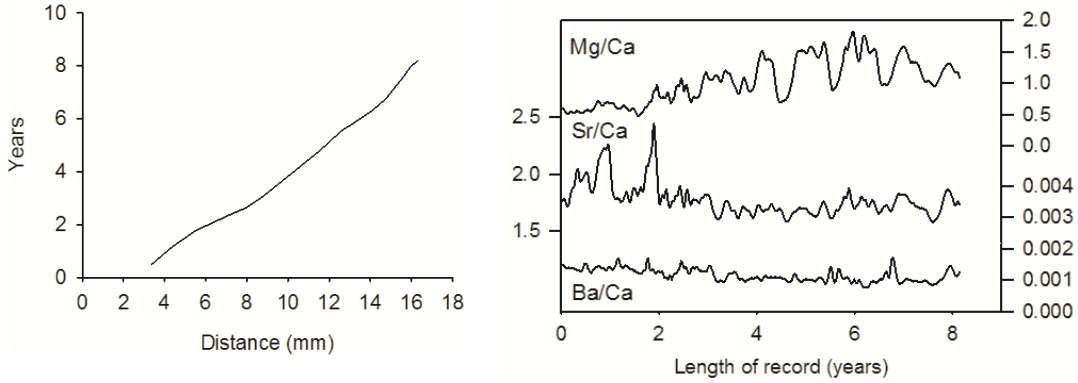

Figure A2.78 Left: Growth curve of T38, calculated using the trace element profile
Right: Trace element profiles of Mg/Ca, Sr/Ca and Ba/Ca on an annual scale. Details in Figure A2.5

T44

T44 is a *T. maxima* dated to 60±4 ka. One thin section measuring approximately 18mm from the inner layer was sampled. The trace element profile is approximately 8 years.

	Species	Length of record	Reef Age (ka)	Extrapolated Age (ka)	Bulk $\delta^{18}O$ (‰)
T44	*T. maxima*	8	60-62	60	-0.1

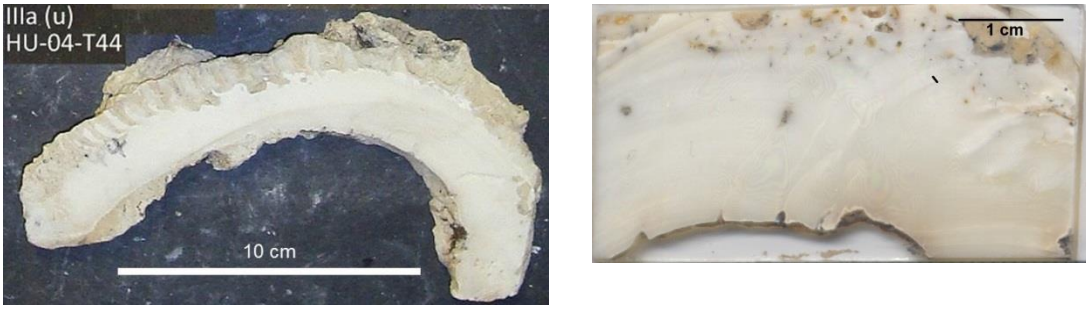

Figure A2.79 Section of Reef IIIa (u) *T. maxima* T44 (left), thin section made from hinge and inner layer (right)

Appendix

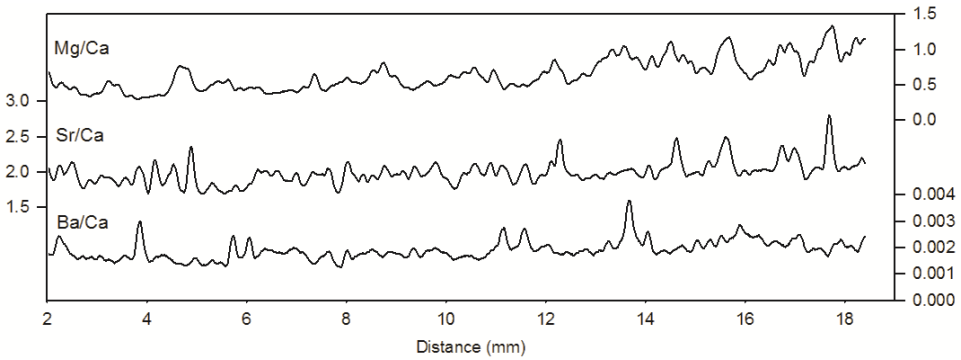

Figure A2.80 Trace element profiles of Mg/Ca, Sr/Ca and Ba/Ca on a distance scale. Details in Figure A2.3

Converting from a distance to an annual scale

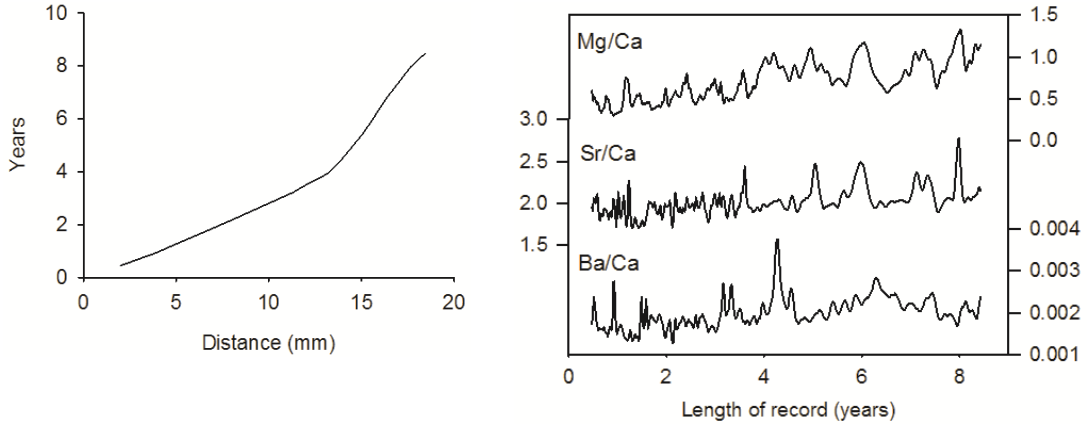

Figure A2.81 Left: Growth curve of T44, calculated using the trace element profile
Right: Trace element profiles of Mg/Ca, Sr/Ca and Ba/Ca on an annual scale. Details in Figure A2.5

3. Comparison of bulk and mean results

Bulk values of $\delta^{18}O$, taken by sampling across all the growth lines of the hinge or inner layer of fossil shells with a handheld drill, were measured in 34 fossil shells from the Holocene and MIS3, and are presented in Welsh (2009). These differ by up to 0.4‰ in the Holocene shells, and 0.5‰ in the MIS3 shells (Figure A3.1). There are several potential reasons for these differences. Mean $\delta^{18}O$ was measured using samples obtained using a MicroMill while bulk $\delta^{18}O$ was measured using a handheld drill. Sampling with a MicroMill measured $\delta^{18}O$ at discrete intervals, and in a number of shells alternate samples were measured, while sampling with a handheld drill measured across all growth lines. There could be a bias with the bulk $\delta^{18}O$ representing more of the juvenile portion of growth.

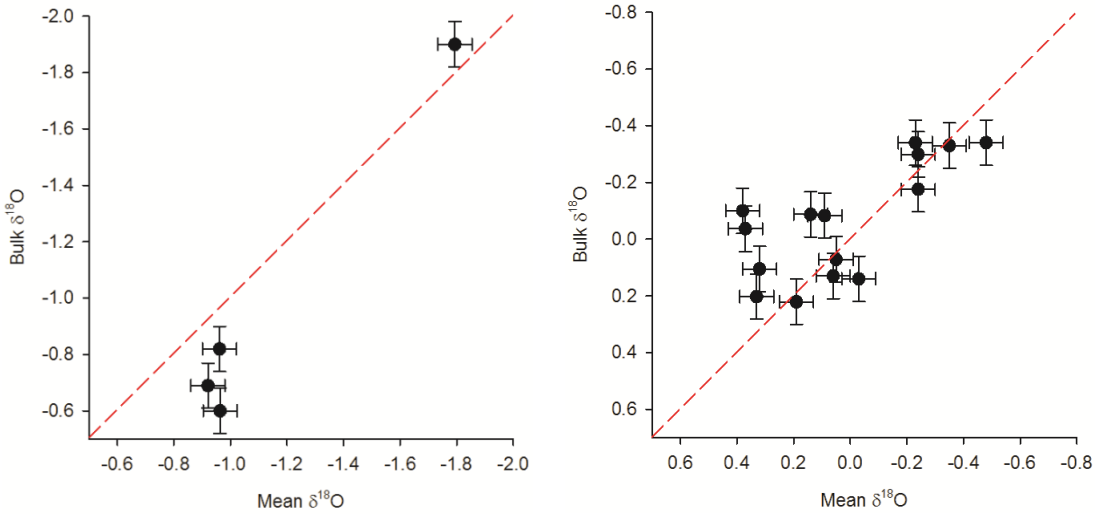

Figure A3.1 Bulk and mean $\delta^{18}O$ measured in Holocene *T. gigas* shells (right) and MIS3 *Tridacna* sp. (left). Dashed line represents equal values of bulk and mean $\delta^{18}O$

4. Comparison of detrending methods

In this study, two shells (T58 and T41) show trends in $\delta^{18}O$ data. In order to examine changes in inter-annual variability as an ENSO signal, these trends were removed in order to not skew the data. Several methods of removing these trends were tested and are shown in the following sections.

48 month running average

One method of removing trends in the $\delta^{18}O$ data is to subtract the 48 month running average from the original time series. This requires padding at either end of the time series.

Polynomial detrending

Another method of detrending is to calculate the first order (linear) and second order polynomial equation for the time series, and then subtracting this from the original $\delta^{18}O$.

Appendix

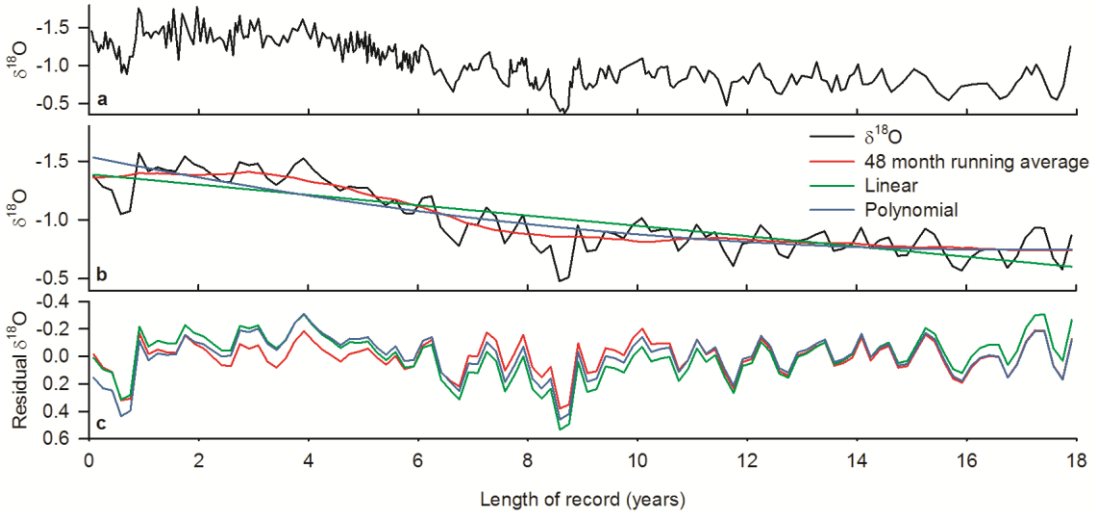

Figure A4.1 Comparison of detrending methods in Holocene *T. gigas* T58 $\delta^{18}O$ record.
a: original $\delta^{18}O$ data series, corrected for ice volume (Chapter 4)
b: $\delta^{18}O$ interpolated to 6 samples a year. Shown are the 48 month running average, and the linear and polynomial fits for the data.
c: $\delta^{18}O$ residual produced by subtracting each of the three fits from b.

The standard deviation of the residual $\delta^{18}O$ time series produced by each method can be compared to the standard deviation of the original $\delta^{18}O$ time series to see the effect detrending has on the data (Figure A4.2). On the whole, the three detrending methods produce similar standard deviation to the original time series, with the exception of samples which have a trend in the raw data series. In these samples (T58 and T41), detrending reduces the standard deviation by at least 0.1.

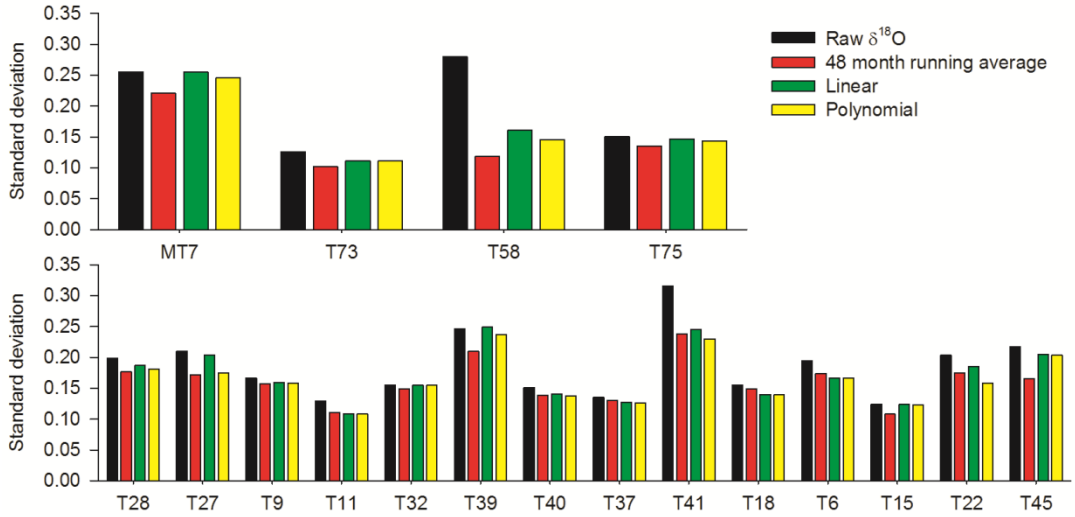

Figure A4.2 Comparison of the standard deviation of the original $\delta^{18}O$ time series and the residual $\delta^{18}O$ time series. Top panel shows the modern and Holocene shells, bottom panel shows the MIS3 shells.

Appendix

References

AHARON, P. 1991. Recorders of reef environment histories: stable isotopes in corals, giant clams and calcareous algae. *Coral Reefs,* 10**,** 71-90.

ELLIOT, M., WELSH, K., CHILCOTT, C., MCCULLOCH, M., CHAPPELL, J. & AYLING, B. 2009. Profiles of trace elements and stable isotopes derived from giant long-lived *Tridacna gigas* bivalves: Potential applications in paleoclimate studies. *Palaeogeography, Palaeoclimatology, Palaeoecology,* 280**,** 132-142.

PUGH, D. T. & RAYNER, R. F. 1981. The Tidal Regimes of 3 Indian-Ocean Atolls and some Ecological Implications. *Estuarine Coastal and Shelf Science,* 13**,** 389-407.

PÄTZOLD, J., HEINRICHS, J. P., WOLSCHENDORF, K. & WEFER, G. 1991. Correlation of Stable Oxygen Isotope Temperature Record with Light Attenuation Profiles in Reef-Dwelling *Tridacna* shells. *Coral Reefs,* 10**,** 65-69.

WATANABE, T., MINAGAWA, M., OBA, T. & WINTER, A. 2001. Pretreatment of coral aragonite for Mg and Sr analysis: Implications for coral thermometers. *Geochemical Journal,* 35.

WATANABE, T., SUZUKI, A., KAWAHATA, H., KAN, H. & OGAWA, S. 2004. A 60-year isotopic record from a mid-Holocene fossil giant clam (*Tridacna gigas*) in the Ryukyu Islands: physiological and paleoclimatic implications. *Palaeogeography, Palaeoclimatology, Palaeoecology,* 212**,** 343-354.

WELSH, K., ELLIOT, M., TUDHOPE, A., AYLING, B. & CHAPPELL, J. 2011. Giant bivalves (*Tridacna gigas*) as recorders of ENSO variability. *Earth and Planetary Science Letters,* 307**,** 266-270.